

Microfabricated Electrospray Thrusters for a Modular Spacecraft Propulsion System

THÈSE N° 6437 (2014)

PRÉSENTÉE LE 31 OCTOBRE 2014

À LA FACULTÉ DES SCIENCES ET TECHNIQUES DE L'INGÉNIEUR
LABORATOIRE DES MICROSYSTÈMES POUR LES TECHNOLOGIES SPATIALES
PROGRAMME DOCTORAL EN MICROSYSTÈMES ET MICROÉLECTRONIQUE

ÉCOLE POLYTECHNIQUE FÉDÉRALE DE LAUSANNE

POUR L'OBTENTION DU GRADE DE DOCTEUR ÈS SCIENCES

PAR

Simon DANDAVINO

acceptée sur proposition du jury:

Dr G. Boero, président du jury
Prof. H. Shea, directeur de thèse
Dr R. Krpoun, rapporteur
Prof. J. A. Schiffmann, rapporteur
Prof. J. Stark, rapporteur



ÉCOLE POLYTECHNIQUE
FÉDÉRALE DE LAUSANNE

Suisse
2014

I'm a very lazy man
but my curiosity always overwhelms my laziness.
— Gatis

To all those who came before me and paved the road...

Acknowledgements

It is rare in life that one encounters the chance to so completely dedicate himself to such a noble endeavour, over such a period, as is the case with a PhD thesis. As in any great journey, great moments abound, and so do darker ones. In both cases, it is a privilege to be able to count on family, friends, team mates and colleagues for support, encouragement and praise.

To my family, and especially my parents Nicole and Adrien, thank you for supporting me throughout all these years. Thank you for understanding my desire to discover the world, and letting me feel at home so far from home. Mylène and Frédéric, I am sure that it is the dynamic environment that we created at home which led me here. Thank you for always being there, I can only look forward to the day when we can again live close to each other.

My friends, near and far, you are what makes life worth living. Mel, Mireille, Jörg, Blanca, Jasmine, every time I see you feels like the last time was yesterday, which I think is all that needs to be said. To the newer ones, that I made here in Switzerland, I will not name you, for you are legion, but you should know that you are why I am here.

I would like also to express my gratitude to my team mates in Flying Angels Bern and Budwig who have so graciously accepted me within their ranks. You brought me balance, comfort, relief and the chance to learn so much about myself. Angels, the journeys that we experienced together reflected in so many ways the one of this thesis. You taught me resilience, courage and the desire to reach beyond my limits.

And to my colleagues at LMTS and SAMLAB, thank you for your presence throughout these four years. It was a pleasure to share so much time with you, from the coffee breaks to the lab journeys, not forgetting FBC of course. Most importantly, thank you for your advice and your willingness to share your knowledge. Çağlar Ataman, who knows where I would be without your unwavering dedication to the MicroThrust project? And Dan Courtney, your expertise in this last year truly inspired me to deepen my own.

I would like to thank my supervisor, Herbert Shea, who believed in me even when I was not sure if I believed in myself. Thank you for your accessibility, advice and trust. Being able to count on such a skilful and kind supervisor is a privilege that not all students can enjoy.

Finally, I extend my deepest gratitude to my jury committee, Prof. Jürg Schiffmann, Prof. John. P. W. Stark, Dr. Renato Krpoun and the jury president Dr. Giovanni Boero who graciously accepted to review this work. Thank you for sacrificing your time to help me improve it.

Neuchâtel, September 3rd 2014

S. D.

Abstract

With the growing capabilities of miniature components and systems, scientific and exploration missions making use of small spacecraft (<100kg) are becoming increasingly promising. The realization of these missions would launch a new era of space exploration, no longer the preserve of large space agencies. Unfortunately, such missions are held back by the lack of a critical technology, a small and efficient propulsion system capable of delivering sufficient velocity changes (ΔV) to complete orbital manoeuvres.

This thesis describes the development of such a system, focusing on the microfabricated electrospray emitter arrays at the core of the thruster. Each emitter aims to operate in the Purely Ionic Regime (PIR), electrically generating a spray of charged molecules and optimizing the propellant usage (specific impulse). Micromachined in silicon, the thrusters boast unmatched precision and integration, with up to 1527 emitters/cm² achieved. For the first time, two-level electrodes are integrated at wafer level, providing extraction and post-acceleration to each emission site. In addition to significantly increased performance, the post-acceleration electrodes enable several new system features (tunable power consumption, thrust and specific impulse) essential to the system. The emitters themselves, 100 μm tall capillaries fabricated by Deep Reactive Ion Etch, have inner diameters as low as $6.9 \pm 0.19\mu m$, the smallest to date. The thrusters were characterized with specific attention to the sprayed beam composition and the effect of the accelerator electrodes. Upwards of 90% ionic content was measured, a record for this type of devices. Operation of the accelerator electrodes was also validated, showing that, as expected, the accelerators did not affect the emission process but successfully improved the performance of the thruster by focusing the beam and increasing the energy of the particles.

In addition to the thruster development, several fundamental aspects of the electrospray emitters were studied. In-situ Scanning Electron Microscope experiments were carried out to understand the spray formation mechanisms and a detailed study of the propellant transport in the capillaries was presented.

Finally, a new type of emitters, fabricated entirely of insulating materials and applied to mass spectrometry was investigated, providing an Earth-based application to the thruster technology.

Keywords: electrospray thrusters, small spacecraft propulsion, microfabrication, high voltage SEM observations, ESI-MS

Résumé

Avec les capacités grandissantes des systèmes et composantes miniaturisées, les missions scientifiques et d'exploration spatiale faisant usage de petits engins spatiaux (<100kg) sont de plus en plus prometteuses. La concrétisation de ces missions lancerait une nouvelle ère d'exploration spatiale, n'étant plus la chasse-gardée des grandes agences spatiales. Malheureusement, de telles missions sont retenues par l'absence d'une technologie critique : un système de propulsion compact et efficace capable de générer suffisamment de changement de vitesse (ΔV) pour compléter des manœuvres orbitales.

Cette thèse décrit le développement d'un tel système, se penchant sur les matrices d'émetteurs micro-fabriqués au cœur du propulseur. Chaque émetteur génère par électronébulisation un jet de particules chargées. Fonctionnant dans un Régime Purement Ionique (RPI), l'utilisation de carburant (impulsion spécifique) est optimisée. Fabriqué en silicium, le propulseur présente une précision et un niveau d'intégration inégalés, avec des densités de 1527 émetteurs/cm². Pour la première fois, deux niveaux d'électrodes sont intégrés, et ce au niveau tranche, fournissant une capacité d'extraction et d'accélération à chaque émetteur. En plus des performances augmentées, l'ajout de la post-accélération amène plusieurs nouvelles capacités (consommation de puissance, poussée et impulsion spécifique accordables) essentielles au système. Les émetteurs, des capillaires de 100 μm de hauteur fabriqué par gravure par ions réactifs profonde (DRIE), ont des diamètres intérieurs allant jusqu'à $6.9 \pm 0.19 \mu m$, les plus petits jamais fabriqués pour cette application. Le propulseur fut caractérisé avec une attention particulière à la composition du jet émis, ainsi qu'aux effets des électrodes d'accélération. Plus de 90% d'ions fut mesuré dans le jet, un record pour ce type d'émetteurs. Le fonctionnement des électrodes d'accélération fut aussi validé, démontrant que, comme prévu, l'accélération n'affectait pas le processus d'émission mais pouvait améliorer la performance du propulseur en concentrant le jet et en augmentant l'énergie des particules émises.

En plus du système de propulsion, plusieurs aspects fondamentaux des émetteurs furent étudiés. Des expériences d'électronébulisation avec observation in-situ au microscope électronique à balayage furent complétées pour mieux comprendre les mécanismes de formation du jet et une étude détaillée du transport du carburant dans les capillaires fut présentée.

Finalement, un nouveau type d'émetteurs, fabriqués entièrement de matériaux isolants et agissant comme ionisateur pour la spectrométrie de masse fut présenté, fournissant une application terrestre à la technologie de propulsion.

Mots-clés : propulsion par électronébulisation, propulsion de petits engins spatiaux, microfabrication, observations SEM à haut voltage, ESI-MS

Contents

Acknowledgements	v
Abstract (English/Français)	vii
List of figures	xix
List of tables	xxi
List of symbols	xxiii
List of publications	xxv
Journal Papers	xxv
Conference proceedings	xxv
Conference proceedings	xxvi
1 Introduction	1
1.1 Interest in small spacecraft missions	1
1.2 Propellant usage of small propulsion systems	3
1.3 Fundamentals of electrospray propulsion	5
1.4 A brief history of electrospray propulsion	8
1.4.1 Early activities	8
1.4.2 Rebirth of electrosprays - American contributions	10
1.4.3 Recent European efforts	14
1.5 The MicroThrust initiative	17
1.6 Summary	21
1.6.1 Thesis novelty	21
1.6.2 Thesis structure	22
2 Electrospray thrusters - Design	23
2.1 Accelerators to improve thruster performance	24
2.1.1 Added features	26
2.2 Capillary emitter design	27
2.3 Electrostatic design	32
2.3.1 Onset voltage model	32
2.3.2 Ion beam optics	42

Contents

2.3.3	Energy and angular efficiency	49
2.4	Electrode erosion and emitter pitch	50
2.5	Final design	52
2.5.1	MicroThrust chips (v3a)	52
2.5.2	High density design (v3b)	53
2.5.3	Performance estimates	55
2.6	Summary	58
3	Electrospray thrusters - Fabrication	59
3.1	Introduction	60
3.2	Capillary emitter wafer	60
3.3	Extraction and acceleration electrode wafer	69
3.4	Wafer-level integration	71
3.5	Principal issues	74
3.5.1	Blocked emitters	74
3.5.2	Emitter-extractor leakage current	78
3.6	Main achievements	80
3.6.1	Overview of fabricated MicroThrust devices	82
3.7	Summary	84
4	Electrospray thrusters - Validation	85
4.1	Setup and assembly	86
4.2	Results and analysis	88
4.2.1	IV characteristics	88
4.2.2	Energy measurements	90
4.2.3	Beam shape measurements	92
4.2.4	Time-of-Flight and performance measurements	94
4.2.5	Stability - Long term tests	97
4.3	Conclusion	100
5	In-situ electrospray SEM observations	101
5.1	Introduction	101
5.2	Setup and procedure	107
5.2.1	Conditions for testing in the SEM	107
5.2.2	Sample description	108
5.2.3	Assembly	113
5.2.4	Voltage application	115
5.3	Results and analysis	122
5.3.1	Liquid deformation	122
5.3.2	Successful emission	126
5.4	Summary	132

6 Conclusion	133
6.1 Future work	135
Bibliography	151
Appendices	153
A Liquid transport and containment	155
A.1 Contact angle measurements	156
A.1.1 Setup and procedure	156
A.1.2 Results and analysis	159
A.2 Capillary filling and holding pressure model	162
A.2.1 Introduction	162
A.2.2 Model description	163
A.2.3 Model summary	171
A.2.4 Experimental validation of holding pressure	176
A.3 Liquid retention under vibration and shock	177
A.3.1 Vibration tests	178
A.3.2 Shock tests	183
A.4 Summary of liquid transport and containment	188
B Insulating electrospray ionisers for mass spectrometry	189
B.1 An overview of electrospray ionisers for mass spectrometry	190
B.2 Design and fabrication	195
B.2.1 Onset voltage simulations	198
B.2.2 Fabrication	201
B.3 Test - insulator/bonded chips	205
B.3.1 Setup and procedure	205
B.3.2 Results	206
B.4 Test - insulator/buried chips	213
B.4.1 Setup and procedure	213
B.4.2 Results	216
B.5 Insulator chips summary	222
Process flows	223
Emitter fabrication metrology	227
Curriculum Vitae	229

List of Figures

1.1	Mass of small satellites launched since 2000.	2
1.2	Achievable ΔV vs propulsion system mass fraction.	3
1.3	Specific impulse vs propulsion subsystem dry mass.	4
1.4	Basic operation of an electrospray thruster	5
1.5	Common types of electrosprays.	7
1.6	Images of early electrospray research.	8
1.7	Diagram and IV curve of early (1993) FEEP thruster	9
1.8	Images of Busek electrospray thrusters	10
1.9	Emitters microfabricated at MIT and Yale	12
1.10	Emitters and sheet laser visualisation setup from Deng et al.	13
1.11	Microfabricated emitters from QMUL group.	14
1.12	Microfabricated electrospray emitters from EPFL	16
1.13	Images of MicroThrust breadboard and simulated mission.	18
2.1	Cross section diagrams of thruster chips with integrated accelerators.	24
2.2	Diagrams of thrust vectoring and power tuning enabled by accelerator.	26
2.3	Polydispersive efficiency vs ion fraction for different droplet size	28
2.4	SEM images of bead filled emitters.	28
2.5	Bead filling diagram	29
2.6	Experiments to determine the void fraction in macroscopic cylindrical beds.	30
2.7	Estimated fluidic impedance of capillary emitters.	31
2.8	Cone shapes used for simulation	33
2.9	Onset voltage simulations	34
2.10	Validation of onset voltage simulations	35
2.11	Onset voltage simulation results	36
2.12	Interactions between geometric parameters	37
2.13	Effect of emitter inner diameter, iso. etch and wall thickness on onset voltage	38
2.14	Effect of emitter outer height and clear out on onset voltage.	39
2.15	Effect of extractor gap, thickness and inner diameter on onset voltage.	40
2.16	Effect of accelerator gap, inner diameter and potential on onset voltage.	41
2.17	Cross section diagram indicating key elements of the simulations.	42
2.18	Simulations of ion trajectories upstream of extractor	43
2.19	Beam shaping simulation results	44

List of Figures

2.20	Beam focusing simulation results	46
2.21	Particle trajectories simulation results	47
2.22	Effect of particle starting position on beam focusing simulations	48
2.23	Diagram of electrospray emitter with beam impinging on extractor electrode. .	50
2.24	Extractor erosion due to beam impingement after several hours spraying. . . .	51
2.25	3D drawings of v3a - BHA40 MicroThrust chip.	52
2.26	Diagrams of thruster stack with key dimensions labelled.	53
2.27	Predicted performance of different designs	56
3.1	Assembly of extractor or electrode wafer	60
3.2	Fabrication steps for the emitter wafers	61
3.3	Typical DRIE etch sequence	61
3.4	"Dots" and "lines" test structures	62
3.5	Front and back of C2W5 emitter	63
3.6	Box plots of emitter inner diameters for v3b wafers	64
3.7	Lamination of photopatternable thin film at CMI	65
3.8	Box plot showing lateral isotropic etch for different chip designs	66
3.9	SEM micrographs of overetched emitters	66
3.10	Test structures following emitter exterior definition	67
3.11	SEM micrographs of single capillary emitters	68
3.12	Fabrication process of the electrode wafer	69
3.13	Process flow and shadow mask pattern	70
3.14	Images of extractor electrodes bonded to glass carrier	70
3.15	Optical images of diced v3a and v3b thruster chips.	71
3.16	SEM micrographs of v3a thruster chips	72
3.17	SEM micrographs of v3b thruster chips	73
3.18	SEM micrographs of blocked v3a thruster chips.	76
3.19	SEM micrographs of blocked v3b thruster chips.	77
3.20	SEM micrographs of v3b thruster chips before and after cleaning at FIB.	78
3.21	IV curves showing leakage and breakdown with test chips	79
3.22	3D drawing and optical image of "isolated" MicroThrust chip	80
3.23	Optical photos of several diced thruster chips.	82
4.1	Diagram of QMUL test setup	87
4.2	Emitter array installed in test assembly	87
4.3	IV curve of 127 emitter array	89
4.4	Bi-polar current traces of 127 emitter arrays	89
4.5	Design of Retarding Potential Analysis (RPA) grid	90
4.6	Retarding Potential Analysis measurements	91
4.7	Beam half angle vs acceleration and extraction voltage.	93
4.8	Time-of-flight curve taken with five accelerating voltages	95
4.9	Polydispersive efficiency vs monomer and dimer fraction	96
4.10	Time of Flight curves with the liquid EMI-SCN	97

4.11 Long duration tests	98
4.12 Device failure due to liquid leakage from assembly	99
5.1 Early photographs of liquid instabilities taken by Zeleny in 1917	101
5.2 Dynamic formation of cone-jet obtained with stroboscopic lighting	102
5.3 Formation of Taylor cone from step change, taken with high speed camera . . .	103
5.4 High speed camera Taylor cone characterization	104
5.5 TEM micrographs of solidified cones from externally wetted needles	104
5.6 Interrogations relative to emission site	105
5.7 SEM micrographs of $50\mu m$ ID emitters filled with $4.63\mu m$ beads	106
5.8 Optical images and electron column diagram of SEM used in this work.	107
5.9 Observation schemes and electron trajectories for SEM experiments	109
5.10 Drawings of thruster chip designed for side-view observation	109
5.11 SEM and optical images of SEM observation thruster chips	111
5.12 SEM micrographs of special thruster chip with bonded molybdenum extractor	112
5.13 Two generations of SEM spray die sockets	113
5.14 3D CAD images highlighted steel tubing used to protect SEM against electrospray.	113
5.15 Optical images of spray assembly mounted in SEM	114
5.16 2d environment used to compute low energy secondary electron trajectories. .	117
5.17 Low energy SE trajectories simulated for several voltage configurations	118
5.18 Simulated electrostatic environments in SEM with different voltage configurations	119
5.19 Simulated electrostatic environments in SEM with different voltage configurations	120
5.20 Test chip C2W4D36 before test, with liquid clearly visible at the emitter tip. . . .	122
5.21 SEM micrographs of emitter with $EMI - BF_4$ bubble	123
5.22 Screen captures of video recording showing deformation of ionic liquid	123
5.23 Pressure simulations corresponding to observed liquid deformations	124
5.24 Electric field simulations corresponding to observed liquid deformations	124
5.25 Diagram of hypothetical bubble inside capillary	125
5.26 Sample C2W4D24 before test	126
5.27 IV sequential sweeps of in-situ electrospray	127
5.28 Screenshots of first video capture with increasing extractor voltage	128
5.29 Screenshots of second video capture with constant extractor voltage of 1700V .	129
5.30 SEM and optical images of thruster chip and assembly after test	130
5.31 Diagram and SEM image of traces on emitter frontside	131
6.1 3D-printed structures	137
A.1 Diagram of device failure caused by liquid wetting on emitter exterior.	155
A.2 Diagram of sessile drop technique	156
A.3 Vacuum contact angle measurement setup	157
A.4 Example images of drops for contact angle measurements	158
A.5 Contact angle measurements at room temperature in vacuum	159
A.6 Temperature influence on contact angle	160

List of Figures

A.7	Environment influence on contact angle	161
A.8	Graph of pressure barriers and fabricated valve from Man et al.	162
A.9	Five regimes considered for liquid transport model	162
A.10	Cross-section diagram of a capillary showing P, V and U	163
A.11	SEM micrograph and labeling of parameters relevant to the liquid transport model	165
A.12	Sphere with cap outlined above capillary	165
A.13	Surface energy (pJ) vs volume(fL) for a $5\mu\text{m}$ ID, $10\mu\text{m}$ OD capillary	172
A.14	Pressure (kPa) vs volume(fL) for a $5\mu\text{m}$ ID, $10\mu\text{m}$ OD capillary	173
A.15	Filling profiles of liquid meniscus for several emitter geometries.	174
A.16	Holding pressures vs contact angle and capillary inner diameter	175
A.17	Holding pressure test setup	176
A.18	Acceptance and qualification of vibration and shock tests.	178
A.19	Sinusoidal vibration test setup.	179
A.20	Six first resonant modes of vibration test attachment bracket	180
A.21	Vibration test levels	180
A.22	EDX analysis of floating particle	181
A.23	SEM micrographs of emitters before and after sinusoidal vibration tests.	182
A.24	Diagram and image of shock test setup	183
A.25	Longitudinal and lateral shock test assemblies.	184
A.26	SEM micrographs of emitters before filling with $EMI - BF_4$	184
A.27	Shock Response Spectrums of shock applied on all samples	186
A.28	Shock test results.	187
A.29	Shock test results.	188
B.1	Cross section diagrams of insulator emitters	190
B.2	Diagram of Electrospray Ionisation (ESI) process for Mass Spectrometry (MS) .	190
B.3	Various types of electrospray emitters for mass spectrometry	192
B.4	Optical image and schematic operation diagram of Advion TriVersa NanoMate	193
B.5	SEM micrographs of Advion TriVersa Nanomate emitters	194
B.6	Cross-section and top-view diagrams of insulator designs	195
B.7	Fluidic impedance of insulating emitters	196
B.8	Onset voltage simulations for insulator emitter chips.	198
B.9	Onset voltage simulations for insulator emitter chips.	199
B.10	Diagram of ionic liquid spilling out of the capillary	200
B.11	Radial electric field simulations in insulator designs	200
B.12	Fabrication steps of bonded (left) and buried (right) insulating emitters.	202
B.13	Optical and SEM images of insulator/bonded type insulating emitters	203
B.14	Optical and SEM images of insulator/buried design insulating emitters	204
B.15	Diagram of standard test setup used to test the insulator/bonded chips	205
B.16	Optical images of die 04 after test	207
B.17	Current plots with varying voltage for the 13th voltage sweep of die 09.	209
B.18	Current plots with varying voltage for the 19th voltage sweep of die 9. Pt.1 . . .	210

B.19 Current plots with varying voltage for the 19th voltage sweep of die 9. Pt.2 . . .	211
B.20 Insulator/bonded die 09 after spray	212
B.21 Optical images and diagram of flow controlled spray test setup	215
B.22 Collected current emitted from d43 emitter.	217
B.23 Still frames extracted from D43 video recording	218
B.24 Still frames extracted from D43 video recording showing breakdown events . .	220
B.25 Optical images and SEM micrographs of D43 after fail	221

List of Tables

1.1	Small spacecraft driven by PDAs and smartphones	2
1.2	Selected miniature in-space propulsion technologies.	4
1.3	Derived and demonstrated ST7 and LISA requirements	11
1.4	MicroThrust propulsion system requirements	19
1.5	Recent microfabricated electrospray emitters for spacecraft propulsion	20
2.1	Effective inner diameter and hydraulic impedances	31
2.2	Simulation parameters of MicroThrust electrospray thrusters	35
2.3	Nominal dimensions of MicroThrust thrusters	54
2.4	Modelled performance of designed electrospray emitters	57
3.1	Dimensions of fabricated emitters (v3a and v3b chips)	64
3.2	MicroThrust die (v3a) delivered to project partner QMUL in 2013.	83
4.1	Measured beam composition using time of flight analysis.	95
5.1	Summary of voltage configurations for SEM observations.	121
A.1	Expected and measured holding pressure values	177
A.2	Sinusoidal vibration tests results.	179
A.3	Shock tests conditions.	185
B.1	Common dimensions of insulator designs	197
B.2	Specific dimensions of insulator designs	197
B.3	Summary of tested insulator/bonded chips.	207
B.4	Summary of tested insulator/buried chips.	216

List of symbols

Symbol	Units	Description
DRIE	-	Deep Reactive Ion Etch
$EMI - BF_4$	-	1-Ethyl-3-methyl-imidazolium tetrafluoroborate
$EMI - Tf_2N$	-	1-Ethyl-3-methyl-imidazolium bis(trifluoromethylsulfonyl)imide
ESI-MS	-	Electrospray ionisers for mass spectrometry
MVD	-	Molecular Vapor Deposition
PIR	-	Purely Ionic Regime
SOI	-	Silicon-on-Insulator
TEC	-	Thermo-electric cooler
ToF	-	Time-of-flight
AU	km	Astronomical unit (146.6×10^9 km)
ϵ_0	$C N^{-1} m^{-1}$	Permittivity of free space ($8.854 \times 10^{12} C N^{-1} m^{-1}$)
g_0	$m s^{-1}$	Gravitational acceleration on earth ($9.81 \frac{m}{s^2}$)
U	-	CubeSat Unit ($10 \times 10 \times 10 cm^2$, 1kg)
α	°	Meniscus subtended angle
β	°	Off-horizontal angle
γ_{sl}	$N m^{-1}$	Solid-liquid interfacial surface tension
γ_{sv}	$N m^{-1}$	Solid-vapor interfacial surface tension
γ_{lv}, γ	$N m^{-1}$	Liquid-vapor interfacial surface tension
δ	°	Off-vertical angle
ΔV	$m s^{-1}$	Delta-V
ϵ	$m s^{-1}$	Void fraction
ζ	-	Ratio of charge to mass ratios
η_T	-	Propulsive efficiency
η_E	-	Energy efficiency
η_θ	-	Angular efficiency
η_P	-	Polydispersive efficiency
θ_c	°	Contact angle
μ	Pa s	Dynamic viscosity
Φ_b	V	Beam potential
a	m	Position of liquid inside capillary
A_{sl}	cm^2	Solid-liquid area

List of symbols

A_{sv}	cm^2	Solid-vapor area
A_{lv}	cm^2	Liquid-vapor area
b	m	Position of liquid on capillary tip
D	m	Capillary inner diameter
D_{eff}	m	Effective capillary inner diameter
D_s	m	Diameter of spheres used to fill capillaries
$E_{a_0}^2$	Vm^{-1}	Normal electric field at Taylor cone apex
f_i	-	Fraction of current carried by species i
I_{sp}	s	Specific impulse
I_{em}	A	Emitter current
I_T	A	Total beam current
k	-	Voltage to electric field coefficient
L	m	Capillary inner height
m	kg	Mass
\dot{m}_p	kg s^{-1}	Propellant flow rate
m_p	kg	Propellant mass
m_{dry}	kg	Spacecraft mass, excluding propellant
OD	m	Capillary outer diameter
P_b	W	Propulsive beam power
P_e	W	Electrical power
q	C	Charge
r_a	m	Radius of curvature of Taylor cone apex
R_{fl}	kg/s/m^4	Radius of curvature of Taylor cone apex
T	N	Thrust
U_0	J	Constant energy value
U_T	J	Total system energy
v_e	m s^{-1}	Particle exhaust velocity
V	m^3	Volume
V_{acc}	V	Acceleration voltage
V_{app}	V	Applied voltage
V_{ext}	V	Extraction voltage

List of publications

Journal articles

1. Dandavino, S., Ataman, C., Ryan, C., Chakraborty, S., Courtney, D. G., Stark, J. P. W., and Shea, H. R. (2014). Microfabricated electrospray emitter arrays with integrated extractor and accelerator electrodes for the propulsion of small spacecraft. *Journal of Micromechanics and Microengineering*, 24(7), 075011. doi:10.1088/0960-1317/24/7/075011
2. Dandavino, S., Courtney, D., Ataman, C., Dadras, M., and Shea, H. Scanning Electron Microscope observations of microfabricated devices operating in electric fields over 10MV / m (pp. 1–4). **(IN PREPARATION)**
3. Chakraborty, S., Ataman, C., Courtney, D. G., Dandavino, S., and Shea, H. (2014). A ToF-MS with a Highly Efficient Electrostatic Ion Guide for Characterization of Ionic Liquid Electrospray Sources. *Journal of the American Society for Mass Spectrometry*, 25(8), 1364–73. doi:10.1007/s13361-014-0914-z
4. Ryan, C., Dandavino, S., Ataman, Ç., Chakraborty, S., Courtney, D. G., de Jong, M., ... Shea, H. R. (2014). Performance of a MEMS electrospray electric propulsion system. *Journal of Aerosol Science*. **(UNDER REVIEW)**

Conference proceedings

1. Dandavino, S., Ataman, C., Chakraborty, S., Shea, H. R., Ryan, C., and Stark, J. P. W. (2013). Design and fabrication of the thruster heads for the MicroThrust MEMS electrospray propulsion system. In 33rd International Electric Propulsion Conference (pp. 1–8). Washington, D.C., USA. - **Best paper of session**
2. Dandavino, S., Ataman, C., Chakraborty, S., Shea, H. R., Ryan, C., and Stark, J. P. W. (2012). Progress Towards a Miniaturized Electrospray Thruster for Propulsion of Small Spacecraft. In 48th AIAA/ASME/SAE/ASEE Joint Propulsion Conference and Exhibit (pp. 1–13). Atlanta, USA.
3. Dandavino, S., Ataman, C., Shea, H. R., Ryan, C., and Stark, J. P. W. (2011). Microfabrication of Capillary Electrospray Emitters and ToF Characterization of the Emitted Beam. In 32nd International Electric Propulsion Conference (pp. 1–10)., Wiesbaden, Germany

List of publications

4. Ryan, C., Daykin-Iliopoulos, A., Stark, J. P. W., Salaverri, A. Z., Vargas, E., Rangsten, P., ... Shea, H. (2014). The MicroThrust MEMS electrospray thruster : results and conclusions. In Space Propulsion 2014 (pp. 1–10). Cologne, Germany.
5. Chakraborty, S., Dandavino, S., Ataman, C., Courtney, D. G., and Shea, H. R. (2013). Development of a ToF setup with an ion - guide for characterization of electrospray microthrusters. In 33rd International Electric Propulsion Conference (pp. 4–11). Washington, D.C., USA. - **Best paper of session**
6. Ryan, C., Daykin-Iliopoulos, A., Stark, J. P. W., Salaverri, A. Z., Vargas, E., Rangsten, P., ... Shea, H. R. (2013). Experimental progress towards the MicroThrust MEMS electrospray electric propulsion system. In 33rd International Electric Propulsion Conference (pp. 1–10). Washington, D.C., USA
7. Ghose, K., Dandavino, S., Meyer, H., Chamot, B., Labrecque-Piedboeuf, J.-F., Josandrinceanu, I., ... Mueller, D. (2013). Gravity Gradient Earth Sensor Experiment on REXUS 11. In 21st ESA Symposium on European Rocket and Balloon Programmes. Thun, Switzerland.
8. Chakraborty, S., Ataman, C., Dandavino, S., and Shea, H. R. (2012). Microfabrication of an Electrospray Thruster for Small Spacecraft. In Power MEMS, Atlanta, USA.
9. Ryan, C., Stark, J. P. W., Ataman, C., Dandavino, S., Chakraborty, S., and Shea, H. R. (2012). MicroThrust MEMS electrospray emitters – integrated microfabrication and test results. In Space Propulsion 2012, Bordeaux, France.
10. Ataman, C., Dandavino, S., and Shea, H. R. (2012). Wafer-level Integrated Electrospray Emitters for a Pumpless Microthruster System Operation in High Efficiency Ion-Mode. In IEEE MEMS. Paris, France.

MicroThrust technical reports

1. Dandavino, S., Ataman, C., and Shea, H. R. (2011). D4.1.1: Detailed design of emitter geometry and extractor geometry (pp. 1–27).
2. Ataman, C., Dandavino, S., and Shea, H. R. (2012). D4.1.2: Report on integration of acceleration electrodes (pp. 1–17).
3. Dandavino, S., Ataman, C., and Shea, H. R. (2012). D4.1.3: Updated MEMS Geometry Design (pp. 1–8).
4. Dandavino, S., Ataman, C., and Shea, H. R. (2011). D4.2.1: Report on wetting properties of ionic liquids (pp. 1–18).
5. Dandavino, S., Ataman, C., and Shea, H. R. (2012). D4.2.2: Report on filling of silicon capillaries for flow impedance control and for different tip geometries (pp. 1–15).

-
6. Dandavino, S., and Shea, H. (2013). D4.2.3: Report on liquid containment in filled capillaries (after shock) (pp. 1–21).
 7. Dandavino, S., Chakraborty, S., and Shea, H. R. (2012). D4.3.2: Complete MEMS thruster chip-stack (pp. 1–8).
 8. Dandavino, S., Ataman, C., and Shea, H. R. (2012). D4.3.3: Second generation MEMS thruster chip-stack (pp. 1–7).
 9. Dandavino, S., Courtney, D., and Shea, H. (2013). D4.3.4: Report on MEMS Microfabrication (pp. 1–27).
 10. Dandavino, S., Courtney, D. G., and Shea, H. (2013). D4.4.1: Report on electrode erosion as a function of operation mode and extractor diameter (pp. 1–12).

1 Introduction

1.1 Interest in small spacecraft missions

Interest in small (<100kg) spacecraft missions has exploded over the last 20 years. In 2013, 90 (out of 205) orbital spacecraft launched fit in this category, while only 16 (out of 89) did in 2003. These satellites are also getting smaller. In 2003, the average mass of such a spacecraft was 42kg, by 2013 this average had gone down to 5kg, with commercial and academic "CubeSats" becoming a well established and relatively common technological platform. The above trend is easily seen in Figure 1.1, which plots the 355 sub-100kg spacecraft launched since 2000. (Data collected from various sources. [1–4])

An important factor explaining this evolution are the more advanced capabilities of small components and systems, which allow for more useful small spacecraft. This is perfectly exemplified by the increased use of smartphones as central systems in the spacecraft. The 4kg Japanese satellite *Cute-1.7-APD-II*, launched on April 28 2008 was predecessor to this family, using an *Hitachi NPD-20JWL* PDA as central processing and memory unit. More recently, British and American organisations launched five spacecraft based on Android smartphones (Table 1.1). These more advanced devices could now additionally provide 6-axis inertial measurements and high resolution cameras, in addition to four times the processing power and 4000x the internal memory capacity of the recently retired Space Shuttle¹.

While the majority of small spacecraft continue to serve as technology demonstrators and have the primary objective to provide hands-on learning experiences for students, an increasing fraction now focuses on their payload and the resulting scientific data.

Unfortunately, small spacecraft remain limited by the lack of a critical technology: a low cost and efficient miniature propulsion system. While several small satellites successfully operated in-space propulsion, none so far had the capability to complete orbital maneuvers, using the propulsion for attitude control or drag compensation only.

¹http://en.wikipedia.org/wiki/IBM_AP-101

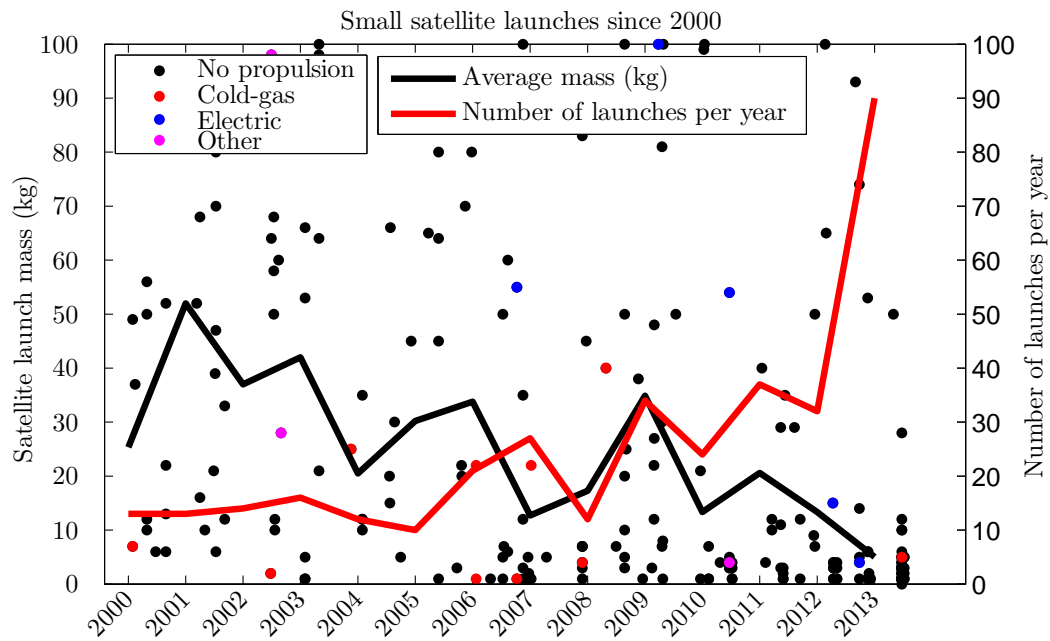


Figure 1.1: Mass of small satellites launched since 2000. Full line follows yearly average and coloured dots indicate satellites with propulsion capabilities. (Data collected from various sources: [1–4])

Table 1.1: Small spacecraft driven by PDAs and smartphones

Name	Operator	Launch date	Smartphone
Cute-1.7-APD-II	Tokyo Institute of Technology	April 28 2008	Hitachi NPD-20JWL
StraND-1 [5]	Surrey Space Systems	February 25 2013	HTC Nexus One
PhoneSat 1.0(Graham)	NASA Ames	April 21 2013	HTC Nexus One
PhoneSat 1.0(Bell)	NASA Ames	April 21 2013	HTC Nexus One
PhoneSat 2.0(Alexander)	NASA Ames	April 21 2013	Samsung Nexus S
PhoneSat 2.4	NASA Ames	April 18 2014	Samsung Nexus S

Yet maneuvering capability is particularly relevant due to the nature of the small spacecraft industry. Indeed, in opposition to their larger cousins, small satellites typically do not have the luxury of choosing their initial orbit. Launched as secondary payloads or as one of many small satellites, they require their own propulsion if they intend to move to a more desirable orbit. More so even than these orbital corrections, the prospect of completing deep space exploration mission using small satellites is fascinating. An efficient propulsion system could be the democratizing technology that grants universities and small organizations a much sought access to deep space.

1.2 Propellant usage of small propulsion systems

The capability of the propulsion system to complete these complex orbital maneuvers is best described by the ΔV metric, which describes the velocity change that can be provided with a given mass (m_p) of propellant in a force-free environment. The well-known Tsiolkovsky rocket equation (Eq. 1.1, where m_{dry} is the total mass of the spacecraft excluding propellant) highlights how the ΔV can be increased either by loading more propellant or by increasing the specific impulse (I_{sp}).

$$\Delta V = I_{sp} g_0 \ln \left(\frac{m_{dry} + m_p}{m_{dry}} \right) \quad (1.1)$$

The I_{sp} describes how efficiently the propellant is used. It is defined as the thrust (T) divided by the propellant flow rate (\dot{m}_p), scaled with Earth's gravity (g_0), as shown in Eq. 1.2. With spacecraft where thrust results entirely from propellant exhaust, the specific impulse is directly proportional to the particle exhaust velocity v_e .

$$I_{sp} = \frac{T}{\dot{m}_p g_0} = \frac{v_e}{g_0} \quad (1.2)$$

Increased propellant loading, however, is not a viable option for small spacecraft since any power and communication system or payload will require a certain amount of mass and volume. If up to 20% of the spacecraft mass is allocated for propellant (Propellant mass fraction $\frac{m_p}{m_p + m_{dry}} = 0.20$) then an I_{sp} of at least 2284s will be required to reach 5000 m/s ΔV (Figure 1.2), in the range required for extraorbital missions. Increasing the specific impulse, then, is the most effective way to reach a high ΔV system.

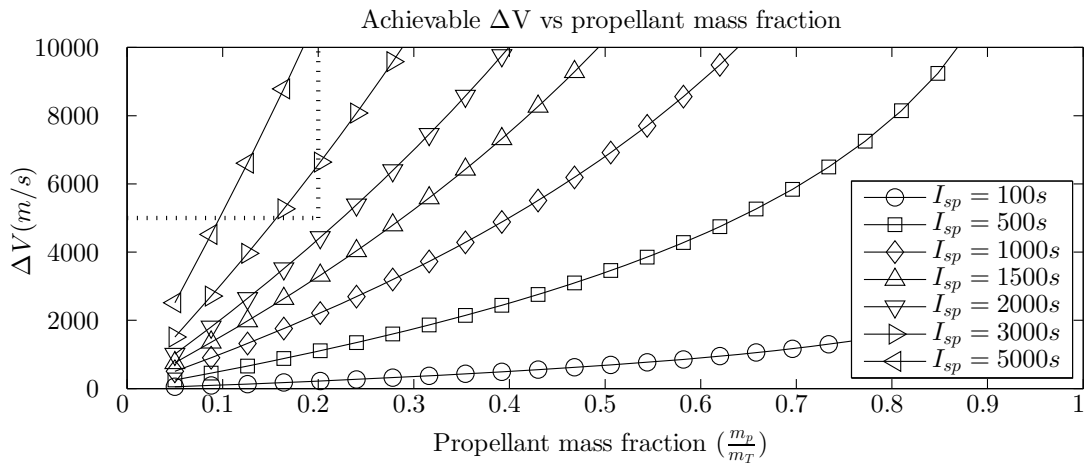


Figure 1.2: Achievable ΔV vs propulsion system mass fraction.

Table 1.2: Selected miniature in-space propulsion technologies.

#	Type	Technology	M_{pd} (kg)	I_{sp} (s)	Thrust (μN)	Power (W)	η_T (%)	TRL	Ref.
1	Cold gas	VACCO	0.5	50	10000	6	N/A	9	[6]
2	Cold gas	Nanospace	0.25	110	1000	2	N/A	5	[6]
3	Resistojet	Busek Micro Resistojet	1.25	150	2000	10	15%	5	[7, 8]
4	Electric	Busek 1cm RFIT	1.25	1800	67	10	6%	4	[7, 8]
5	Electric	Busek BHT200 Hall thruster	10*	1390	13000	200	44%	9	[7, 8]
6	Electric	JPL miniature Xenon Ion Thruster (MiXI)	5*	3000	3000	50	44%	5	[9–11]
7	Electrospray	This work (expected)	0.55	3300	300	17	29%	3	[12]

*estimated system mass

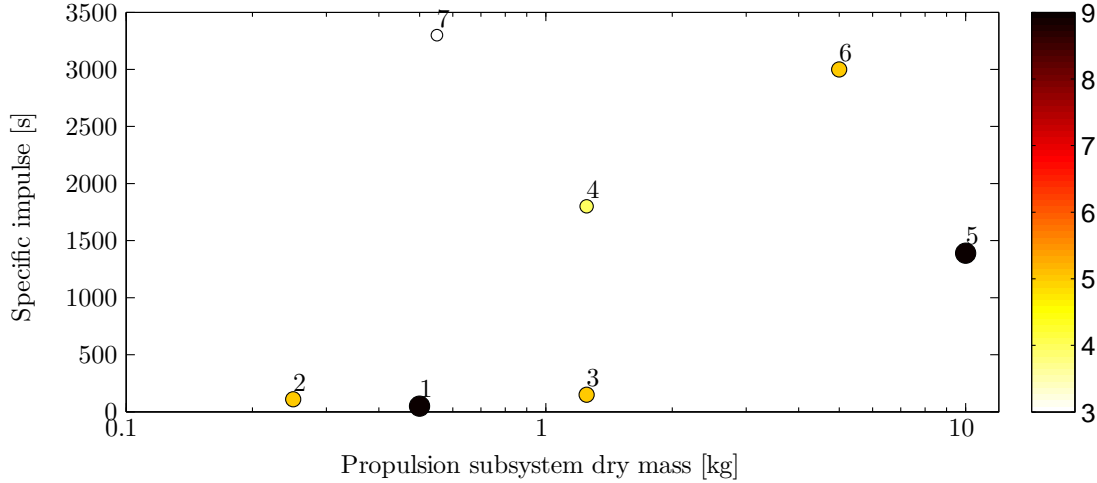


Figure 1.3: Specific impulse vs propulsion subsystem dry mass. The number labels correspond to the technologies listed in Table 1.2 while the color coding indicates the Technology Readiness Level.

Several technologies are being proposed to answer the need of miniature in-space propulsion. These competing technologies are displayed in Table 1.2 and Figure 1.3. Yet in most cases, the main objective is not to provide high ΔV capability but rather to allow attitude control and orbital corrections. Electrospray thrusters remain one of the most promising technology capable of filling this gap, delivering high specific impulse in a small package. What's more, electrospray are particularly prone to modularity. For one, they do not, when operating with passive feeding, require centralized pressurized tanks and can be entirely self-contained. Operating in both polarities, they avoid neutralisers, another step towards self-sufficiency. Most importantly, and in opposition to many other electric propulsion technologies, their performance does not scale down with their size. As such, they were included in NASA's Space Technology Roadmap for In-Space Propulsion Systems [13].

1.3 Fundamentals of electrospray propulsion

Electrospray propulsion is particularly prone to scalability and modularization. Electrostatically evaporating and accelerating charged particles directly from their liquid state (Figure 1.4), it generates thrust by direct momentum transfer with few sources of efficiency loss. The absence of large magnetic fields or ionization chambers is an advantage over many other electric propulsion technologies. Arrays of emitters can also generally be segmented without intrinsic losses to the thruster performance, a key element towards the creation of a modular system.

In operation, a conductive liquid propellant is transported to an extraction site where a large electrical field is applied by precisely aligned electrodes. Increasing the electrical pressure, the liquid's surface tension can be overcome, deforming the liquid meniscus into a conic shape (Taylor cone [14]), which to a first order stabilizes with a half-angle of 49.3° . The sharpened liquid tip leads to a large electric field concentration, in the order of 1 GV/m [15], sufficient to atomize the liquid and generate a high velocity particle spray. The spray can be composed of small droplets or, if the dimensions, liquid properties, and applied field are adequate, ions [16]. Recently, several research groups have turned to ionic liquids, most commonly the liquids 1-Ethyl-3-methyl-imidazolium tetrafluoroborate ($EMI - BF_4$) and 1-Ethyl-3-methyl-imidazolium bis(trifluoromethylsulfonyl)imide ($EMI - Tf_2N$), for propellant. These liquids have the advantage of displaying no measurable vapour pressure, a critical requirement for their use in space. They also display the high surface tension and conductivity necessary for ionic operation. The extraction field is provided by the first electrode stage (V_{ext}) while later stages (V_{acc}) can provide acceleration and focusing of the spray. A particularity of electrosprays is that the particle dimensions, which play a key role in determining the performance of the system can be modulated according to the operating conditions.

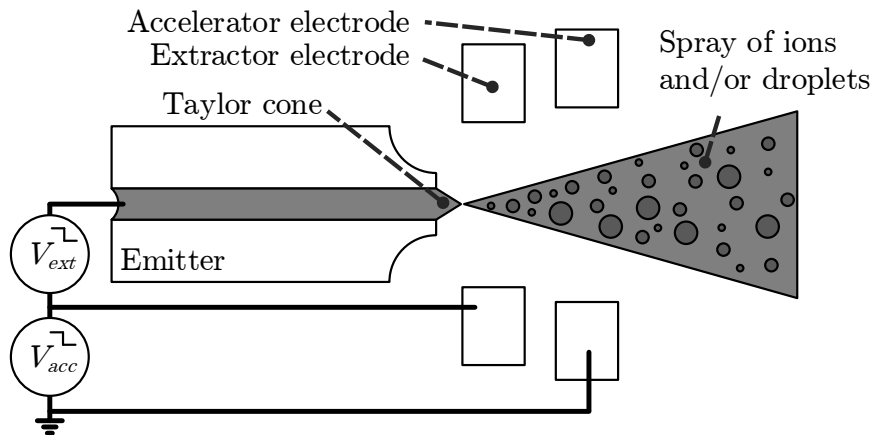


Figure 1.4: Basic operation of an electrospray thruster with an extraction and acceleration stage. A potential V_{ext} is applied between the conductive liquid propellant and an extraction electrode aligned with the capillary emitter to generate the spray. An accelerator electrode can provide an additional potential V_{acc} to increase the thruster performance.

From the basic equation of thrust ($T = \dot{m}_p v_e$), the propellant flow rate can be related to the emitted current ($I_T = \dot{m}_p \frac{q}{m}$) and the particle velocity to the applied beam potential ($v_e = \sqrt{2\Phi_b \frac{q}{m}}$) to obtain Eq. 1.3 and Eq. 1.4 ($\Phi_b = V_{ext} + V_{acc}$ in the ideal case), where m is the emitter particle mass and q its charge. These equations, valid for the ideal cases with no sources of efficiency loss, highlight the T and I_{sp} dependence on the charge over mass ratios of the emitted particles, with highest specific impulse when operating in the Purely Ionic Regime (PIR).

$$T = I_T \sqrt{2\Phi_b \frac{m}{q}} \quad (1.3)$$

$$I_{sp} = \frac{1}{g_0} \sqrt{2\Phi_b \frac{q}{m}} \quad (1.4)$$

By varying the operational conditions (back pressure, extraction voltage), it is possible to control the particle size, making for unique throttling capabilities. Operating in the Purely Ionic Regime (PIR), the thruster can reach unmatched specific impulse (>3000s at 1000V for the propellant $EMI - BF_4$), yet at the cost of low thrust per emitter (10's of nN per emitter). This limitation, however, can be overcome by the parallel operation of large arrays of emitters.

To a large extent, this last element explains the general tendency over the last decade to turn to microfabrication to produce the electrospray thrusters. Microfabrication also provides a natural evolution of the technology by building on its strengths, allowing the creation of highly integrated, compact systems ideal for miniature spacecraft. It also permits the fabrication of small and repeatable emitter features, key to achieving the high fluidic impedance and thereby low flow rates required for PIR.

Typically, microfabricated electrospray emitters can be externally [17], porously [18] or internally [19, 20] fed. Figure 1.5 shows diagrams of the different types of emitters. Porous (Figure 1.5a) and externally wetted (Figure 1.5b) emitters rely entirely on capillarity to transport the propellant to the extraction site. The pressure inside the liquid is also passively determined by the specific geometry (e.g. pore size) of the structure. For internally fed (which includes slit) emitters (Figure 1.5c and Figure 1.5d), active backpressure control can be used to control the pressure inside the liquid and to affect the flow rates. Porous, externally fed and slit emitters simultaneously generate several Taylor cones per emission site while internally fed emitters are more predictable, with a single cone per emission site, at the cost of lower emitted current (per emitter).

In the next section, we revisit the creation of electrosprays over the last century, attempting to describe how they evolved from electrical novelty to a mission-ready propulsion system.

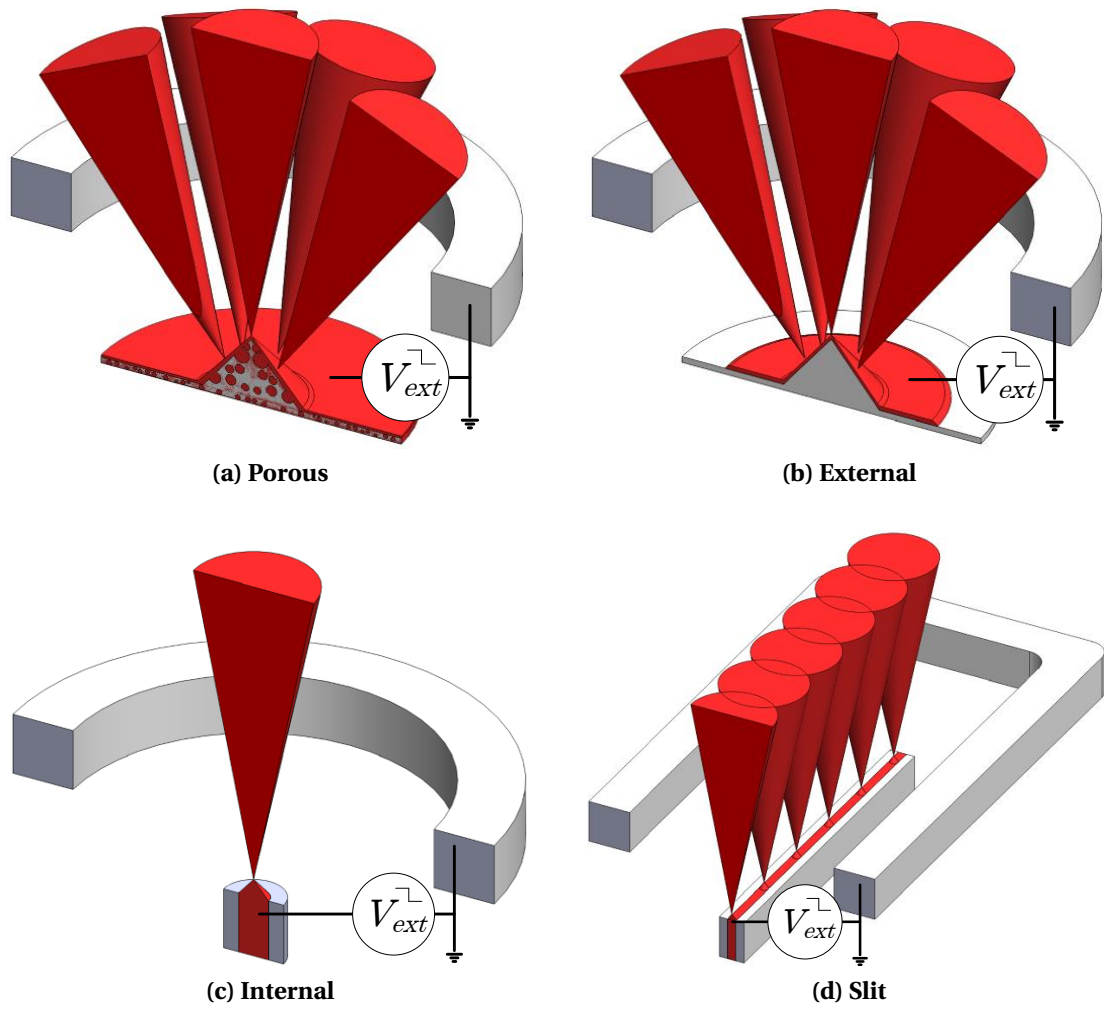


Figure 1.5: Common types of electrosprays.

1.4 A brief history of electrospray propulsion

1.4.1 Early activities

Today's electrosprays can be traced back to experiments performed at Yale University and at the University of Minnesota in the 1910's by John Zeleny [21–23]. He observed that when a charged conductive liquid inside a hollow glass tube was placed opposite a grounded metal plate, the liquid tip would deform. In certain cases, this deformation would take the form of a cone with a jet at its apex generating a spray of particles. It took over half a century for an adequate physical description of this cone to be presented, by Sir Geoffrey Taylor in 1964 [14]. Sir Taylor described how an unstable equilibrium between an external electric field, an applied pressure and its surface tension could indeed deform a liquid into the shape of a cone, with the precise half-angle of 49.3° (Figure 1.6a). More recently, De La Mora [24] expanded the theory, describing how convex or concave cones could be seen according to the pressure (positive or negative) present inside the cone.

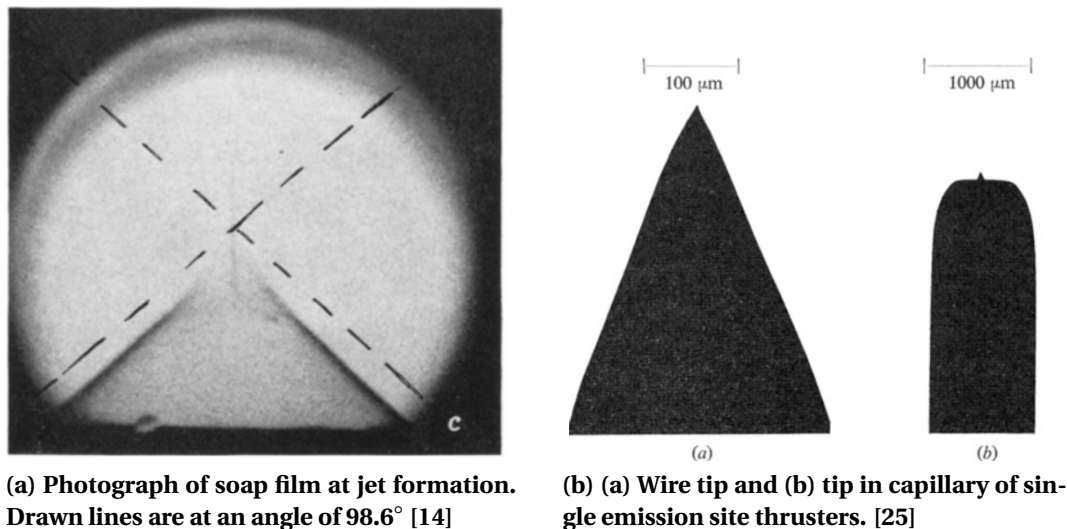


Figure 1.6: Images of early electrospray research.

But already in the early 1960's, endeavours to use electrosprays for spacecraft propulsion began in the United States. Their potential had been quickly recognized: like other types of electric propulsion, they had a high theoretical specific impulse, but in addition their simplicity made them prone to miniaturization in terms of mass, volume and power consumption [26].

A comprehensive review of such efforts is presented in [27] and describes how much of the initial work was focused on finding emitter geometries and adequate propellants (often glycerol based), with ionic liquids still relatively unknown. This development period culminated in 1974 with the design and test by TRW Inc. of a 432 hollow needle emitter using a solution of sodium iodide and glycerol and displaying a combined thrust of 4.45mN and specific impulse of 1365s, operating at 12.2kV [27]. Following this, budget restrictions, mainly due to the arrival of the Space Shuttle, led to a 20 year hiatus during which little direct progress was made.

1.4. A brief history of electrospray propulsion

In Europe, activities were started in 1969 by the European Space Research Organization (ESRO) and revolved initially around the use of linear slit emitters. The University of Southampton quickly became involved, at first using closely-spaced (150 - 200 μm) commercial razor blades to form the slits. The search for a suitable propellant also resulted in a glycerol/sodium iodide solution [27]. Experiments with different emitter geometries [28] eventually led to a single emission site design consisting of a sharpened tip embedded within a hollow pen (Figure 1.6b) [25]. Unfortunately, once again in the mid 1970s administrative considerations led to a stoppage of research activities in this field. Field-Emission Electric Propulsion (FEEP), a subset of electrosprays where molten metal (Cesium, Rubidium, Indium) is used as propellant, also appeared around that time. In a 1988 paper, Petagna et al. describe the early FEEP development at ESRO:

"The basic laboratory investigation phase covered the period 1972 to 1980. During this period the basic physics problems were clarified and the major engineering problems concerning the manufacture of the emitter were solved thus enabling the initiation of the industrial development phase." [29]

Five years later, Gonzalez², Saccoccia³ and von Rohden presented updated results of the FEEP slit thrusters (Figure 1.7), referring to a target mission "SAGITTARIUS", a gravity wave detection experiment, which was to become LISA (Laser Interferometer Space Antenna). This work was eventually taken over by Italian company ALTA-Space who had been selected to provide a FEEP propulsion system for LISA Pathfinder. Recent publications by ALTA-Space introduced "IL-FEEP" where the molten Cesium was replaced by the ionic liquids $EMI-Tf_2N$ [30] and $EMI-BF_4$ [31].

Russian activities also progressed in parallel at the Moscow Aviation Institute for 35 years until 1995. The system then presented had a thrust of 1 mN and a specific impulse of 1000s at a voltage of 15 kV. [32]

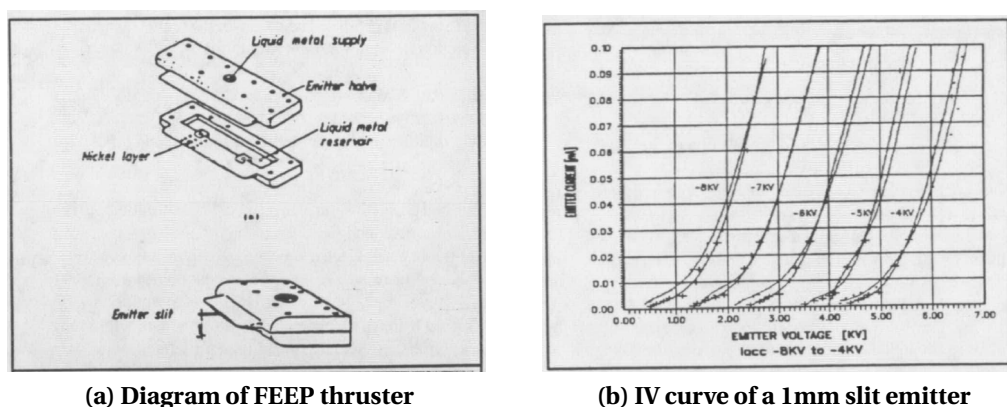
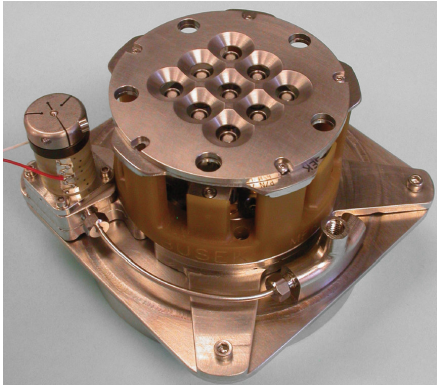


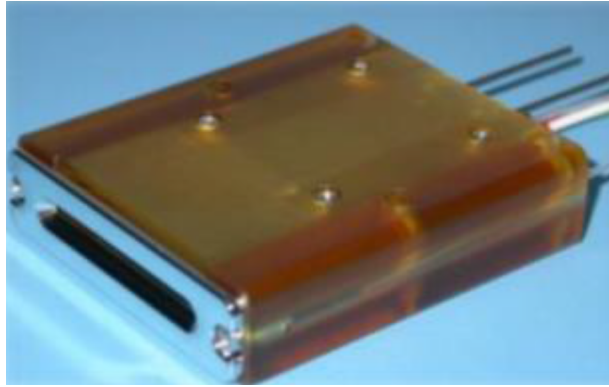
Figure 1.7: Diagram and IV curve of early (1993) FEEP thruster [33]

²presently the head of Electric Propulsion Section at ESA

³presently the head of the Propulsion and Aerothermodynamics Division at ESA



(a) Standard Lisa/ST7 module.



(b) Miniature "CubeSat" module.

Figure 1.8: Images of Busek electro spray thrusters (propellant reservoir and high voltage electronics not included). [7, 8]

1.4.2 Rebirth of electrosprays - American contributions

With the increase in popularity of small satellites as well as the prospect for high precision, high ΔV missions, interest in electro spray thrusters resurfaced at the end of the 20th century. This rebirth in the US took the form of a collaboration between professor Martinez-Sanchez of MIT, professor Fernandez de la Mora of Yale and Dr. Vlad Hruby of Busek Co. [32]. Ionic liquids this time became a choice candidate as propellant, with the demonstration that they could be used in purely ionic mode ($EMI - BF_4$ in 20 and 40 μm inner diameter hollow needles [16]), maximizing their charge-over-mass ratio and consequently specific impulse.

With Yale continuing research on propellant, MIT focused on the development and characterization of thruster configurations. Paulo Lozano, at the time a PhD student under professor Martinez-Sanchez, worked at first with commercially available pulled silica capillaries with tip diameters down to of 5 μm on beam characterization and showed how they could be operated in a mixed ion-droplet mode. [34, 35] This research eventually branched to Busek who delivered in 2008 an electro spray-based thruster system for the LISA Pathfinder mission (Figure 1.8a), which will be launched in 2015. This system, although too large to be used for small spacecraft provided invaluable proof that electrosprays had the required performance and reliability for concrete missions. Ziemer et al. [36] described extensively the qualification of this system, with results summarized in Table 1.3. To note is the low specific impulse in this thruster, a result of a mixed or droplet mode operation and which results in low potential ΔV ($\approx 150 m/s$ for a 4kg satellite) [8]. More recently, this system evolved into a more compact system compatible with smaller spacecraft (Figure 1.8b). It still provides low I_{sp} and ΔV ($\approx 75 m/s$ for a 4kg satellite) [8] but remains the highest TRL electro spray thruster system .

Martinez-Sanchez and the MIT team moved on to externally wetted tip emitters which allowed more stable ion-mode operation and provided further insight on the beam characteristics and propellant behaviour [37–41]. Of specific interest is the 2004 article [37] in which Lozano

1.4. A brief history of electrospray propulsion

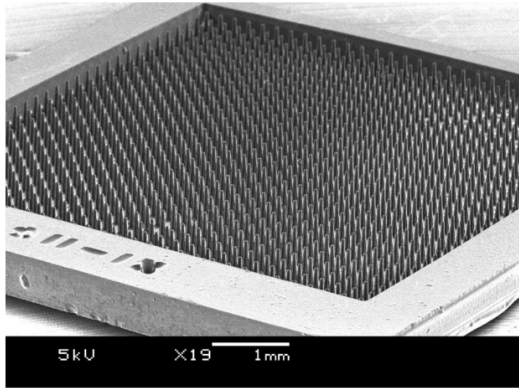
Table 1.3: Derived and demonstrated ST7 and LISA requirements, reproduced from [36].

Requirement	ST7	LISA	Demonstrated
Thrust range	5 to 30 μN	5 to 30 μN	4.35 to 35.8 μN
Thrust precision	0.1 μN	0.1 μN	0.08 μN (0.01 μN calc.)
Thrust noise	0.1 $\mu N/Hz$ (5Hz control loop)	0.1 $\mu m/Hz$ (5Hz control loop)	0.01 $\mu m/Hz$ (3×10^{-5} -3 Hz) 0.1 $\mu m/Hz$ (3-4 Hz)
DRS Drag-free-bandwidth	1×10^{-3} - 3×10^{-2} Hz	3×10^{-5} -1 Hz	3×10^{-5} -4 Hz
Control loop bandwidth	1×10^{-3} -4 Hz	3×10^{-5} -4 Hz	3×10^{-5} -4 Hz
Thrust command rate	10 Hz (0.1 s latency)	TBD	10 Hz (0.1 s latency, 0.4 settle time)
Thrust range response time	100s	TBD	<10s
Specific impulse	150s	TBD	150s (200s typical)
Operational lifetime	2160 h	40000 h	3478 h during FLT 2B (245Ns total impulse, 113g of propellant)
Plume half-angle	35° (95% current)	TBD	< 23° (95% current)

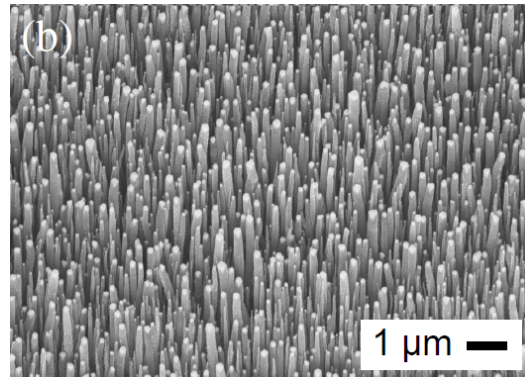
described the formation of double layers at the surface of the emitters resulting from a prolonged operation in a given polarity. He proposed that when operating in an ionic mode, the counter-ions left behind in the reservoir would diffuse to the surface of the “hot” electrode and create a double layer which, if left unchecked, would eventually generate a sufficiently high potential to initiate electrochemical reactions. Alternating the polarity of the extraction voltage, and therefore the polarity of the ions emitted, at even the slow frequency of 1 Hz was reported to solve this problem. This group also recently experimented with another method to improve this scheme [42], where distal electrodes are used to make contact with the liquid propellant away from the emission site, a method more commonly used in electrosprays for mass spectrometry.

The emitters, until then fabricated with conventional techniques, were also transferred to a micromachining process in which arrays of 1024 emitters were fabricated in black silicon (Figure 1.9a) [17, 43, 44]. A later generation of devices proposed the integration of carbon nanotubes on the emitter surface to improve wetting of the structures (Figure 1.9b) [45]. However, there remain disadvantages to externally wetted thrusters most notably in terms of poorly controlled liquid transport.

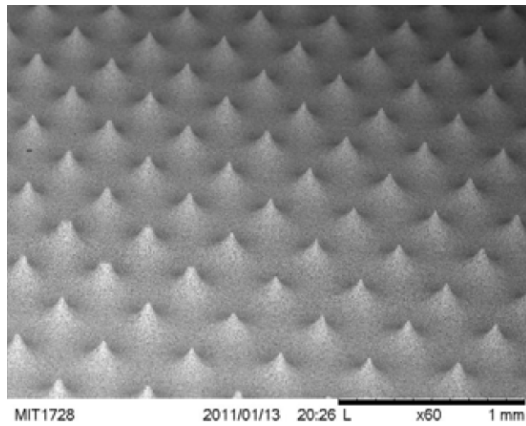
Hence the MIT efforts shifted to the use of micromachined porous tips, first made of tungsten and nickel [18, 46–48] which allowed better capillary liquid transport and yielded stable PIR operation. A recent published paper from this group reported ionic mode operation with thrust values (per emitter) in the range of $0.048 \mu N$ at -2088V and $0.116 \mu N$ at 2437V (using $EMI - BF_4$, direct measurements performed at Busek) [48]. The latest devices proposed by this group were fabricated using insulating porous materials, either by sintering of glass microspheres [49] (Figure 1.9d) or laser machined of porous glass [50] (Figure 1.9e).



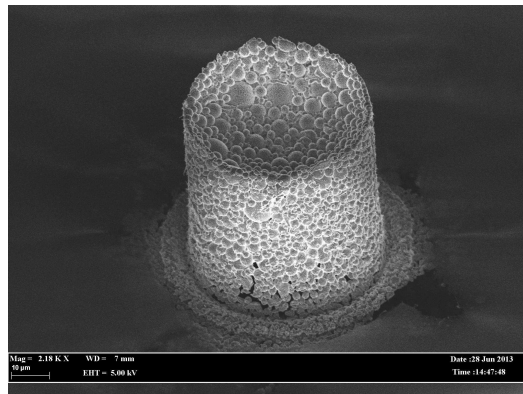
(a) Array of 1024 externally wetted silicon emitters from Velasquez et al. - 2006 [43]



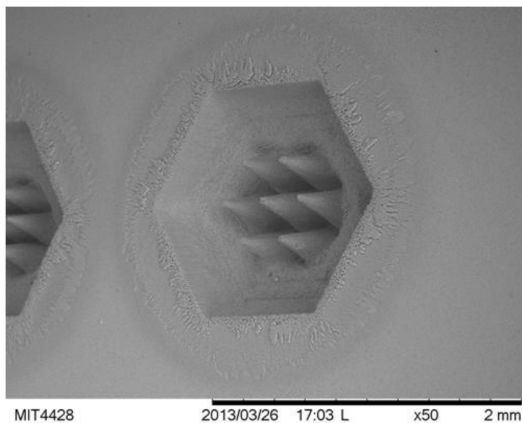
(b) Externally wetted, CNT coated, silicon emitters coated from Hill et al. - 2013 [45]



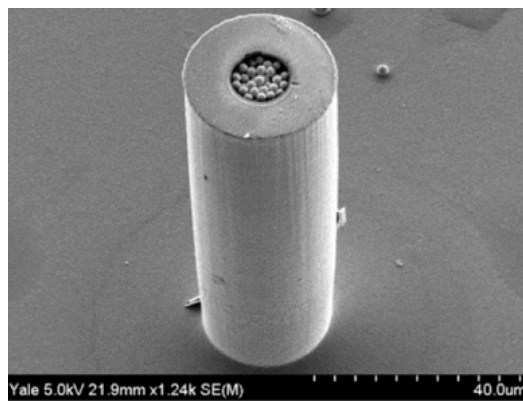
(c) Porous nickel emitters from Courtney et al. - 2012 [18]



(d) Porous emitters fabricated by glass sintering from Xie et al. - 2013 [49]



(e) Laser machined porous emitters from Coffman et al. - 2013 [50]

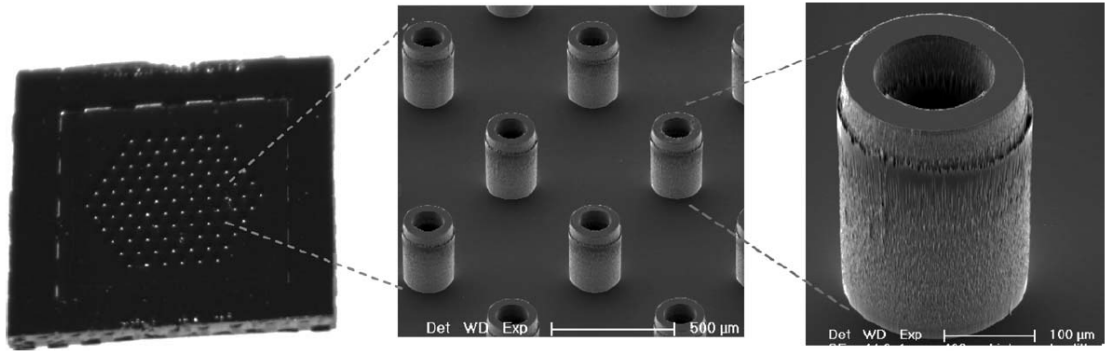


(f) Bead-filled silicon capillary emitter from Lenguito et al. - 2014 [51]

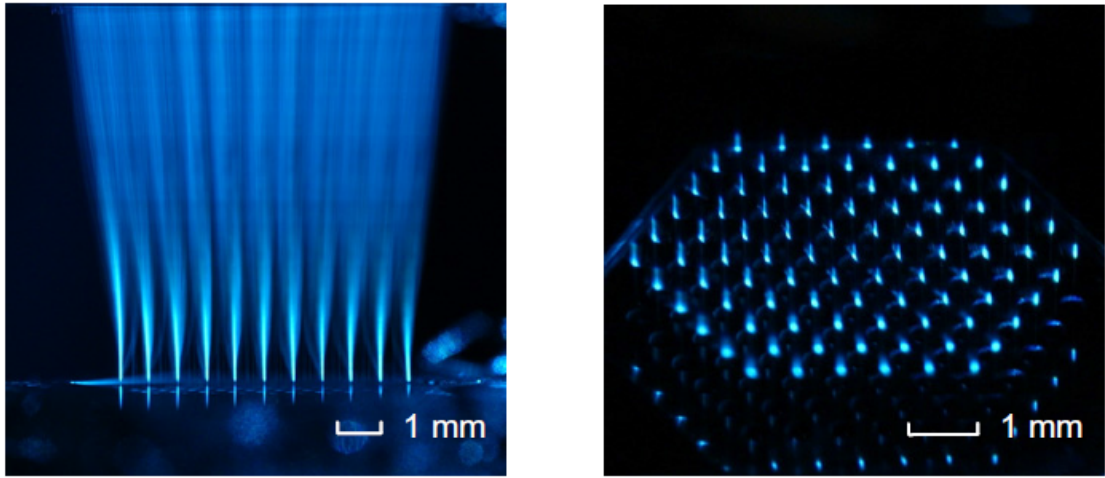
Figure 1.9: Six generations of microfabricated emitters from MIT (a)-(e) and Yale (f).

1.4. A brief history of electrospray propulsion

Professor Gamero-Castaño, having received his PhD under Prof. Martinez-Sanchez in 1999 went on to work first at Busek [52], then in 2004 at the California Institute of Technology's Jet Propulsion Laboratory, where he studied space-charge effects in electrosprays in vacuum [53] and electrospray beam composition [54]. He then received a position at the University of California Irvine, shifting focus on deposition and etching applications [55]. He also studied the cone-jet transition region using an impressive combined Time-of-Flight/Retarding Potential Analyzer setup [56]. Collaboration with JPL on electrosprays continues to this day under the leadership of Dr. John Ziemer [57].



(a) Microfabricated silicon emitters from Deng et al. [19]



(b) Sheet laser test setup from Deng et al. [19, 58]

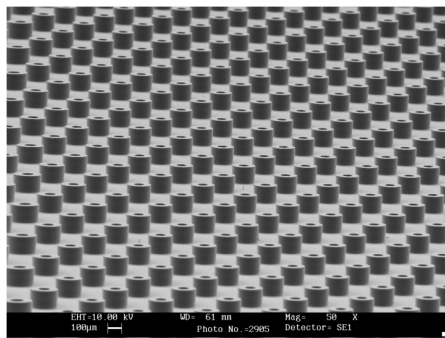
Figure 1.10: Emitters (a) and sheet laser visualisation setup from Deng et al. [19, 58]

This period also saw several direct contributions from De La Mora's group, including studies on the effect of liquid properties on the electrospray [40, 59], a study on the surface tension and contact angle (vs glass) of several ionic liquids [60] and a review on the fluid dynamics of Taylor cones [24]. Also at Yale, Prof. Alessandro Gomez's group made contributions in the development of pressure-fed microfabricated silicon capillary emitters (Figure 1.9f) [20, 51, 61] which shared many similarities with those of our group [62]. Thrusts up to $2.6\mu N$ and I_{sp} up to 780s could be computed from Time-of-Flight measurements with these devices (7 emitter

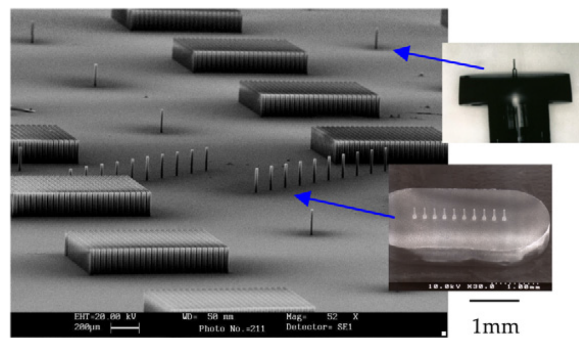
arrays), at 1.37 kV using pure ethylammonium nitrate (EAN). Working with Gomez, PhD student Weiwei Deng also made several contributions to the field. Operating in pressure-fed droplet mode, he could use a unique He-Ne sheet laser setup (Figure 1.10b) to validate the firing patterns [19, 58] and establish guidelines in the minimal hydraulic impedance required to have homogeneous spray across arrays of emitters [19, 58]. He used an analytical model and FEM simulations to study space-charge effects as a function of flow rate [58] and studied the response of a Taylor cone to a step change in voltage [63].

Graduated from Prof. Gomez's group in 2008, Deng also went on to found an electro spray research group at the University of Central Florida. While initially also working with micro-fabricated silicon capillaries (Figure 1.10a, [19, 64]), he eventually transited to conventional methods to fabricate "relatively large" emitters in polymers and metal [65] and started focusing on printing applications of electro sprays [66, 67].

1.4.3 Recent European efforts



(a) Microfabricated silicon emitters from Stark et al. [68]



(b) Microfabricated silicon dioxide emitters from Wang et al. [69]

Figure 1.11: Microfabricated emitters from QMUL group.

What could be called the second stage of European electro spray thruster research was initiated in the early 2000s in the United Kingdom. The University of Southampton once again became a prominent actor when Mark Paine, having just received his M.Sc. from Martinez-Sanchez's group at MIT, joined their ranks in 2000. He presented in his 2002 PhD thesis a design for microfabricated internally wetted (hollow needle) thrusters [70]. John Starks' group at the Queen Mary University of London (QMUL) had also in parallel been working on microfabricated out-of-plane hollow needle emitter arrays (Figure 1.11a) [68, 71] and in 2002 received Dr. Paine as a post-doc. He continued to work on this topic [72, 73], eventually focusing on the printing applications of electro sprays [74, 75]. Work to develop electro spray thrusters at QMUL still continued however [76]. A 2007 paper [69] from Rutherford Appleton Laboratory and QMUL presents an innovative fabrication process in which arrays of silicon dioxide nozzles are fabricated through a sequence of Deep Reactive Ion Etches (DRIE) and a thermal oxidation (Figure 1.11b). The QMUL group also developed a pressure based flow meter (precision of 0.3

1.4. A brief history of electrospray propulsion

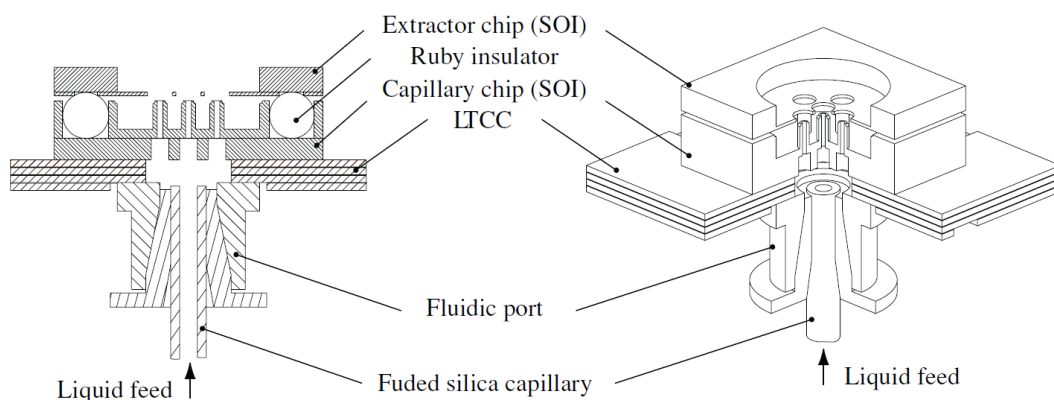
nL/s [77]) allowing studies of the effects of liquid conductivity [78] and voltage [79, 80] on flow rate and electrospray.

It is around this time, in 2004, that EPFL's Microsystems for Space Technologies Laboratory (LMTS), headed by Prof. Herbert Shea, became involved in electrospray thrusters in close collaboration with QMUL. This involvement was embodied by a PhD student, Renato Krpoun, at LMTS from 2004 to 2008.

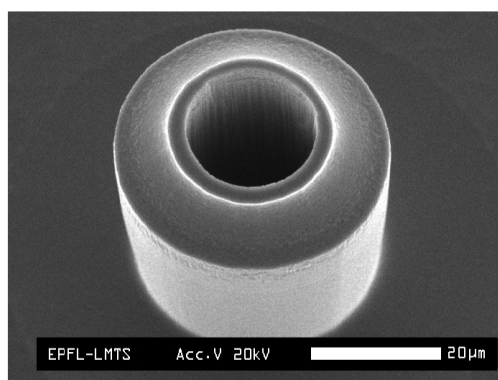
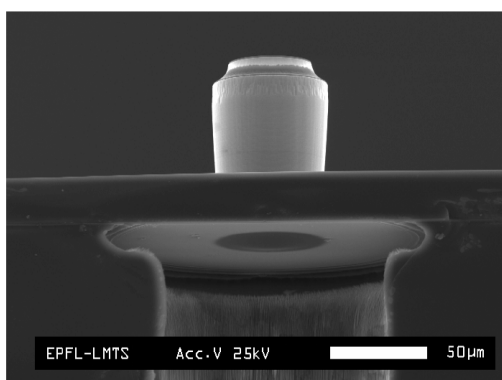
Krpoun built on the progress made by QMUL and incorporated improvements in the microfabrication process inspired by other efforts in the development of electrospray ionisers for mass spectrometry [81, 82]. The emitters were silicon based and fed through capillary action from a reservoir on the back of the silicon chips. A positive or negative voltage was applied to the liquid reservoir while the extractor plate, also micromachined in silicon, was grounded [83]. The emitters and extractors were fabricated separately and the singulated die were assembled with the use of four 200 μm diameter ruby balls placed manually on the emitter die in trenches aligned with extractor die grooves (Figure 1.12a). This provided better than 2 μm alignment and allowed for easy disassembly of tested die. The emitters (Figure 1.12b) had inner diameters of 24, 28 or 32 μm [32], which proved too large to provide sufficient hydraulic impedance. The resulting flow was too high, such that ion mode operation could not be achieved. In addition, the low impedance increased the occurrence of failures due to liquid overflow. In an effort to correct this problem, Krpoun devised a post-fabrication process in which he filled the emitters with small silica beads and solidified them with a silanization step (Figure 1.12c). As a result, ionic mode operation was successfully achieved with $EMI - BF_4$ with a resulting specific impulse of 3500s at 1200V [62]. Krpoun went on to successfully test arrays of 19 capillaries, although the emitted current was lower than expected (when compared to single capillaries) [62]. He also witnessed evidence of sputtering of the underside of the annular extractor, indicating a larger than expected beam spread (Figure 1.12d) [62]. Krpoun additionally proposed a model [83] to determine the voltage at which emission should start as a function of several parameters such as the extractor dimensions and position.

In 2009, the QMUL/EPFL association was extended to include several key players in the field of advanced space propulsion and microsystems in Europe. The consortium, which saw the addition of TNO (Netherlands), Nanospace (Sweden) and the EPFL Space Center to QMUL and EPFL-LMTS was charged to conduct an ESA funded study on "MEMS-based Electric Propulsion". They concluded that a system based on the Krpoun/LMTS thrusters was the most promising to provide propulsion capabilities to small spacecraft [26]. Following this study, the consortium was joined by SystematIC (a Dutch IC design company) and the EU-FP7 project MicroThrust kicked-off in late 2010 with the goal to, within three years, bring a system based on the electrospray thrusters described above to TRL 5.

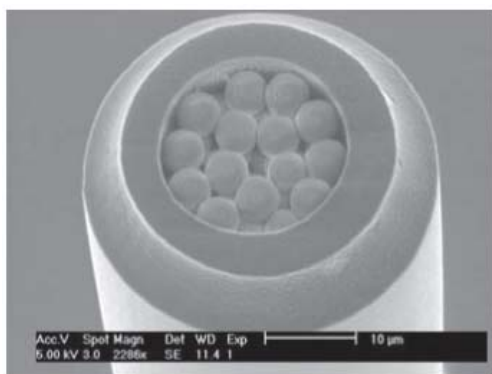
A majority of the work described in this thesis stand as part of the efforts of this consortium. LMTS's responsibilities were to design and fabricate the thruster chips (THC) at the core of the system. The devices would then be integrated and characterized by project partner QMUL.



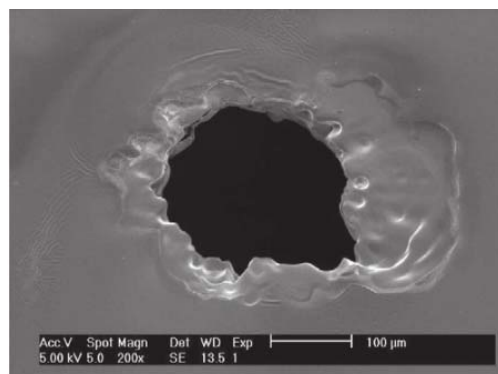
(a) Cross section diagram. [62]



(b) SEM micrographs of emitters. [84]



(c) SEM micrograph of capillary filled with 4.7 μm diameter silica beads. [32]



(d) Degraded silicon extractor following 64h of spraying. [62]

Figure 1.12: Microfabricated electrospray emitters from EPFL [32, 62, 84]

1.5 The MicroThrust initiative

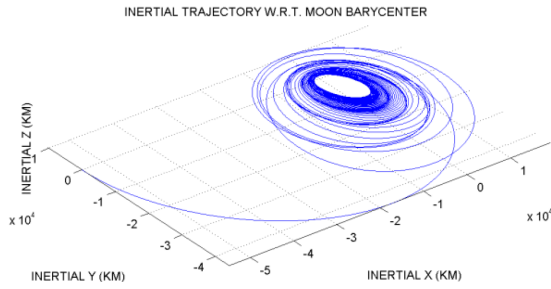
The MicroThrust project was an European project funded by the EC Seventh Framework Programme (theme FP7-SPACE-2010, grant 263035) spanning from December 2010 to December 2013. The overall objective was to build and test a breadboard version of a modular miniature electric propulsion system capable of scientific exploration missions.

The system was targeted at high ΔV missions, although fine-positioning was also considered. Figure 1.13a shows an example of a computed Moon trajectory compatible with the micro-fabricated electrospray emitters of this work. Figure 1.13b is an image of the final assembled breadboard module, including propellant storage and feeding and high-voltage electronics, compatible with four thruster chips (only one is mounted, in the top right slot).

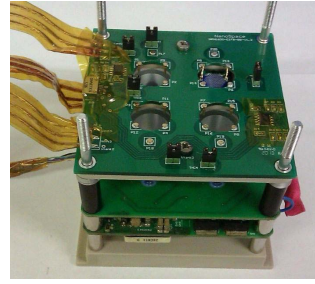
With the aim of high efficiency, low footprint and modularity, a preliminary design of the thruster module was proposed. Figure 1.13d represents a diagram of the thruster concept, where pairs of emitters operate in synchronized and opposite polarities. Alternating the polarity is useful to avoid charge imbalance in the propellant reservoir which could lead to electrochemical degradations. Working with two emitters of opposite polarities, it is possible to operate without an external neutraliser while keeping spacecraft neutrality at all times.

Early system design also established that the devices should be operated with no active pressure control, which would require pressurized tanks and lines, adding system mass. The power supply was designed by SystematIC to provide up to 3.8kV total potential, divided between the extractor and accelerator electrodes. It was expected that the thrusters would operate with an extraction voltage of approximately 800V, while the remaining 3000V would be used for acceleration.

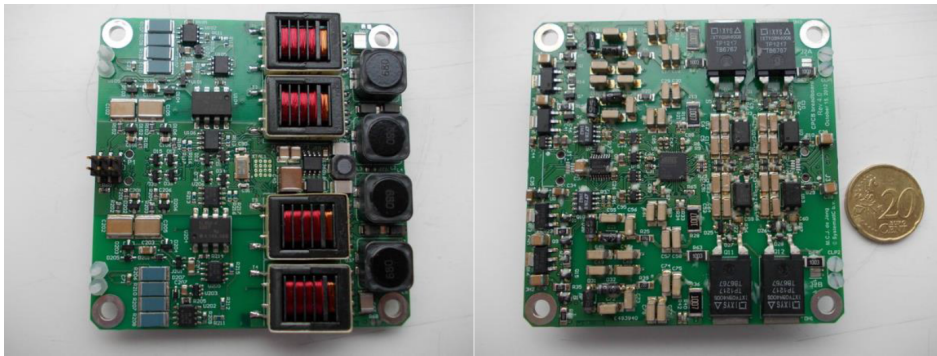
Table 1.4 lists several specific requirements established by the project team and which guided the design of the microfabricated electrospray THC.



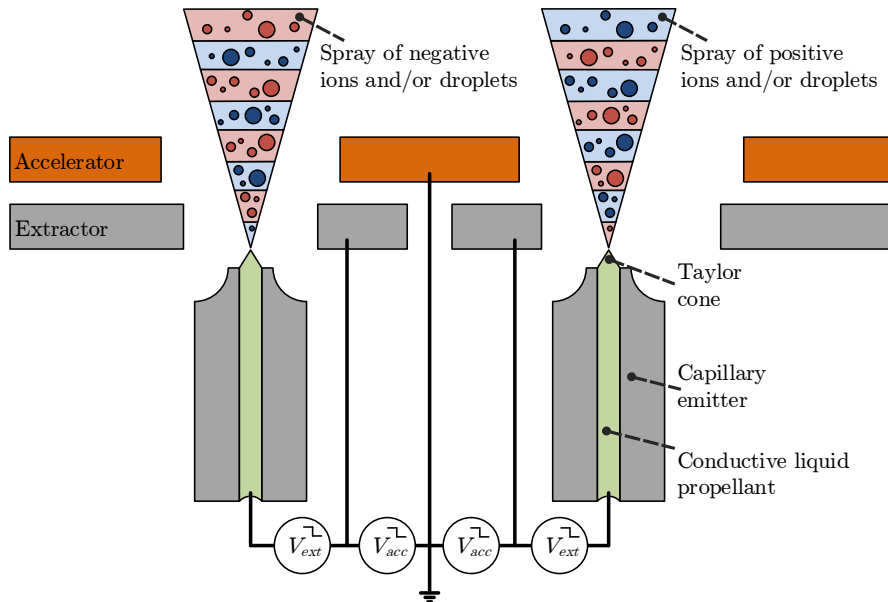
(a) Computed trajectory for travel to the moon. [85]



(b) Final MicroThrust breadboard assembly with a single electro-spray thruster (top right). [85]



(c) High voltage PCB developed in MicroThrust project. [85, 86]



(d) Concept of emitter pairs working in synchronized and opposite polarities, as used in MicroThrust. Alternating the polarity of the emitted particles avoids charge buildup in the reservoir. Working in pairs of opposite emitters, spacecraft charging can be avoided.

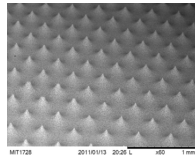
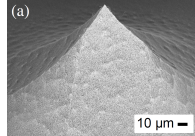
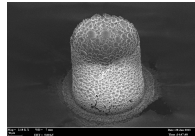
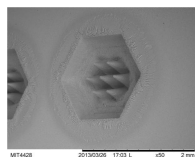
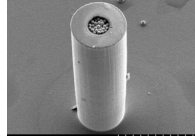
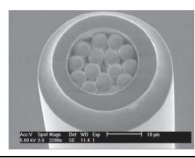
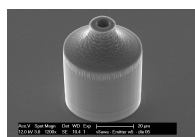
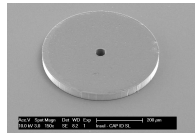
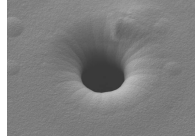
Figure 1.13: Images of MicroThrust breadboard and simulated mission.

Table 1.4: MicroThrust propulsion system requirements [12].

Requirement	
1	The MicroThrust propulsion system shall be designed for exploration mission destinations including the Moon, NEO, Sun-Earth Lagrange points and Mars. The total ΔV capability of the MicroThrust propulsion system shall be greater than or equal to 5km/s .
2	The MicroThrust propulsion system shall be designed to provide accelerations at 1AU that are greater than or equal to 0.1 mm/s^2 . This minimum acceleration ensures feasibility of the low-thrust trajectory in space and controllability of the satellite during cruise.
3	The produced thrust to power ratio of the MTPS shall be greater than $20\mu\text{N/W}$ (50W/mN) when considering the power as the total input power to the propulsion system.
4	The propulsion specific impulse at full power shall be greater than or equal to 3000s for interplanetary exploration missions.
5	The thruster lifetime of the MTPS shall be greater than or equal to 13 000 hours over the range of considered I_{sp} . The MTPS system shall be designed to survive and be able to operate during 4 years after launch.
6	The MTPS in its smallest configuration shall fit in a volume defined by 1U out of the 3U CubeSat volume. This volume is approximately $10 \times 10 \times 10\text{ cm}^3$. This volume excludes solar panels.
7	The envelope of the TMS shall be limited to $84 \times 84 \times 75\text{ mm}$.
8	The total dry mass of the overall MicroThrust propulsion system (including TMS, PCS, and EPS external tank and all feeding systems) shall be lower than 100gr. per kg of launch mass (10% propulsion system mass fraction). This mass fraction does not include solar panel masses.
9	The total wet mass of the overall MicroThrust propulsion system (including TMS, PCS, EPS, and total propellant) shall be lower than 300gr. per kg of launch mass (30% propulsion system mass fraction). This mass fraction does not include solar panel masses.
10	The MTPS shall consume less than 5W per kg of spacecraft launch mass.

Chapter 1. Introduction

Table 1.5: Overview of recent microfabricated electrospray emitters for spacecraft propulsion.

Group		Type	Fabrication method	Propellant Feeding	Image
MIT [18]	2012	Porous	Electrochemical etching of nickel	Passive	
MIT [45]	2013	Externally wetted	Isotropic RIE & carbon nanotube growth from bulk silicon	Passive	
MIT [49]	2013	Porous	Sintering of glass microbeads in silicon SOI wafer mold	Passive	
MIT [50]	2013	Porous	Laser machining of porous glass	Passive	
Yale [51]	2014	Internally wetted	DRIE from bulk silicon & bead filling	Pressure-fed	
EPFL [62]	2009	Internally wetted	DRIE & isotropic RIE from SOI wafer & bead filling	Pressure-fed	
EPFL (This work)	2014	Internally wetted	DRIE & isotropic RIE from SOI wafer	Passive	
EPFL (This work)	2014	Internally wetted	Laminated film photopatterning	Passive	
EPFL (This work)	2014	Internally wetted	Laminated film photopatterning and Parylene-C deposition	Pressure-fed	

1.6 Summary

Over the last decade, propulsion systems based on electrosprays have received increasing attention due to their unmatched potential in achievable ΔV for small spacecraft. Several research groups still attempt, using different emitter designs, to produce a microfabricated system sufficiently stable to be tested in real flight conditions (Table 1.5). One of the main concern lies with the propellant feeding mechanism. Generally, the trend goes towards increased fluidic impedance, required to stabilize flow across arrays [19] and reach the low flow rates required for PIR. Leakage current and/or breakdown, often due to propellant overflow, is a common failure cause of this type of thrusters. Operating in passive feeding mode, with no overpressure applied from the back of the emitter, largely mitigates this problem. Yet PIR has never been achieved using passively fed, internally wetted emitters, as targeted by this work.

1.6.1 Thesis novelty

As part of the MicroThrust project, a principal objective of this work was to design and fabricate thruster chips capable of meeting the harsh requirements of a high ΔV propulsion system. As such, a new chip design and improved fabrication processes were proposed, for the first time including complete wafer-level integration of the electrodes. The design also included the world's first integrated 2-stage (extractor and accelerator) electrodes for electrosprays. This design was based on detailed analytical and finite element modeling modeling of the onset voltages and ion optics.

These new MicroThrust devices were characterized by project partners at the Queen Mary University of London and showed upwards of 90% ionic content in passive feeding, a record for internally fed capillary emitters. Focusing and acceleration of the plume was also confirmed.

An advanced design of electrospray thrusters is also presented, boasting an extremely high emitter density enabled by the grouping of the accelerator electrodes, and with finer features and a more reliable fabrication process.

In addition, in-situ observation of the electrospray sources inside a Scanning Electron Microscope (SEM) were attempted, in an effort to study the formation of the Taylor cone. While it was not possible to image the cone once spray initiated, most probably due to the interaction between the cone and the secondary electron trajectories, valuable information on the wetting behavior of the ionic liquid was obtained as well as a better understanding of the emitted plume. Also, several lessons were learned which should prove useful when attempting to make SEM observations in the presence of high electric fields, a domain largely unexplored.

Furthermore, the thesis provides novel supporting work in relation to liquid transport and containment inside the capillaries, including an analytical model of the wetting behavior of the liquid at the tip of the emitters. The wetting properties of two ionic liquids on several surfaces were also characterized, as well as their propensity to be contained in microcapillaries

under static acceleration, shock and vibration conditions.

Finally, novel insulator based designs relevant to mass spectrometry are presented, providing an Earth-based application of the technology developed for the electrospray thrusters.

1.6.2 Thesis structure

The core of this thesis describes the design (chapter 2) and fabrication (chapter 3) of the thruster chips which served as the MicroThrust emitters. The devices were modeled in order to yield a design capable of meeting the MicroThrust requirements and a fabrication process capable of implementing these devices is detailed. Their characterization is then presented in chapter 4.

Following the validation of the thrusters, chapter 5 focuses on the in-situ SEM observations performed in order to acquire a better understanding of the emission and failure processes.

The supporting liquid containment work is included in the appendix (Appendix A), as well as the novel insulator designs to be used as electrospray ioniser sources for mass spectrometry (ESI-MS) (Appendix B).

2 Electrospray thrusters - Design

A major step undertaken by this work has been to provide a fully integrated second electrode stage. The addition of these additional electrodes, labeled *accelerators*, has tremendous impact on the system performance. They simultaneously increase the specific impulse, thrust and system efficiency, and also introduce new system features, such as power tuning and thrust vectoring. Here, the design of such thruster chips, with integrated accelerator is presented. The devices described in this work are the first electrospray emitters which integrate two electrode levels, let alone at wafer level.

Two designs are described. The first, targeted specifically at the MicroThrust project is labeled v3a and focuses on larger arrays of emitters to be used with individual extractors and accelerators. The second design, v3b, is partly targeted at process improvement. This second version also has much higher packing density which makes it incompatible with individual accelerators. However, grouped accelerator electrodes, although potentially not as effective to accelerate the beam, could be used. The design of the thrusters described here is limited to the silicon chip itself. It does not include system considerations such as multi-chip architecture, power supply development or reservoir feed system. Instead, it focuses on the precise geometry of the chip, estimating how this geometry will affect the performance of the system.

The chapter is split in four sections. First, the capabilities and performance gains of a thruster with integrated accelerators are studied. Next, the design of the emitter itself is presented, with focus on the capillary's fluidic impedance. Third, the electrode configuration is studied, including simulations of the beam shaping capabilities of accelerators. Last, some estimates of the expected performance of the different designs are given.

Parts of this chapter were published in:

Dandavino, S., Ataman, C., Ryan, C. N., Chakraborty, S., Courtney, D. G., Stark, J. P. W., & Shea, H. R. (2014). Microfabricated electrospray emitter arrays with integrated extractor and accelerator electrodes for the propulsion of small spacecraft. Journal of Micromechanics and Microengineering, 24(7), 075011. doi:10.1088/0960-1317/24/7/075011

2.1 Accelerators to improve thruster performance

An objective of this work was to design and fabricate an advanced thruster prototype capable of meeting the rigorous requirements of the MicroThrust project. This performance was generally described by three metrics: thrust (T), specific impulse (I_{sp}) and propulsive efficiency (η_T). As mentioned earlier, array fabrication was critical to the success of the thruster due to the minute thrust levels achieved in PIR. The approach taken here was to target a geometry suitable for PIR, thus maximizing I_{sp} and η_T , while in parallel maximizing emitter packing density to allow the fabrication of larger arrays in the available space ($< 70cm^2$), thus increasing thrust. Given the non-zero beam half-angle, and to avoid electrode impingement, it was clear that a thinner electrode stack would be key to a high emitter density. From this aspect, micro-assembly provided a tremendous advantage over conventional fabrication techniques.

Figure 2.1 shows a cross section of the proposed devices. Compared with previously fabricated devices[62], they use a simpler, improved emitter fabrication process and wafer-level bonding of two-level electrodes. The new process permits the large scale fabrication of high aspect ratio capillaries with the smallest $\approx 6.5\mu m$ inner diameters to date. Microsandblasted glass is used as a handle layer, carrying both extractors and accelerators. Design v3a is considered safer, delivering individual acceleration to each emission site while v3b pushes the packing density with a one-accelerator, multiple emitter configuration.

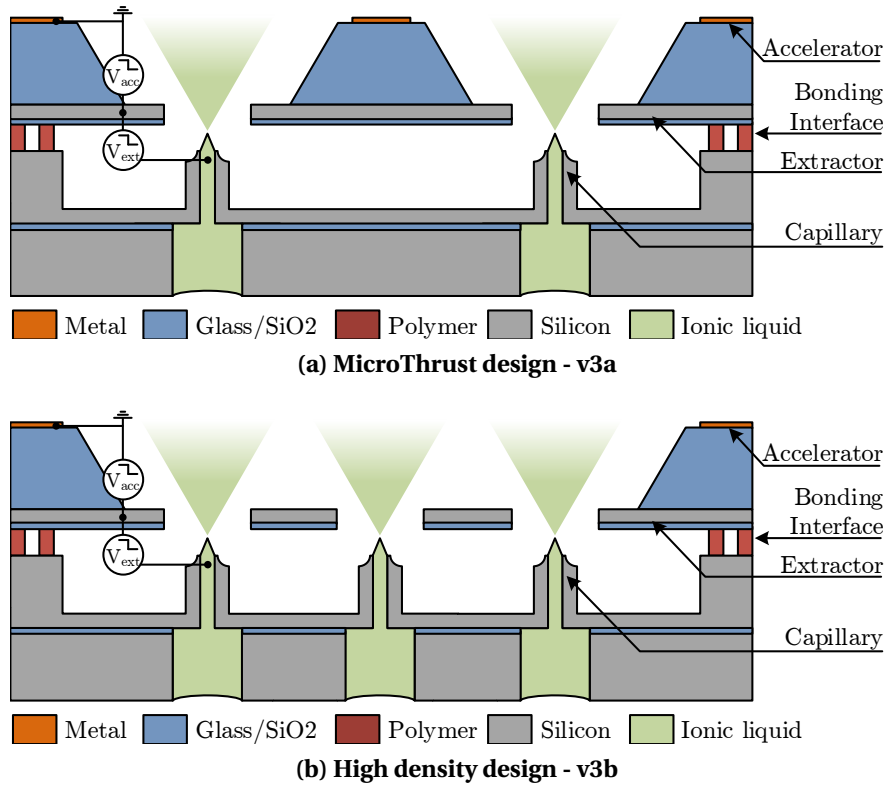


Figure 2.1: Cross section diagrams of thruster chips with integrated accelerators.

2.1. Accelerators to improve thruster performance

Before delving into the specifics of the thruster design, it is useful to describe more accurately the performance metrics of the electrospray thruster. The propulsive efficiency in particular is a metric that has not as yet been discussed. It determines how much input electrical power (P_e) should be provided to generate a certain thrust (or specific impulse). Not including power wasted due to leakage current, either from the voltage converted or the thruster assembly, the propulsive efficiency is the ratio between the propulsive beam power P_b and the input electrical power P_e :

$$\eta_T = \frac{P_b}{P_e} = \frac{\frac{T^2}{2\dot{m}_p}}{I_{em}V_{app}} = \frac{TI_{sp}g_0}{2P_e} = \eta_P\eta_E\eta_\theta \quad (2.1)$$

The polydisperse efficiency η_P , the energy efficiency η_E and the angular efficiency η_θ are, assuming sufficient physical clearance of the electrodes and low propellant evaporation, the principal sources of propulsive efficiency loss [87]. Eq. 2.2 and Eq. 2.3, in which the efficiency factor has been included, highlight how both thrust and specific impulse are increased by supplying additional electrical power to the thruster.

$$T = I_T \sqrt{2V_{app}\eta_T \frac{m}{q}} = \sqrt{2\eta_T I_T \frac{m}{q} P_e} = \sqrt{2\eta_T \dot{m}_p P_e} \quad (2.2)$$

$$I_{sp} = \frac{1}{g_0} \sqrt{2V_{app}\eta_T \frac{q}{m}} = \frac{1}{g_0} \sqrt{\frac{2\eta_T P_e}{\dot{m}_p}} \quad (2.3)$$

Unfortunately, for a given thruster geometry, stable spray only occurs in a relatively small extraction voltage range, limiting the ability to boost performance by a direct increase of V_{ext} . This limitation is overcome by the introduction of the acceleration electrode, since the applied potential V_{app} can now be increased while keeping V_{ext} at an optimal level. Of course, the square root relationship between the performance increase and electrical input power indicates that the advantages of acceleration will diminish with increasing voltage, limiting the scale-up potential. Yet at the modest voltages of a few kV, which can well be supplied by miniaturized power sources [86], the increase in thrust and I_{sp} can have a major impact on the mission design and feasibility, entirely justifying the additional power requirement.

Thus purely from a performance point of view, a design which can increase the overall propulsive efficiency is extremely desirable. In the next sections, it will be shown how the emitters are key to optimising the polydisperse efficiency, while the energy and angular efficiencies are improved through careful electrode design.

2.1.1 Added features

In addition to the direct performance improvements, accelerators bring several system features useful for the thruster module.

One of those is the capability to tune thrust without affecting the emission process. In this way, optimal conditions can be set on the extraction voltage to yield a desirable operation point and adequate charge balancing, while keeping flexibility on the thrust. Charge balancing is critical both from a spacecraft neutrality point of view, and also to avoid electrochemical reactions in the propellant reservoir [37].

A thruster module based on the microfabricated electrosprays would most probably be composed of several chips, which could potentially be addressed individually. It is a great advantage of this technology that the thruster can so easily be partitioned without significant loss of performance or increased mass and volume. With emitters positioned away from the center of the spacecraft, thrust vectoring can be used to rotate the spacecraft, compensating for trajectory perturbations (Figure 2.2a).

Accelerators can also be used to tune the power consumption of the thrusters (Figure 2.2b). This is particularly relevant for missions going towards or away from the sun, where available power will vary ($E_{sun} = \frac{129.3}{D^2} \text{ mW cm}^{-2}$), where D is the distance from the Sun in AU). Once again, optimal extraction conditions can be ensured even with variable power.

Finally, a configuration which may appear counter-intuitive but which could yield interesting results is to use these extra electrodes to decelerate the particles. For thrusters where the emitted current is proportional to the extraction voltage, which is often the case here, this could permit a higher emission current for a given power consumption (V_{app} is reduced). Although this configuration would have reduced specific impulse and efficiency, as will be shown in the next section, it would have higher thrust, since $T \propto I_T \sqrt{V_{app}}$. Thus for a given power, and given the choice, it is better to increase current than beam potential to increase thrust.

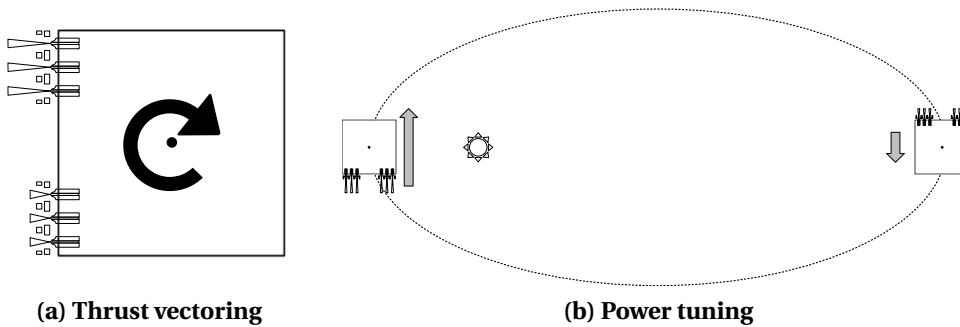


Figure 2.2: Diagrams of thrust vectoring and power tuning enabled by accelerator.

2.2 Capillary emitter design

In addition to its primary role of bringing the propellant to the emission site, the capillary emitter and its geometry are of crucial importance to the performance of the thruster. Being the highest impedance component in the fluidic path (at least in the case of microfabricated emitters), it effectively drives the propellant flow rate. A high impedance will lead to a low flow rate, critical to reaching the high I_{sp} , high η_P , PIR. A key dimension for the capillary emitter design then is its inner diameter, which in turn determines its fluidic impedance.

In this section, the design of this impedance is studied, with an attempt to determine what emitter dimensions would be sufficient to achieve ionic operation.

First, though, it is important to review a source of potential thruster performance loss, the polydisperse efficiency. This metric, entirely related to the composition of the beam, describes how the efficiency of the device will vary as we attempt to reach the ionic regime.

The polydisperse efficiency (Eq. 2.4) results from the extraction and acceleration of different particle species. For two distinct and discrete species, where f_1 is the fraction of the current carried by the smaller species (with larger q/m) and ζ is the ratio of the charge-over-mass ratios (smaller mass/larger mass), η_P is written as [87]:

$$\eta_P = \frac{\left(1 - (1 - \sqrt{\zeta}) f_1\right)^2}{1 - (1 - \zeta) f_1} \quad (2.4)$$

The polydisperse efficiency is related to the composition of the spray as generated by the extraction electrode. It stems from the fact that it takes more energy to accelerate smaller particles (ions) to reach a given thrust than it does with larger ones. Figure 2.3 plots η_P for different droplet masses. The larger the droplet size, the more quickly the efficiency drops off when ions are introduced.

Although electrosprays operating in the droplet mode have been shown to display remarkable size homogeneity [88] and consequently large η_P , the droplet mode inevitably leads to low specific impulse (Eq. 2.3). To increase the I_{sp} , the droplet size must be reduced, which often leads to a gradual increase in ion content and lower efficiency. Operation in the PIR, with little to no droplets (well below 1%) present, offers a solution to this tradeoff. In this case, both high efficiency and specific impulse are achieved, explaining why PIR is such an attractive operation mode. As highlighted by Figure 2.3, it is clear that if PIR is targeted, it must be achieved, since even a small fraction of droplets will have grave consequences for the performance of the system.

One path leading to the ionic regime, as demonstrated by Krpoun [62], is the increase of the emitter's hydraulic impedance. Prior to this work, devices fabricated at LMTS relied on

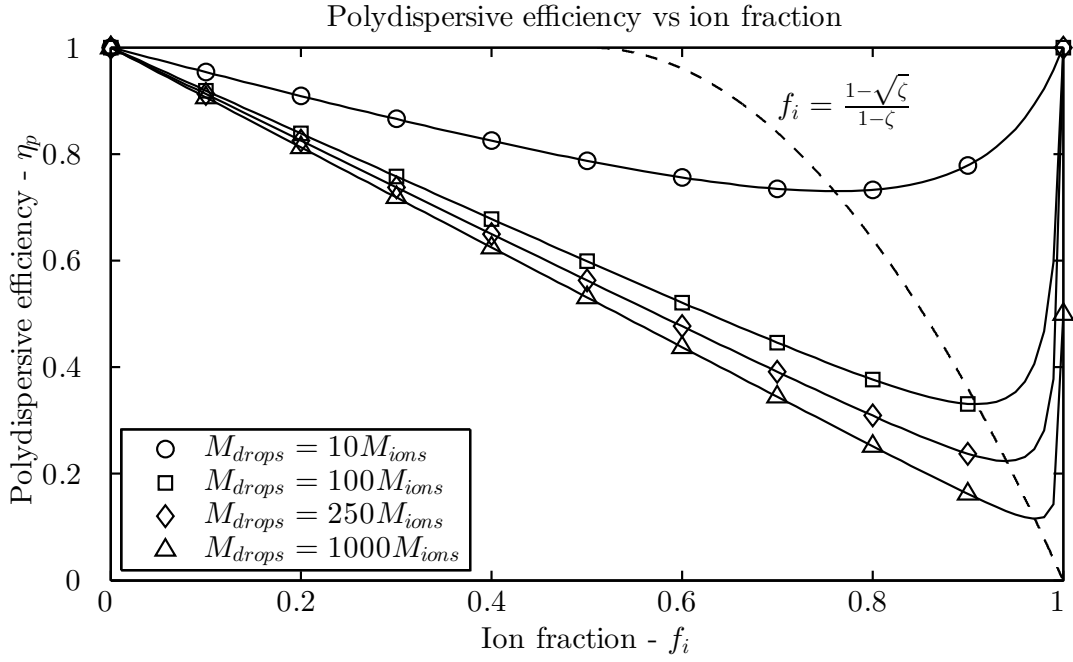


Figure 2.3: Polydispersive efficiency vs ion fraction for different droplet size. Larger droplets lead to a sharper decline in efficiency. Approaching PIR, small amounts of droplets quickly reduce the efficiency. The dashed line follows minimum efficiency points, corresponding to $f_i = \frac{1-\sqrt{\zeta}}{1-\zeta}$

the filling of wider capillaries ($24 \mu m$ inner diameter) with silica microbeads to achieve this (Figure 2.4). This novel process, which was reproduced by Lenguito et al. [51] at Yale, proved to be an excellent means of increasing the impedance and allowed ionic operation with these larger capillaries.

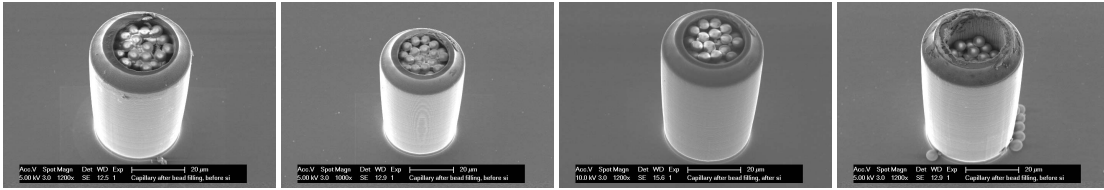


Figure 2.4: SEM images of bead filled emitters.

However, with increasing focus on the fabrication of large arrays, this method becomes impractical due to the random arrangement of the beads and emitter to emitter variability which can lead to non-uniformities in operation. Instead, improving the etching step of the emitter interiors to allow narrower emitters is a more uniform and reliable way to achieve this high impedance.

As a design guideline, the aim is nevertheless to achieve similar impedance to the bead-filled capillaries. A significant difference remains that these earlier emitters were operated with active pressure control, making it difficult to guarantee that the new emitters, even with equal

impedance would be equally ionic. Yet one can expect that a passively fed capillary operated in the same conditions and having no backpressure would necessarily have a flow rate lower or equal to a pressurized one, which would be consistent with PIR.

A model adapted from Ergun [89] was used to compute the impedance of the bead-filled emitters. With Eq. 2.5, the effective inner diameter D_{eff} of the emitter is computed, which is then inserted in the Hagen-Poiseuille equation (Eq. 2.6). Figure 2.5 shows how a large capillary of diameter D , filled with spheres of diameter D_s , is modeled as a smaller capillary of diameter D_{eff} .

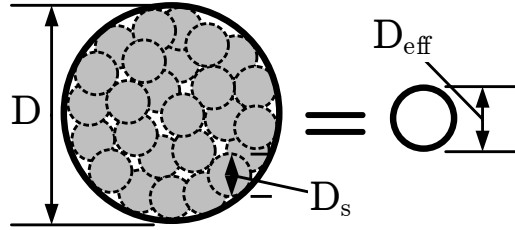


Figure 2.5: Diagram showing how a cylinder of diameter D , filled with spheres of diameter D_s , is modelled as a smaller cylinder of diameter D_{eff}

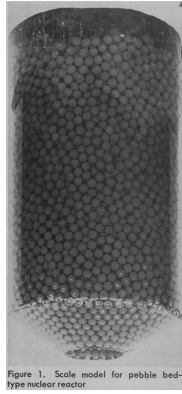
$$D_{eff} = \sqrt[4]{\frac{128}{600} \frac{D_s^2 D^2 \epsilon^3}{(1 - \epsilon)^2}} \quad (2.5)$$

$$R_{fl} = \frac{128 \mu L}{\pi D_{eff}^4} \quad (2.6)$$

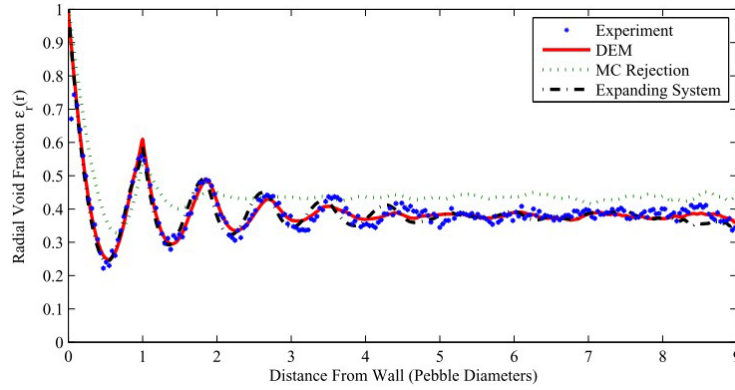
In Eq. 2.5 and Eq. 2.6, μ is the dynamic viscosity of the fluid ($0.038 \text{ Pa} \cdot \text{s}$ for $EMI - BF_4[60]$), L is the length of the capillary and ϵ is the void fraction, which ranges from 0 to 1 and describes the packing of the beads inside the cylinder. Yet determining an accurate value of the ϵ is far from trivial.

The distribution of beads in macroscopic cylindrical beds was extensively studied, in particular in view of its applications to chemical reactors, heat exchangers and nuclear reactors. While early experiments were very "mechanical", for example using epoxies to solidify pebbles in a given configuration before analyzing cut samples [90, 91], a more recent experiment by Auwerda et al. [92] used a non-destructive scanning gamma-ray setup to generate a complete description of the void fraction in a cylinder.

In agreement with the previous experiments, Auwerda found, both through model and experiment, that ϵ stabilized to 0.4 starting $5 D_s$ from the wall (Figure 2.6b). Closer to the wall, though, the packing varied considerably, with ϵ oscillating between approximately 0.25 and



(a) Macroscopic pebble bed used to measure void fraction. [90]



(b) Modeled and measured radial void fraction. [92]

Figure 2.6: Experiments to determine the void fraction in macroscopic cylindrical beds.

0.65. In the earlier bead filled capillaries, the cylinders themselves measured $24\mu\text{m}$ and the beads $5\mu\text{m}$, so that the "stabilized" value of 0.4 could never be reached. Instead, the actual impedance can be more fully described using a range of D_{eff} resulting from void fractions ϵ ranging from 0.25 ($D_{eff} = 3.0\mu\text{m}$) to 0.65 ($D_{eff} = 9.1\mu\text{m}$). With these considerations, Figure 2.7 shows how the bead filled emitters from [62] compare with the emitters presented in this work.

Aiming for the high end of this range, $5.0 \pm 0.5\mu\text{m}$ inner diameters emitters were targeted, providing a high impedance with an expected uniformity of $\approx 21\%$ (Calculated as $(R_{max} - R_{min}) / R_{avg}$). As will be discussed in the next chapter, lateral attack during the etch process led to slightly wider fabricated devices, as shown in Table 2.1. The table also shows how two types of devices, with $50\mu\text{m}$ and $100\mu\text{m}$ emitter height were fabricated for the v3b design. Considered in the coordinates of Figure 2.6, the devices fabricated in this work are expected to have 0.5 - 1 order of magnitude lower impedance than the target and be in the lower range of the bead-filled emitters. The devices also have excellent uniformity, with calculated variations below 2%.

Table 2.1: Effective inner diameter and corresponding hydraulic impedance of latest generations of electrospray emitters fabricated at EPFL. Values under parenthesis represent an estimation. Min/-max values correspond to median $\pm 1\sigma$. For the v3b chips, two emitter heights, $50\mu\text{m}$ and $100\mu\text{m}$ were fabricated.

Gen.	D_{eff} (μm)			R_{fl} ($\text{kg s}^{-1} \text{m}^{-4}$)			Variation (%)
	Min	Mean	Max	Min	Median	Max	
Krpoun 2009 [62]	(3.0)	(5.4)	(9.1)	(2.25e16)	(1.67e17)	(1.81e18)	412
This work - targeted	4.5	5.0	5.5	1.69e17	2.48e17	3.78e17	20.7
This work - v3a	7.40	7.90	8.40	3.11e16	3.98e16	5.16e16	8.1
This work - v3b ($50\mu\text{m}$ height)	5.55	5.69	5.83	6.61e16	7.33e16	8.16e16	1.4
This work - v3b ($100\mu\text{m}$ height)	6.71	6.90	7.09	6.13e16	6.83e16	7.64e16	1.5

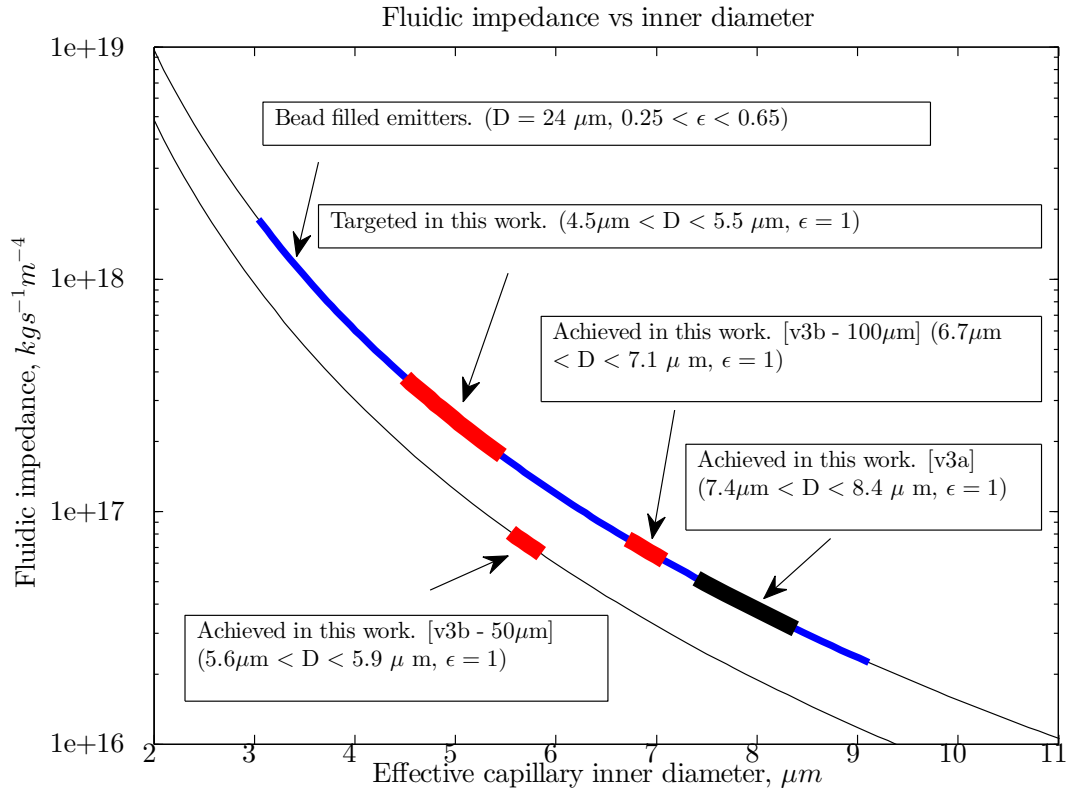


Figure 2.7: Estimated fluidic impedance of capillary emitters.

2.3 Electrostatic design

Although the emitter design was expected to be a more determining factor in terms of the nature of the emitter species, the electrode design was also of critical importance to the operation conditions.

Even for a given operation regime and propellant flow rate, different electrode geometry would determine the operation points in terms of voltage and beam angle, thus having a direct impact on the device performance.

To study these conditions, a complete electrostatic model of the thruster device was implemented in COMSOL and is presented in this section. The objective was to provide a general picture of the behaviour of the devices, focusing on two aspects. In the first part, the effect of different geometries on the turn-on, or onset voltage (V_{onset}) of the spray is evaluated. Second, the ion optics resulting from the introduction of the accelerator electrodes are studied. In relation to these results, the energy and angular efficiency of the thrusters will be discussed, completing the performance estimate model.

2.3.1 Onset voltage model

An important objective was to minimize the extraction voltage. While a higher V_{ext} may have been useful to increase the beam energy and thruster performance, a lower voltage at this level lead to a more reliable chip and simpler system design. Post-acceleration, which could now be achieved using the acceleration electrode, was the preferred choice to increase the performance.

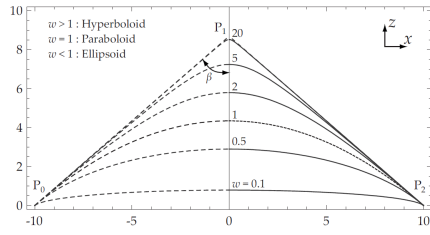
A complete design study was done, systematically evaluating the effect of each parameter over their potential range. The general design philosophy was to optimize performance while also improving manufacturability. Understanding the importance of each geometric parameter was necessary to choose which feature tolerances could be loosened to improve manufacturability and which should be the focus of tighter control. The baseline of the geometry was similar to that of previous thruster generations [62], although adjusted for the smaller emitter dimensions and accelerator integration.

The simple model used an iterative procedure, adapted from that published by Krpoun [83], to compute the required voltage (V_{onset}) to generate a 1V/nm electrical field at the emitter tip, a value reported to be sufficient for ion extraction [15]. This geometry assumes that emission onset occurs following a smooth quasi-static transition from a conic shape, as opposed to a snap-in from a state where the liquid is contained inside the capillary, as shown in Figure 2.8c.

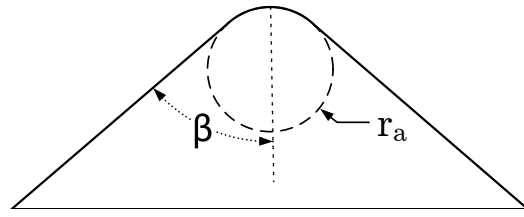
Unlike Krpoun, who had used a conic Bernstein-Bézier curve to describe the liquid tip just before emission, here the tips were modeled as 49.3° truncated cones topped by spherical caps (Figure 2.8). This approximation is certainly "unphysical" for large tip radii, but converges accurately to Krpoun's model as the tip is sharpened. The cone is modeled as a solid, perfectly

conductive surface which is gradually sharpened. The COMSOL simulations allowed the computation, for each tip radius, of the constant coefficient $k(r_a)$ relating the applied voltage and electrical field at the tip. Next, the equilibrium field which could physically balance the liquid's surface tension was computed at the apex for a given radius using Eq. 2.7 [93]:

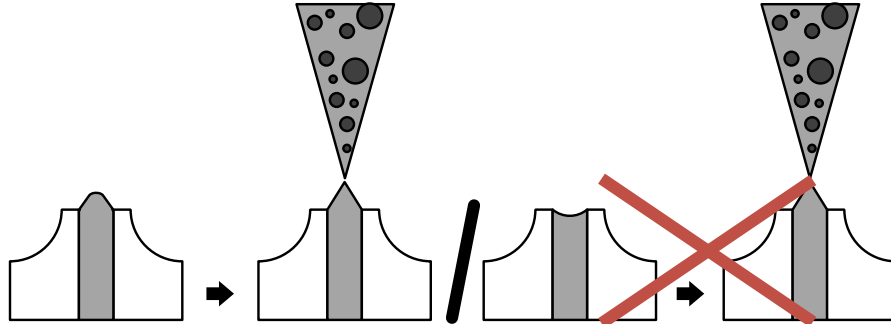
$$\frac{2\gamma}{r_a} = \frac{1}{2}\epsilon_o E_{a_o}^2 \quad (2.7)$$



(a) Conic function used by Krpoun[83] to model the Taylor cone with half angle $\beta = 49.3^\circ$ ($p_x = 10$)



(b) Truncated cone used in this work with half angle $\beta = 49.3^\circ$ and radius r_a



(c) Diagram showing how emission initiates from a conic shape, iteratively sharpened until the electric field at the tip reaches 1V/nm.

Figure 2.8: Cone shapes used for simulation

Once a tip radius sufficiently sharp to yield a 1V/nm electrical field was found, the corresponding voltage (V_{onset}) was computed using the $k(r_a)$ value.

The electrical potential boundary condition was applied on the exterior surface of the liquid cone and the silicon emitter as shown in Figure 2.9b. For computational rapidity, the model was axisymmetric.

In addition, it was assumed that the cone base was constrained to the inner diameter of the emitter. Such a case was observed by Deng et al. [63] using pressure fed emitters when using very electric fields, which is expected to be the case here. Validating this assumption was one of the objectives of the SEM in-situ experiments described in chapter 5.

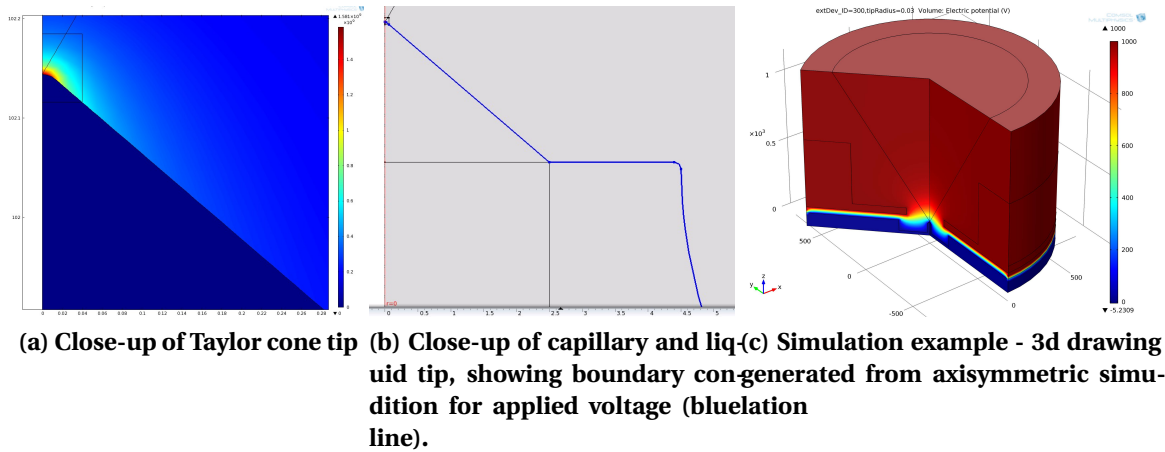


Figure 2.9: Onset voltage simulations

To evaluate its accuracy, the model was compared against measured onset voltage data obtained using devices from a previous generation (labeled V2, fabricated and tested early in the thesis). Thrusters with extractor inner diameters of 150, 200, 250 and 300 μm were operated, although only a single data point is available for each dimension. As shown in Figure 2.10, the model shows good agreement, although it appears to underestimate the onset voltage by 10-16%. Such a difference may have been due to variations in the shape of the cone, or the presence of a jet, present due to the large droplet content of these earlier devices. More important than the absolute values, though, is that the model describes accurately the relative effect of the extractor dimensions, with almost equal slopes when the data is fitted linearly (1.16 $\text{V}/\mu\text{m}$ for the measured data vs 1.14 $\text{V}/\mu\text{m}$ for the simulated points).

Table 2.2 lists the labeling of each parameter considered in the simulation, (See Figure 2.11) as well for labeling of the simulated dimensions. The values in bold indicate the "baseline" values. Unless otherwise specified, these were kept constant while a parameter under test was iterated through its specified values.

Figure 2.11 summarizes the effects of each parameter on the onset voltage. Each of these parameters is also plotted individually in Figure 2.13, Figure 2.14, Figure 2.15 and Figure 2.16. Results show that the extractor inner diameter in particular is a parameter that should be minimized to reduce the onset voltage. The extractor-emitter gap is also important, although below 25 μm spacing, the reduction in onset becomes less pronounced and may be outweighed by the potentially increased leakage current and electrical breakdown issues. On the other hand, a smaller gap amplifies the extractor inner diameter effect, as shown in Figure 2.12a. It also has the added advantage of allowing smaller extractor inner diameters before beam impingement becomes problematic.

The emitter clear-out, the distance between the emitter and the surrounding bulk silicon also has a major impact, although only for small values of the clear-out. Above approximately

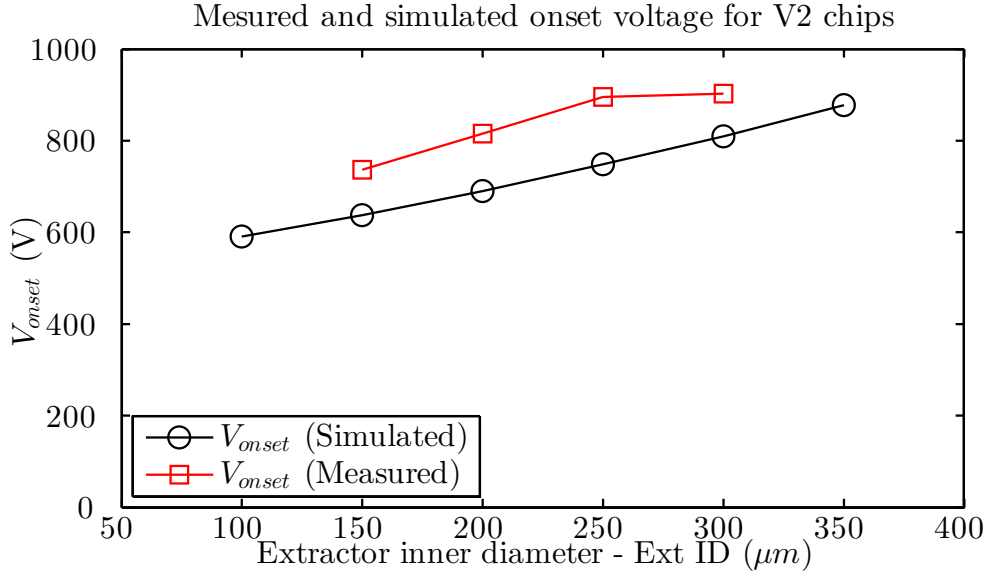


Figure 2.10: Comparison between measured and simulated onset voltages for a previous generation of electrospray thrusters.

Table 2.2: Simulation parameters of MicroThrust electrospray thrusters. (All dimensions in micrometers.)

Parameter	Identification	Simulated dimension (μm)
Emitter inner diameter	Cap ID	1, 3, 5 , 10, 20, 50
Emitter wall thickness	Cap Wall	3, 5, 10 , 20, 50
Emitter isotropic etch radius	Cap isoEtch	0, 3, 5, 8 , 9, 10
Emitter outer height	Cap OH	10, 20, 30, 50, 80
Emitter clear out	Cap CO	12.5, 52.5, 112.5, 212.5 , 562.5
Extractor electrode diameter	Ext ID	50, 100, 150 , 200, 300, 500
Extractor electrode thickness	Ext dev H	1, 5, 10, 25, 50 , 100
Extractor-emitter gap	Ext gap	0, 15 , 25, 50, 100
Glass thickness	Ext handle H	150, 200, 250 , 300, 350
Accelerator electrode diameter	Acc ID	250, 450, 650 , 850, 1050
Acceleration voltage	V_{acc}	0 , 1000, 2000, 3000

100 μm , there is almost no longer any effect on the onset, as seen in Figure 2.14b. Applied to emitter arrays, this value may be a good indication of the minimum pitch if interactions between emitters should be avoided.

The next most important design parameter is the radius of the isotropic tip etch which is used to sharpen the tip. Generally, this etch should be as large as possible, within the confines of manufacturability, so that the electrical field will be more focused on the liquid cone. Interestingly, this constraint becomes increasingly important as the inner diameter of the emitter is reduced, as shown in Figure 2.12b since a smaller cone will be more affected by its

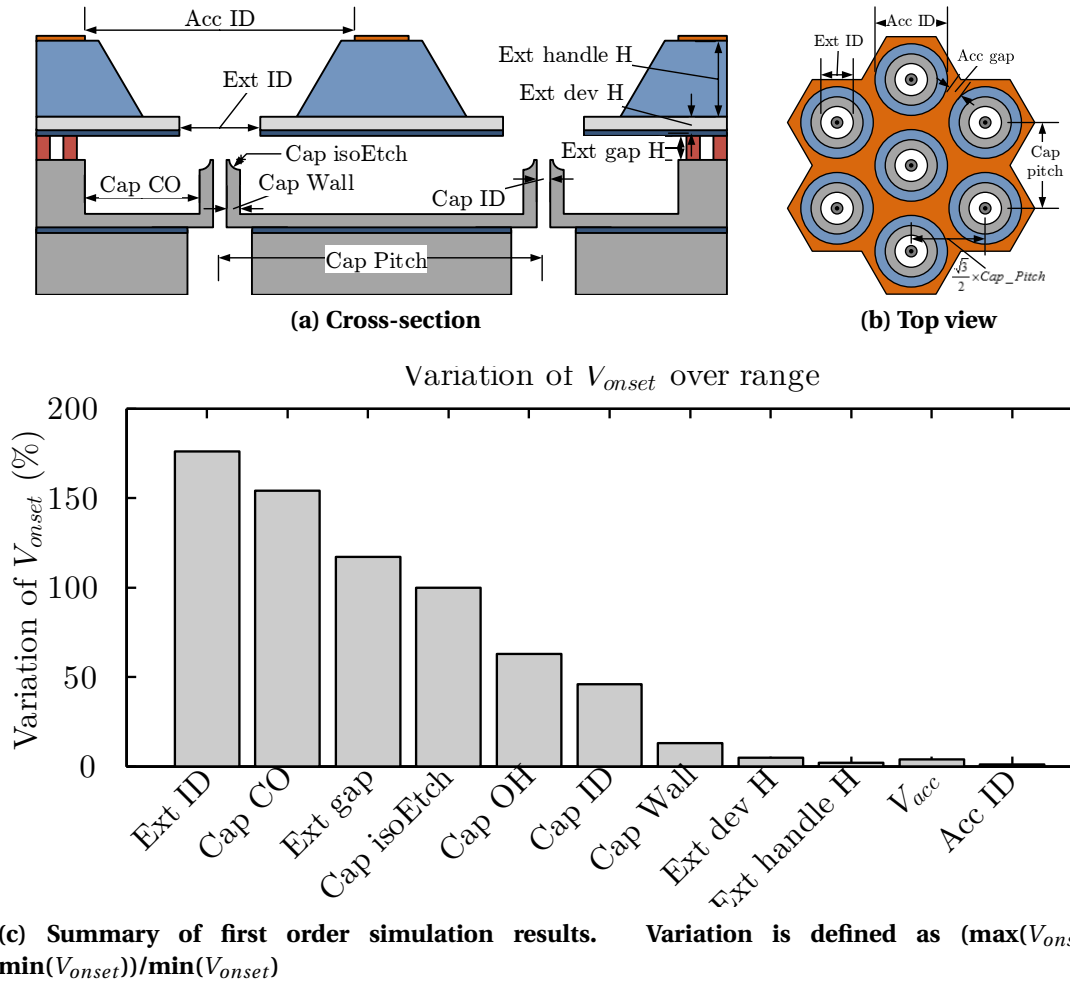


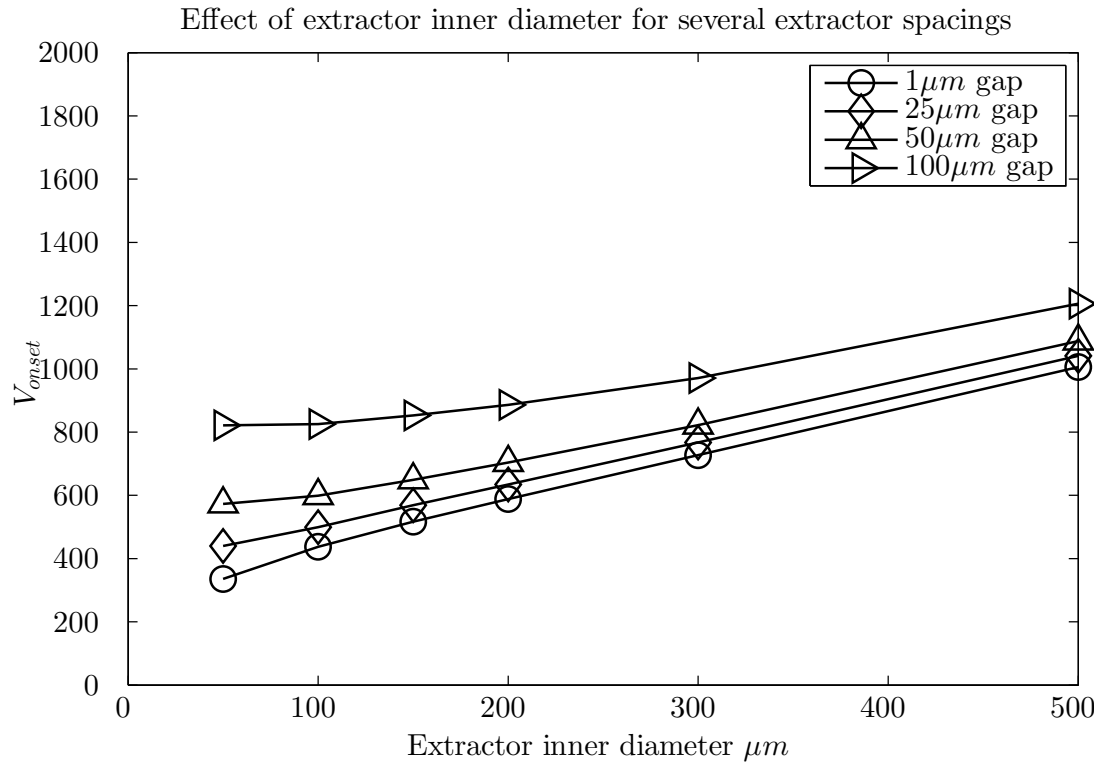
Figure 2.11: Summary of onset voltage simulation results

immediate surroundings.

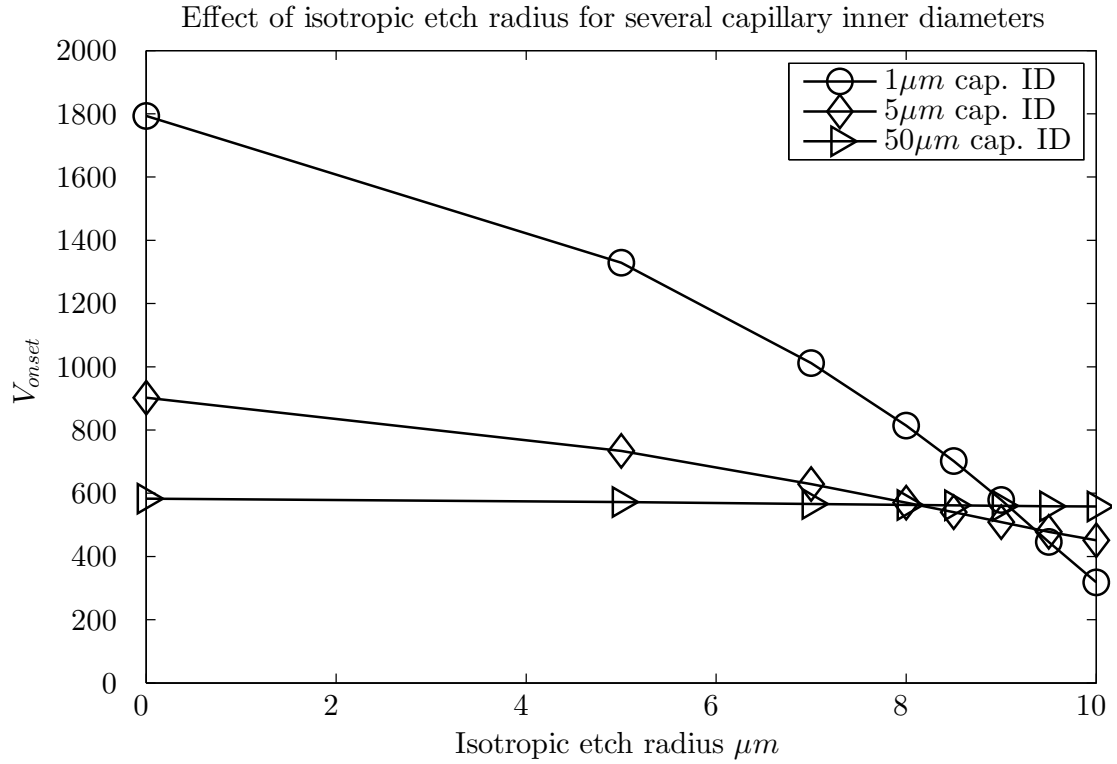
Finally, the free-standing height of the emitter (Cap OH) has a large effect below $\approx 30 \mu\text{m}$. Reducing this height is however desirable from a manufacturing point of view: a shorter emitter interior will much more easily be etched, potentially leading to higher and more uniform fluidic impedance. (The fluidic impedance is proportional to the height of the emitter but to the fourth power of the inner diameter.)

The simulations also highlight an important element regarding the accelerator electrodes, namely that they have little to no impact on the electrical field at the tip of the emitter. This is in fact a very desirable situation since it allows decoupling the design of each electrode.

The specific dimensions chosen for the thrusters of this work are listed in section 2.5, along with the modeled onset voltage.



(a) Interaction between extractor spacing and inner diameter



(b) Interaction between tip isotropic etch and emitter inner diameter

Figure 2.12: Interactions between geometric parameters

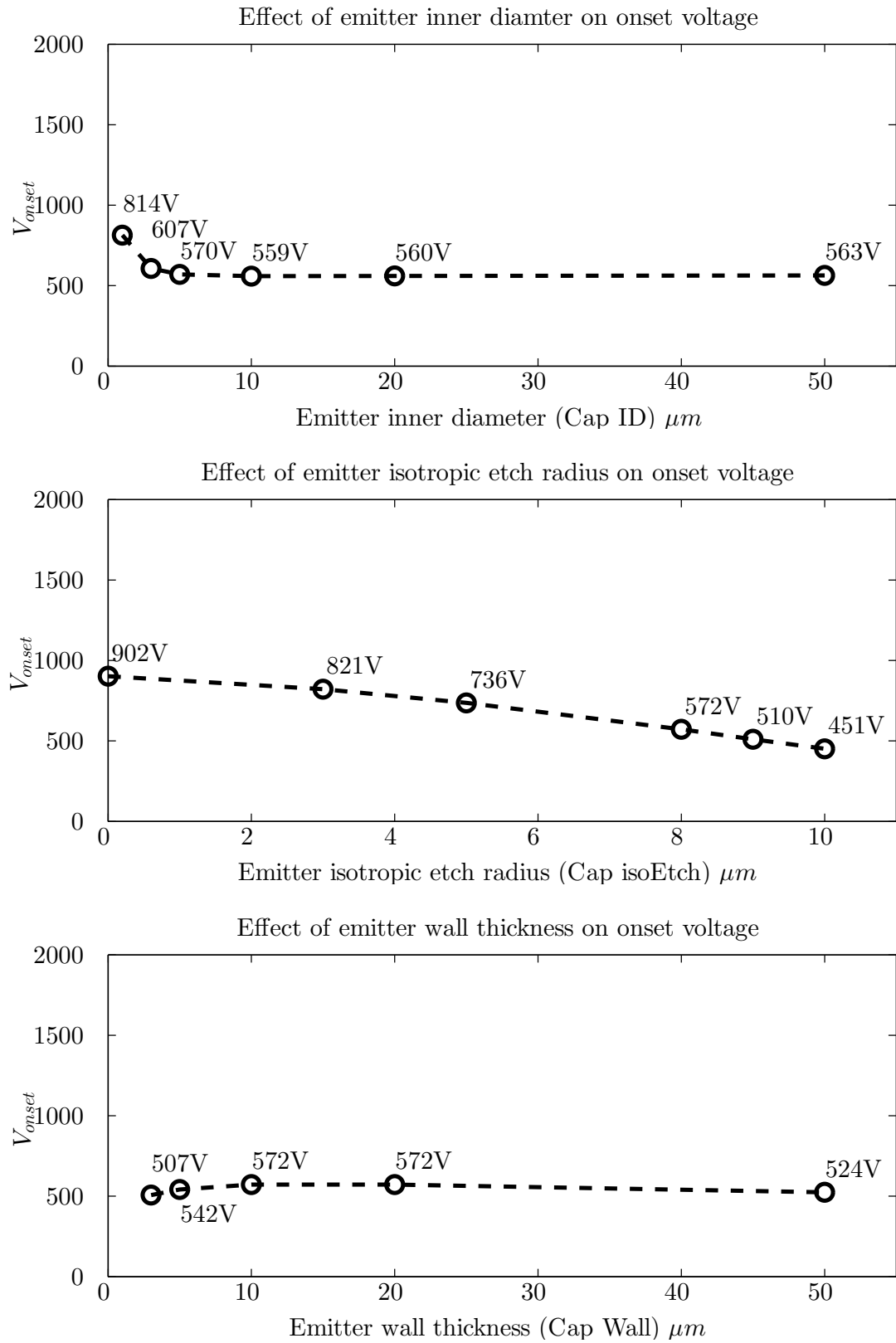


Figure 2.13: Effect of emitter inner diameter, isotropic etch and wall thickness on onset voltage.

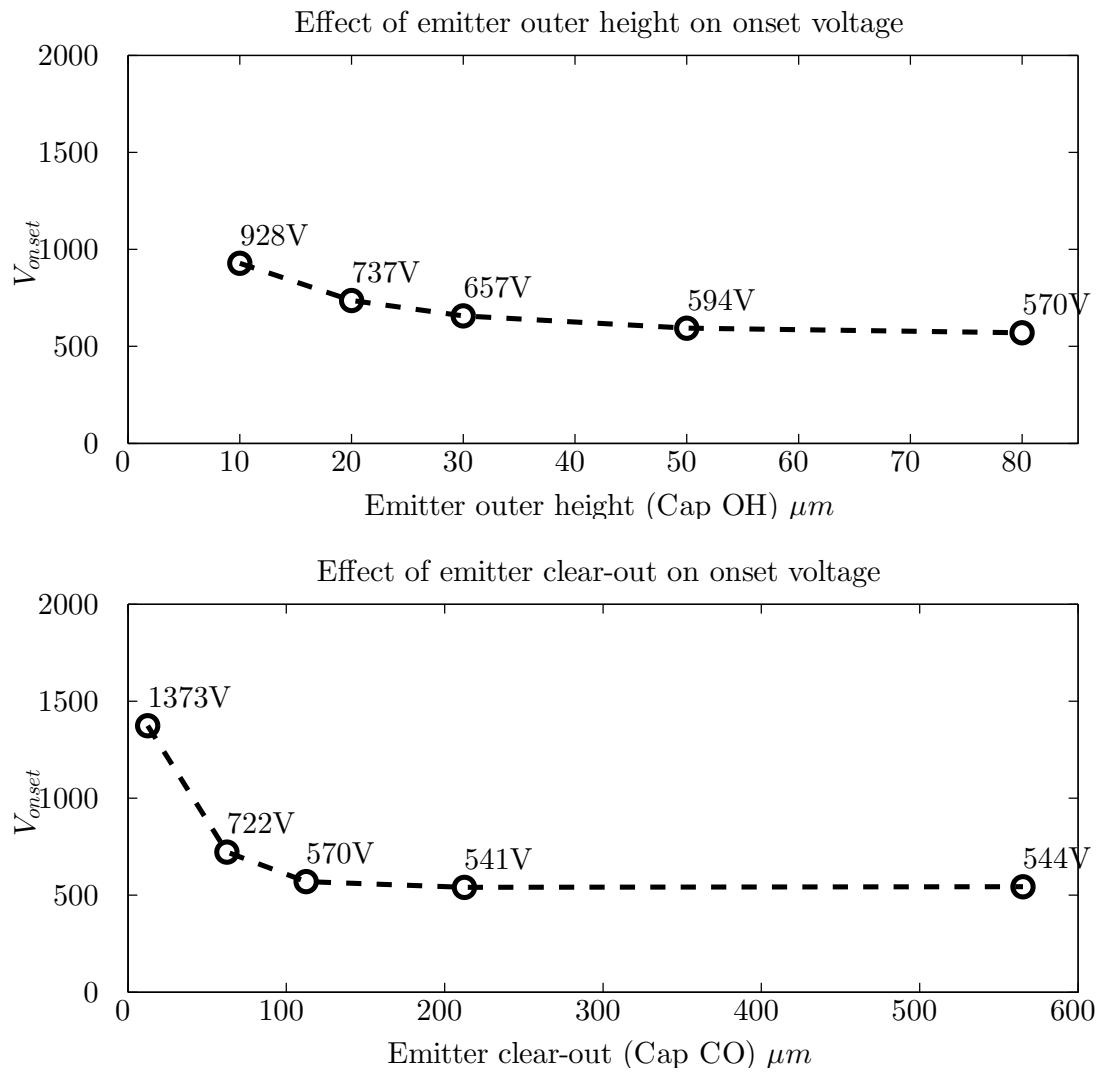


Figure 2.14: Effect of emitter outer height and clear out on onset voltage.

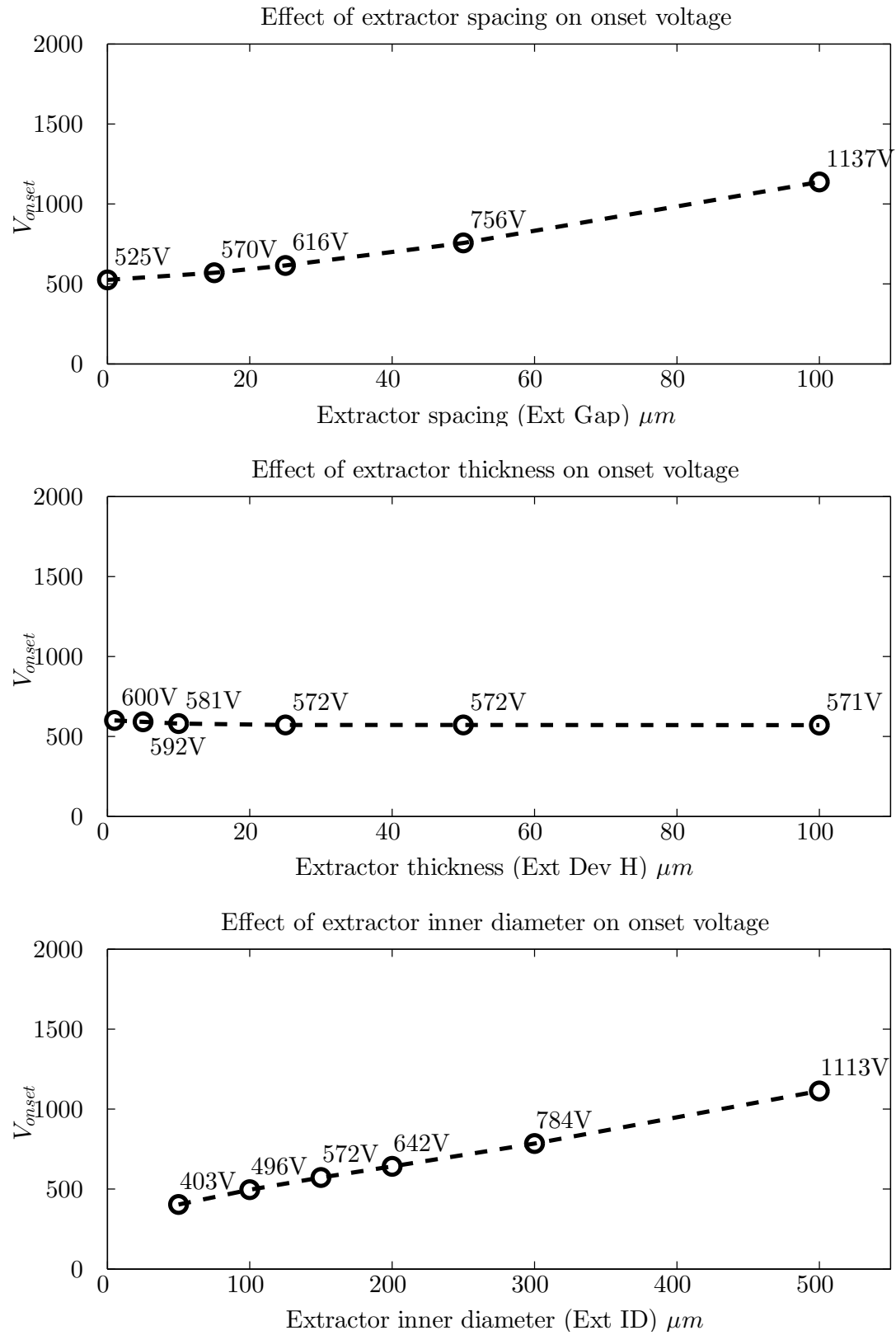


Figure 2.15: Effect of extractor gap, thickness and inner diameter on onset voltage.

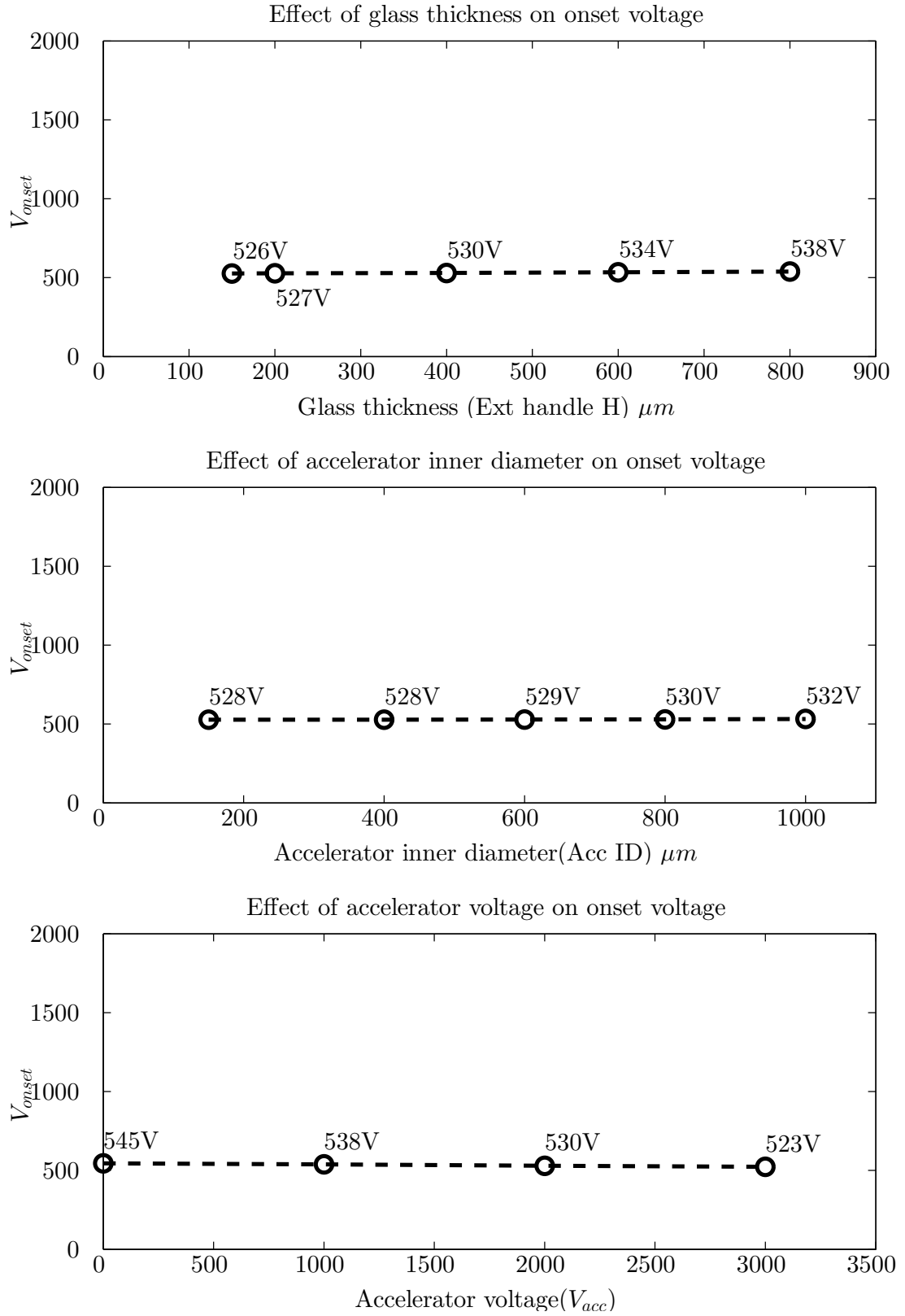


Figure 2.16: Effect of accelerator gap, inner diameter and potential on onset voltage.

2.3.2 Ion beam optics

Taking advantage of the particle tracing module, COMSOL was also used to simulate the focusing effect of the accelerator. The objective of these simulations was not to reproduce the actual emission direction in the spray, but rather get a comparative description of the accelerator's effect.

Indeed, accurately representing the emitted spray in the simulated environment is a challenging problem. The principal difficulties lies in correctly setting the initial ion energies and directions, as well as properly defining the meniscus shape where the ions originate. For example, the presence of a jet would entirely modify the electrical field around the emission sites, sites which become much more difficult to adequately define. Even assuming the absence of a jet, the specific curvature of the cone wall and the radius of curvature of the tip are not well known and require new assumptions.

Thus, simulations of the absolute ion trajectories are not presented in this work. Instead, the relative focusing effect of the accelerators is studied, focusing which determines the performance improvement brought by the accelerators and serves as a guide for the design of the accelerator electrodes. To achieve this relative evaluation, an original method to simulate the ion trajectories is presented.

With this method, a single particle is generated with 1000eV from the edge of the extractor with an initial angle off-axis $BHA_{initial}$ (Figure 2.17). The value of 1000eV corresponds approximately to a particle which would have been extracted from a Taylor cone and accelerated by an extraction voltage in the range of 1kV (not considering energy losses). The direction of the particle is then re-evaluated well downfield from the accelerator electrode, when it has reached full acceleration and has a stable trajectory.

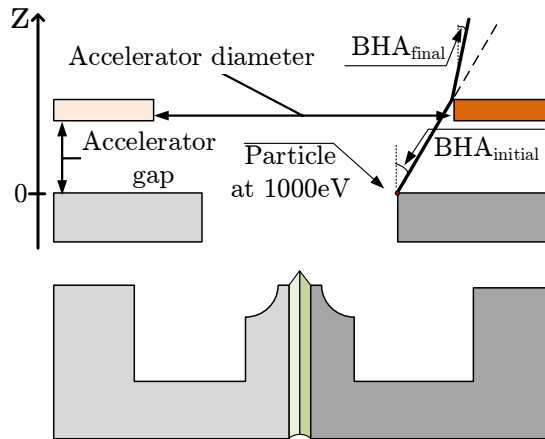


Figure 2.17: Cross section diagram indicating key elements of the simulations. Particles are generated at 1000eV from the edge of the extractor with a starting angle $BHA_{initial} = 30^\circ$. For each geometry, the final angle BHA_{final} in the accelerated cases are compared to the unaccelerated case. Parameters varied are the accelerator diameter and extractor-accelerator gap.

This scheme, although somewhat artificial, is convenient as it permits any starting particle angle to be set in order to match the experimental results. The electrical field was computed in all regions of the stack with the accelerator grounded, the extractor at a variable voltage (V_{acc}) and the emitter at 1000V above the accelerator (V_{ext}). The main advantages of this scheme are its simplicity and the fact that it makes few assumptions concerning the shape of the meniscus and the energy of particles just extracted from their liquid state. It also allows comparison with experimental data since the initial trajectory of the ions can be matched to the measured unaccelerated beam, isolating the effect of the accelerators.

Finally, it is important to mention that this method can be used since the electrical field between the emitter and extractor is effectively unaffected by the acceleration voltage, allowing decoupling of the extraction and acceleration effects. This independence was already identified when the onset voltage simulations were performed, and can be verified by a simple set of simulations. To achieve this, a simple meniscus composed of a sphere capped-cone, similar to the one presented in section 2.3.1 was used as emission site from which 10 particles were generated, as shown in Figure 2.18a. The radius of the spherical section was $1\mu m$ and the particles were emitted with 10eV. As is seen in Figure 2.18b, the particles generated were effectively unaffected by the acceleration voltage until they passed the extractor, where they then began to focus according to the applied acceleration. This simulation confirms that, in terms of beam shaping, the effect of the extractor and accelerator can be entirely decoupled.

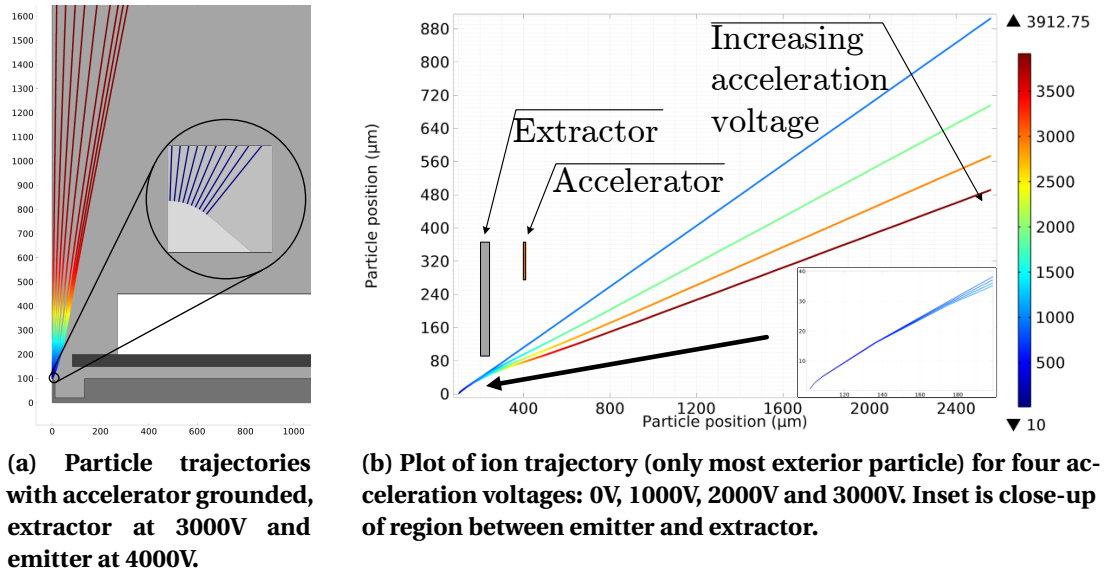


Figure 2.18: Simulations of ion trajectories originating from a sphere ($1\mu m$ radius) capped Taylor cone. 10 particles are emitted normally from the spherical cap with 10eV starting energy. The accelerator is grounded, the extractor at 3000V and the emitter at 4000V. The acceleration electrode only affects the particle trajectory in the region downstream of the extractor electrode. Color bar corresponds to particle energy in eV.

With confidence in the chosen simulation scheme, a simulation procedure was established.

For a given geometry, once the field was computed, a particle was generated at the exit point of the extractor electrode, as shown in Figure 2.17. The particle had an energy of 1000eV and an initial angle $BHA_{initial} = 30^\circ$. This angle was chosen so that the particle would not physically impact the acceleration electrode in any simulated configurations, allowing the comparison of different geometries. The accelerator inner diameter and the extractor/accelerator spacing were varied, respectively from $450\mu m$ to $1050\mu m$ and from $150\mu m$ to $350\mu m$.

Note that the nature of the species (ion or droplet) was irrelevant in this case, as only the particle energy ($q \cdot V_{beam}$) affected the trajectory. The particle direction was probed once it had been fully accelerated, $1000\mu m$ to $2000\mu m$ from the exit of the accelerator (BHA_{final}), and compared with the direction at the exit of the extractor to get the relative focusing.

For these two design parameters, Figure 2.19 shows how the beam half angle is reduced when introducing acceleration. Typically, a 30-35% reduction is achievable with 3000V acceleration voltage ($BHA_{final} \approx 19^\circ$). The accelerator inner diameter has little effect on the final beam half angle, while larger spacing between the extractor and accelerator provides increased focusing. However, the effect is, at least in the range studied, almost negligible.

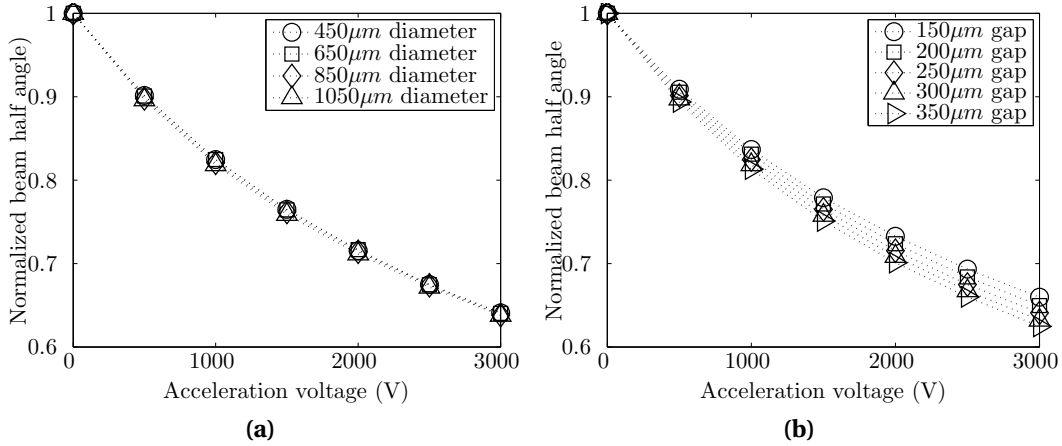


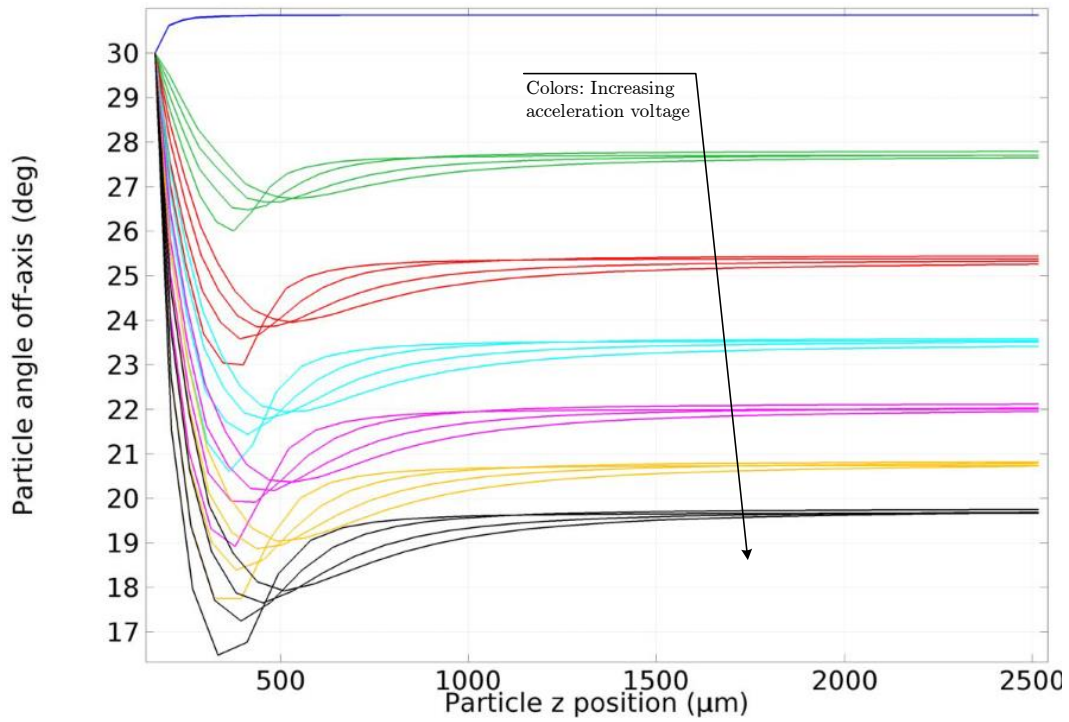
Figure 2.19: (a) Normalized BHA_{final} vs acceleration voltage for four accelerator inner diameters. (Extractor/accelerator spacing is set to $250\mu m$.) (b) Normalized BHA_{final} vs acceleration voltage for three accelerator/extractor spacings. (Accelerator inner diameter is set to $540\mu m$.) 30-35% focusing is obtained, depending on the accelerator dimensions.

Figure 2.20 plots the particle's angle off-axis as it travels in the axial z position, for the parameters studied. In this figure, different colors represent different acceleration voltages, increasing in 500V steps from top to bottom. Different curves of the same color correspond to the different levels of the parameters.

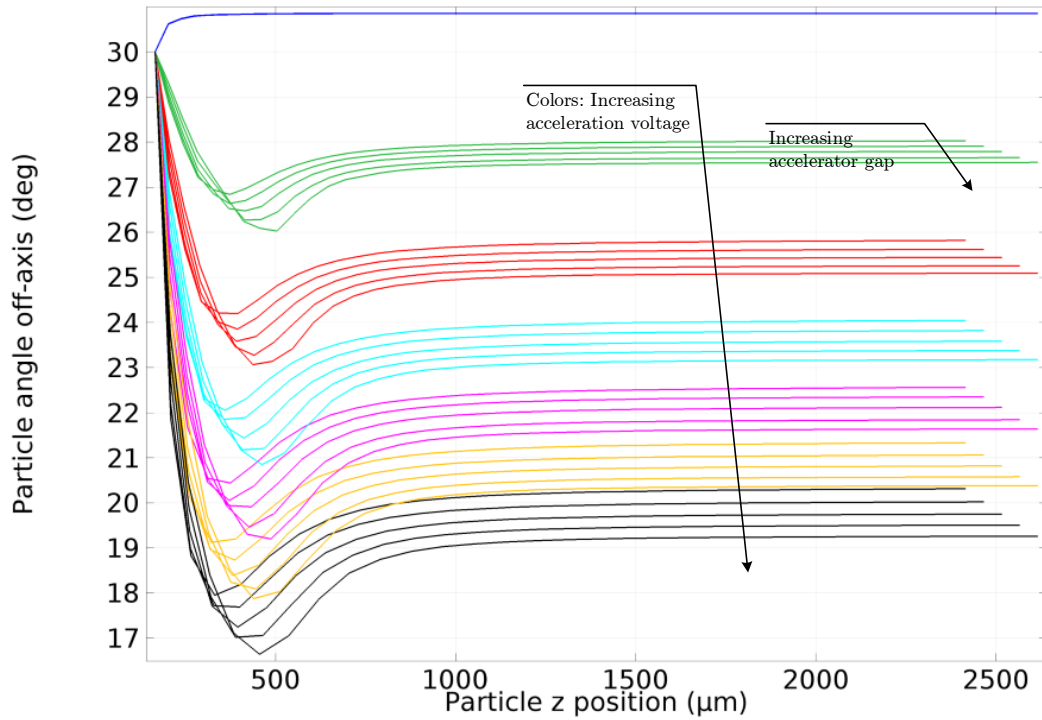
A very interesting feature that is made apparent by these curves is the complex initial trajectory that the particle follows. For the first few hundred microns (in the axial direction), the particle is initially attracted to the center of the electrode, as seen by the initial dip in the curves. The particle is then de-focused, and reaches within a few hundred microns more its stable

trajectory. Figure 2.21, where particles are traced for four acceleration voltages (0V, 1000V, 2000V and 3000V from right to left) highlights this behavior. The early curving is in fact caused by the radial electrical fields amplified by the sharp corners of the electrode, as shown in the inset, and explains the differences seen between the different geometries. Note that this effect is related to the starting position of the particle. If the particle is generated further from the extractor, it will experience less initial deflection, as shown in Figure 2.22.

Generally, however, the feature dominating the focusing is simply the increased kinetic energy of the particles in the axial direction, a result of the higher potential applied. This explains why very little geometric effect is seen in the curves of Figure 2.19. Thus, the simulations are promising both regarding the accelerator's ability to focus the beam and in the robustness of the effect against fabrication defects.



(a) Varying accelerator inner diameter.



(b) Varying accelerator gap.

Figure 2.20: Particle angle off-axis as it travels in the axial z direction. Data is plotted for five acceleration voltages (0V, 500V, 1000V, 2000V, 2500V and 3000V) and varying accelerator inner diameter (top) or gap (bottom). Colour scheme corresponds to applied acceleration voltage.

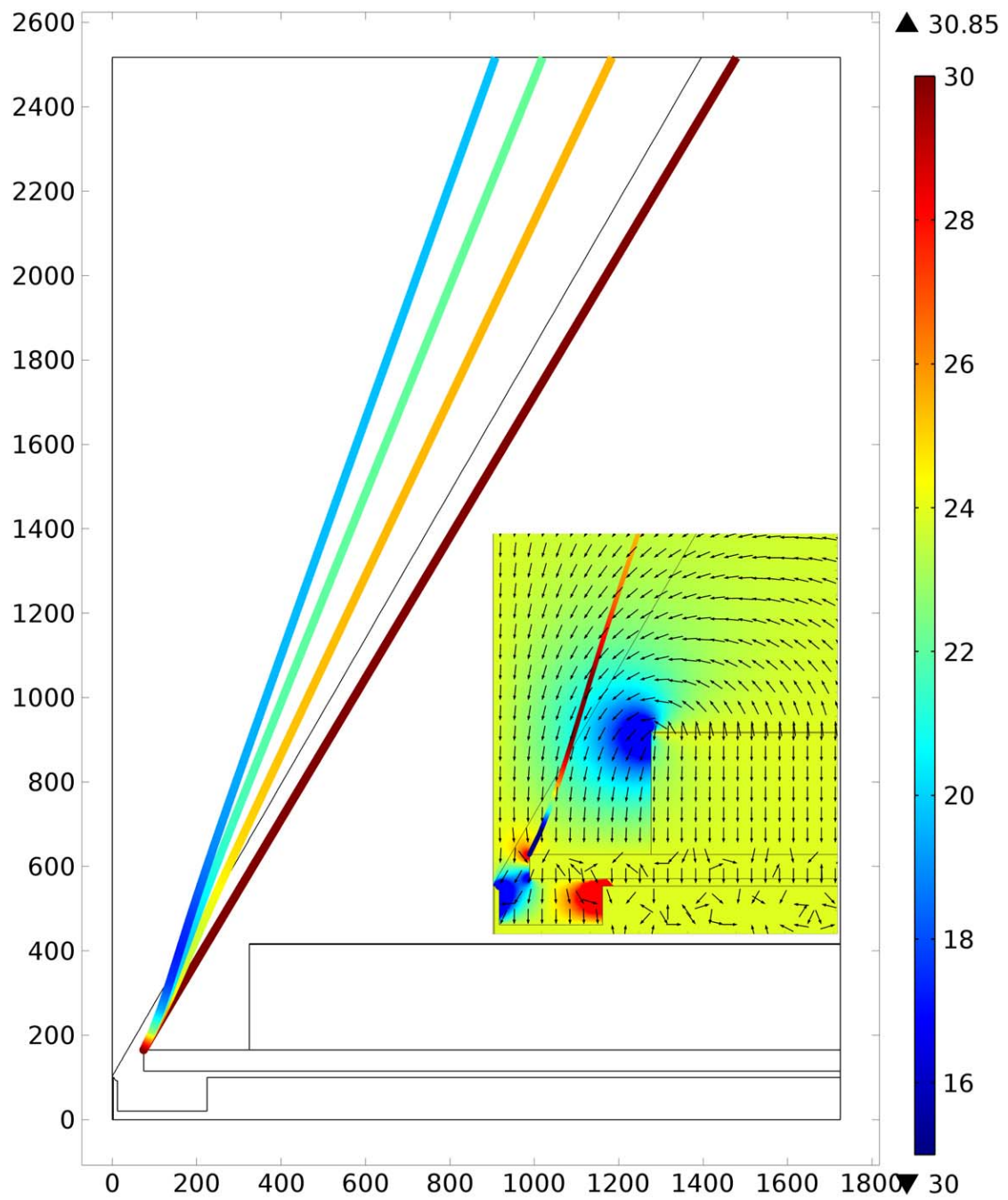
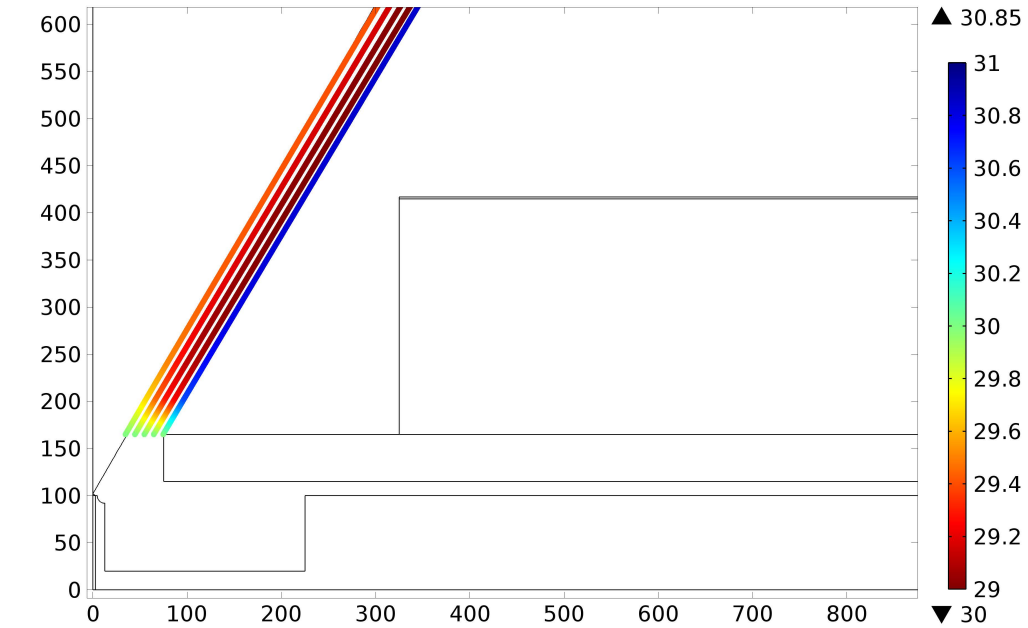
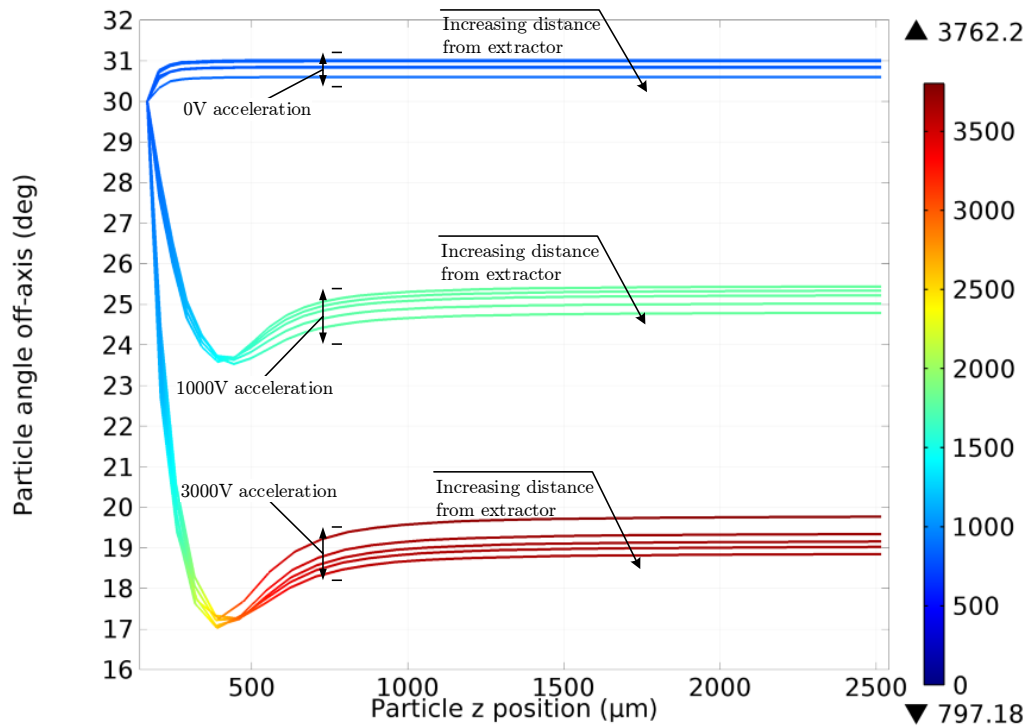


Figure 2.21: Four particles subjected to increasing acceleration voltage, from right to left: 0V, 1000V, 2000V, 3000V. Color bar represents particle angle off-axis. Inset: Surface is radial electric field acting on particle. Particle color is off-axis angle.



(a) Five particles generated at different starting positions, in $10\mu\text{m}$ steps from the extractor, with no acceleration. Color bar represents particle angle off-axis.



(b) Particle beam half-angle for three acceleration voltages (0, 1000, 3000V) and five starting positions. Color scheme corresponds to particle kinetic energy, in eV.

Figure 2.22: Effect of particle starting position on beam focusing simulations

2.3.3 Energy and angular efficiency

The energy efficiency, given by Eq. 2.8 [94], relates the equivalent potential Φ_b that will be reached by an emitted particle going through an electric field provided by electrodes at potential V_{app} .

$$\eta_E = \frac{\Phi_b}{V_{app}} = 1 - \frac{V_{loss} + RI}{V_{app}} \quad (2.8)$$

While the ion trajectory simulations confirmed that particles having exited the emission region would indeed reach kinetic energies corresponding to the applied voltage, losses can occur in the emission process. Indeed, V_{loss} in Eq. 2.8 is related to the electrical energy required to form the cone and extract particles from the liquid while RI is the potential drop due to ohmic losses in the liquid.

For a highly conductive ionic liquid, R is approximated to 0. V_{loss} is not related to the post-acceleration and is constant regardless of the acceleration potential applied, such that the efficiency will increase with the applied voltage. The value of V_{loss} is difficult to predict and can be most easily measured through the use of Retarding Potential Analysis (RPA). Here, the value of 100eV is used, as previously reported for this type of emitters, emitting in mixed droplet/ion mode [62]. In the PIR, energy losses below 15eV have been reported [39, 95], such that 100eV remains a conservative value.

For a spray with current uniformly distributed over a cone of beam half-angle (BHA) θ , the angular efficiency is given by Eq. 2.9[94]. The angular efficiency describes the momentum wasted by the off-axis component of the emitted particles and depends inversely on the acceleration voltage.

$$\eta_\theta = \cos^4\left(\frac{\theta}{2}\right) \quad (2.9)$$

Electrospray sources operating in the PIR have reported BHA in the order of 15° to 20° [38], although sources in mixed ion/droplet mode have exhibited wider plumes of 30° - 40° [96, 97].

From the ion-optics simulations performed, one can expect in the range of 35% focusing. For a plume initially having 30° beam half-angle, this would correspond to an angular efficiency increase from 87% to 95%.

2.4 Electrode erosion and emitter pitch

Completing the design of the thruster, a critical element that must be considered to determine the packing density is the electrode degradation resulting from beam impingement.

Electrode and wall erosion are key lifetime limiting factors in electric propulsion systems [98–100]. The source of such erosion is usually a combination of chemical attack by reactive ions and mechanical sputtering produced by high kinetic energy particles. In most cases, the erosion leads to thruster degradation and failure. This has specifically been observed by Krpoun et al.[32, 62] for this type of devices and identified as a principal long-term failure cause. In fact, it is not surprising that electrode erosion/modification resulting from beam impingement is an issue, considering that it has been proposed to use electrospray sources specifically for etching [95, 101] and deposition [66, 67, 102] applications. Gamero-Castaño et al. [55] further described how high velocity impact of nanodroplets on silicon was sufficiently energetic to cause phase transition.

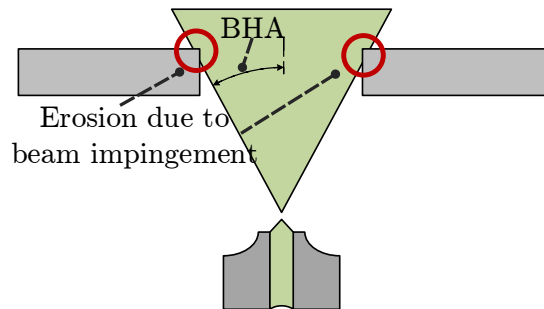
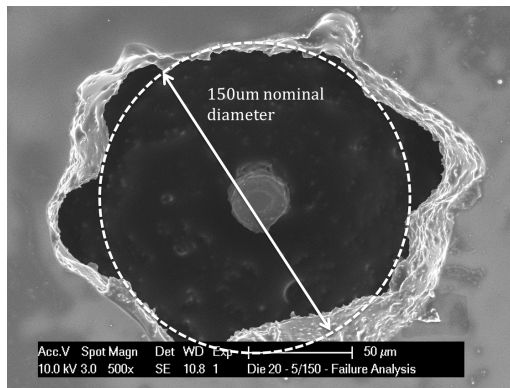


Figure 2.23: Diagram of electrospray emitter with beam impinging on extractor electrode.

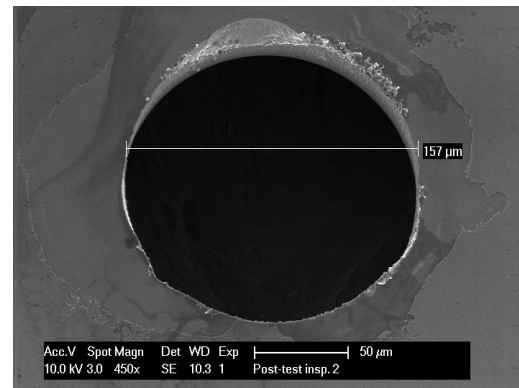
Yet electrospray thrusters possess some features which hint that electrode erosion can be entirely avoided. Unlike both Hall and ion thrusters, there is no high energy plasma which must be generated and used to ionize a sea of particles. As such, there is no reaction chamber where ions are contained before being accelerated to create thrust. Instead, the ions rest passively in liquid form until they are being extracted and accelerated. This means that erosion of chamber walls by particles before extraction is not an issue.

A second important aspect is that, unlike in ion thrusters, there are no neutrals in the emitted beam. Ionic liquids have negligible vapor pressure and so there can be no evaporation of slow neutrals. In addition, there is no forced external flow of particles, meaning that all particles in the beam had to have been extracted electrostatically from the liquid itself. Even if fragmentation occurs after extraction, all the resulting particles, which may be neutral, still keep a high kinetic energy. Therefore, it is expected that the barrel and pits-and-grooves erosion seen in ion thrusters will not be present in electrosprays.

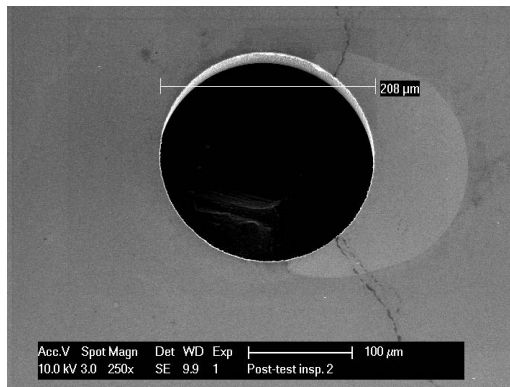
Finally, a valuable feature of this internally fed emitters is that the extraction is done at discrete locations (the tips of the capillaries) precisely controlled in space. The emitted spray takes a finite shape originating from these tips, such that the kind of sputtering experienced by Hall



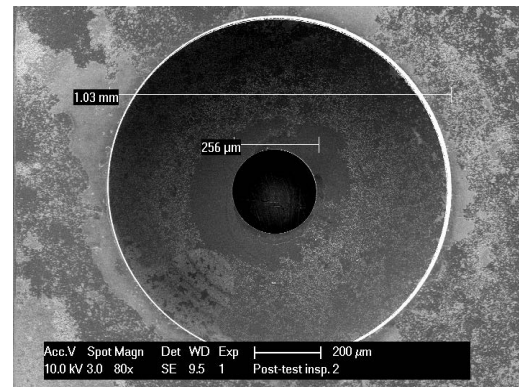
(a) R3W1D20. 150μm extractor. Clearance = 35°.



(b) R3W4D01. 150μm extractor. Clearance = 37°.



(c) R3W4D02. 200μm extractor. Clearance = 45°.



(d) R3W4D03. 250μm extractor. Clearance = 51°.

Figure 2.24: Extractor erosion due to beam impingement after several hours spraying.

thrusters can be avoided.

Indeed, it seems that through careful design of the geometry, i.e. by providing sufficient electrode clearance for the plume, erosion will be non-existent. Thus a good characterization of the spray half-angle is a critical input to this design.

While early devices assumed approximately 30° plume half-angle, extensive experiments performed at LMTS by fellow PhD student S. Chakraborty determined that the plume could in fact spread to as much as 40° – 45° [97, 103]. Observations of devices after test were consistent with these measurements, as shown in Figure 2.24. Extractors which provided less than 40° clearance were consistently degraded while larger extractors were not.

Thus this 40° value should be considered a minimum to avoid electrode erosion, driving the minimum inner diameter of the extractor.

2.5 Final design

2.5.1 MicroThrust chips (v3a)

With the above considerations, a design for the MicroThrust breadboard chips (labelled v3a), including an acceleration electrode, was proposed. The specifics of this design were proposed by Dr. Çağlar Ataman, a collaborator at LMTS. The main objectives for these devices were to reduce the onset voltage and maximize emitter density, while targeting PIR operation. The extractor electrode was designed at $168\mu\text{m}$, enough to allow $\approx 40^\circ$ beam half-angle clearance and the extractor-emitter gap kept at $50\mu\text{m}$. Insulation between the extractor and accelerator electrode levels was provided by $250\mu\text{m}$ of glass and was the driver for the packing density of the emitters.

Thinner glass would have been sufficient in terms of insulation, but handling of $< 250\mu\text{m}$ wafers proved to be difficult. The $250\mu\text{m}$ thickness, expected to insulate upwards of 15 kV, allowed significant flexibility in the system, effectively permitting any acceleration voltage to be applied within the limitations of typical small spacecraft.

Three variants were fabricated (BHA30, BHA40 and BHA50), allowing increasing beam-half angle clearance at the accelerator level. The opening of the glass on the top side, had diameters of $370\mu\text{m}$, $540\mu\text{m}$ or $765\mu\text{m}$. The final baseline thruster included 127 emitters packed with a density of 213 emitters per cm^2 . Variants had 91 (125 emitters/ cm^2) and 167 emitters (257 emitters/ cm^2). All dimensions of the v3a chips are given in Table 2.3.

Figure 2.25 shows 3D models of the BHA40 chip, with 127 emitters. Two pairs of contact pads, accessible from the top of the die are used to access the extractor and electrodes, without requiring wirebonding. Pairs of contact pads are beneficial to distribute equally any force applied by contact pins and also permit the verification of electrical contact by measuring the resistance between both pins.

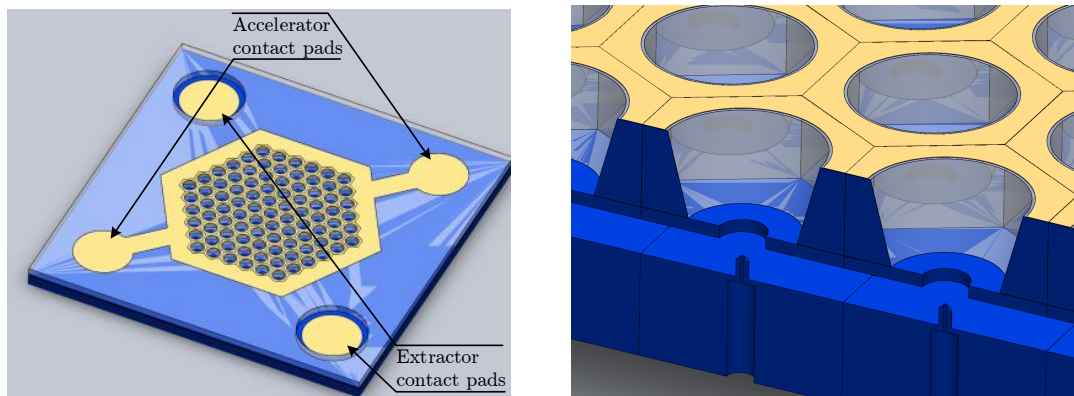


Figure 2.25: 3D drawings of v3a - BHA40 MicroThrust chip.

2.5.2 High density design (v3b)

Also included in Table 2.3 are the dimensions and potential performance of the exploratory v3b chips, designed and fabricated in parallel. This second set of devices was not made to be compatible with individual accelerators, taking instead the risk of using "grouped" accelerators. Using one large accelerator allows for much greater packing density (>1500 emitters/ cm^2), although the focusing effects may well be less advantageous. Nevertheless, given that the simulations indicated that the increased axial potential was the dominating factor, it was believed that these devices could benefit from both high packing density and the advantages of accelerators.

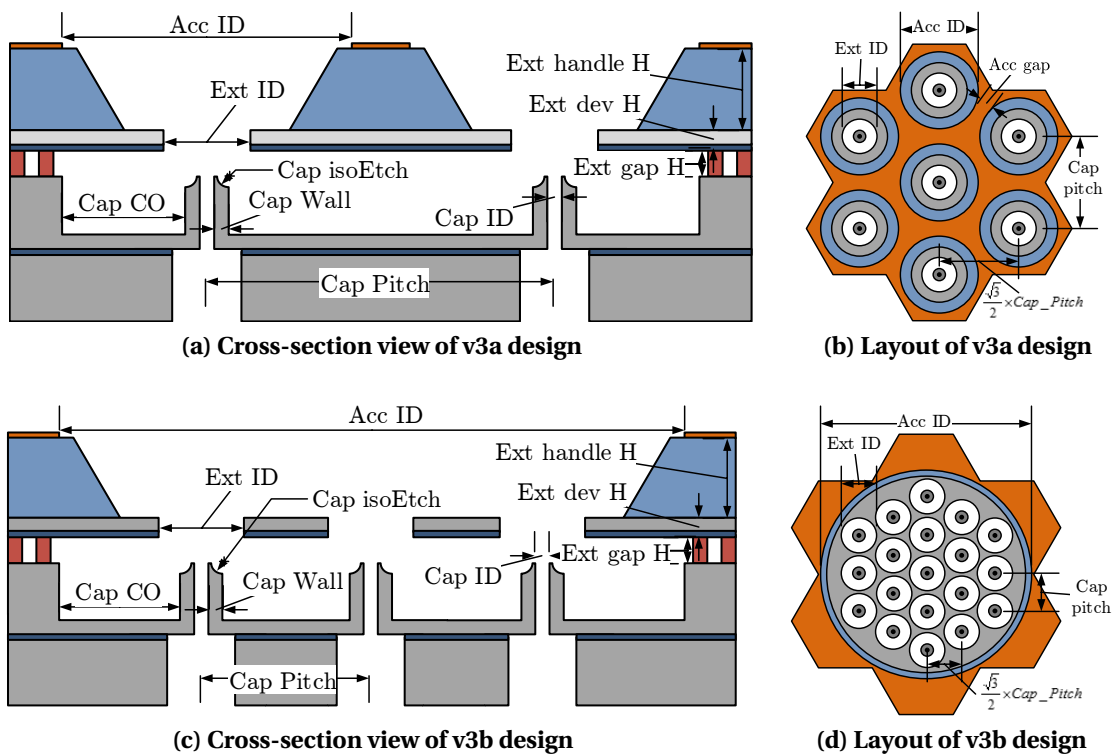


Figure 2.26: Diagrams of thruster stack with key dimensions labelled.

Chapter 2. Electrospray thrusters - Design

Table 2.3: Nominal dimensions of MicroThrust electrospray thrusters (v3a and v3b chips). (All dimensions in micrometers.)

Parameter	Identification	v3a	v3b
Emitter			
Emitter inner diameter	Cap ID	5	5
Emitter wall thickness	Cap wall	20	20
Emitter pitch	Cap pitch	670/737/963	275
Emitter clear-out	Cap CO	N/A	N/A
Number of emitter rings	Cap nRings	5/6/7	0/2/4/6
Reservoir inner diameter	Cap res ID	100	100
Emitter outer height	Cap OH	80	80
Emitter isotropic etch radius	Cap isoEtch	15	15
Emitter handle thickness	Cap handle H	350	350
Emitter BOX thickness	Cap BOX H	2	2
Emitter device thickness	Cap dev H	100	100
Extractor			
Extractor electrode diameter	Ext ID	168	150/200/250/300
Extractor electrode thickness	Ext dev H	50	50
Extractor-emitter gap	Ext gap H	50	50
Extractor opening diameter (top)	Ext handle ID	370/540/765	1000
Insulating oxide thickness	Ext insOxide H	2	2
Accelerator			
Glass thickness	Ext handle H	250	N/A
Accelerator electrode diameter	Acc ID	370/540/765	N/A
Accelerator to accelerator spacing	Acc gap	150	N/A
Accelerator thickness	Acc dev H	0.4	N/A
	Die size	15 000	10 000
Calculated dimensions			
Capillary outer diameter	Cap OD	45	45
Number of emitter	n_{em}	91/127/169	1/19/61/127
Emitter density (emitters/cm ²)	ρ_{em}	257/213/125	1527
Beam half-angle (clearout) - Ext.	θ_h ext	39	36/44/51/56
Beam half-angle (clearout) - Accel.	θ_h acc	28/37/47	N/A

2.5.3 Performance estimates

Combining the effect of increased beam potential and propulsive efficiency, and using the simulations described in this section, it was possible to estimate the expected performance for the different designs. Table 2.4 describes for several types of PIR (positive, negative, bipolar), the performance that could be expected from both designs, with and without acceleration, using the propellant $EMI - BF_4$. For the v3a design, all three variants are included, although the difference in performance is only reflected in the thrust density ρ_T . For the v3b design, the columns correspond to the different extractor inner diameters. Note that the beam potential V_{app} corresponds to the simulated onset voltage for the unaccelerated cases, and to 4000V for the accelerated cases.

The principal and most debatable assumption used to build the table is the beam current (per emitter), which was assumed to be 200nA. While the value of this current does not influence the specific impulse or propulsive efficiency, it is linearly proportional to the power and thrust per emitter and the depending values. Still this value is in the range (100-250nA) typically seen for this type of thrusters, with internally fed capillaries each with a single extraction site [104].

It is also assumed that the beam current is uniformly distributed in a cone of half angle BHA and that, in accordance with the above simulations, this angle is reduced from 30° to 20° in the presence of acceleration. This assumption however has less impact, only affecting the efficiency of the thruster.

The sequence used to compute the values in Table 2.4 is as follows:

$$\dot{m} = I_{em} \sum f_i \left(\frac{q}{m} \right)_i \quad (2.10)$$

$$P_{em} = I_{em} (V_{ext} + V_{acc}) \quad (2.11)$$

$$I_{sp} = \frac{1}{g_0} \sqrt{\frac{2\eta_T P_{em}}{\dot{m}}} \quad (2.12)$$

$$T_{em} = g_0 I_{sp} \dot{m} \quad (2.13)$$

$$\rho_T = \frac{T_{em}}{\rho_{em}} \quad (2.14)$$

$$\rho_P = \frac{T_{em}}{P_{em}} \quad (2.15)$$

The table shows the total power consumption for a 3U CubeSat, with the required $300\mu N$, as well as the associated ΔV , assuming 20% propellant mass fraction.

A first observation of the table reveals that, for all cases considered, acceleration is necessary in order to meet the 3000s requirement with these designs. The ΔV target can be achieved without acceleration, although marginally. The thrust density is principally a function of the emitter density (v3a vs v3b design) although acceleration allows some v3a designs to reach

an acceptable value at 4000V. The total power consumption ($P_{300\mu N}$) remains in all cases in acceptable limits, even for the case of a fully accelerated v3b chip.

The fabrication of such devices, however, is challenging. As highlighted in 2.4, tens of thousands of emitters ($N_{300\mu N}$) are required to generate the complete thruster system. While acceleration helps greatly in this regard, roughly dividing $N_{300\mu N}$ by two, even this reduced number is extremely challenging and requires a high yield fabrication process. Certainly, though, the fabrication, assembly and packaging of such arrays with conventional techniques would be virtually unachievable.

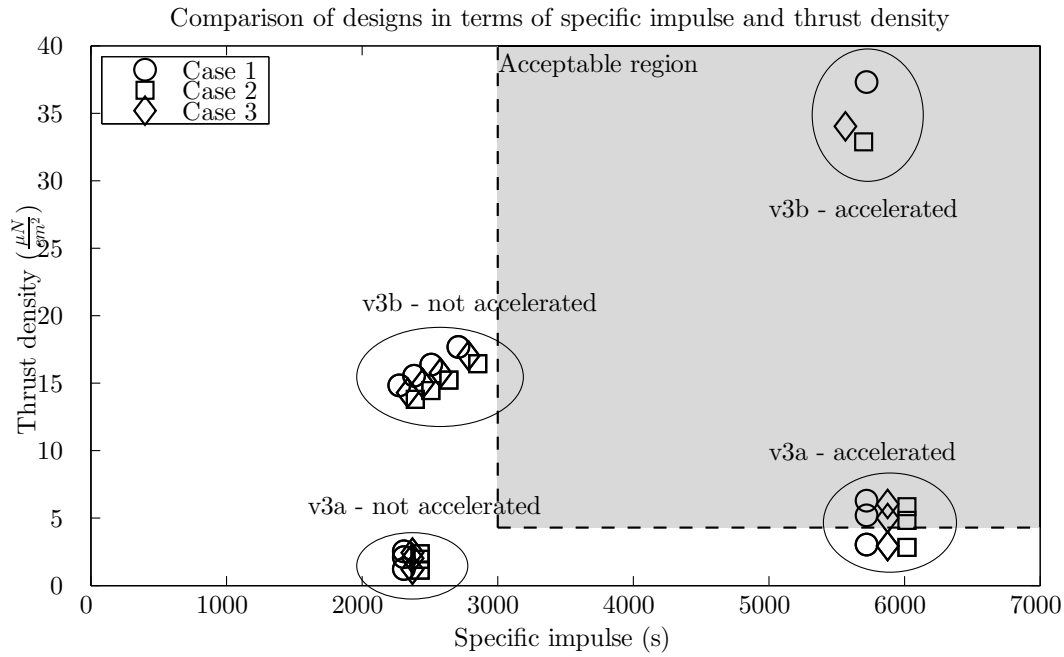


Figure 2.27: Predicted performance of different designs in terms of specific impulse and thrust density.

2.5. Final design

Table 2.4: Predicted performance of designed electrospray emitters for different operation regimes. "Unaccel." columns indicate that no acceleration is used, with the applied voltage obtained from onset voltage simulations. In the cases of "acc." columns, the applied voltage is 4000V. 200nA beam current was assumed in all cases.

ID	Units	Req.	v3a		v3b				
			Unaccel.	Acc.	Unaccel.				Acc.
			BHA30/40/50	BHA30/40/50	E150	E200	E250	E300	(All)
ρ_{emi}	$\frac{emi}{cm^2}$	-	257/213/125	257/213/125	1527				1527
V_{app}	V	-	785	4000	762	827	897	971	4000
P_{emi}	μW	-	157	800	152	165	179	194	800
η_E	-	-	0.87	0.97	0.87	0.88	0.90	0.97	0.97
η_θ	-	-	0.87	0.94	0.87				0.94
Case 1: Positive PIR operation (50/50 monomer/dimer) $\dot{m} = 4.36e - 13, \eta_p = 0.94$									
η_T	-	-	0.71	0.86	0.71	0.72	0.74	0.79	0.86
I_{sp}	s	-	2308	5719	2274	2383	2510	2711	5719
T_{em}	nN	-	9.9	24.4	9.7	10.2	10.7	11.6	24.4
ρ_T	$\frac{\mu N}{cm^2}$	>4.3	2.5/2.1/1.2	6.3/5.2/3.0	14.8	15.6	16.4	17.7	37.3
ρ_P	$\frac{\mu N}{W}$	>20	62.8	30.6	63.8	61.6	59.8	59.7	30.6
$P_{300\mu N}$	W	<15	4.8	9.8	4.7	4.9	5.0	5.0	9.8
$N_{300\mu N}$	-	-	30410	12274	30866	29459	27970	25895	12274
ΔV	km/s	>5	5.1	12.5	5.0	5.2	5.5	5.9	12.5
Case 2: Negative PIR operation (50/50 monomer/dimer) $\dot{m} = 3.85e - 13, \eta_p = 0.92$									
η_T	-	-	0.70	0.84	0.70	0.70	0.72	0.78	0.84
I_{sp}	s	-	2429	6018	2393	2507	2641	2852	6018
T_{em}	nN	-	9.2	22.7	9.0	9.5	10.0	10.8	22.7
ρ_T	$\frac{\mu N}{cm^2}$	>4.3	2.4/2.1/1.1	5.8/4.8/2.8	13.8	14.5	15.2	16.5	34.7
ρ_P	$\frac{\mu N}{W}$	>20	58.4	28.4	59.3	57.3	55.6	55.5	28.4
$P_{300\mu N}$	W	<15	5.1	10.6	5.1	5.2	5.4	5.4	10.6
$N_{300\mu N}$	-	-	32693	15237	32693	32506	32143	30962	13195
ΔV	km/s	>5	5.4	13.2	5.2	5.5	5.8	6.2	13.2
Case 3: Bipolar PIR operation (50/50 monomer/dimer) $\dot{m} = 4.08e - 13, \eta_p = 0.93$									
η_T	-	-	0.70	0.85	0.70	0.71	0.73	0.78	0.85
I_{sp}	s	-	2372	5876	2337	2448	2579	2785	5876
T_{em}	nN	-	9.5	23.5	9.4	9.8	10.3	11.2	23.5
ρ_T	$\frac{\mu N}{cm^2}$	>4.3	2.4/2.0/1.2	6.1/5.0/2.9	14.3	15.0	15.8	17.0	35.9
ρ_P	$\frac{\mu N}{W}$	>20	60.5	29.4	61.4	59.3	57.6	57.5	29.4
$P_{300\mu N}$	W	<15	5.0	10.2	4.9	5.1	5.2	5.2	10.2
$N_{300\mu N}$	-	-	31580	14718	31580	31400	31049	29908	12746
ΔV	km/s	>5	5.2	12.9	5.1	5.4	5.6	6.1	12.9

2.6 Summary

In this chapter, the design of the next generation silicon thruster chips was presented. This design included for the first time integrated accelerator electrodes, which can be used to boost thruster performance while enabling several key system capabilities.

Of particular interest to the design was a study of the capillary emitter fluidic impedance, necessary to compare these new devices with their previous generation.

A complete design study of the geometry was also done, evaluating the influence of the different parameters on the onset voltages of the emitters. The geometry was also simulated with respect to its influence on beam focusing.

Following these studies, two novel designs were presented. The first design, v3a was specifically targeted at the MicroThrust project, meeting the project's performance requirements in terms of specific impulse, thrust and power density. The second design targeted finer emitter features with higher density. The second design had more design variants, notably with respect to the number of emitters and served to develop a simpler, more reliable fabrication process, which will be detailed in the next section.

3 Electrospray thrusters - Fabrication

In this chapter, the advanced microfabrication processes yielding the silicon thruster chips are presented. While initially done entirely at the COMLAB facilities of CSEM in Neuchâtel, the processes were increasingly transferred to the EPFL CMI facilities in Lausanne. This transfer, which required significant development work, was justified by the expected temporary shut-down of COMLAB's cleanroom facilities and the decreasing EPFL presence in these installations.

In this respect, the MicroThrust compatible devices (v3a) were a hybrid, with the emitter wafers fabricated in COMLAB and the electrode wafers in CMI. These emitter wafers were principally fabricated by Dr. Çağlar Ataman with support from the author and the COMLAB technical staff.

All electrode wafers were completed at CMI, as were the v3b chips. Unless specified otherwise, the procedures presented in this chapter correspond to the new, CMI, process which should be used as reference for the future fabrication of thrusters.

This chapter sequentially describes the three processes used in the fabrication of the thrusters: the emitter wafer fabrication (section 3.2), the electrode wafer fabrication (section 3.3) and wafer-level assembly (section 3.4). The main achievements of the processes are described in section 3.6.

Parts of this chapter were published in:

Dandavino, S., Ataman, C., Ryan, C. N., Chakraborty, S., Courtney, D. G., Stark, J. P. W., & Shea, H. R. (2014). Microfabricated electrospray emitter arrays with integrated extractor and accelerator electrodes for the propulsion of small spacecraft. Journal of Micromechanics and Microengineering, 24(7), 075011. doi:10.1088/0960-1317/24/7/075011

3.1 Introduction

The proposed microfabrication process requires the assembly of two wafers, labeled emitter and electrode, bonded at wafer-level. Fabricating the emitters and electrodes separately is useful to ensure optimal conditions for the fabrication of each, increasing the yield of the devices. The electrode wafer can be replaced by a simpler, *extractor*, wafer, as shown in Figure 3.1. The extractor process was described previously [32, 103, 105] and will not be presented here.

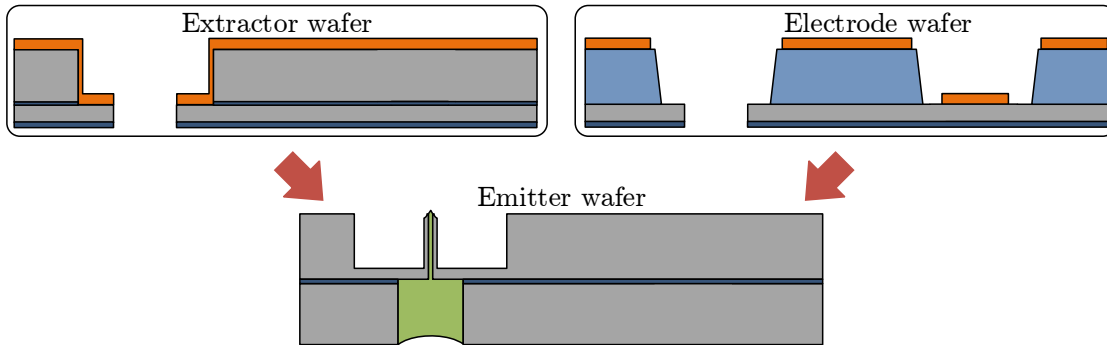


Figure 3.1: Diagram showing how either an extractor or a 2-level electrode wafer can be bonded to an emitter wafer

3.2 Capillary emitter wafer

The emitter process presented here is an evolution of that proposed by Krpoun [32, 62, 84] which in turn involved elements from Griss et al. [82]. The principal fabrication steps of the emitter wafer are shown in Figure 3.2.

One of the main focus of this work has been to optimize the emitter interior etch sequence to yield the smallest and most uniform capillaries to date. With this focus, the capillary interior etch was moved to the beginning of the process, which meant cleaner wafers and more uniform etches. A typical etch sequence, such as the one followed for this procedure, is displayed in Figure 3.3. In the sequence, a silicon dioxide hard mask, first patterned using photopatternable resist, is used to pattern the silicon. The same procedure was also used to defined the backside reservoir as well as the emitter exteriors, with the exception that in the latter case the photoresist was removed only after the silicon etch.

The $1.5\mu\text{m}$ thick silicon dioxide hard mask used in all three etches is grown thermally at the beginning of the process on the starting SOI wafer ($100/2/350\mu\text{m}$). Due to the higher selectivity of the CMI etch processes, this layer could be thinner than the $2.2\mu\text{m}$ thick oxide used at COMLAB, allowing for shorter process times and higher resolution. Typically, $6\ 100 \pm 200\ \text{\AA}$ of oxide remained after 60 minutes of silicon DRIE.

The oxide layer is patterned using a $1.1\ \mu\text{m}$ thick AZ ECI 3027 positive photoresist. This resist

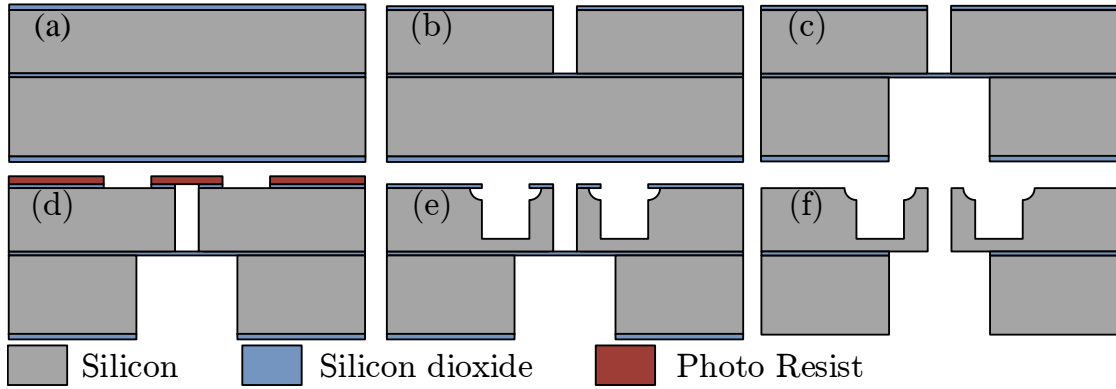


Figure 3.2: Fabrication steps for the emitter wafers. (a) The SOI wafers have $100\ \mu\text{m}$ thick device layer, $2\ \mu\text{m}$ thick buried oxide layer, and $500\ \mu\text{m}$ thick handle layer. With DRIE, first the capillary emitter interiors (b) and the backside reservoir is patterned (c). Thick resist is spun on the frontside and patterned to define the emitter exteriors (d), which are etched in two steps (e) before the buried oxide is removed by vapor HF (f).

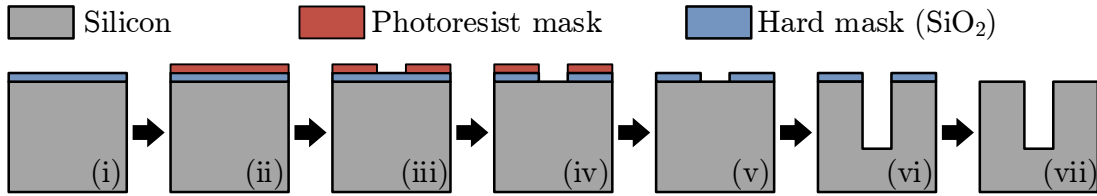
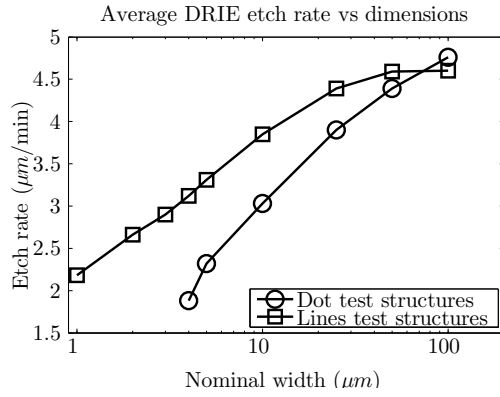


Figure 3.3: Typical etch sequence when using DRIE. (i) Growth of thermal silicon oxide as hard mask. Spinning (ii), then patterning (iii) of photoresist. (iv) patterning of hard mask followed by removal (v) of photoresist. (vi) Deep Reactive Ion Etch (DRIE) of silicon, followed by removal of hard mask (vi), at the end of the entire process.

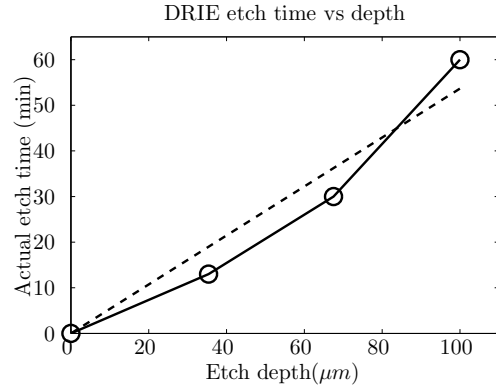
must be spun without the Edge Bead Removal (EBR) option, which rinses the resist on the edge of the wafer. Doing so would expose the silicon to attack at the wafer edge. With the silicon attacked around its entire edge, the wafer becomes much more fragile and prone to breakage.

Performing this etch first in the process is advantageous from the point of wafer cleanliness. The absence of patterns and defects on the backside increases the quality of wafer clamping, ensuring good cooling of the wafer and better etch repeatability. As described in the previous chapter, the inner dimensions of the emitters, defined by this etch, are critical to the operation regime of the thrusters.

Note that if marks at this level will serve to align subsequent masks, care should be taken to protect them during the silicon DRIE, or else they will be almost entirely destroyed. Kapton tape can be applied after the oxide etch and before the silicon etch to preserve the marks. The tape is then removed with the wafer submerged in acetone. It was found that manually removing excess glue using a small brush soaked with acetone before cleaning in Piranha and plasma O_2 gave best results.



(a) Average etch rate for dots and lines test structures.



(b) Non linearity of etch rate vs depth. Fitted average (dashed line) serves as visual guide.

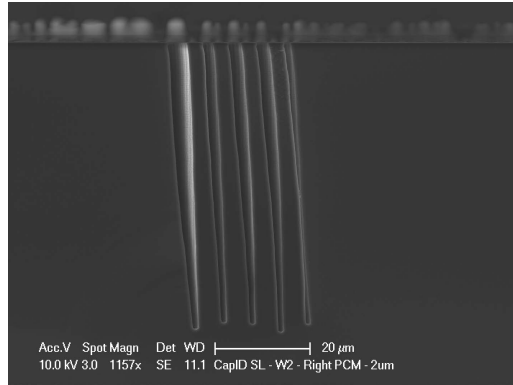
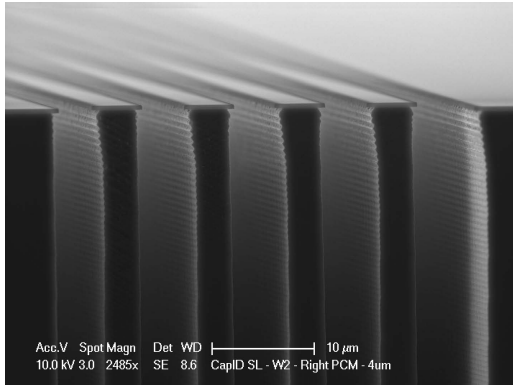
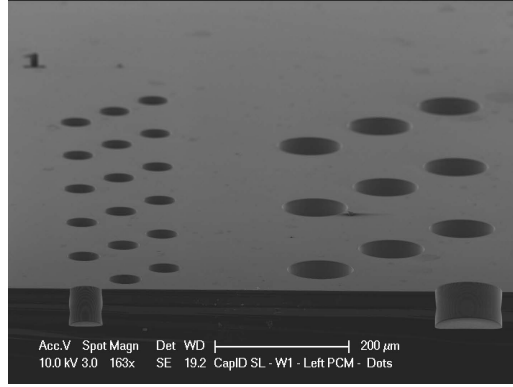
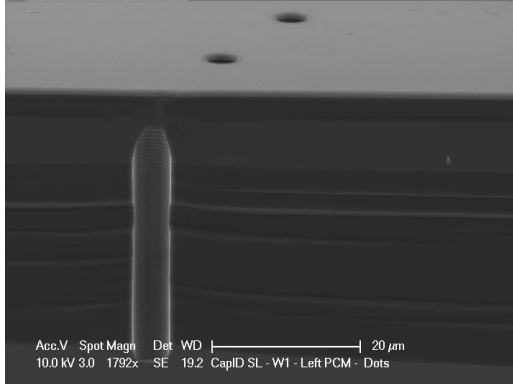


Figure 3.4: "Dots" and "lines" test structures used to characterize the capillary interior etch.

Good characterization of the etch rates was necessary before performing the etch due to the high dependence of the etch rate on the structure width and depth, as shown in Figure 3.4a and Figure 3.4b. For the tool and recipe used in this work (*Tool: AMS200, Recipe: SOI_accurate_-*), 55-60 minutes are sufficient to etch a $100\mu\text{m}$ deep emitter. Images of test structures which were used to characterize this etch are also shown in Figure 3.4.

Emitters fabricated in COMLAB (v3a) have inner diameters measured at $7.9 \pm 0.5\mu\text{m}$ (1σ),

while the CMI emitters (v3b) have inner diameters as low as $6.4 \pm 0.5 \mu\text{m}$ (1σ), in both cases for $100 \mu\text{m}$ deep capillaries. Three wafers were also fabricated using starting material with a $50 \mu\text{m}$ silicon device, resulting in shorter etches and smaller inner diameters. For one wafer, inner diameters as low as $4.5 \pm 0.11 \mu\text{m}$ were achieved, although dimensions of $5.7 \pm 0.14 \mu\text{m}$ were more typical.

Table 3.1 lists the measured final dimensions for 2 wafers of the v3a design and 6 v3b wafers. This table also lists, for the v3b wafers, the dimensions at two earlier stages of the etching procedure, after develop (step (iii) in Figure 3.3) and hard mask definition (step (v) in Figure 3.3). The abrupt widening in the lateral dimensions during the final etch (Figure 3.6 corresponds to lateral attack of the silicon during DRIE. This widening is generally very stable and, as expected, more pronounced for longer etches. To compensate for this effect, a next version of the mask set could include offsets, with the emitter interior drawn at $3.5\text{-}4.5 \mu\text{m}$, depending on the silicon device layer. The walls of the emitter interior are almost perfectly vertical, with less than 1° off-axis, as shown in Figure 3.5. With the recipe used, the emitter slightly narrows with depth, reducing by approximately $2 \mu\text{m}$ in diameter over $100 \mu\text{m}$ depth.

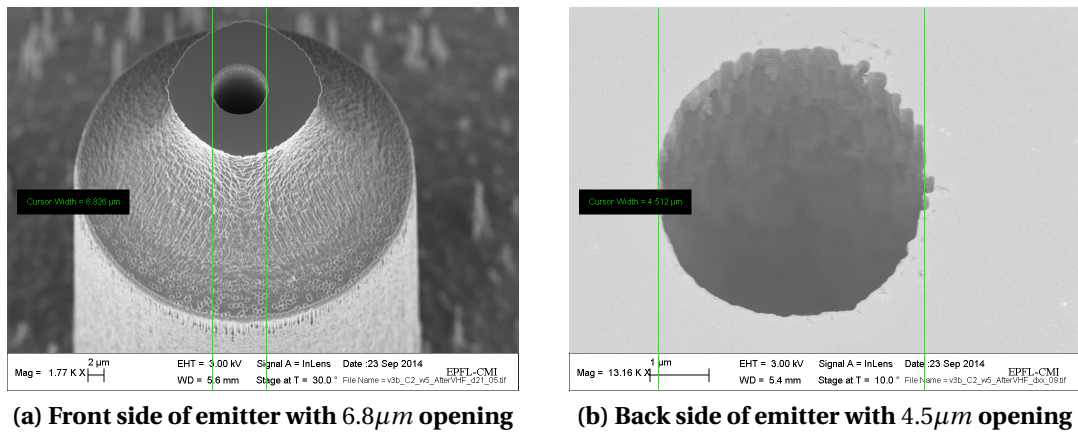


Figure 3.5: Front and back of emitter orifice for v3b wafer C2W5, showing $> 89^\circ$ verticality.

It is also interesting to consider specifically the wafer L1W6 (Figure 3.6b), which exhibited the smallest inner diameters. One major difference with this wafer is that it was part of a different run and fabricated almost a year earlier from all the others wafers. Thus the etching tool (AMS200) may have been in a different state which could have resulted in less lateral attack. In addition, at the time a different tool (AMS200 instead of SPTS) was used to complete the oxide hard mask etch. Better verticality of the oxide walls with this earlier tool could have contributed to smaller lateral attack. Thus further investigation of this tool to complete the hard mask etch at this step could be beneficial, although the mask biasing is a preferred option.

In any case, complete evaluation of the current emitters should be performed before continuing with further optimization of this step. Indeed, the $5.0 \mu\text{m}$ value was a somewhat arbitrary target and the current emitters, already in the targeted range, may have sufficiently high

Chapter 3. Electrospray thrusters - Fabrication

Table 3.1: Nominal and measured dimensions of fabricated emitters (v3a and v3b chips). (All dimensions in micrometers. \pm value corresponds to standard deviation σ , number in parenthesis corresponds to sample size.

Run	Wafer	Device layer thickness	Emitter inner diameter (μm)		
			Develop (iii)	Hard mask (v)	Final (vii)
COMLAB - v3a					
1	W1	50	N/A	N/A	7.94 ± 0.27 (2)
1	W5	50	N/A	N/A	7.87 ± 0.62 (4)
CMI - v3b					
1	W6	50	4.91 ± 0.05 (3)	4.49 ± 0.15 (3)	4.50 ± 0.11 (6)
2	W1	50	4.77 ± 0.01 (3)	4.75 ± 0.07 (3)	5.65 ± 0.13 (2)
2	W3	50	4.72 ± 0.04 (3)	4.83 ± 0.02 (3)	5.70 ± 0.15 (10)
2	W4	100	4.75 ± 0.07 (3)	4.71 ± 0.07 (3)	6.37 ± 0.49 (16)
2	W5	100	4.76 ± 0.03 (3)	4.68 ± 0.10 (3)	6.90 ± 0.19 (12)

impedance for ionic operation.

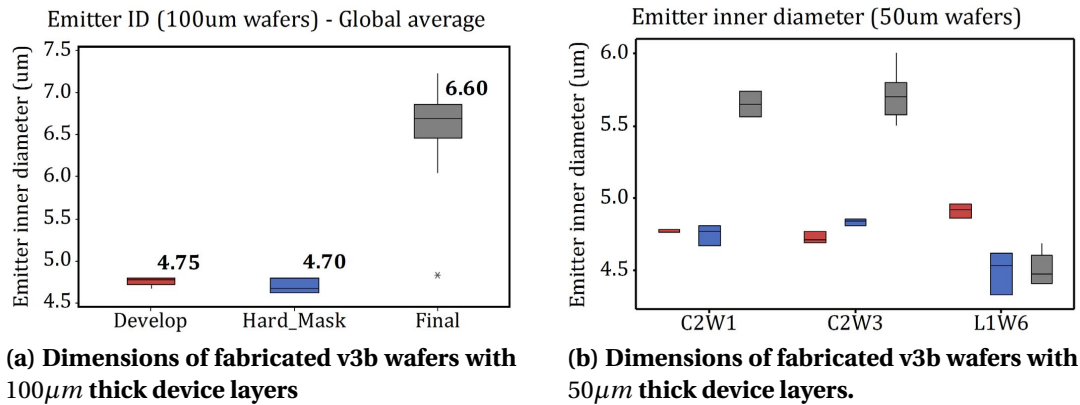


Figure 3.6: Box plots of emitter inner diameters at several steps in the etch procedure.

Next, the liquid reservoir is patterned by DRIE on the backside of the wafer, stopping on the buried oxide (Figure 3.2 c). The dimensions of the structures are relatively large, with 100 μm diameter, and it is possible to monitor the etch and continue it until the buried oxide is reached. 42-45 minutes are required to etch a 380 μm deep reservoir (*Tool: A601E, Recipe: Si_ambient2*). Once again, it is critical to avoid EBR when preparing the resist for this etch.

Third, the exterior of the emitters is patterned (Figure 3.2c). At COMLAB, the resist used for this step is a 4.8 μm thick 10:1 AZ9260:PGMEA mixture spun at 3500 RPM. This resist exhibited sufficient viscosity to cover the emitter orifices cleanly and provide a uniform surface suitable for photoexposition. However, in many cases resist residues remained inside the emitters, even after several attempts at plasma O_2 cleaning. Thus the CMI process introduced a laminated thin film (MX5015, from Dupont©) as photomask. The film is applied semi-manually on the

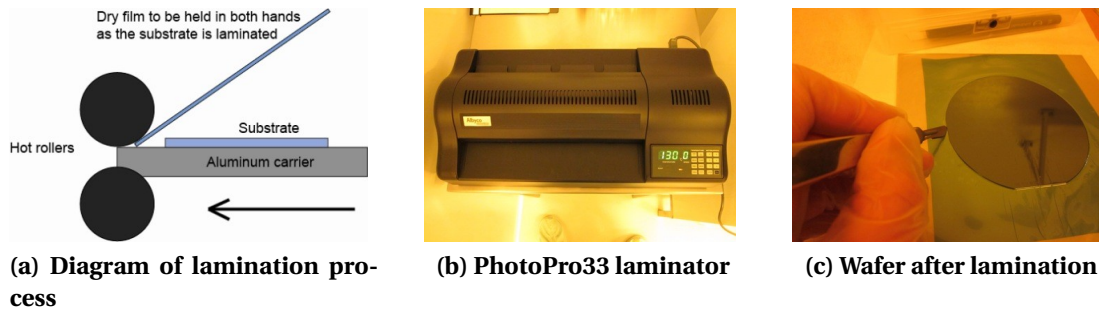


Figure 3.7: Lamination of photopatternable thin film at CMI. All images from CMI (<http://cmi.epfl.ch/>)

substrate using a PhotoPro 33 laminator (Figure 3.7b). The wafer is placed on a 1mm thick steel plate, which is fed in between two rollers held at 100°C (Figure 3.7a). After lamination, the excess film is cut from the edge of the wafer (Figure 3.7c).

To improve adhesion, it is recommended to bake the wafer at 100° for 45s after lamination and exposition. However, this step **must absolutely be avoided**, since air trapped in the capillary emitter interior cavities will expand and create bubbles at the front of the wafer, preventing proper patterning of the emitter exteriors.

The exposition of the film is straightforward, but the development of the film is challenging. Due to the small size of the final islands ($45\mu\text{m}$ diameter), they have a high tendency to delaminate. Best results were obtained using a standard Ordyl developer available at CMI, diluted with DI water at 1:25. It is crucial to dry the wafers as soon as possible after the development is finished, since development continues even in water. Typically, the wafers are dried using a manual spinner at 3000 RPM after 15s rinsing.

The oxide hard mask is then patterned before a final, two-step dry etch is performed. The first step sharpens the emitter tip, reducing the onset voltage and restricting the ionic liquid from overflow. This first etch should not include the polymerization step necessary for DRIE and be almost entirely isotropic. Still, it was found that a small chuck bias was necessary in order to get acceptable uniformity across the wafer. This etch is however transport limited, such that local loading has a large influence on etch rate. Hence, it is virtually impossible to have perfectly etched tips both for single emitters and arrays of emitters within a wafer. With the tool and recipe used (*Tool: AMS200, Recipe: Si_iso_bias*), about 1.5-2 minutes were necessary to properly etch single emitters, although this would systematically over-etch arrays. Figure 3.8, shows metrology results for one wafer (C2W5) which was etched for 1m35s. In this case, the single emitters were etched laterally by approximately $11.5\mu\text{m}$ (from each side) whereas the lateral attack on the 127 emitter arrays was closer to $9.5\mu\text{m}$. Achieving precisely sharp emitters is also tricky since it is difficult to evaluate the emitters from top view: an emitter can appear perfectly etched from top, but actually be punctured below the tip, as shown in Figure 3.9a.

Figure 3.10 shows images of test structures at various steps in the procedure, with the hard mask oxide still present or removed.

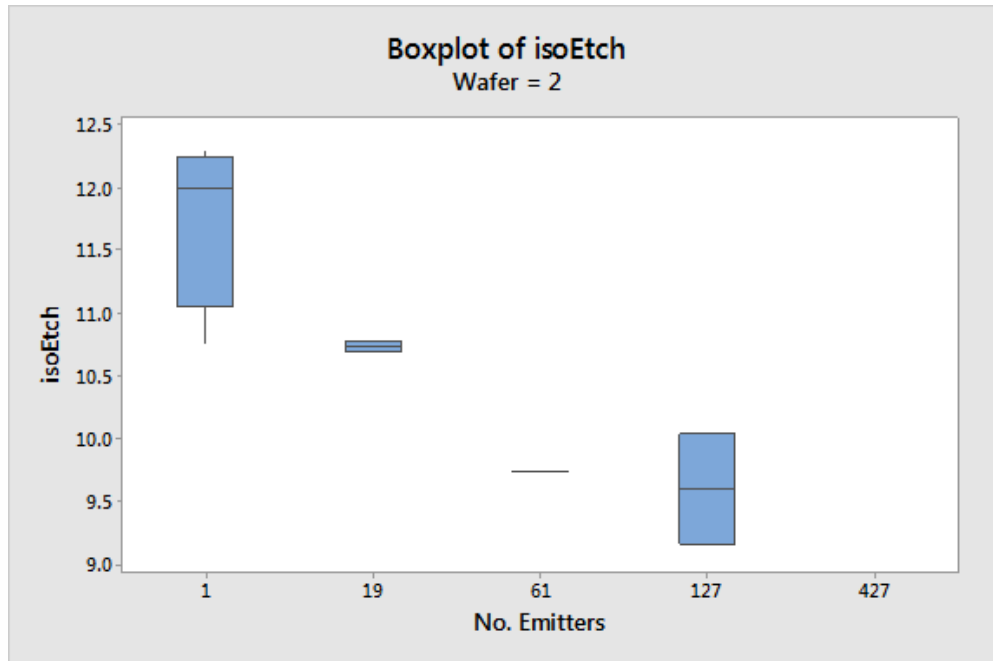


Figure 3.8: Box plot showing lateral isotropic etch for different chip designs within a wafer. Being transport limited, the structures with larger etched areas (large arrays) are etched more slowly than the single emitter chips.

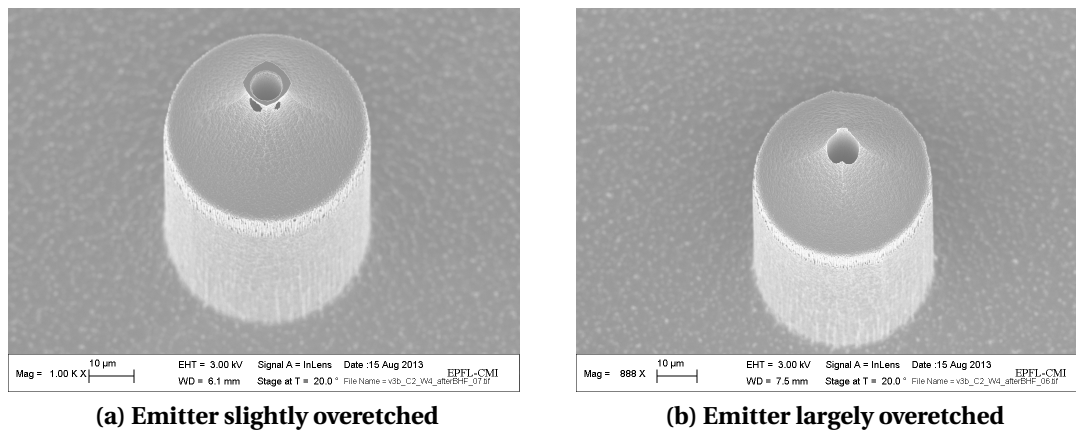
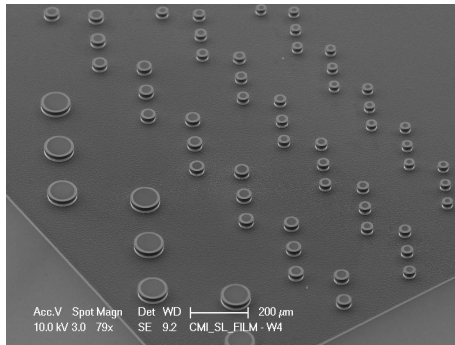


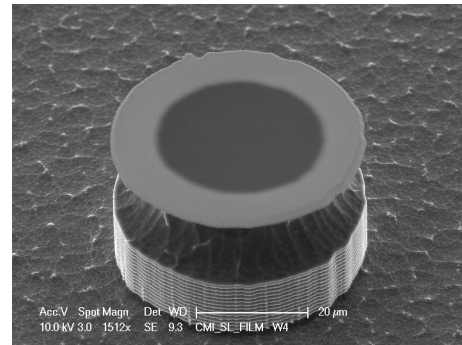
Figure 3.9: SEM micrographs of overetched emitters

The second step is a standard DRIE and provides clearance from the emitter tip to the silicon bulk (Figure 3.2 d-e). Figure 3.10 shows images of test structures after this procedure.

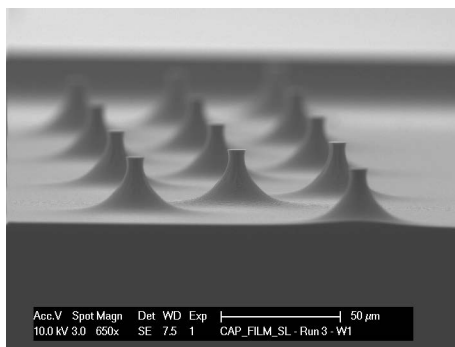
A final vapor HF etch is done to remove the BOX, connecting the backside reservoir to the capillary emitter. SEM micrographs of completed single emitters (top side) are seen in Figure 3.11.



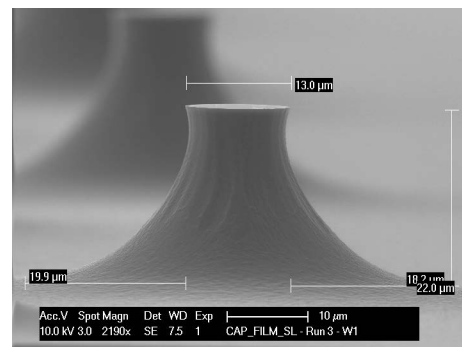
(a) SiO_2 hard mask is still present



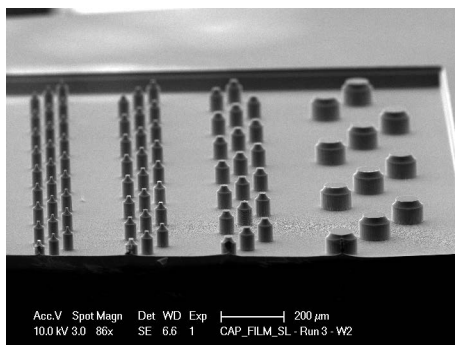
(b) SiO_2 hard mask is still present



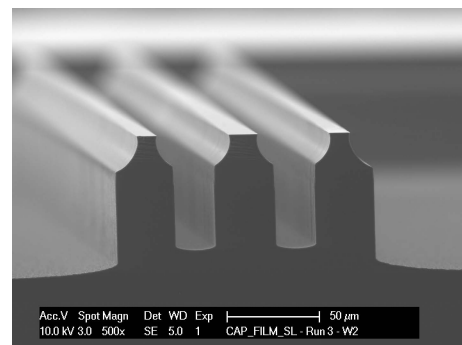
(c) Anisotropic etch was skipped



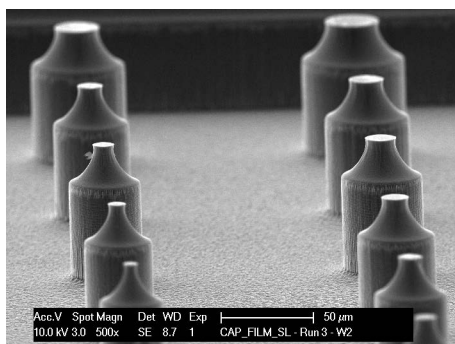
(d) Anisotropic etch was skipped



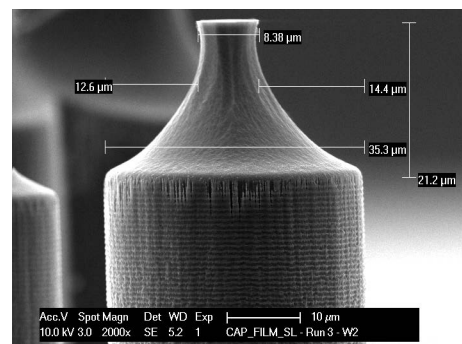
(e) Standard process



(f) Standard process

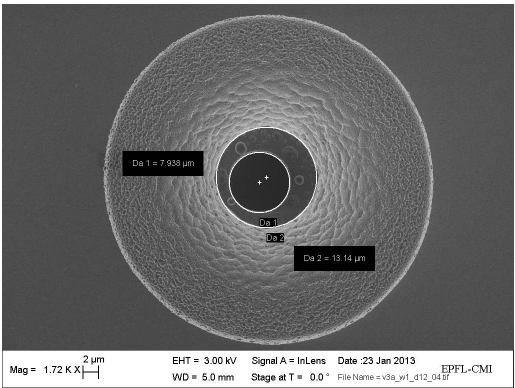


(g) Standard process

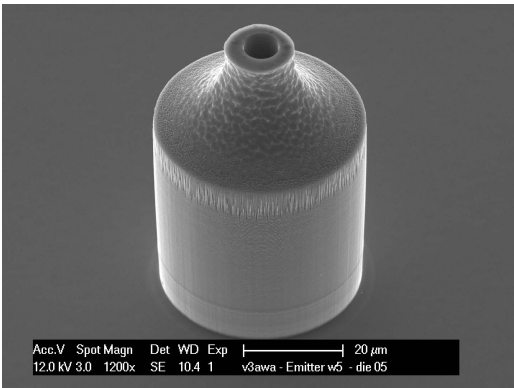


(h) Standard process

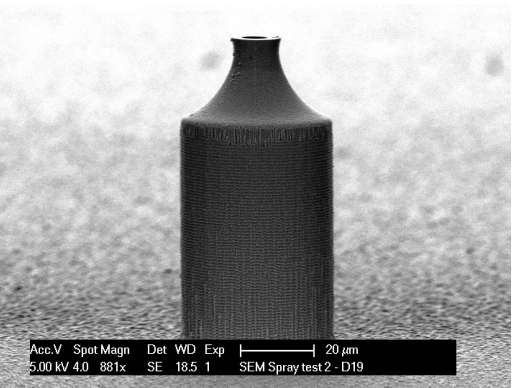
Figure 3.10: Test structures following emitter exterior definition



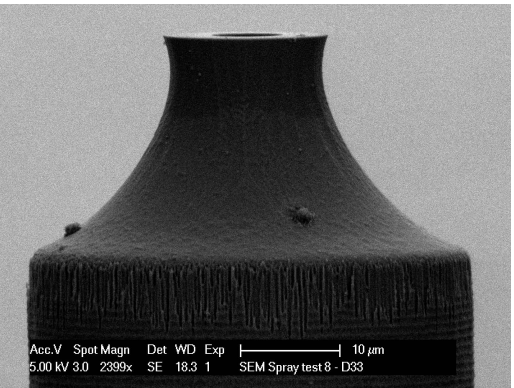
(a) v3a emitter fabricated at COMLAB



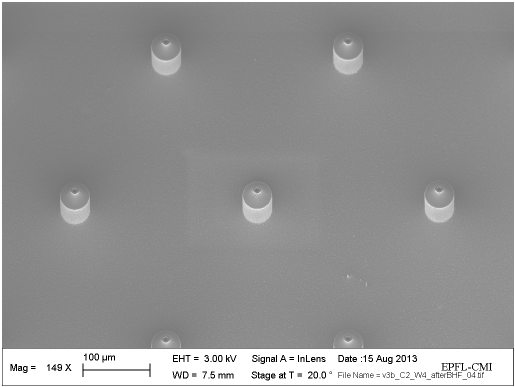
(b) v3a emitter fabricated at COMLAB



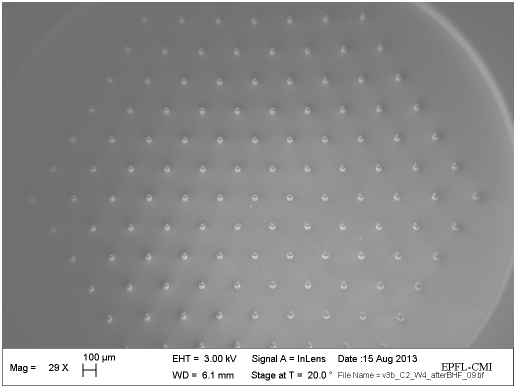
(c) v3b emitter fabricated at CMI



(d) v3b emitter fabricated at CMI



(e) v3b emitter array fabricated at CMI



(f) v3b emitter array fabricated at CMI

Figure 3.11: SEM micrographs of single capillary emitters, highlighting the sharpened tip of the emitter.

3.3 Extraction and acceleration electrode wafer

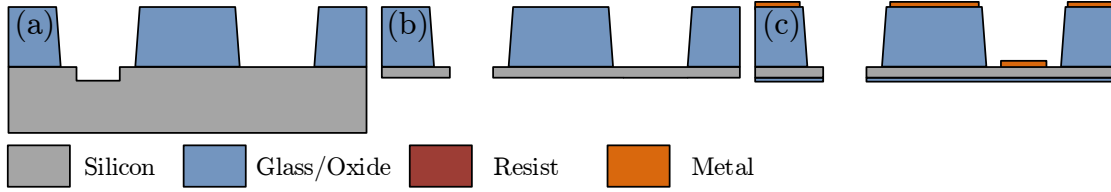


Figure 3.12: Fabrication process of the electrode wafer. (a) The patterned glass, $250\mu\text{m}$ thick, is patterned by micro sandblasting before anodic bonding to a patterned silicon wafer. The wafer is ground and polished (b) before oxide and metal are deposited on the bottom and top, respectively (c).

The novel electrode process provides each emitter with an individual extractor and, for the first time, accelerator electrode.

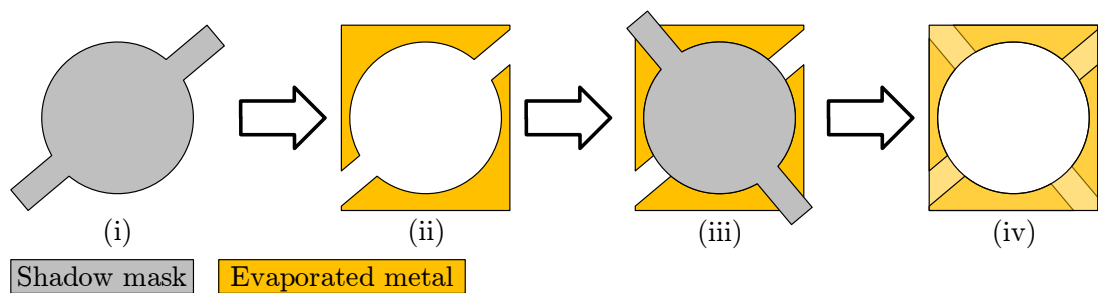
The process begins with the anodic bonding of a $300\mu\text{m}$ thick silicon wafer to a $250\mu\text{m}$ thick Borofloat 33 wafer patterned by micro sandblasting (Figure 3.12(a)). With its low thermal expansion coefficient ($3.25 \cdot 10^{-6} \text{K}^{-1}$), Borofloat 33 is a viable alternative to Pyrex for anodic bonding.

Due to the nature of the anodic bonding process, sodium ions migrate to the front of the glass wafer and aggregate into visible defects. While these are not believed to be largely problematic, they represent at least an aesthetic defect. They can be avoided by using a third glass wafer on top of the electrode stack. Surprisingly, this works well even with the alignment procedure, i.e. the middle sandwiched glass wafer was not seen to shift during handling, which would cause misalignment.

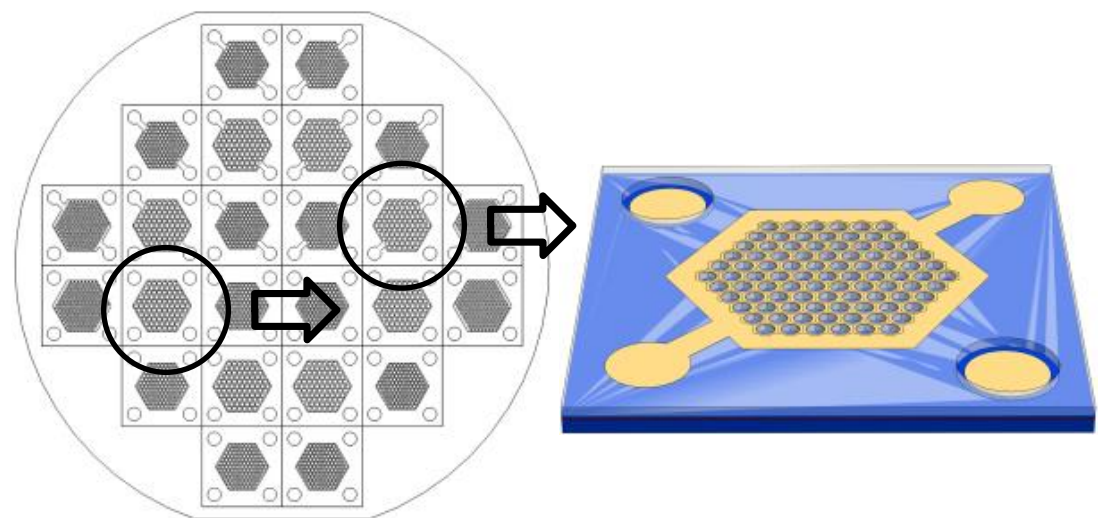
The silicon wafer is patterned prior to bonding through a single DRIE, while the glass is patterned by a novel micro-sandblasting method[106] offered by EPFL spinoff company Icoflex¹. Although limited aspect ratios can be achieved with this technique (of the order of 1:1) and despite being less precise than photo-patternable glasses, it offers reasonable side-wall angles ($15\text{-}20^\circ$) and is well suited for this application, being a fast and inexpensive wafer-level technique. A similar process was also used by Lenard et al. from Sandia National Laboratories to fabricate FEEP thrusters [107].

After bonding, the silicon is ground and polished to a thickness of $50\mu\text{m}$ to reveal the extractor pattern and create through-wafer openings. $2\mu\text{m}$ silicon dioxide is then sputtered on the bottom of the wafer to provide electrical insulation between the extractor and emitter levels, and metal is evaporated on the front side through a shadow mask to create the accelerator electrodes (c). Due to the insular nature of the patterns to be masked, two depositions (200nm thickness) are required to generate the adequate electrode pattern, each rotated by 180° (Figure 3.13). SEM and optical images of bonded electrodes, before metal deposition, are shown in Figure 3.14.

¹www.icoflex.com

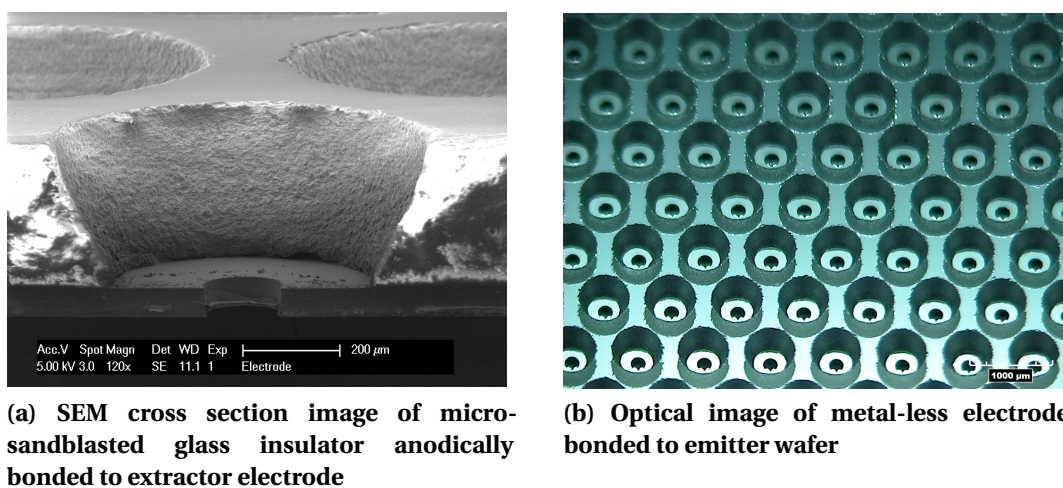


(a) Simplified process sequence for patterning of accelerator electrodes. Metal evaporation is done twice with a metal mask, with 180° rotation of the mask between each run.



(b) Wafer layout of shadow mask, showing both sections which will contribute to the deposition for a particular BHA50 chip.

Figure 3.13: Flow and pattern used to deposit accelerator electrodes in a two-step process.



(a) SEM cross section image of micro-sandblasted glass insulator anodically bonded to extractor electrode

(b) Optical image of metal-less electrode bonded to emitter wafer

Figure 3.14: Images of extractor electrodes bonded to glass carrier. Accelerator metal is not present.

3.4 Wafer-level integration

In a final microfabrication step, the emitter and electrodes are wafer-level bonded using a dry photo-patternable laminated film (MX5050). This is the same resist as had been used for the capillary exterior patterning, but $50\mu\text{m}$ thick instead of $15\mu\text{m}$. Earlier devices did use the $15\mu\text{m}$ film, but this provided insufficient electrical insulation. Although the bulk film's breakdown strength was measured at 2.3kV, experiments showed that leakage occurred at the edge of the die where conductive silicon dust generated at dicing contaminated the film.

The resist is laminated on the silicon side of the electrode wafer and patterned by standard negative lithography and development. Alignment of the two wafers is done in a Suss Microtech MA6/BA6 in bond alignment configuration and the stack bonded by thermo-compression at 150°C and 0.3 MPa in a Suss Substrate Bonder SB6.

The alignment procedure to position wafers for bonding generally uses a jig with three clamps that are closed to hold the wafers together once they are aligned. It was found that these are generally closed too violently for the thin glass wafers, often leading to cracked or chipped wafers. It is recommended to close the clamps manually and gently instead of relying on the automated function.

Final alignment is typically better than $10\mu\text{m}$. Figure 3.15 show optical images of finished die while Figure 3.16 and Figure 3.17 are SEM micrographs of the assembled thruster stacks.

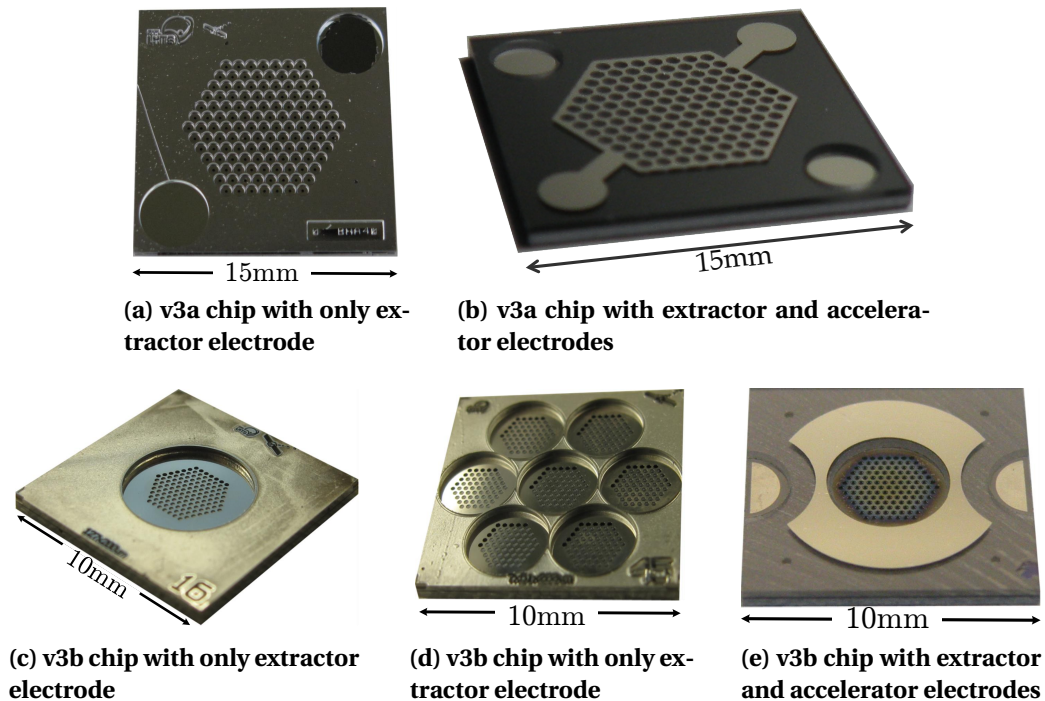
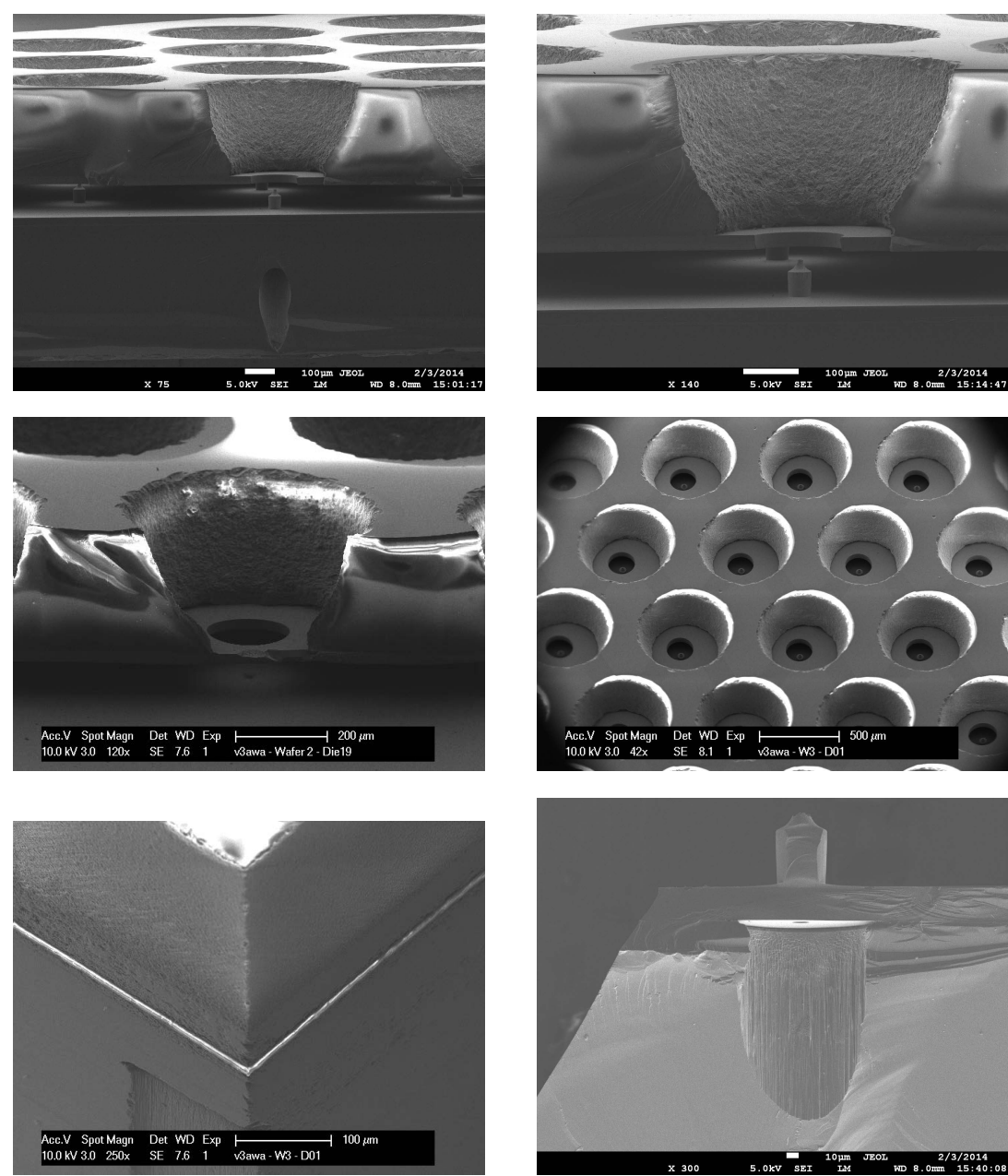


Figure 3.15: Optical images of diced v3a and v3b thruster chips.



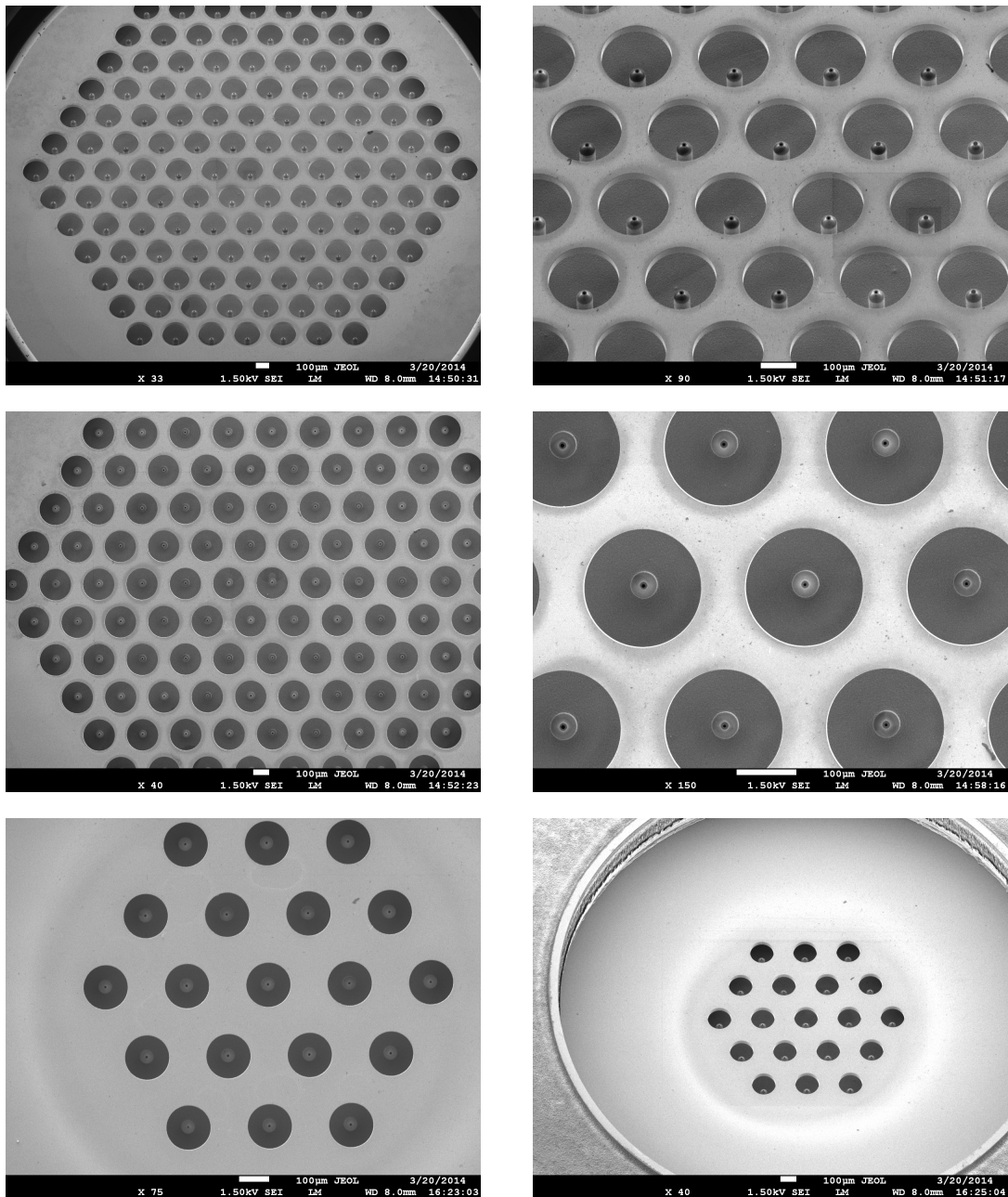


Figure 3.17: SEM micrographs of v3b thruster chips showing arrays of emitters aligned to individual extractor electrodes.

3.5 Principal issues

3.5.1 Blocked emitters

While advantageous from a structural point of view, performing their inner etch first renders the capillary emitters susceptible to blocking. This in fact turned out to be the main sources of die defects with the latest generations of devices. Typically, between 0 and 100% of emitters could be blocked in a given die, although the yield varied considerably according to the wafer fabrication. Several sources of blocking were identified and are in this section. Figure 3.18 and Figure 3.19 show images of blocked emitters from v3a and v3b devices.

While earlier devices, in particular those of the v3a design fabricated in COMLAB, suffered heavily from emitter blockage, with up to 100% of the emitters blocked. Later devices which implemented the recommendations described in this section exhibited less than 1% emitter blockage.

Standard spun resist is used to pattern the emitter exterior

v3a devices, fabricated in COMLAB, used the standard viscous resist spun on the surface of the wafer to allow the patterning of the emitter exterior. In many cases, resist could apparently not be removed, even after extensive plasma O_2 cleaning attempts. Figure 3.18 shows images of some blocked emitters, coming from two wafers of this design. To avoid this problem, laminated film should be used at this step.

Laminated film use in bonding

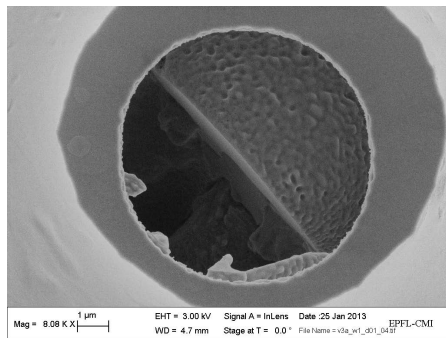
If the bonding film is applied to the emitter wafer, it will penetrate to a shallow depth inside the emitter and can lead to blockage. This lamination is similar to the one that should be used to pattern the emitter exterior with one big difference: in the case of the exterior patterning, a stripping step is done to remove all residues. The stripping is much more aggressive than the development, and so the procedure that requires lamination, development and strip does not leave residues, while the one that requires only lamination and development does. To avoid this problem, the bonding film should be applied on the electrode wafer.

Residues from insufficient rinsing

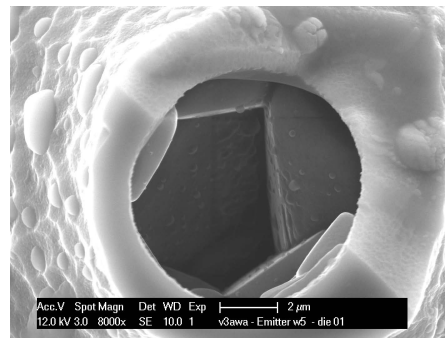
In some cases, some residues are seen well inside the emitters which are not due to laminated film. Figure 3.19g and Figure 3.19h show images of the backside of v3b capillary emitter, at the base of the liquid reservoir. Some polymeric residues are seen which appear to be sucked in to the capillary. These residues may be avoided through good rinsing and drying of the emitters. The small capillary emitters, however, make both these steps difficult. Indeed, even when submerged in water, liquid transport inside the small capillaries is difficult. Drying is

also more effective when using nitrogen guns than with standard spin dryers.

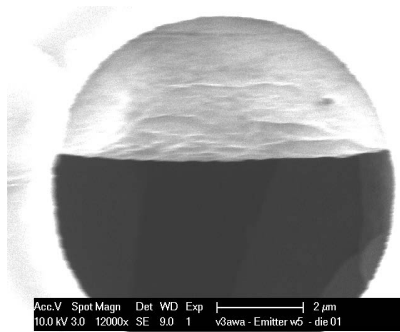
At least the buffer HF step use to remove the oxide hard mask at the end of the process has been identified to yield such defects. For this type of residues, high power plasma O_2 cleaning has been seen to be a very effective cleaning method.



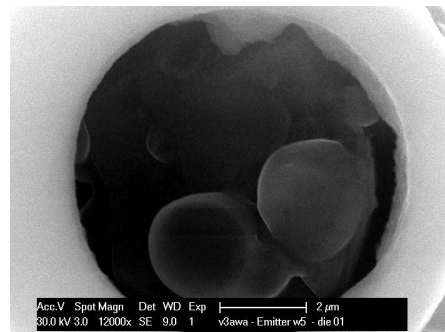
(a) W1D01: Frontside



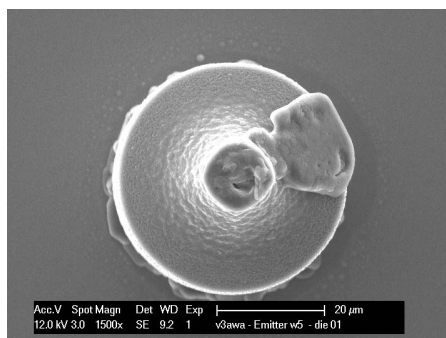
(b) W5D02: Frontside



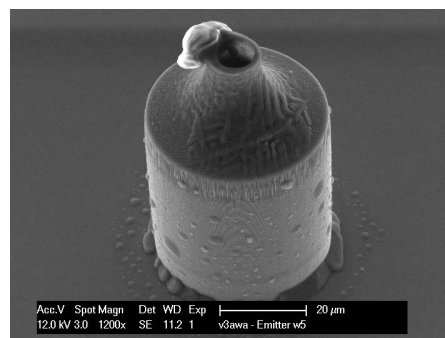
(c) W5D01: Frontside



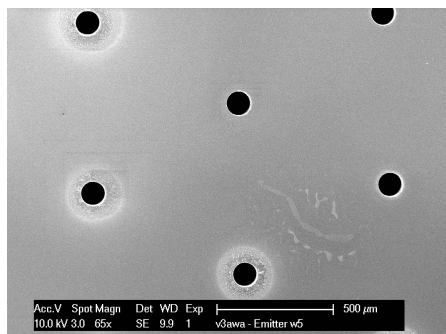
(d) W5D01: Frontside



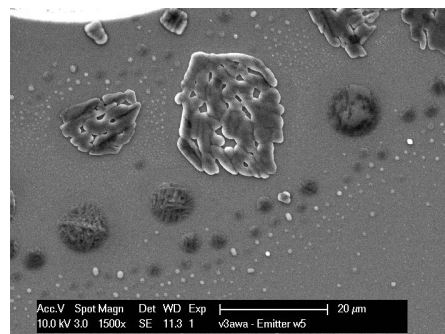
(e) W5D01: Frontside



(f) W5D01: Frontside

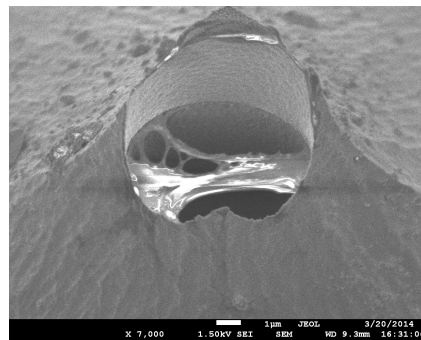


(g) W5D01: Backside

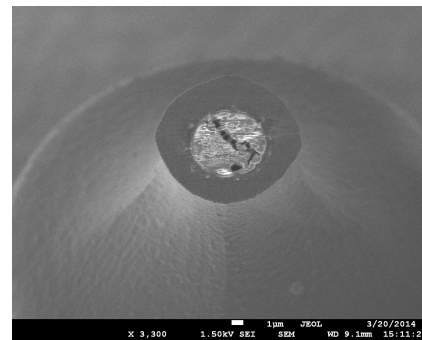


(h) W5D01: Backside

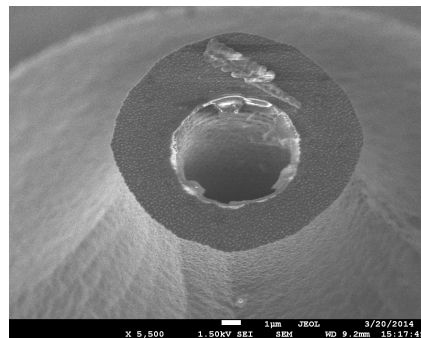
Figure 3.18: SEM micrographs of blocked v3a thruster chips.



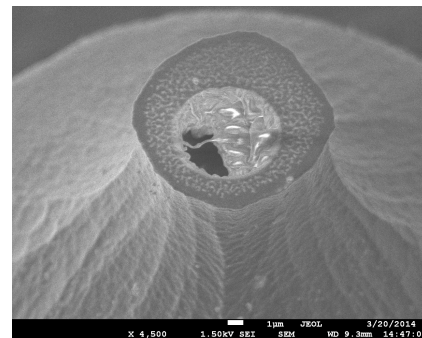
(a) W4D15 Emitter 14: Frontside



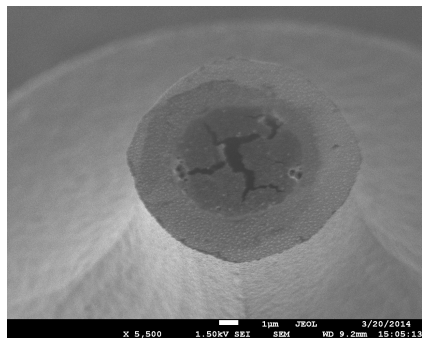
(b) W4D15 Emitter 21: Frontside



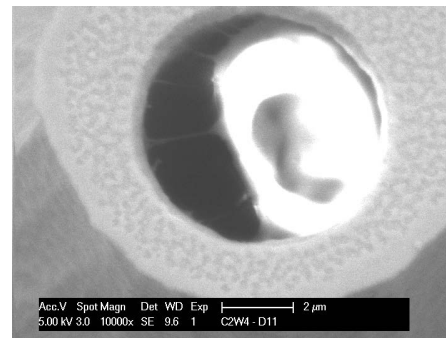
(c) W4D15 Emitter 25: Frontside



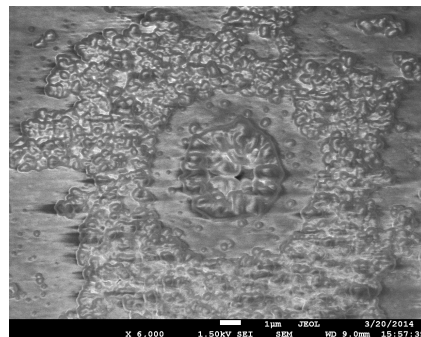
(d) W4D11 Emitter 12: Frontside



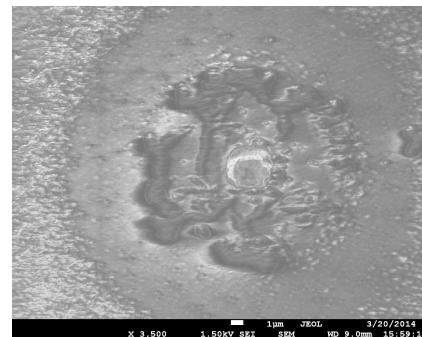
(e) W4D13 Emitter 88: Frontside



(f) W4D11 Emitter 19: Frontside



(g) W4D11 Emitter 17: Backside



(h) W4D11 Emitter 02: Backside

Figure 3.19: SEM micrographs of blocked v3b thruster chips.

Emitter cleaning

Attempts at cleaning using isopropanol, acetone, Piranha and plasma O_2 have systematically failed. However, it was possible to recover some blocked die using Focused Ion Beam, as shown in Figure 3.20. While the cleaning step itself requires only a few minutes, the procedure, including sample handling, positioning and focusing, is long and expensive. Thus this method could be applied to single emitters of crucial importance, but was not used to clean arrays.

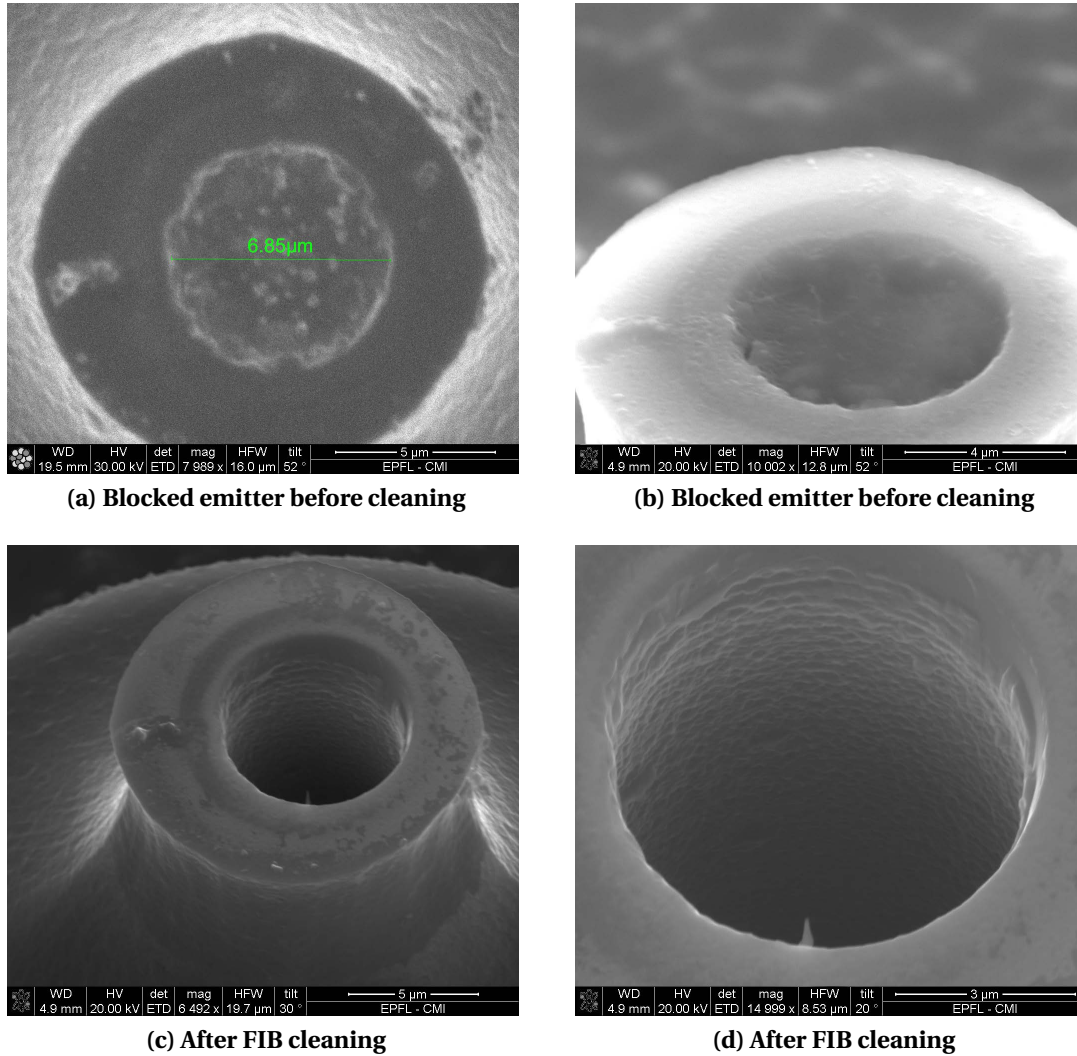


Figure 3.20: SEM micrographs of v3b thruster chips before and after cleaning at FIB.

3.5.2 Emitter-extractor leakage current

Earlier devices, bonded with $15\mu m$ thick film (MX5015) suffered from high leakage currents and often experienced electrical breakdowns. This problem was unexpected since the breakdown voltage of this film, in perfect conditions, was measured to be approximately 2.3kV. To

investigate the problem, several chips were prepared, with bonding at wafer or die level, using both 15 μm and 50 μm films. The devices were subjected to aggressive leakage/breakdown tests by the QMUL partners, with results shown in Figure 3.21. Figure 3.21a shows how the die-level bonded chips behaved somewhat erratically: the thick film did not appear significantly better than the thin one. In fact ohmic leakage seemed to occur with the thick film, possibly a result of contamination during assembly. Using wafer-level bonding, the results were more consistent: thin film almost systematically led to electrical breakdown below 1200V while the thick film provided good insulation, in all but one case.

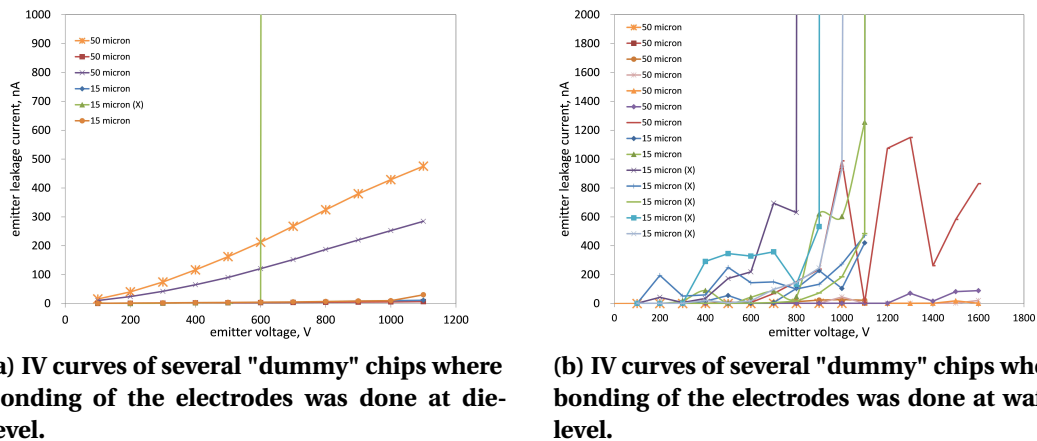


Figure 3.21: IV curves showing leakage currents and electrical breakdown with several "dummy" chips bonded at die or wafer level. The "dummy" chips are plain silicon chips with no patterning, but bonded and diced in normal conditions. Credit QMUL.

Thus it was concluded that while wafer-level bonding was more consistent, the dicing process of bonded stacks could degrade the insulation. It appears that conductive silicon dust generated at dicing could become attached to the edges of the film and create non-ohmic, but potentially catastrophic leakage paths. The issue of dust contamination resulting from dicing is commonly known [108], and so dicing above conductive metal structures is generally avoided. In this case, using the thicker film is beneficial, but comes at the cost of lower achievable emitter density. Indeed, a thicker electrode stack translates into wider accelerator openings to clear a given plume, increasing pitch.

A better solution is to provide a "guard-ring" around the edge of the sensitive area, which should be put at the same potential as the emitter wafer (Figure 3.22a). This design is made possible by the nature of the electrode process, which allows completely isolated silicon electrodes suspended by the glass carrier. Modified v3a devices were successfully fabricated (Figure 3.22b) by re-working already completed electrodes. This was done using laminated film, applied on the bottom of the wafer to pattern the insulating oxide and silicon extractor. Normally, this patterning should be done from the start along with the extractor electrodes. Unfortunately, the heavy reworking in this case seemed to damage the insulating oxide, and these test chips did not appear to be more resistant to leakage.

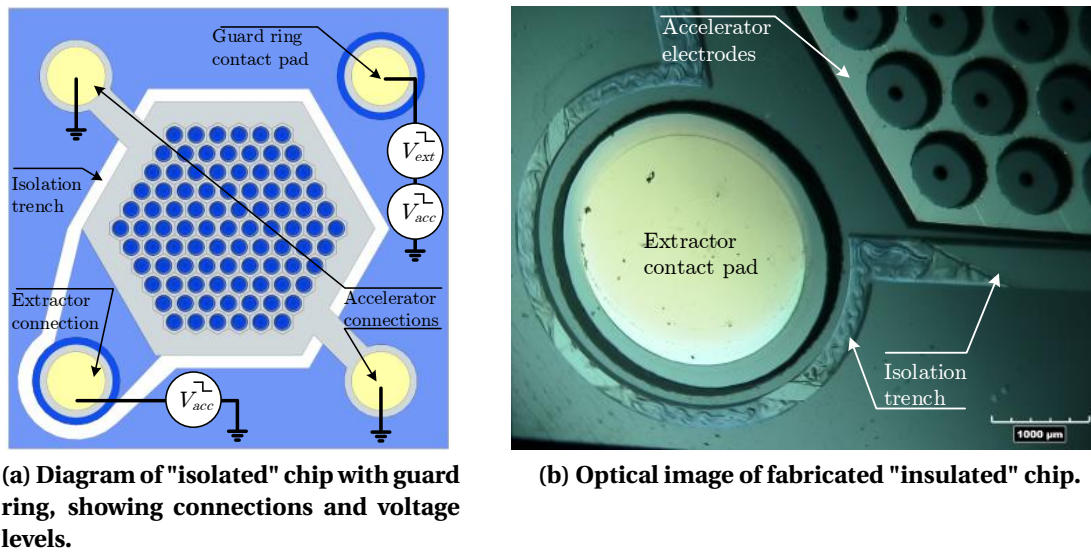


Figure 3.22: 3D drawing and optical image of modified MicroThrust chip with extractor electrodes isolated from die edge.

3.6 Main achievements

Rather than single recipe development, the difficulties encountered in the process described above were more of an integration nature. Thus it is the combination of steps which made the completion of the devices challenging. In this respect, several key achievements can be listed, which were instrumental to the high yield fabrication of the thruster devices.

Emitter wafer

- Optimized emitter interior etch uniformity and quality
 - Moved emitter interior etch to beginning of process
 - Reduced masking layers thickness
 - Selected and characterized recipes to minimize overetch and rework
- Optimized emitter yield
 - Introduced photopatternable laminated film, dramatically reducing the occurrence of blocked emitters
 - Selected and characterized isotropic etch recipe
- Optimized process for wafer yield and quality
 - Removed backside mask level
 - Solved issues with broken wafers due to incorrect Edge Bead Removal selection
 - Tracked complete metrology of fabricated devices

Electrode wafer

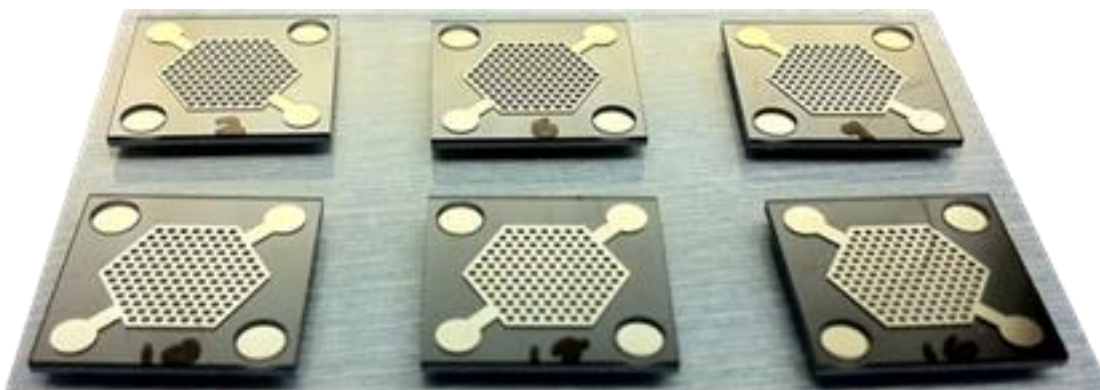
- Introduced a novel application of micro-sandblasting
- Introduced double-shadow mask metal deposition, capable of reliably depositing metal over large topology without leaving contaminants
- Optimized anodic bonding process for wafer yield and quality
 - Introduced manual clamping to avoid damaged wafers
 - Introduced sandwiched wafer to prevent sodium contamination

Wafer assembly

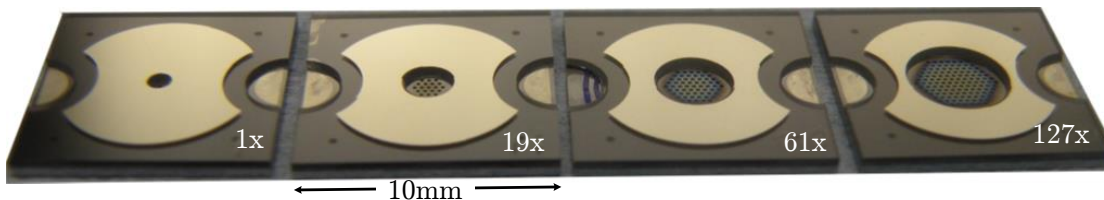
- Introduced and optimized thin film lamination and patterning
 - Selected optimal bonding film thickness to provide sufficient electrical insulation
- Optimized thermo-compressive bonding recipe to ensure good adhesion and alignment
 - Optimized pressure to ensure sufficient adhesion at dicing while avoiding broken wafers
- Proposed a new "guard-ring" design variant, where the active region is suspended from the glass handle structure and completely isolated from the emitter region.

3.6.1 Overview of fabricated MicroThrust devices

As a result of the above developments, 42 chips could be delivered to project partner QMUL over the course of a 4 months period, as shown in Table 3.2, well above the required 12. Figure 3.23a is an optical image of 6 die prepared for the 07/03/13 shipment. Table 3.2 lists for each die the type of array, bonding method and thickness as well as the outgoing inspection results. To validate the quality of the die, four 2-point resistance measurements were done, measuring the conductivity between pads in a given layer and insulation between layers. The emitter yield is also given, resulting from 100% optical inspection from blocked or broken emitters. Backside illumination was a convenient way to determine the quantity of blocked emitters, as only unblocked emitters allowed light to pass.



(a) 127x emitter v3a chips ready for shipping



(b) 1x, 19x, 61x and 127x emitter high density v3b chips with grouped accelerators

Figure 3.23: Optical photos of several diced thruster chips.

3.6. Main achievements

Table 3.2: MicroThrust die (v3a) delivered to project partner QMUL in 2013.

Ship. date	Wafer ID	Die ID	Die type	Bonding type	Thick (μm)	R_{acc} (Ω)	R_{ext} ($k\Omega$)	$R_{acc-ext}$ ($M\Omega$)	$R_{ext-emi}$ ($M\Omega$)	Yield (%)
26/02	2	4	BHA50	Wafer	15	8.1	1.3	N/A	N/A	92
26/02	2	5	BHA50	Wafer	15	9.7	2.0	N/A	N/A	77
26/02	2	8	BHA50	Wafer	15	8.0	1.2	N/A	N/A	92
26/02	2	14	BHA50	Wafer	15	7.6	1.6	N/A	N/A	99
26/02	2	17	BHA50	Wafer	15	7.9	2.8	N/A	N/A	96
26/02	2	20	BHA50	Wafer	15	7.3	0.6	N/A	N/A	90
07/03	2	3	BHA40	Wafer	15	N/A	6.0	N/A	N/A	90
07/03	2	6	BHA40	Wafer	15	N/A	3.3	N/A	N/A	77
07/03	2	9	BHA40	Wafer	15	N/A	2.5	N/A	N/A	98
07/03	2	10	BHA40	Wafer	15	N/A	1.8	N/A	N/A	86
07/03	2	15	BHA40	Wafer	15	N/A	1.0	N/A	N/A	94
07/03	2	16	BHA40	Wafer	15	N/A	0.9	N/A	N/A	94
05/04	1	-	BHA50	Die	50	6.0	0.9	N/A	N/A	77
05/04	1	-	BHA50	Die	50	6.0	0.9	N/A	N/A	53
05/04	1	-	BHA50	Die	50	7.0	0.5	N/A	N/A	81
05/04	1	-	BHA50	Die	15	6.0	0.5	N/A	N/A	47
05/04	1	-	BHA50	Die	50	6.0	0.3	N/A	N/A	87
05/04	1	-	BHA50	Die	15	6.0	0.4	N/A	N/A	46
25/04	4	1	BHA40	Die	50	30.0	1.8	>200 M	>200 M	96
25/04	4	8	BHA50	Wafer	50	23.0	1.8	>200 M	>200 M	98
25/04	4	9	BHA40	Wafer	50	18.0	0.8	>200 M	>200 M	98
25/04	4	10	BHA40	Die	50	17.0	1.2	>200 M	>200 M	98
25/04	4	11	BHA50	Die	50	21.0	0.8	>200 M	>200 M	93
25/04	4	15	BHA40	Wafer	50	18.0	0.9	>200 M	>200 M	100
25/04	4	16	BHA40	Wafer	50	17.0	0.6	N/A	N/A	100
25/04	4	17	BHA50	Wafer	50	21.0	0.8	N/A	N/A	100
25/04	4	19	BHA40	Wafer	50	30.0	0.7	N/A	N/A	98
25/04	4	20	BHA50	Wafer	50	24.0	0.5	N/A	N/A	99
25/04	4	21	BHA50	Wafer	50	22.0	0.6	N/A	N/A	100
25/04	4	22	BHA40	Wafer	50	22.0	0.7	N/A	N/A	99
07/06	3	11	BHA50	Die	50	11.5	900.0	>200 M	>200 M	93
07/06	3	15	BHA40	Die	50	10.5	700.0	>200 M	>200 M	97
07/06	3	16	BHA40	Die	50	10.1	1100.0	>200 M	>200 M	84
07/06	3	20	BHA50	Die	50	10.6	600.0	>200 M	>200 M	86
07/06	3	3	BHA40	Die	50	11.3	7000.0	>200 M	>200 M	76
07/06	4	5	BHA50	Die	50	20.0	700.0	>200 M	>200 M	90
07/06	4	6	BHA40	Die	50	22.0	>200 M	>200 M	>200 M	95
07/06	4	14	BHA50	Die	50	25.0	800.0	>200 M	>200 M	100
07/06	5	1	BHA40	Die	50	N/A	N/A	>200 M	>200 M	100
07/06	5	4	BHA50	Die	50	N/A	N/A	>200 M	>200 M	98
07/06	5	5	BHA50	Die	50	N/A	N/A	>200 M	>200 M	100
07/06	5	9	BHA40	Die	50	N/A	N/A	>200 M	>200 M	40

3.7 Summary

In this chapter, details of an advanced microfabrication process were presented. This process, a progression over that presented by Krpoun et al. [62], is the first to allow integration at wafer-level of a two-level electrode. The two-level stack is supported by a glass wafer patterned by an original microsandblasting technique, allowing the fabrication of clean and reproducible through-wafer orifices.

The emitters fabricated have the smallest inner diameters reported for this type of devices, leading to a high and uniform fluidic impedance, a useful feature to increase the ionic content and efficiency of the beam. An original photo-patterning method using laminated film was also introduced, in order to reduce the occurrence of emitters blocked by polymeric residues. A similar laminated film, although of different thickness, was used to complete the wafer-level bonding of the electrode and emitter levels, yielding highly uniform thruster chips with excellent alignment and good electrical insulation.

Several difficulties arose and were solved in the development of this process, and finally it was possible to make many thruster devices, sent for testing by project partner QMUL.

In the next chapter, a small subset of this characterization is presented, sufficient to validate the performance of the chips, with particular focus on the operation of the accelerator electrodes.

4 Electrospray thrusters - Validation

As part of the MicroThrust project, the silicon thrusters presented in the last chapters were extensively characterized by Dr. Charles Ryan, from project partner Queen Mary University of London (QMUL). While data analysis was still under way at the time of writing this thesis, sufficient data was available to provide a first demonstration of the performance of the devices and validate the operation of the accelerators.

This chapter presents a subset of the collected data, sufficient to determine the thruster thrust, specific impulse, efficiency and power consumption. Thus unipolar and bipolar IV, Retarding Potential Analysis (RPA), beam shape, time-of-flight and stability measurements are presented.

To date, the v3b devices have not been tested and all results presented here are from the v3a design.

Most of the data presented here is expected to be published in the following paper:

Ryan, C., Dandavino, S., Ataman, Ç., Chakraborty, S., Courtney, D. G., de Jong, M., ... Shea, H. R. (2014). Performance of a MEMS electrospray electric propulsion system.

Parts have also been published in:

Dandavino, S., Ataman, C., Ryan, C. N., Chakraborty, S., Courtney, D. G., Stark, J. P. W., & Shea, H. R. (2014). Microfabricated electrospray emitter arrays with integrated extractor and accelerator electrodes for the propulsion of small spacecraft. Journal of Micromechanics and Microengineering, 24(7), 075011. doi:10.1088/0960-1317/24/7/075011

and

Ryan, C., Daykin-Iliopoulos, A., Stark, J. P. W., Salaverri, A. Z., Vargas, E., Rangsten, P., ... Shea, H. R. (2013). Experimental progress towards the MicroThrust MEMS electrospray electric propulsion system. In 33rd International Electric Propulsion Conference (pp. 1–10). Washington, D.C.

4.1 Setup and assembly

The QMUL test setup (Figure 4.1) consisted of two chambers; a main chamber for spraying and a second for the storage of the ionic liquid. The propellant was transferred through a glass capillary by over pressurizing the second chamber with nitrogen and dropped on the backside of the assembly, where capillarity transported it to the emitter tip. The spray direction was vertically downwards and consequently a small backpressure contribution was possible. Up to 10mm of liquid could be added to the holder reservoir, leading to a maximum pressure head of 1.2 mbar.

The thruster chip was mounted on a peek holder, as illustrated in Figure 4.2. Electrical connections to the extractor and accelerator were made from the front side with four gold coated spring loaded pogo-pins (Mill-Max part no. 0850). The same four pins held the chip in place, providing sufficient force to ensure a good seal of the liquid reservoir on the backside of the chip. Connection to the emitter was done through the ionic liquid, via a central aluminium section inserted in the holder. The accelerator was grounded, while both extractor and emitter potentials were raised above ground to generate extraction and/or acceleration. The ionic liquid $EMI - BF_4$ was used as propellant.

The holder was attached to a linear translation stage which could be moved vertically by 150mm to change the distance between the thruster assembly and the target. The emitted spray was collected either by a large (220mm)circular plate situated 300-500mm downstream (Figure 4.1a) or by a small Kimball Physics FC-72 Faraday cup (11mm diameter aperture) mounted on a 280mm translation stage 235mm downstream (Figure 4.1b). The collector translation stage could move horizontally on one axis, mapping the plume which was assumed to be axisymmetric. With this setup, angle-resolved measurements up to 31° beam half angle could be taken. All the emitters of an array were contained within a 6mm radius of the center, so that the effect of their finite position on the measured beam profile was negligible.

The first configuration, with the large plate, was used for Time-of-flight (ToF) and IV measurements, with 20° to 12° beam half-angle subtended by the plate, depending on the mount position. For the collection of ToF data, a DEI PVX-4150 high speed switch was used to rapidly (within 20ns) turn off spraying by connecting the extractor to the emitter potential. Monitoring the flight time of the particles, it was possible to determine their nature and consequently the generated Thrust, Specific impulse and propulsive efficiency [109].

In all cases, current was measured on the emitter, extractor and accelerator by measuring the voltage drop across 100k Ω power resistors. The voltage measurements were then transmitted to a measurement PC via optical coupling. Current collected by the targets (large plate of Faraday cup) was amplified using a Femto DHPC-100 high-speed variable-gain current amplifier connected to a LeCroy Wavesurfer 422 oscilloscope.

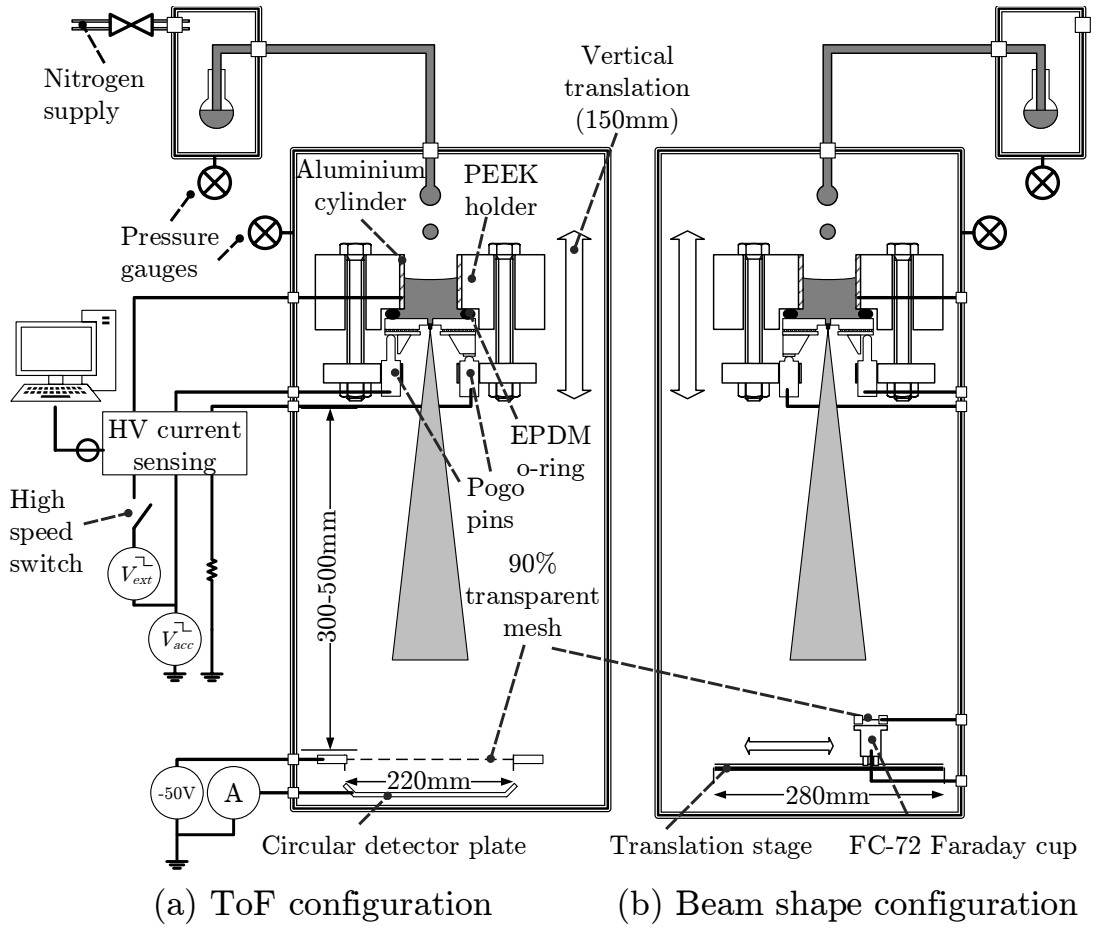


Figure 4.1: Diagram of QMUL test setup. For beam shape measurements, the large (220mm) target plate (a) is replaced by a small Faraday cup mounted on a small translation stage (b)

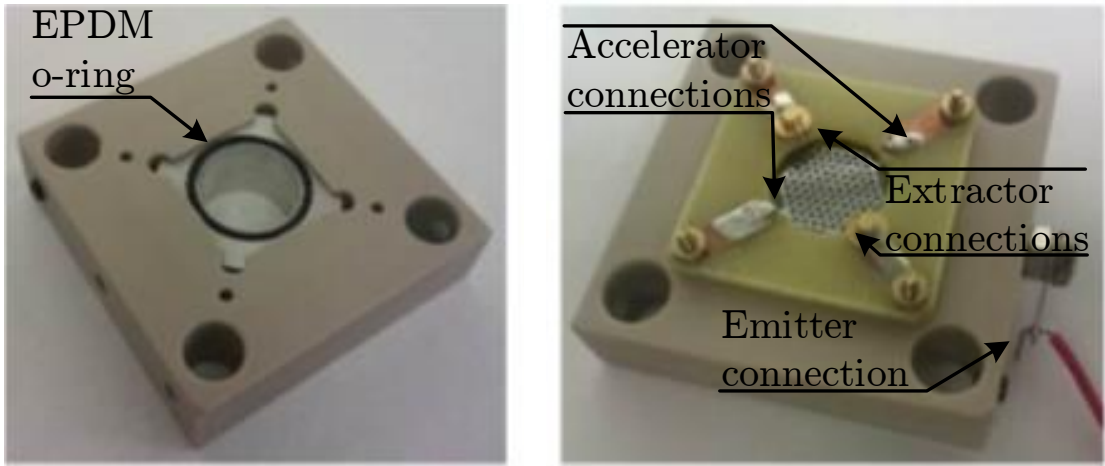


Figure 4.2: Emitter array installed in test assembly. Contact to the extractor and accelerator electrodes can be verified in-situ by measuring the resistance between two opposite pins. (Note that in some cases, this simple holder was replaced by the larger MicroThrust breadboard module described in [85])

4.2 Results and analysis

4.2.1 IV characteristics

Figure 4.3 plots the current measured at the emitter against the applied voltage difference between the emitters and the extractor (V_{ext} - refer to Figure 4.1 for labelling of the voltages). The emitted current was proportional to the plume current and was used as reference here since not all emitted current was collected. The spray was generated using a chip of the v3a - BHA40 design, i.e. an array of 127 emitters, with $540\mu m$ inner diameter accelerator diameter. In these experiments, current measured on the extractor and accelerator electrodes was negligible, so that the plume current could be assumed to be equal to the source current. This absence of leakage between the extractor and emitter, with upwards of 800V applied across $50\mu m$ spacing, is a significant achievement and a powerful justification of the wafer-level bonding process described earlier. Spray initiated at just over 750V, a value in good agreement with the simulated onset voltage of 785V.

Data is plotted for various acceleration voltages (V_{acc}), the voltage applied to the extractor to raise it above ground. The accelerator was at ground throughout.

Data shows a strong linear dependency between the emitted current and the extraction voltage, with a slope of $\sim 0.4\mu A/V$. This strong relationship is in agreement with previous studies using large electrospray thruster arrays operating close to PIR [18]. It could be explained by increasing numbers of emitters "turning on" as the extraction voltage is increased or by a larger current due to an increased flow rate resulting from the higher electrostatic pull.

The curve also confirms an independence of the emitted current from the acceleration voltage. This major result demonstrates that the electric field within the emitter-extractor region is not affected by field conditions downstream, as had been predicted by the onset voltage simulations. As mentioned previously, this represents an important feature of the propulsion system in terms of system flexibility, since it allows the independent selection of the optimal operation points for the extraction and acceleration voltages. For example, it allows independent control of emitted current and power consumption.

The chips were also operated in bi-polar mode, a configuration useful to avoid charge imbalance in the propellant reservoir. Figure 4.4 shows a section of a bi-polar test, where several traces were synchronized at their first rising edge. In this case, the y-axis is the collected downstream current while the x-axis is time. The system was run at several frequencies, from 0.1 to 10 Hz, although no acceleration voltage was used with this configuration. Bi-polar operation with post-acceleration would have required more complex coordination of the voltage levels and as well as 4 high voltage sources, which were not available. Alternatively, a high voltage Power and Control System (PCS), such as the one developed by SystematIC [86] would have been required. While such characterisation of the PCS was indeed initiated by QMUL, the results are not presented here. (See instead [85])

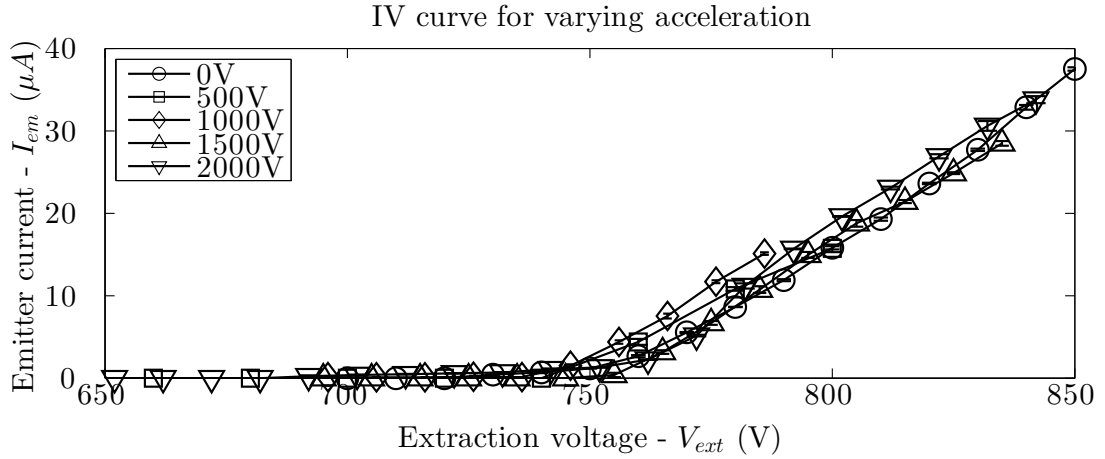


Figure 4.3: IV curve of 127 emitter array, showing the source current as a function of extraction voltage. Several curves, at different acceleration potentials, are plotted. The plot highlights the independence between the IV characteristics and the acceleration voltage. Credit QMUL.

Nevertheless the experiments performed without accelerators are sufficient to validate the bi-polar operation of the devices. For all frequencies, the current is seen to rise to about 25% of its stable value within 2.5ms, a result consistent with other work for emitters operation in PIR [38] and droplet [63, 75] mode. This rise can be associated to the initial formation time of the Taylor cone.

A second, longer, rise is also observed, this time frequency dependant. While the source of this rise remains undetermined, it can be speculated that the cone could take additional time to reach a stable state after being switched on. This observation would be consistent with the work from Chiarot et al. [110], which focused on cone-jet formation in response to an abrupt voltage application and where stabilization times of the order of 0.1s were seen.

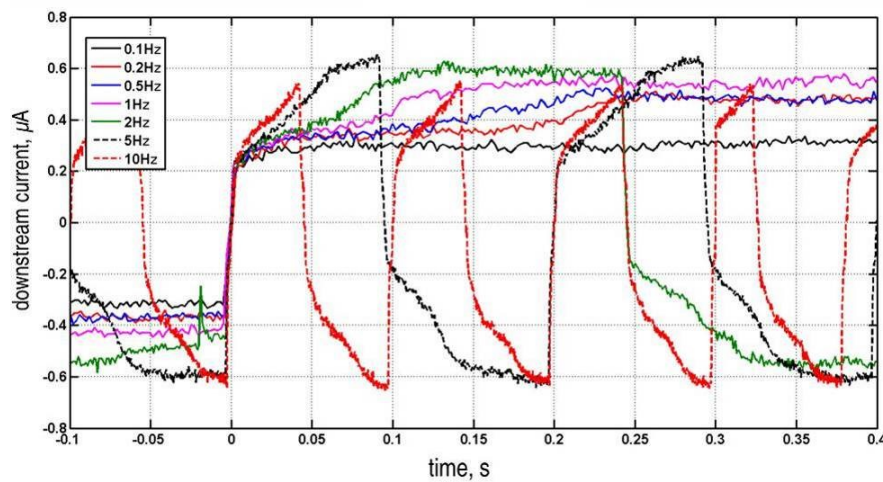


Figure 4.4: Bi-polar current traces, showing collected current emitted from 127 emitter arrays operated at $\pm 900\text{V}$ and alternating at 7 frequencies. Credit QMUL.

4.2.2 Energy measurements

In order to determine the true energy of the emitted particles, an element critical to computing the beam energy efficiency η_E , Retarding Potential Analysis measurements were carried out by Dr. Daniel Courtney at EPFL. The RPA measurements were done in an EPFL vacuum setup, which is not detailed here, but is similar to the QMUL setup. The major difference though was in the target: the collector was a small metal plate situated a few cm from thruster emitter and included a 5-grid RPA grid in between the emitter and the collector.

The 5-grid RPA, could be used to create an electrostatic barrier, blocking the particles with insufficient energy. By sweeping the barrier through a large voltage range, the energy of the particles forming the beam could be mapped.

In the arrangement used, the outer two grids were set to ground while the central one set to V_{ret} , the retarding potential. The remaining two grids were set to $0.96V_{ret}$, increasing the resolution of the setup [111]. Spacing between the three inner grids was set to 2.54mm while the outer grids were separated from the inner ones by 8.9mm. The total transparency of the arrangement was 43%. Finally, the detector itself was biased at +10V, in order to reduce secondary electrons emission.

Figure 4.5 shows a 3D CAD diagram of the grid setup as well as a sketch of the voltage potentials applied at each grid.

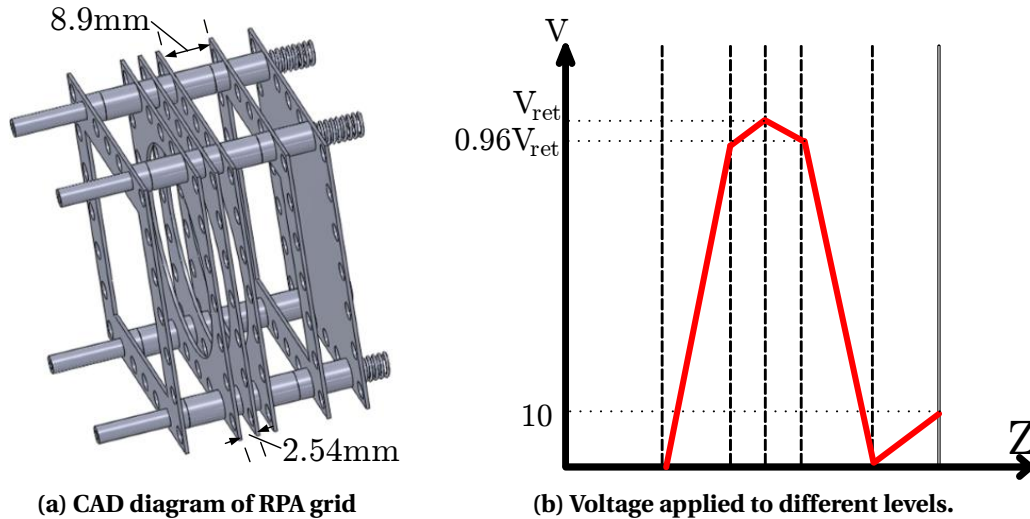
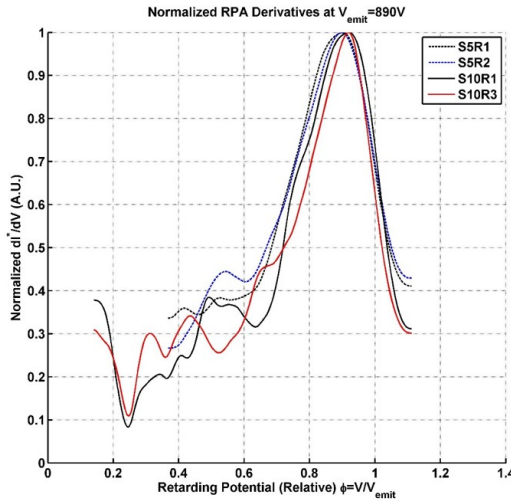


Figure 4.5: Design of Retarding Potential Analysis (RPA) grid

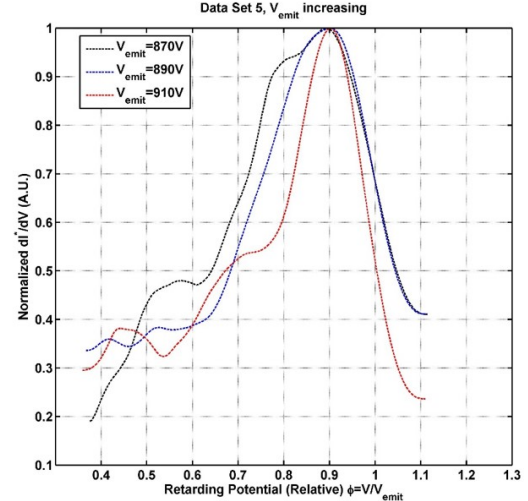
A v3a - BHA40 (127 emitters) chip was tested, leading to the results shown in Figure 4.6. For several extraction voltages, sequentially applied, the retarding grid potential V_{ret} was rapidly swept from $\approx 0.2V_{ext}$ to $1.1V_{ext}$. In Figure 4.6, the vertical axis shows the derivative of the measured current with voltage, highlighting potentials which correspond to large current drops.

The analysis clearly shows an energy peak centered at $0.9V_{ext}$, when 870-910V extraction voltage was applied. Thus the peaks indicate an energy deficit of $\approx 90eV$, slightly lower than the 120eV that could be observed by Krpoun et al. [62] with the bead-filled emitters. Recall that in the performance estimate model presented earlier, an energy deficit of 100eV was assumed.

The peak width of $0.15-0.3V_{ext}$ is also narrower than what had previously been observed, with an apparent narrowing at higher voltage. Still the peak is much wider than that which could be expected from sources operating in the ionic regime [39], hinting to some droplet presence. The presence of a tail at lower energies is also a hint of droplets. Visual observations confirmed the presence of considerable liquid on the detector plate, again supporting the presence of droplets in the plume.



(a) Normalized beam energy profile for several repeated retarding potential (V_{ret}) sweeps for a 890V extraction voltage.



(b) Normalized beam energy profile for three extraction voltages.

Figure 4.6: Retarding Potential Analysis measurements

4.2.3 Beam shape measurements

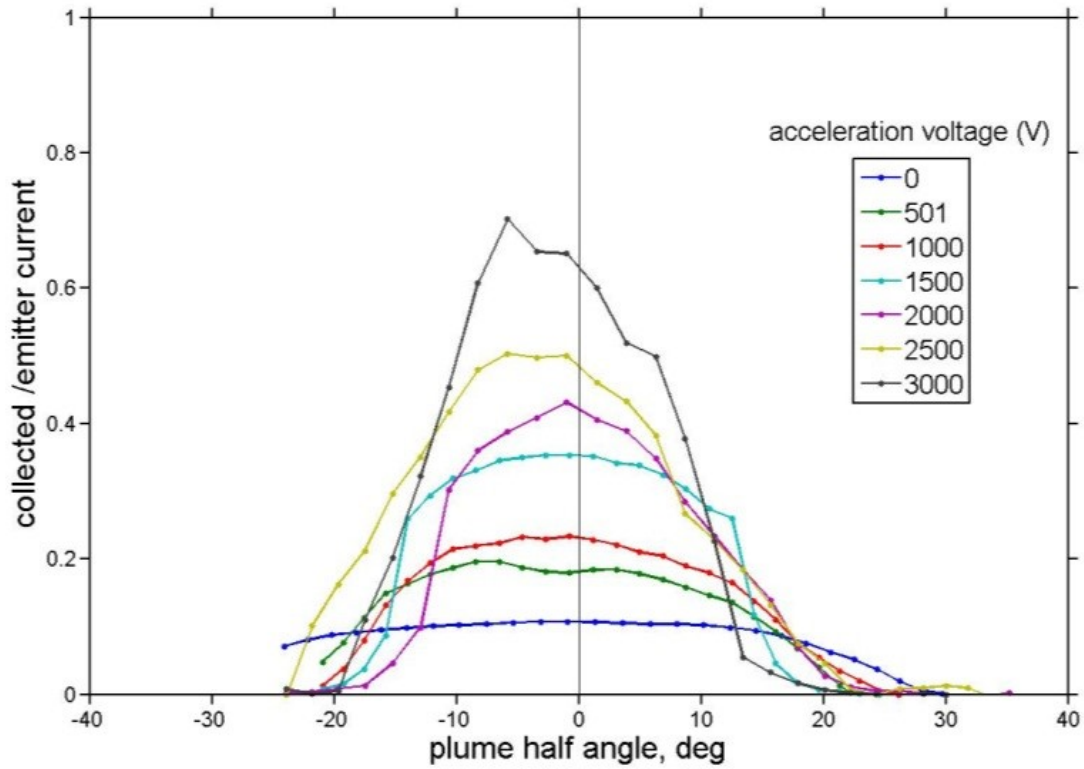
Beam shape measurements were taken to validate the ability of the accelerator electrodes to focus the spray, thus increasing the thruster's angular efficiency.

Figure 4.7a is an example of the plume profile generated from an 127 emitter array as the applied acceleration voltage V_{acc} was increased from 0 to 3000V. These measurements were taken using the translating Faraday Cup setup described earlier and, once again, the device used was of the v3a - BHA40 design. The value of the BHA was taken by integrating the profile curve with a 90% confidence interval, i.e. the critical BHA is that which includes 90% of the total current.

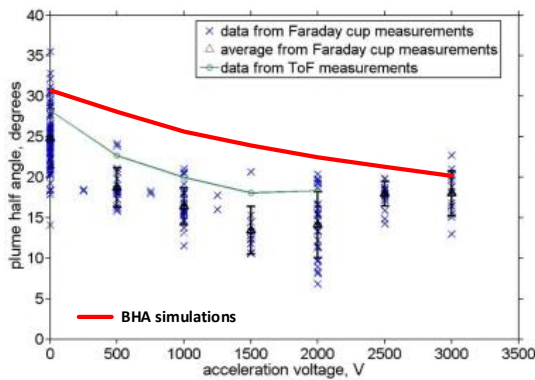
A clear focusing effect is seen, with the plume profile reduced from $\sim 25^\circ$ to $\sim 15^\circ$. Figure 4.7b plots the measured beam half-angle as a function of applied acceleration voltage. In this plot, an additional curve (solid green) is traced, corresponding to an alternative means of determining the BHA. With this method, the BHA is calculated by measuring the fraction of current collected by the large plate as a function of acceleration voltage. Thus at low acceleration, a smaller portion of the plume is subtended by the plate. This method assumes a uniform particle distribution inside a cone of half angle BHA. The focusing observed is in good agreement with the ion-optic simulations, which predicted a $\sim 65\%$ reduction in beam half-angle with this voltage applied. The expected BHA as a function of voltage is also plotted in Figure 4.7b in thick red. The agreement is good, although the actual device appears to focus more effectively at lower voltage, stabilizing in the range of 1500V. This stabilization could be explained by space-charge effects which prohibit the focusing of the beam beyond a certain point. Note also that the measured data point are not the full beam width, but rather the width that contains 95% of the current, whereas the simulations do attempt to represent the full width.

The data in this plot is highly scattered, at least partially a result of instabilities in the thruster operation. The plume angle is also seen to depend on the extraction voltage, as plotted in Figure 4.7c. This dependence explains some of the variability seen in Figure 4.7b, since the data in the plot was taken at many extraction voltages. It could again be caused by an increasing number of emitters turning on with voltage, which could lead to space charge effects or other more complex beam interaction effects. It is also likely that the beam composition would be modified with increasing extraction voltage, with increasing amounts of droplets at higher voltage. As mentioned previously, electrospray sources operating in the PIR have reported BHA in the order of 15° to 20° [38], although sources in mixed ion/droplet mode have exhibited wider plumes of 30° - 40° [96, 97].

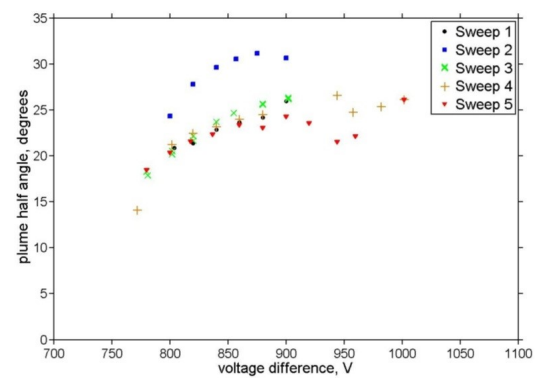
In any case, it is evident that the accelerators successfully focused the spray. With the model presented earlier, and assuming uniform spray, which is not exactly the case here, an angular efficiency increase from 91% to 97% is calculated.



(a) Example of plume profile with varying acceleration. As the acceleration is increased, the width of the beam decreases while the amount of current collected close to the center is increased. Credit QMUL.



(b) Measured beam half angle vs acceleration voltage. Points indicate direct and averaged measurements taken using the translating Faraday Cup setup. Green solid line is interpolated using the large plate setup, where larger beam fraction is collected with increasing accelerator voltage. Red solid line is simulated BHA.



(c) Calculated beam half angle vs extraction voltage. The beam is seen to widen as the extraction voltage is increased

Figure 4.7: Beam half angle vs acceleration and extraction voltage. Credit QMUL.

4.2.4 Time-of-Flight and performance measurements

Time-of-Flight measurements were used to determine the nature of the emitted species and calculate the performance parameters. A sample ToF spectra showing typical results for the v3a devices is presented in Figure 4.8.

The plot displays two large drops corresponding to the arrival of ions (monomers and dimers) followed by a quickly decreasing droplet tail. The inset in Figure 4.8 presents a simplified profile of the plume, where the beam is composed of three species: monomers, dimers and droplets. Approximating the beam to this simplified model is a convenient way to compute analytically the performance parameters of the thruster (thrust, specific impulse and efficiency).

While in some cases, 95% ion contents were observed [112], typical results of emitter arrays show that the beam is composed at 90% of ions (70% monomers and 20% dimers) with the remaining droplets being clusters with a mass equivalent up to ≈ 540 monomer ions. The mass equivalent value was computed by reading the location Figure 4.8 where the droplet tail reaches zero, and thus corresponds to the largest droplets. The particle current fractions are also read in Figure 4.8 from the highly accelerated curves. In this case, the full beam (or close to) is focused and captured by the collector plate, whereas for lower acceleration, only part of the beam is collected and the results not representative.

Interestingly, the droplet quantity remains constant with all acceleration voltages, hinting that droplets compose the center of the beam while the outer perimeter is dominated by ions. This result is consistent with the excellent work of Chiu et al. [113]

The droplet size is read from Figure 4.8 and corresponds to the point where current reaches zero, such that all particles have arrived at the collector. Thus it represents the largest droplets present in the plume. The droplet fraction is read from the graph by considering the normalized current after all ions have arrived (time corresponding to 10^3 amu in Figure 4.8). Making this assumption that all droplets are of the "maximum" size will lead to a slight underestimation of the polydisperse efficiency of the thruster.

Using a three-species model, Table 4.1 lists the calculated flow rates, efficiency, specific impulse, thrust and power consumption that would result from this beam composition with all the designs fabricated. All values have been divided by the array size and are consequently average values per emitter. Taking into account the presence of a third particle type (monomer, dimer and droplet), the polydisperse efficiency equation presented in chapter 2 (Eq. 2.4) was modified (Eq. 4.1), with f_3 the fraction of current carried by the droplets, ϵ and α respectively the monomer/dimer and dimer/droplet mass ratios.

$$\eta_p = \frac{(1 - (1 - \sqrt{\epsilon}) f_1 - (1 - \sqrt{\alpha}) f_3)^2}{1 - (1 - \epsilon) f_1 - (1 - \alpha) f_3} \quad (4.1)$$

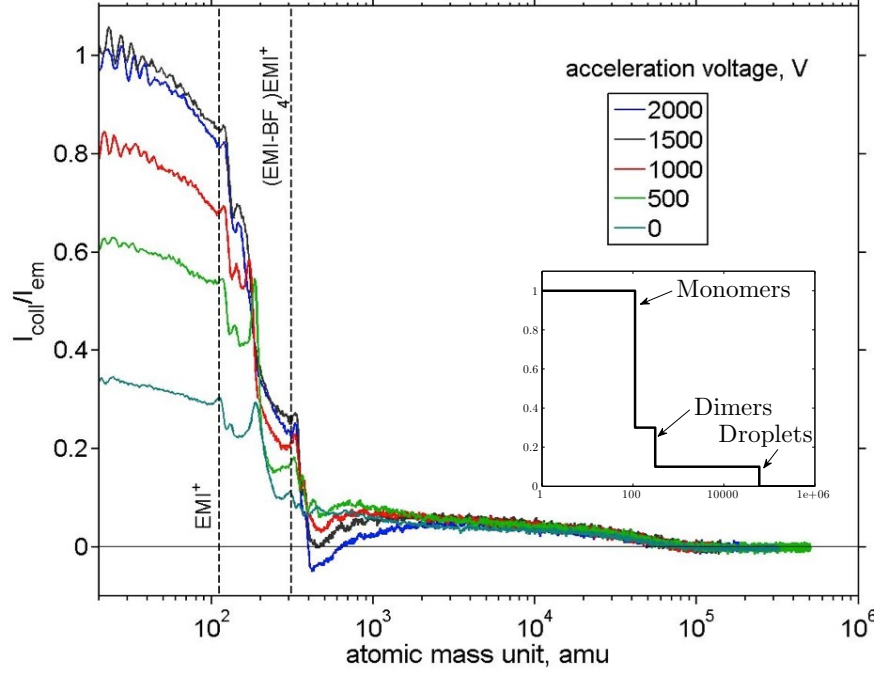


Figure 4.8: Time-of-flight curve taken with five accelerating voltages, using a 91 emitter array. The increased focusing due to acceleration enables the capture of increasingly larger portions of the beam, as reflected by the higher starting current. Credit QMUL.

Table 4.1: Calculated thruster performance using typical beam composition measured by time-of-flight analysis.

ID	Units	Req.	v3a		v3b				Acc. (All)
			Unacc. BHA30/40/50	Acc. BHA30/40/50	E150	E200	E250	E300	
ρ_{emi}	$\frac{emi}{cm^2}$	-	257/213/125	257/213/125	1527				1527
V_{app}	V	-	785	4000	762	827	897	971	4000
P_{emi}	μW	-	157	800	152	165	179	194	800
η_E	-	-	0.90	0.98	0.90	0.90	0.90	0.90	0.98
η_θ	-	-	0.87	0.94	0.87				0.94
Typical measured composition (70/20/10 monomer/dimer/droplet) $\dot{m} = 1.27e-11$, $\eta_p = 0.20$									
η_T	-	-	0.16	0.18	0.16	0.16	0.16	0.16	0.18
I_{sp}	s	-	200	491	197	206	214	223	491
T_{em}	nN	-	25.0	61.3	24.6	25.7	26.7	27.8	61.3
ρ_T	$\frac{\mu N}{cm^2}$	>4.3	6.4/5.3/3.1	15.8/13.0/7.6	37.6	39.2	40.8	42.5	93.6
ρ_P	$\frac{\mu N}{W}$	>20	159.4	76.6	161.7	155.2	149.1	143.3	76.6
$P_{300\mu N}$	W	<15	1.9	3.9	1.9	1.9	2.0	2.1	3.9
$N_{300\mu N}$	-	-	11992	4895	12171	11683	11218	10782	4895
ΔV	km/s	>5	0.44	1.08	0.43	0.45	0.47	0.49	1.07

Sp. 1: $f_1=0.7$, $(q/m)_1 = 8.68e5$ C/kg; Sp. 2: $f_2=0.2$, $(q/m)_2 = 3.12e5$ C/kg; Sp. 3: $f_3=0.1$, $(q/m)_3 = 1.61e3$ C/kg

Clearly, the presence of droplets in the plume is extremely damaging to the performance of the thruster, in particular in terms of the efficiency, which in turn has a dramatic impact on the thrust and specific impulse of the device, bringing it well outside of its required window. Applying Eq. 4.1 to the ratio observed results in $\eta_P = 0.20$. In fact, this efficiency is close to the curve minimum of 0.16, shown by Figure 4.9. This minimum occurs when no dimers are present and the beam is composed of 96% monomers.

Nevertheless, it is not entirely unexpected to have a small droplet presence, considering that the impedance of these emitters was not as high as targeted. Unfortunately, it was not possible within this work to test the v3b chips have an higher impedance due to their smaller inner diameter.

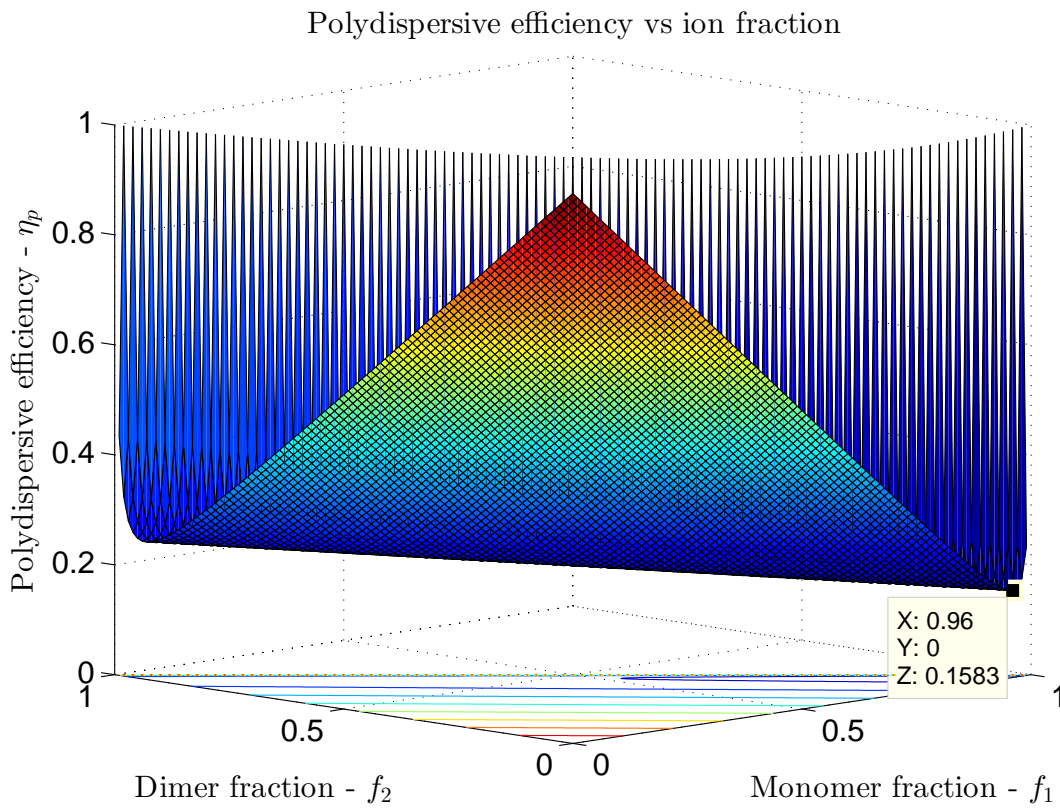


Figure 4.9: 3D curve showing polydispersive efficiency as a function of monomer and dimer fraction. Droplets, in this case have a mass equivalent to 540 monomers, compose the remainder of the beam. The curve minimum occurs when no dimers are present and the beam is composed of 96% monomers.

Alternatively to increasing the impedance, it was also proposed by Dr. Ryan to use another ionic liquid, namely 1-Ethyl-3-Methylimidazolium Thiocyanate (EMI-SCN) as propellant. The conductivity and surface tension of EMI-SCN (purchased from IoLiTec Ltd.) were respectively measured at 1.85 S/m and 41.9 mN/m.

Figure 4.10 show two ToF traces obtained with a single emitter (earlier chip version) and an 127 emitter array from the v3a design. These traces show a much higher ionic content and indicate an interesting research avenue towards increased performance of the thruster.

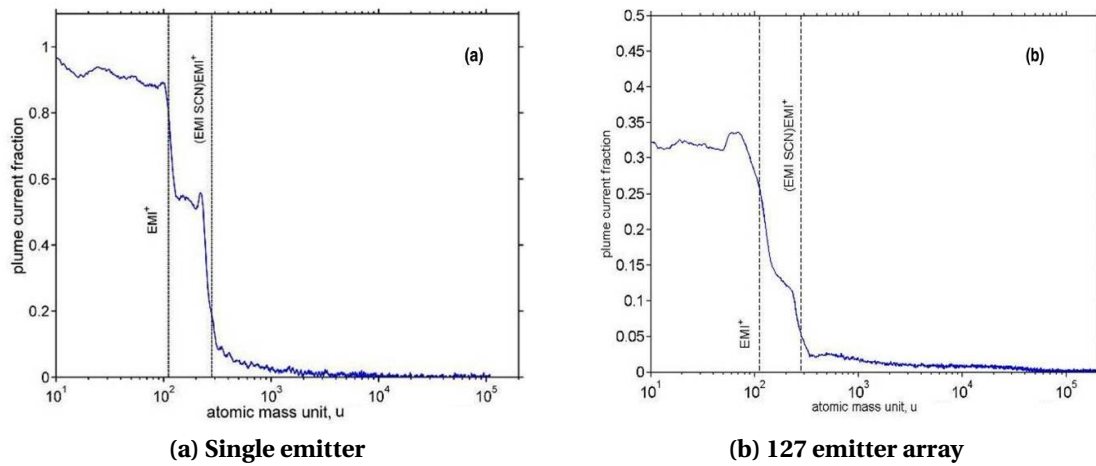
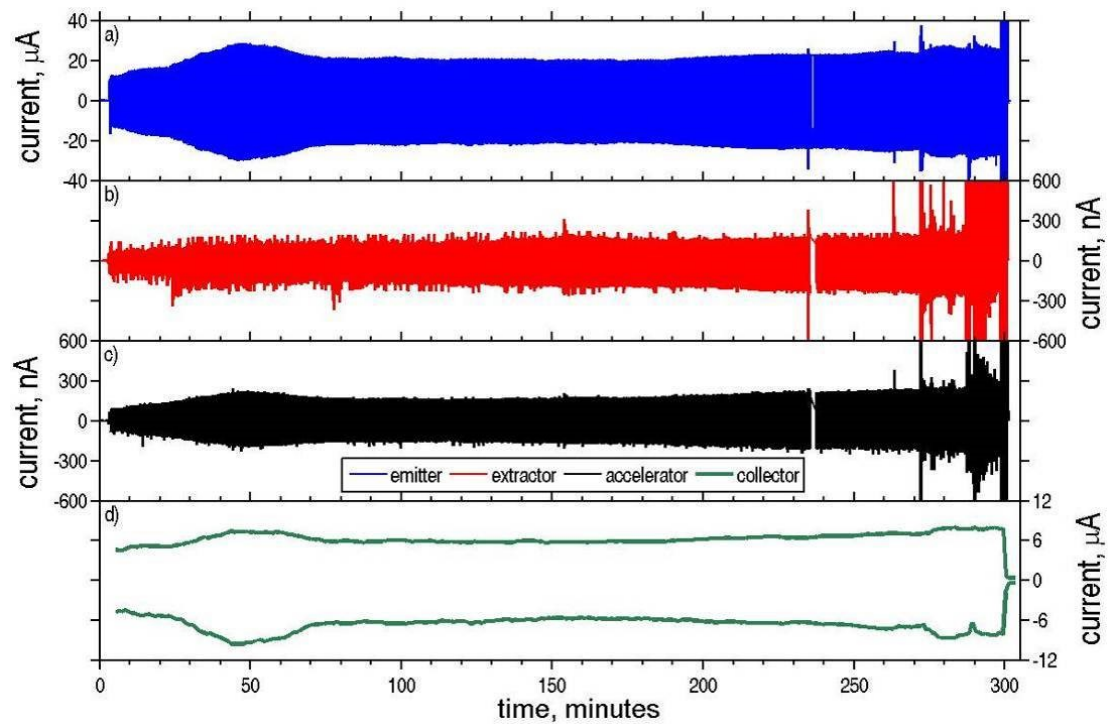


Figure 4.10: Time of Flight curves with the liquid EMI-SCN. Credit QMUL.

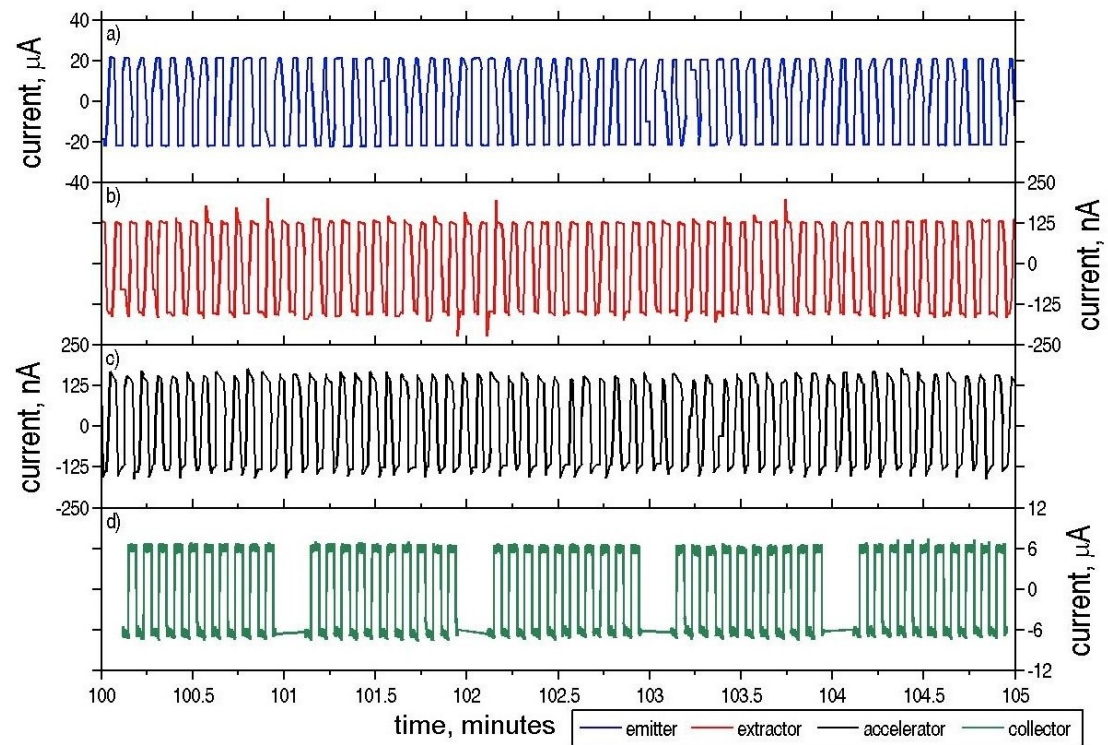
4.2.5 Stability - Long term tests

Bi-polar stability measurements were attempted on a 91 emitter - BHA50 thruster. The device was operated in the "large plate" setup with the extraction voltage (800V) switching at 0.2 Hz. No acceleration voltage was applied.

Figure 4.11 shows the current traces obtained through this experiment. Approximately 1.1 cm³ had been placed in the holder reservoir which was not refilled during the experiment. With the beam characteristics and flow rates outline above, this reservoir was expected to allow constant spray for close to 300 hours. In the end, the device could be run constantly for close to 5 hours before it failed due to a short circuit between the emitter and extractor. The emitted and collected current levels are piece-wise very stable although some slow patterns are seen, for example around the 50 minutes point. This indicates that in order to keep charge neutrality and to ensure constant performance of the thruster, current feedback should be included to precisely control the extraction voltage applied.



(a) 5 hour period

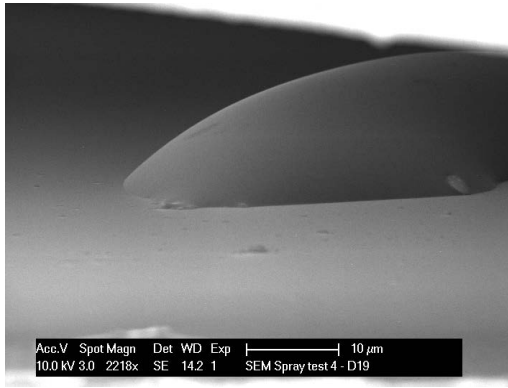


(b) Five minute period. Artificial gaps in the collected current are due to the measurement setup periodically holding measurements for 10 seconds.

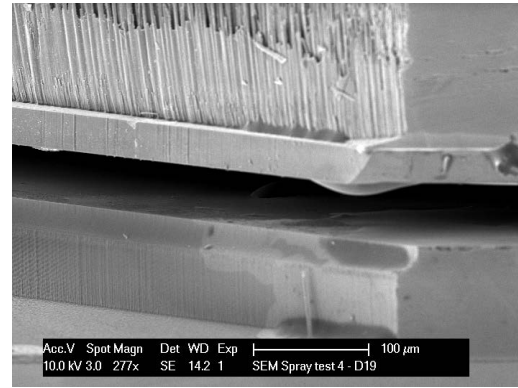
Figure 4.11: Long duration tests. Credit QMUL.

The failure after five hours is believed to be a result of liquid spillage from the tip of the emitter or intercepted by the extractor electrode. At $165\mu m$, the extractors of this design were sufficiently large the majority of the spray to pass unhindered, but may have intercepted a small part of the beam. It is also possible that liquid spillage from the assembly could have led to devices failure. Figure 4.12 is an example of an experiment performed at EPFL where drops of liquid were observed in between the emitter and extractor electrodes before spray could be initiated.

Clearly, this issue of short lifetime would need to be solved in order to meet the demands of a real mission, which should require thousands of hours of operation. The failure is not however intrinsically linked to the electrospray technology. As mentioned in the introduction of this thesis, electrospray thrusters qualified for the Lisa Pathfinder mission could be operated for close to 3500 hours [36]. Devices used by QMUL in this project could commonly be intermittently operated for over a week, accumulating spray time in the range of 12h.



(a) Drop of $EMI - BF_4$ liquid in between emitter and extractor



(b) Drop of $EMI - BF_4$ liquid in between emitter and extractor

Figure 4.12: Device failure due to liquid leakage from assembly, creating a short circuit before spray could be initiated.

4.3 Conclusion

Characterization of the emitter arrays has shown very promising results in terms of the usability of acceleration electrodes. It was successfully shown that the acceleration and extraction stages could be decoupled, an important element to simplify the system and mission design. Beam shape focusing was also effective, with measured beam half-angles being focused from approximately 25° to 15° with 3000V acceleration. The energy properties of the beam were characterized, with typical energy deficits of about 10% of the applied extraction potential.

The composition of the beam, with 90% ions, is approaching the desired Purely Ionic Regime, although the small amount of droplets drastically reduced the achieved specific impulse and efficiency. With the droplet size seen here, the minimum theoretical polydispersive efficiency occurs at 94%, close to the present situation. Thus a further reduction in the droplet content is inevitable if this system is to be used to provide high ΔV capabilities to small spacecraft.

5 hour of continuous bi-polar operation was achieved, although this remains well below the thousands of hours required for a typical mission. The failure of the devices is believed to be caused by liquid spillage, leading to leakage current and short circuit.

Next steps should include a complete characterization of the v3b chips, which could be compared in terms of beam composition to the v3a devices. It would also be interesting to validate whether the "grouped accelerator" design of v3b is as effective at focusing the beam, as is suggested by ion optics simulations. With their much higher density, the v3b may also introduce some space charge and density-related effects which would be useful to study. Also, the promising ionic liquid EMI-SCN should be studied further, characterizing its emitted plume composition under different conditions.

It is relevant, however, to also proceed to more fundamental experiments to study the operation and failure of the emitters. As such, the next chapter presents electrospray experiments performed inside a Scanning Electron Microscope, with the goal to observe in-situ the Taylor cone during and after spray.

5 In-situ electrospray SEM observations

5.1 Introduction

An image is worth a thousand words, or so the saying goes. Perhaps this mantra served as inspiration to the many researchers who have attempted, and often succeeded, over the past 100 years in applying various visualisation techniques to the study of electrosprays, particularly focusing on Taylor cones and their formation. Already in one of his original papers [22], Zeleny showed in 1917 crude photographic images of cone formation and droplet ejection (Figure 5.1) which helped him provide the first descriptions of the electrospray process.

Since then, methods have evolved significantly, both in terms of resolution and capture speed. While early work focused on static Taylor cones, the recent tendency is to observe and describe the cone dynamics, in particular during their formation. Notable work of this kind includes a 2004 paper by Marginean et al. [114] in which stroboscopic lighting was used to observe pulsating electrosprays (Figure 5.2). They found clear evidence of standing waves on the surface of the cone and described how the Taylor cone semi-vertical angle was not constantly fixed at 49.3° but could in fact vary between 40° and 65° in these dynamic conditions.

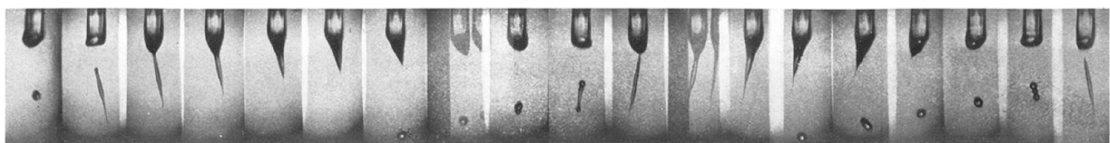


FIG. 1.

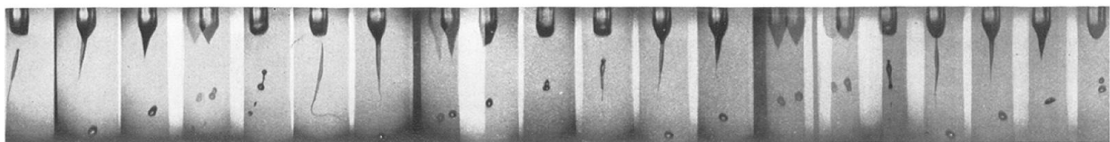
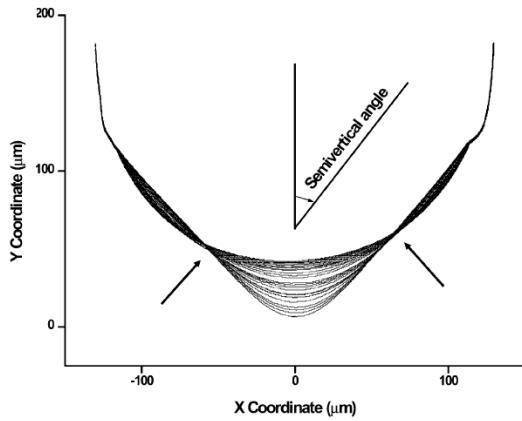
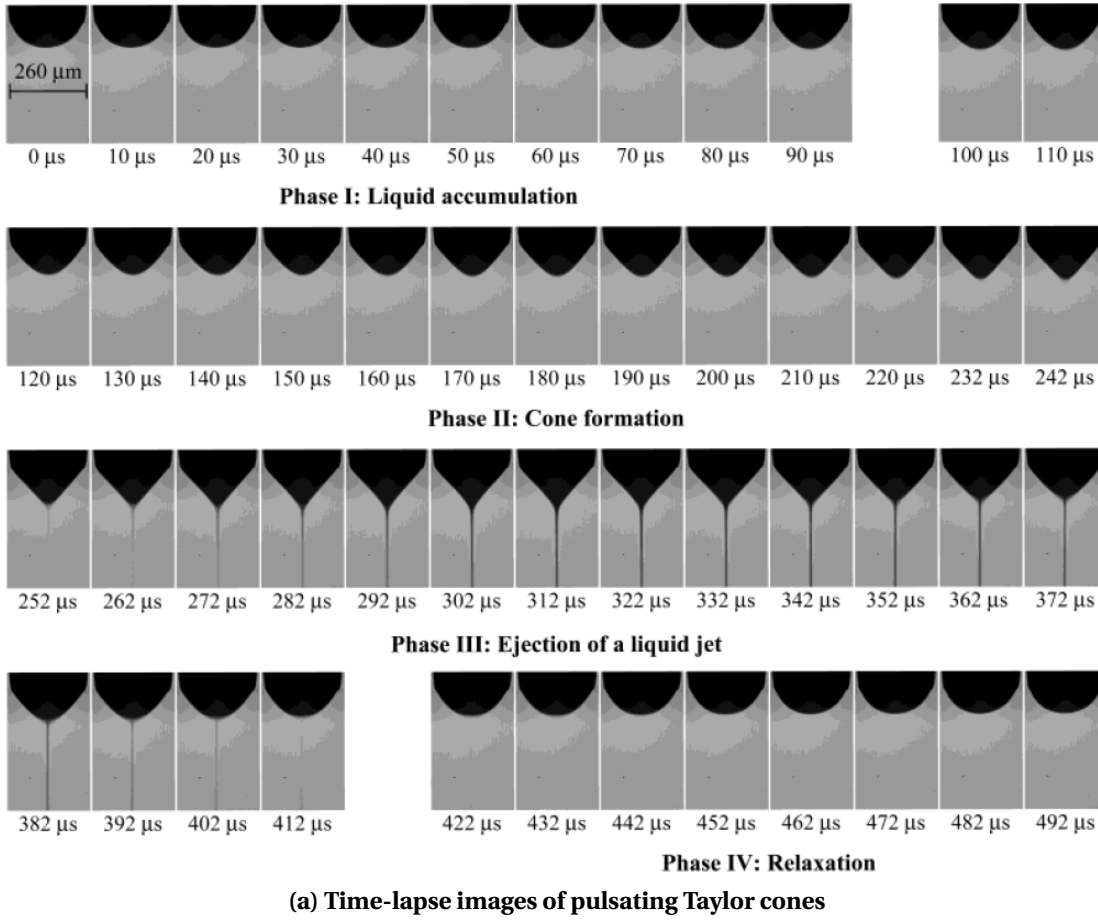
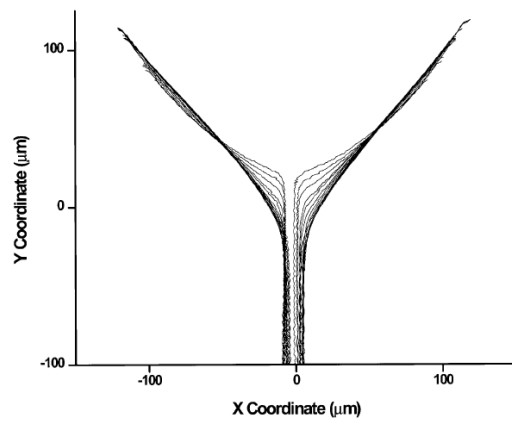


FIG. 2.

Figure 5.1: Early photographs of liquid instabilities taken by Zeleny in 1917. The liquid sprayed is ethyl alcohol, charged at 5000-6000V. The diameter of the glass tubing seen in the images is 0.92mm. [22]



(b) Liquid surface contour extracted from time-lapse images. Image processing parameters 1.



(c) Liquid surface contour extracted from time-lapse images. Image processing parameters 2.

Figure 5.2: Dynamic formation of cone-jet obtained with stroboscopic lighting observation of a pulsating Taylor cone obtained by Marginean et al. in 2004. The emitter is a 130 μm ID, 260 μm OD stainless steel needle and the sprayed solution (aqueous methanol or acetonitrile) is fed using a syringe pump at 2 μL/min. The emitter is held between 2.9 kV and 3.1 kV. [114]

Another notable contribution was provided by Deng et al. in 2011 [63]. In this case, a step voltage was applied to microfabricated internally fed silicon emitters of approximately $90\mu\text{m}$ inner diameter and $180\mu\text{m}$ outer diameter and the initial cone formation captured using a high speed camera (Figure 5.3). They showed how the Taylor cone and spray stabilized within 0-10ms, with faster settling in the presence of a higher electrical field, although this also depended on the feeding rate. They mentioned in passing that with high electrical fields, the cone could anchor at the inner diameter of the emitter, although this environment was much less stable.

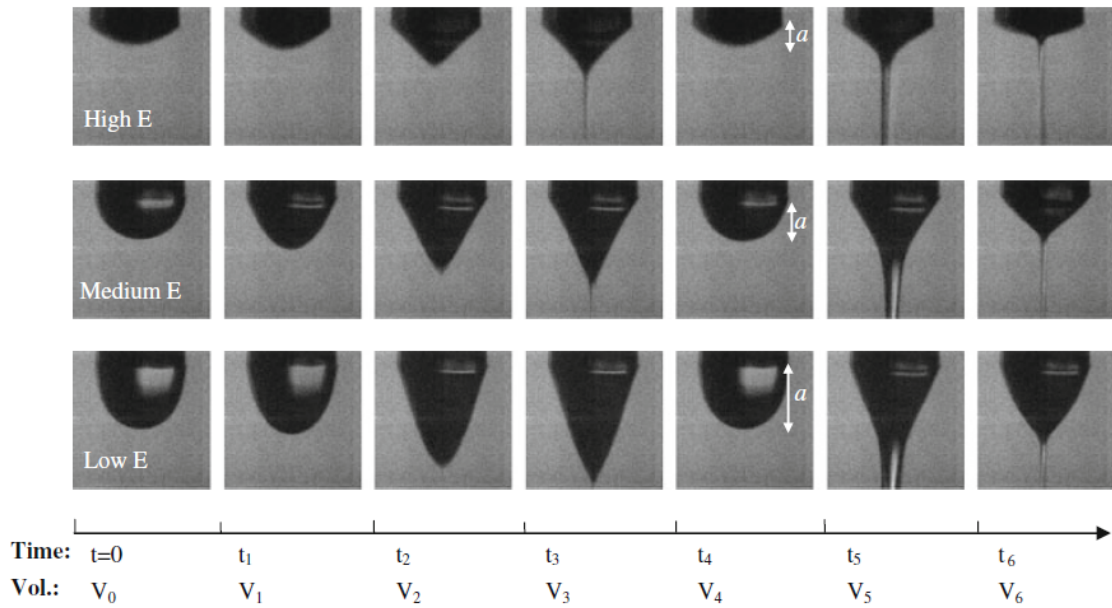


Figure 5.3: Formation of Taylor cone from step change, taken with high speed camera. The emitter is a $\approx 90\mu\text{m}$ ID, $180\mu\text{m}$ OD, microfabricated capillary and pure ethanol is fed using a syringe pump at 0.4mL/min . The emitter is held at 1200V (high E), 1000V (medium E) or 850V (low E). [63]

High speed cameras were also used by Tran et al. [115] and Chiarot et al.[110] in 2009, in the first case to study oscillation modes and resonant frequencies of the meniscus and in the second to also study responses to abrupt voltage steps (See Figure 5.4). Pulsations and cone dynamics were also extensively studied by John Stark's group at QMUL [73, 75, 116] between 2006 and 2009.

However, most of these observations were applied to relatively "large" emitters, always operating in mixed or droplet mode. For ionic, or nearly ionic emitters, very little observation was reported. Transmission Electron Microscope (TEM) observations could be done for small emitters generating ionic sprays of liquid metal[117–122] and more recently $EMI - \text{BF}_4$ [123] (Figure 5.5). Although this last work used externally wetted tungsten needle emitters, it remains particularly exciting as it showed an unexplained liquid solidification during observation, with cones still present with no voltage applied.

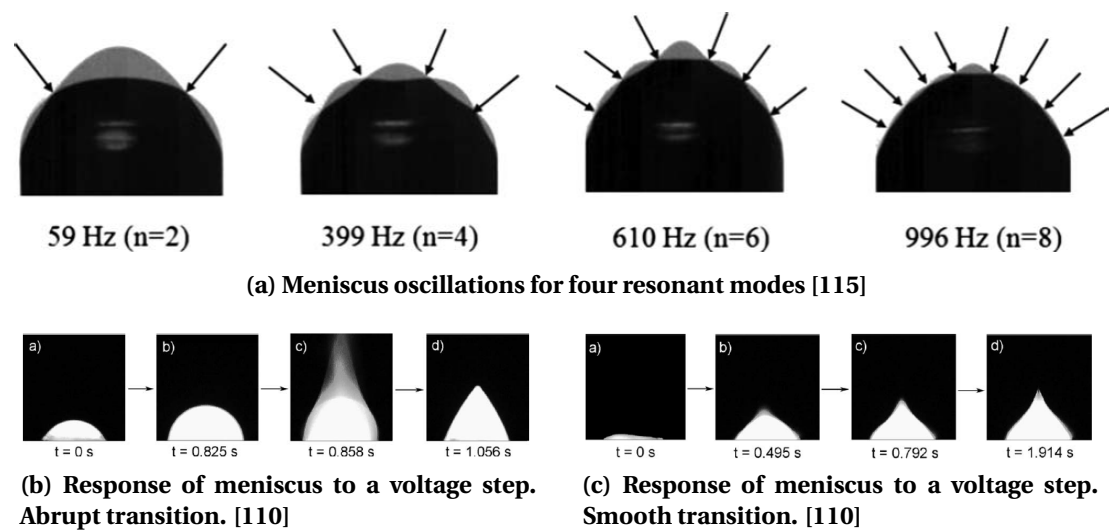


Figure 5.4: High speed camera Taylor cone characterization by Tran [115] and Chiarot [110]

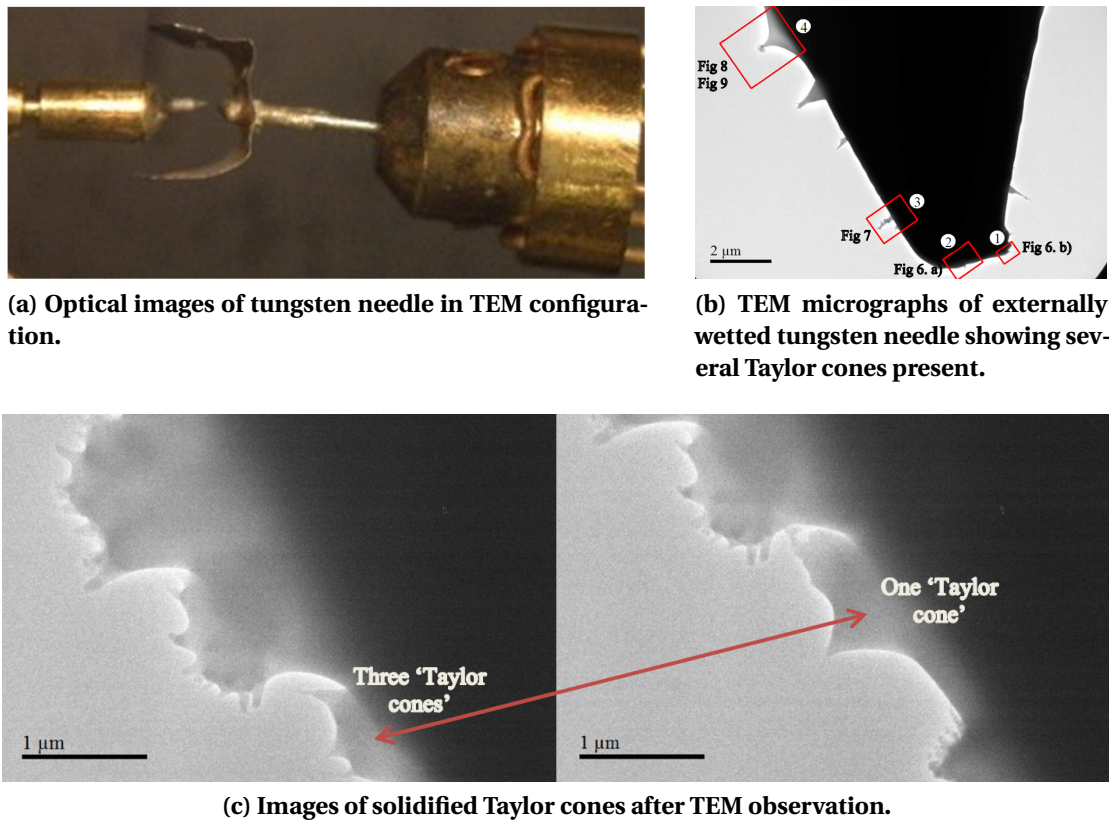


Figure 5.5: TEM micrographs of solidified cones (post-spray) from externally wetted needles [123]

Thus many questions remain to be answered relative to small ($< 10\mu\text{mID}$) internally wetted emitters, operating in or close to the ionic regime. Is the liquid meniscus contained inside the capillary until it snaps in to a cone, or does it gradually deform as with larger emitters? With a low flow rate and approaching PIR, is the cone anchored at the interior or exterior of the capillary? Is a jet present, or does emission start directly from the cone tip? How are the cone angle and shape affected by the applied voltage? And what is the behaviour of the liquid in terms of transport? Does it wet the sidewalls of the emitter or remain constrained to the tip? How is the stability of the cone and how repeatable is its shape?

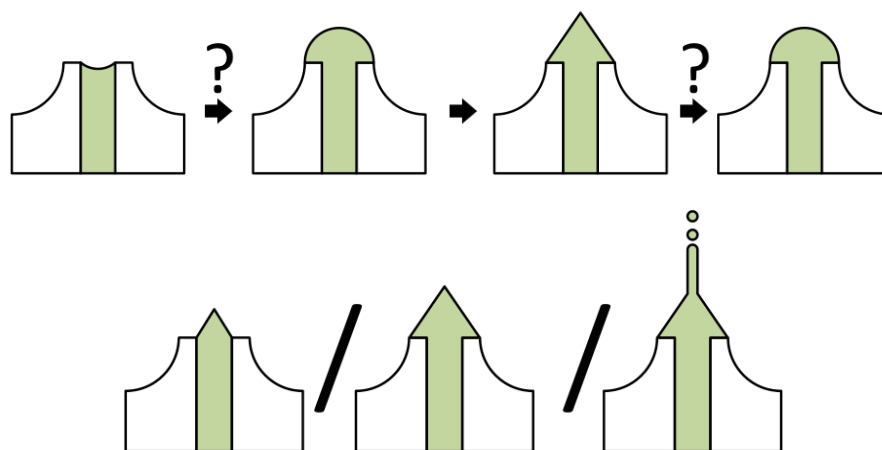


Figure 5.6: Interrogations relative to emission site. Is a spray present? Where is the cone anchored? How is the liquid contained?

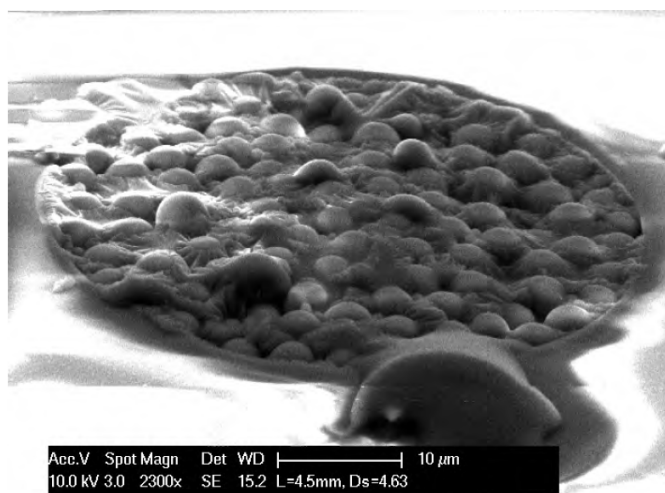
Answering even a few of these questions, while challenging, thus remains an honourable scientific endeavour. In this work, this is attempted by conducting in-situ observations of microfabricated internally fed emitters inside a Scanning Electron Microscope. The SEM is an attractive tool in this case first since it allows extremely high resolution images of even a microscale cone to be taken, in theory even allowing measurement of the nanoscale apex radius of curvature. Contrary to the TEM, it also permits perspective observations and the ability to observe not just the profile, but the surface of the cone itself.

Clearly, though, this kind of observations presents several practical difficulties. Fundamentally, it was also uncertain whether it would at all possible to image any relevant Taylor cone feature in the presence of such extreme electric fields, considering that a SEM relies on low energy secondary electrons making their way to the detector. Additionally, the scanning electron beam could affect the liquid cone, perhaps with results similar to the solidification observed in the TEM. Yet early observations performed internally by MSc student Jérôme Favre in 2010 [124] were encouraging in that they confirmed that the liquid could be reasonably imaged even at high voltage (Figure 5.7). This test was made using a bead-filled $50\mu\text{m}$ glass capillary filled with $4.63\mu\text{m}$ silica beads as emitter source and a large non-microfabricated extractor (unknown dimensions). Spray could not be initiated with up to 2kV potential applied.

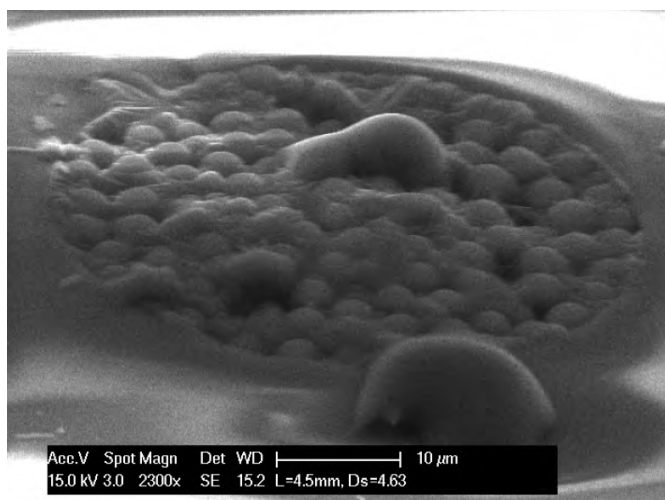
This chapter presents original work towards in-situ SEM observations in which the spray

Chapter 5. In-situ electrospray SEM observations

is generated and captured inside the SEM chamber, using internally fed silicon capillary of dimensions corresponding to the v3b design described earlier. Spray was successfully emitted and contained inside the test assembly placed inside the SEM. However, it was not possible, in the experiments described here, to get clear images of the cone itself, apparently due to interactions between the spray and the secondary electrons necessary for imaging.



(a) Emitter voltage: 1500V



(b) Emitter voltage: 1800V

Figure 5.7: SEM micrographs of $50\mu\text{m}$ ID emitters filled with $4.63\mu\text{m}$ beads from Favre et al. [124]

5.2 Setup and procedure

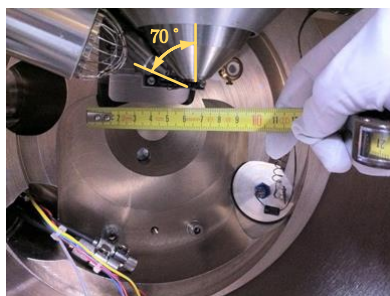
5.2.1 Conditions for testing in the SEM

Attempting to observe inside a SEM an active electrospray poses several difficulties. For one, the very tight dimensions of the chamber interior demand a very compact test assembly, which must be solidly attached to the SEM sample holder. Figure 5.8a and Figure 5.8b show optical micrographs of the tool used in this work (FEI/Philips XL30 ESEM-FEG, at CSEM Neuchâtel), showing both the exterior of the tool and the interior of the chamber. In Figure 5.8b, the exit aperture of the electron source column is seen on top of the image and points downwards. The secondary electron detector, seen on the left of Figure 5.8b, is placed about 5cm from the aperture and forms a 70° angle with the column.

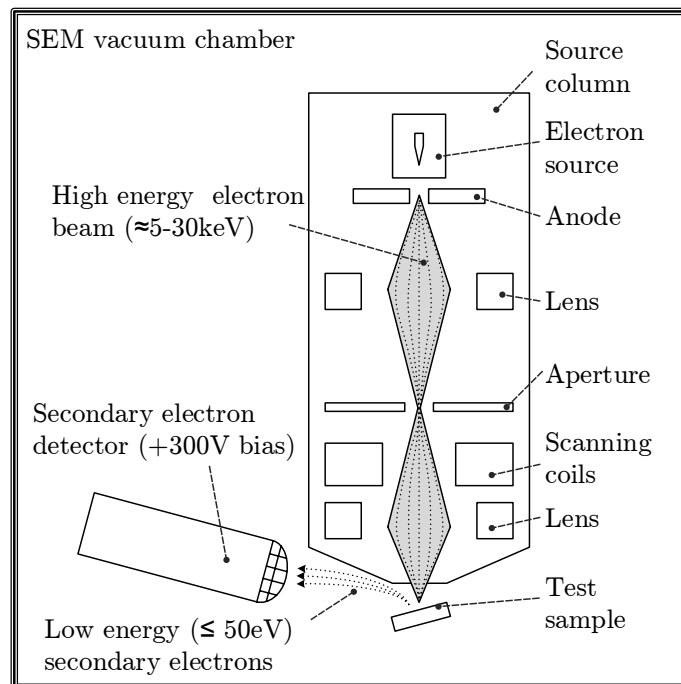
The source column is composed of a series of electrostatic lenses and ion focusing elements, as represented schematically in Figure 5.8c. The electrons are generated by field emission from a tungsten filament and accelerated to high energy, in the range of 1-30 keV (user selectable). When the high energy electrons hit the sample, low energy ($\leq 50\text{eV}$) secondary electrons are generated and can be captured by the detector. In these experiments, the detector was always biased at its maximum value of +300V.



(a) Optical photo of SEM



(b) Interior of SEM showing electron source (top) and secondary electron detector (left, with grid)



(c) Diagram of typical SEM column showing incident electron beam and collected secondary electrons.

Figure 5.8: Optical images and electron column diagram of Scanning Electron Microscope (XL30 ESEM-FEG, from CSEM Neuchâtel) used in this work.

Clearly, a fundamental difficulty of this work was that the high electrical fields present at

and around the capillary emitter tip which would undoubtedly affect the trajectory of the secondary electrons. The electrons emitted with low energy are sandwiched in between the extractor and the emitter, separated by $\approx 100\mu\text{m}$ gap. Thus, it was important in this work to minimize the extraction voltage by reducing the extractor inner diameter and gap. Typically, relatively good image quality could be obtained up to about 1kV and image quality started quickly degrading above this value. Above 2kV, any imaging was extremely difficult.

It was crucial for this work that the assembly would completely protect the SEM, in particular the electron source column, against any contamination of ionic liquid. It was also critical to avoid high voltage short circuits with the SEM chamber which could be highly damaging to the tool.

From an image quality aspect, several conditions had to be considered which could degrade the quality of images that could be obtained. First, with a complex assembly, it was practically inevitable to have a larger working distance than the recommended 10mm, but this distance should nevertheless be minimized. In the experiments presented here, working distances of 16-21mm were achieved. The assembly also had to be very rigid in order to avoid vibrations which would greatly degrade the image. It was also important to take care of charging surfaces, which are common when using insulating spacers.

Furthermore, the liquid transport and containment had to be carefully considered. Unlike with the standard spray experiments, it was decided in this case not to transfer the liquid propellant to the thruster inside the chamber itself, a method required to keep the liquid in vacuum at all time. Filling the reservoir in ambient and transporting the assembly to the SEM thus exposed the ionic liquid to air, so that H_2O absorption could have occurred, leading to outgassing in the chamber. Outgassing is particularly damaging if conductive liquid is expelled from the reservoir, leading to leakage currents or short circuits.

5.2.2 Sample description

Protection of the SEM against ionic liquid contamination was a top priority for this work. Initially, it was planned to conduct the observations with a "top-view" scheme, looking down at the emitter tip at a $30\text{-}45^\circ$ angle, through the extractor and just outside the plume, as shown in Figure 5.9a. Due to the wider than expected beam spread measured with these emitters, it was however not possible to guarantee that contamination would not occur with this configuration. Instead, it was preferred to observe the tip below the extractor, at the much higher angle of $80\text{-}90^\circ$. To achieve this, it was necessary to fabricate specially designed thruster chips, which were included in the v3b mask set. These chips used a single-level extractor, fabricated in a process similar to that described by Krpoun [32] and in previous work [103, 105].

On these chips, the device layer leading to the emitter on two sides was entirely etched. The extractors were also patterned to clear an observation window. The inner diameter of the

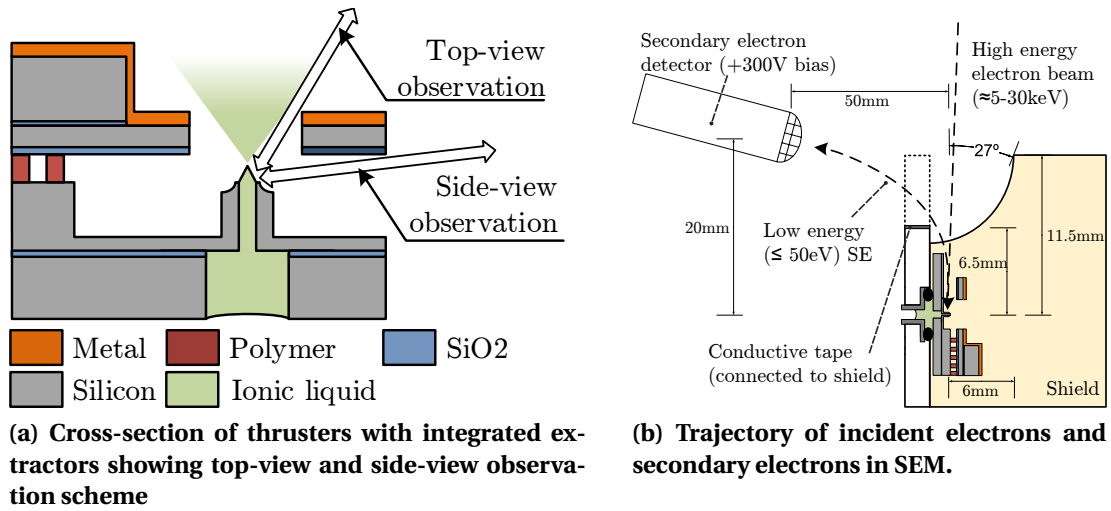


Figure 5.9: Observation schemes and electron trajectories for SEM experiments

extractor was set at $400\mu\text{m}$, enough to permit top-view observation at $\approx 65^\circ$. Using the new wafer-level bonding process, gaps of $\approx 50\mu\text{m}$ could be achieved. Wafer-level bonding became particularly useful in this case, since it was possible to fabricate extractors with a layout that could not have been achieved otherwise. Indeed, the very thin and fine extractor could not have been handled without breaking if diced before bonding to an emitter. The extractors were thin silicon rings (100 or $200\mu\text{m}$ wide, $\approx 30\mu\text{m}$ thick) held on two sides by $1\text{mm} \times 2\text{mm}$ triangular sections of thin silicon. This fine extractor allowed for more viewing angles of the emitter tip and was meant to minimize beam interception, also having less effect on the secondary electrons. Attaching the extractors on only two sides was also compatible with TEM observations, although these were finally not carried out in this work.

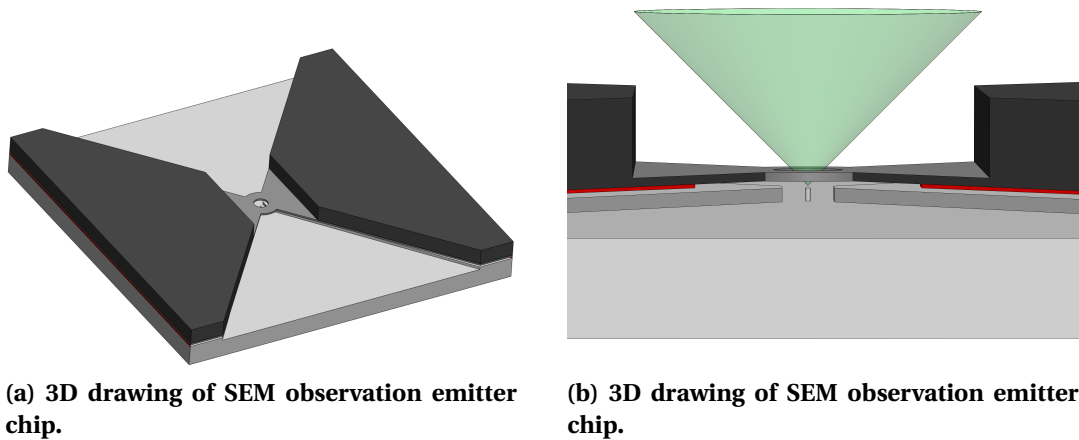


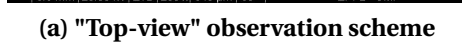
Figure 5.10: Drawings of thruster chip designed for side-view observation

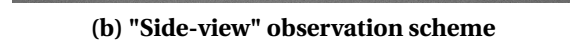
Chapter 5. In-situ electrospray SEM observations

According to the onset simulations, the extractors were expected to require an onset voltage of about 1000V. Figure 5.11 shows SEM and optical images of these chips.

Due to nature of the chip, there is no direct line of sight between the emitted secondary electrons and the detector. Thus while the actual point where the scanned electrons hit the sample can be more or less predicted, it is extremely difficult to determine the exact trajectory of the secondary electrons emitted.

With a limited number of chips available, some devices were also reworked after an initial unsuccessful observation. They were cleaned and re-bonded at die level to an extractor. In this case, however, it was not possible to re-use silicon extractors, which were too fragile when separated from the emitter. Instead, laser-machined molybdenum extractors, $100\mu\text{m}$ thick, were assembled using $100\mu\text{m}$ thick doubled-sided Kapton tape with a Fineplacer die-level bonded. Molybdenum was chosen for its high Young's modulus (329GPa) which allows for the fabrication of thin structures without significant deformation. A thin structure is critical to minimize extractor inner diameters for a given beam half angle. These later extractors had inner diameters of $250\mu\text{m}$, $300\mu\text{m}$ and $350\mu\text{m}$ (Figure 5.12), respectively allowing beam half-angle clearances of 32° , 37° and 41° . Smaller inner diameters were necessary to reduce the onset voltage with the larger emitter-extractor spacing resulting of the Kapton tape thickness. Some beam impingement with these beam clearances was expected.





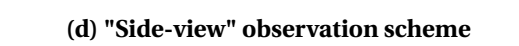


Figure 5.11: SEM and optical images of single



mitter special thruster chips designed and fab

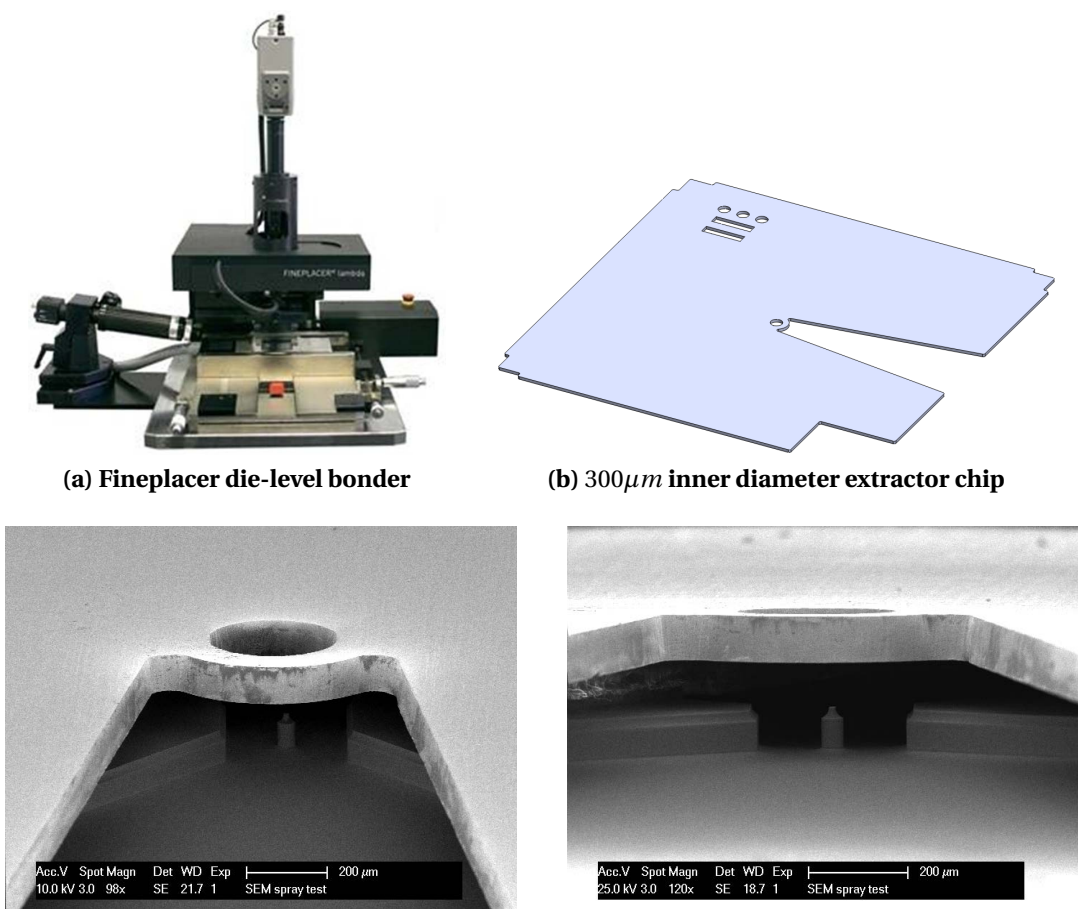


Figure 5.12: SEM micrographs of special thruster chip with bonded molybdenum extractor

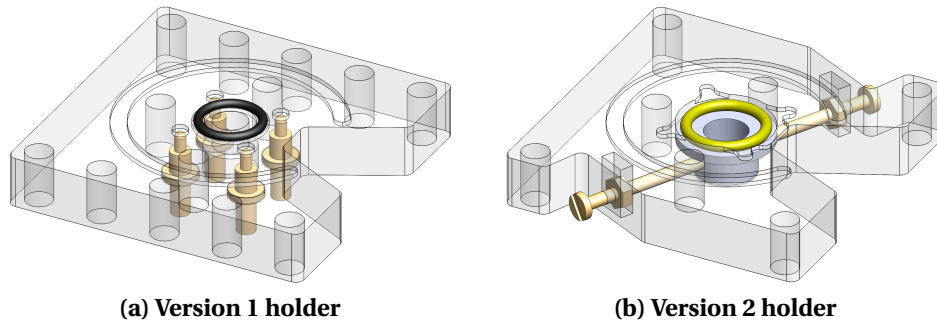


Figure 5.13: Two generations of die sockets for SEM spray experiments. In (a), contact is done directly to the silicon using spring loaded pogo-pins (Mill-Max part 0850-0-15-20-83-14-11). In (b), contact is achieved using a central cylindrical metal section and a conductive o-ring. (Parker Hannifin Corp part 10-00-2777-1215)

5.2.3 Assembly

Continuing to respond to the constraints listed earlier, several iterations of die sockets were fabricated in POM, with the last two versions shown in Figure 5.13. In version 1, four spring loaded pogo-pins (Mill-Max part 0850-0-15-20-83-14-11), of the same type used for standard spray tests were used to contact the silicon chip directly. This however proved to be an unreliable method to apply the emitter potential. Pushing the test sample against these pins, it was also more difficult to avoid liquid spillage from the o-ring. In version two, connection was done through a central cylindrical zinc-plated steel section (a truncated rivet M5 UT/FEF 3, KVT-Fastening part 103041) supporting a conductive Ag/Cu silicone o-ring (Parker Hannifin Corp part 10-00-2777-1215). Two spring-loaded screws clamped the test chip against the o-ring, allowing for easy and reliable assembly. The metal section was accessed from the side of the holder via two M1.5 screws. This assembly proved most reliable to contain liquid and establish the potentials and could be entirely disassembled for cleaning.

For both versions, a custom machined cylindrical tube was used to act as a shield to prevent liquid contamination of the SEM. Figure 5.14 shows 3d images of the test assembly. The shield has a 30° observation window, thus blocking 60° beam half-angle spray. Figure 5.15 shows a diagram and optical images of the test assembly inside the SEM.

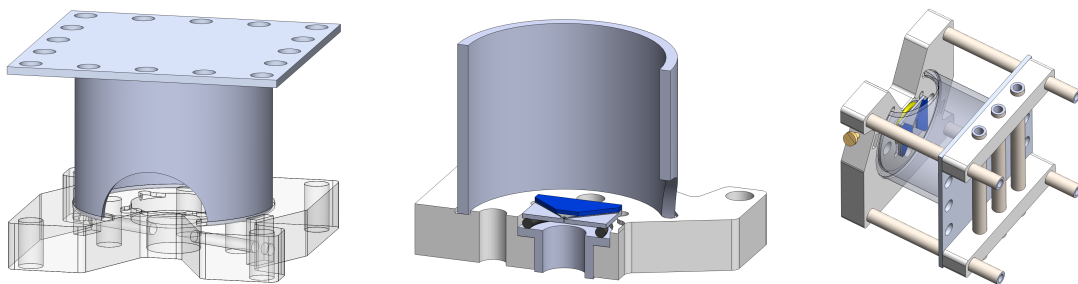


Figure 5.14: 3D CAD images highlighted steel tubing used to protect SEM against electrospray.

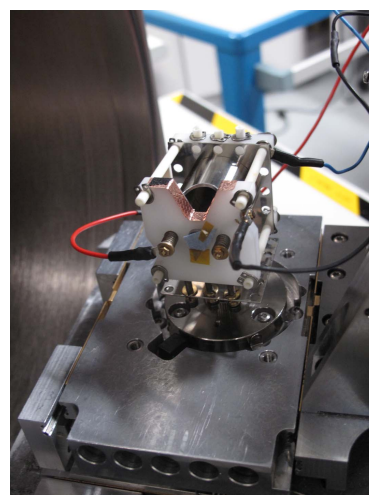
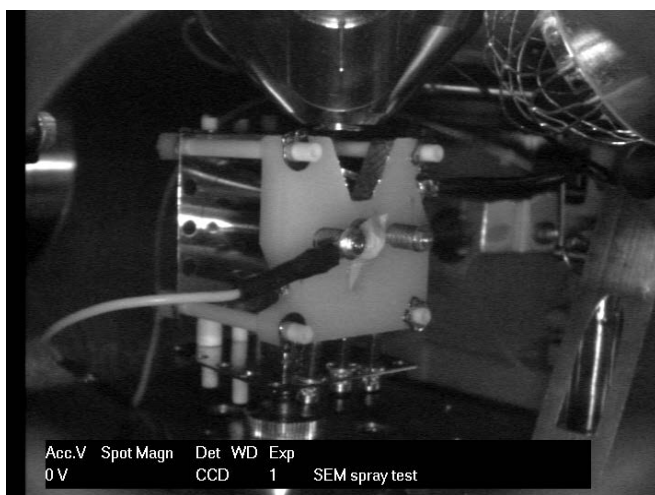
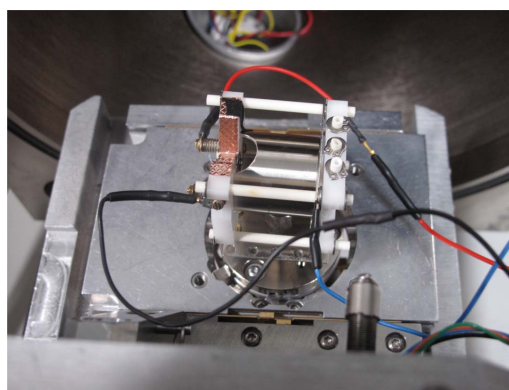
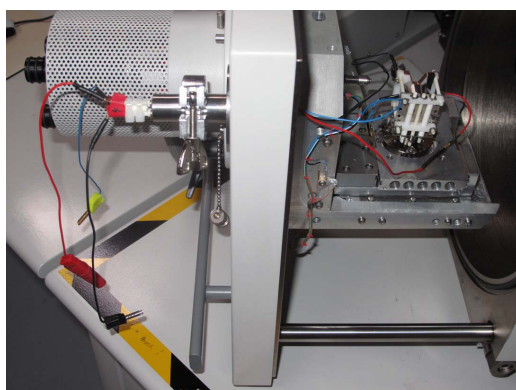
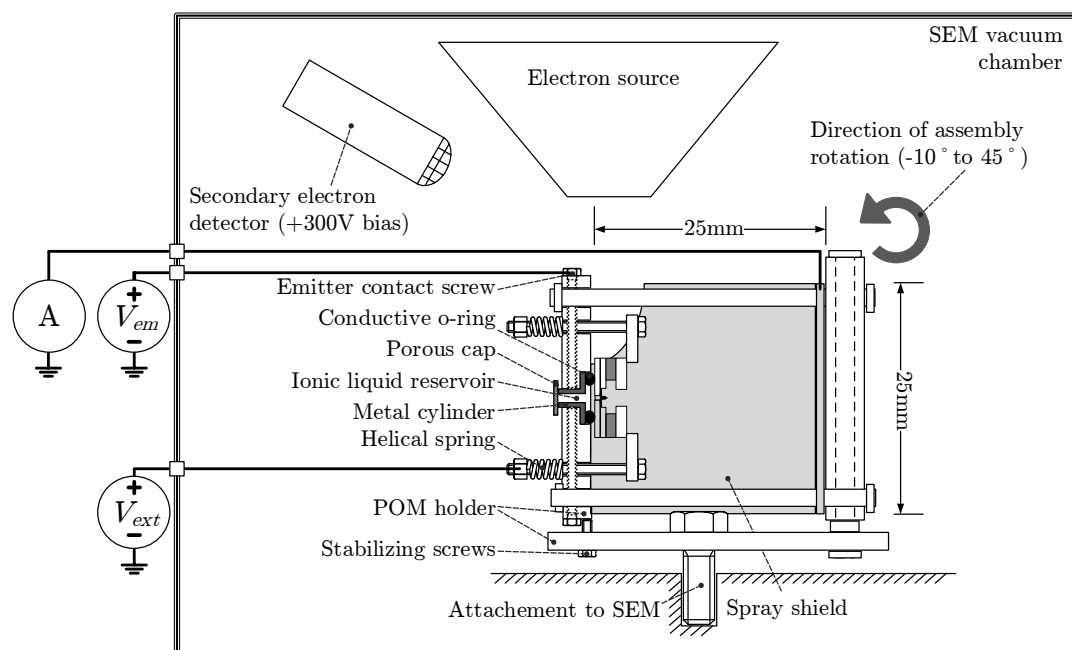


Figure 5.15: Optical images of spray assembly mounted in SEM

A piece of blue wipe was used as porous lid to the liquid reservoir region, allowing air to be evacuated while preventing splashing of the ionic liquid propellant ($EMI - BF_4$) due to outgassing. This splashing, which typically led to leakage currents or short circuits, was observed both for these experiments and in other vacuum chambers when several ml of liquid were present. Even with the porous lid, it was necessary to put very little liquid in order to mitigate this problem.

Three connections, for the emitter, extractor and shield, were fed through using a vacuum KF flange. The shield was connected to a Keithley 2410 sourcemeter, capable of measuring nA scale currents and, if necessary, applying a bias on the shield. The high voltages, connected to either the emitter or the extractor were provided by Stanford Research System PS350/5000V sources. To avoid charging effects, conductive tape, connected to the shield, was used to cover the insulating POM holder in the section between the chip and the trajectory to the secondary electron detector. To reduce vibrations, the assembly was stabilized using three M2 screws, straining the assembly into a rigid position. Both these features can be seen in the images of Figure 5.15.

5.2.4 Voltage application

Choosing the optimal configuration to apply the voltages on the emitter, extractor and shield was not a trivial issue as the image quality varied significantly depending on the configuration. As shown in 5.9b, low energy secondary electrons were required to exit the emitter region and curve around the assembly to make their way to the detector.

While the complex trajectory of the SE could not be fully described, 2D simulations were run to determine which configuration would be best to allow the electrons to at least exit the high field region around the emitter. These simulations considered only passive conditions, studying the electron trajectories in the absence of electrospray but of course with high voltages applied.

In a second step, the most promising configurations were re-evaluated in a full 3D environment, this time to determine how they would affect an actual emitted electrospray.

Secondary electron trajectory simulations

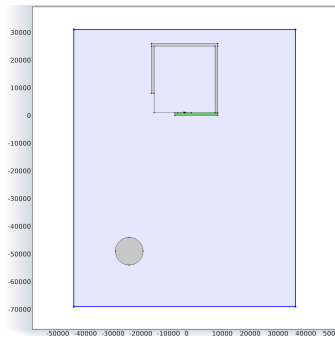
Secondary electron particle tracing simulations were performed in a two dimensional environment representing a cross-section of the chamber interior. Low energy (50eV) electrons were emitted normally to the sidewall of the emitter in the direction of the detector, and their trajectories plotted as they travelled through the high electric fields. It was expected that if they at least escaped this region, they might reach the detector or generate other secondary electrons which would, thus permitting image acquisition. In an actual observation, the rasterizing beam only illuminates a small spot (\approx nm size) at a given time, from which SE are emitted. Thus the simulations shown in this section, in which electrons are simultaneously emitted from the length of the emitter, should rather be considered as a superposition of

sequential emissions. Of course, in reality, numerous electrons are continually emitted from a probed spot.

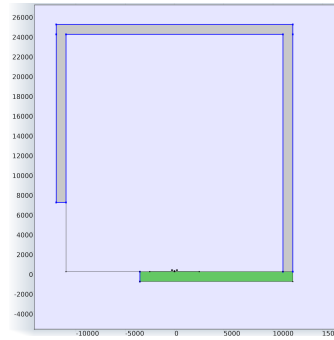
The detector was modeled as a disc and located 5cm from the emission source. The shield was modeled with accurate dimensions, with walls placed 12mm from the emission site and an opening of 6mm height. Ground was applied on the outside wall of the SEM chamber, while different potentials were applied on the shield, emitter and extractor. The emitters were modeled with dimensions corresponding to available v3b devices. The simulations were done using a bonded molybdenum extractor, which was expected to represent a worse case for the observation conditions due to its more bulky structure. Figure 5.16 shows images of the environment, including the boundaries on the model ground (chamber wall), shield and emitter. Figure 5.16 also shows computed electric potential for the specific case where the emitter and shield are grounded and the extractor is kept at a positive high voltage. In all simulated cases, the detector was biased at +300V. These simulations did not include space charge effects or avalanche electron generation.

Several configurations were simulated, as shown in Figure 5.17. In all cases where a high negative potential was applied on the extractor (a, c), it was seen that the emitted particles, repelled by the high negative potential, impacted the emitter. The same occurred when the emitter was biased at a high positive voltage (e). Such a situation was expected to yield highly degraded images, since few, if any, SE would be capable of reaching the detector. More encouraging results were obtained with either the emitter grounded and extractor at high voltage (b, d), or the emitter biased at a high negative potential with the extractor and shield grounded (f). In all cases, though, these simulations showed that emitted low energy particles should not, in the absence of more complex interactions included here, reach the detector, even with the latter highly biased at +300V. In the simulations performed, either the particles were intercepted by the extractor, or were directed away from the shield opening (located on the bottom left of the graphs in Figure 5.17).

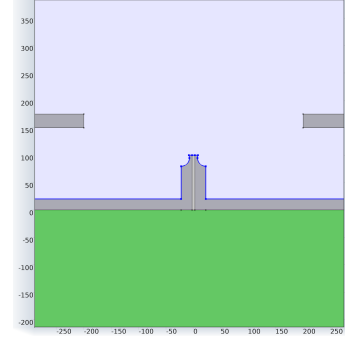
Cases (b) and (d, f) in Figure 5.17 differ fundamentally in one aspect. In the first case, a different potential is applied between the extractor and the shield, resulting in a non-zero electrical field inside the shielded volume. In the other cases, the high electrical field is contained to the volume between the emitter and extractor. Thus the simulations in the next section aim to evaluate the effect of this difference for an emitted spray.



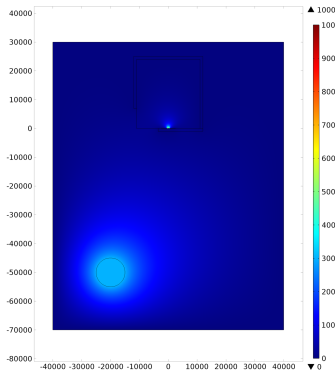
(a) Complete 2d model, with model ground boundaries highlighted in blue.



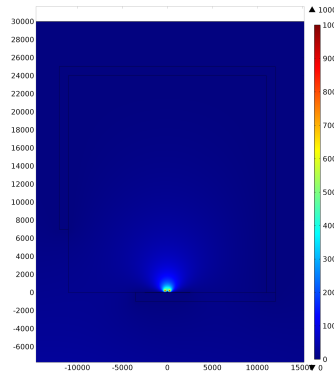
(b) Shield section of 2d model, with shield boundaries highlighted in blue.



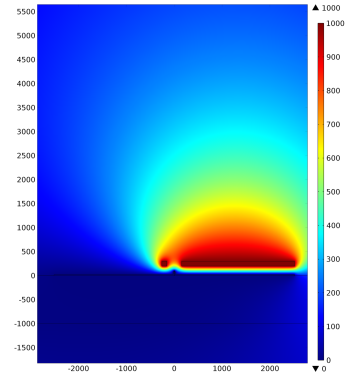
(c) Emitter section of 2d model, with emitter boundaries highlighted in blue.



(d) Complete 2d model showing electric field (surface) and voltages (equipotential lines). (Emitter: 0V, Extractor: 1kV, Shield: 0V, Detector: 300V)

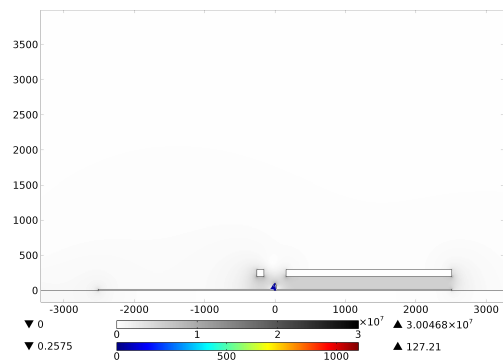


(e) Region around emitter, showing electric field (surface) and voltages (equipotential lines). (Emitter: 0V, Extractor: 1kV, Shield: 0V, Detector: 300V)

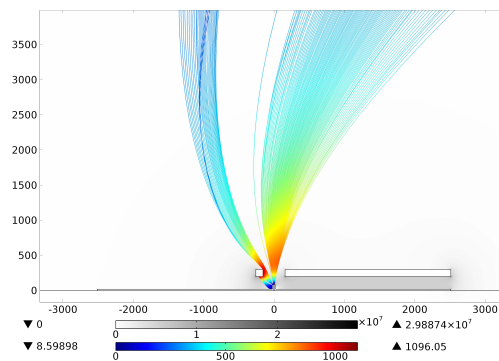


(f) Close-up emitter region, showing electric field (surface) and voltages (equipotential lines). (Emitter: 0V, Extractor: 1kV, Shield: 0V, Detector: 300V)

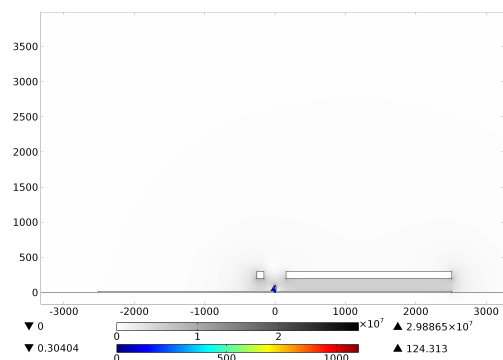
Figure 5.16: 2d environment used to compute low energy (50eV) secondary electron trajectories. (a), (c) and (d) show boundary conditions on the shield and emitter. (b), (d) and (f) show computed potential (V).



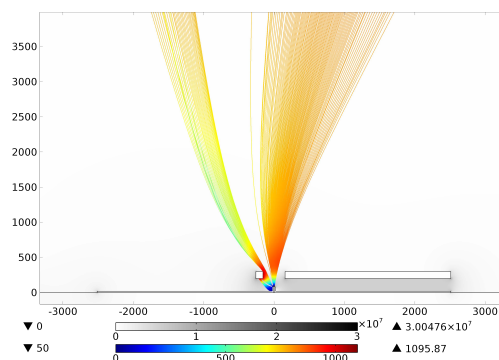
(a) Emitter: 0V, Extractor: -1kV, Shield: -1kV



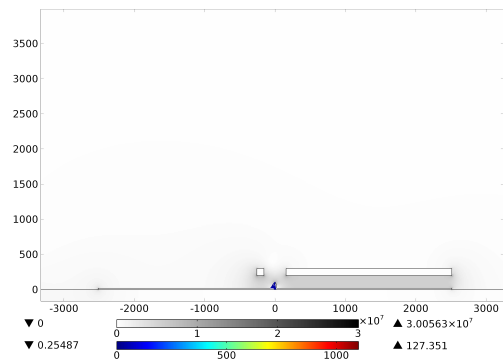
(b) Emitter: 0V, Extractor: 1kV, Shield: 0V



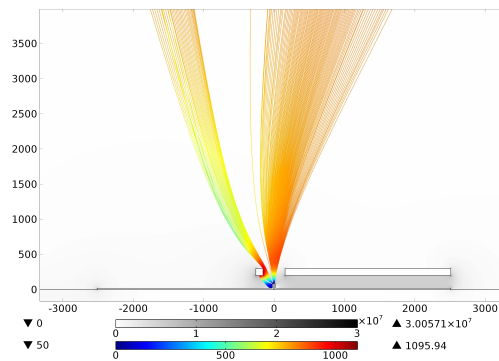
(c) Emitter: 0V, Extractor: -1kV, Shield: 0V



(d) Emitter: 0V, Extractor: 1kV, Shield: 1kV



(e) Emitter: 1kV, Extractor: 0V, Shield: 0V



(f) Emitter: -1kV, Extractor: 0V, Shield: 0V

Figure 5.17: Low energy SE trajectories simulated for several voltage configurations. Surface (grayscale) represents electric field norm (MV/m) and trajectories are colored with particle energy (eV).

Sprayed particle tracing simulations

In this second set of simulations, the objective was to compare the trajectories of particles emitted from the electrospray, in the different configurations. This time a full-3d model of the chamber interior was put in place. The shield and detector were modeled as before, although now in three dimensions. One hundred particles were emitted from a sphere-capped cone (Figure 5.18a). The radius of the capping sphere was $1\mu m$ and the angle of the cone 49.3° , and the particles were emitted from the spherical cap in a uniform distribution. The extractor used was again of the bonded molybdenum type, with an opening on only one side.

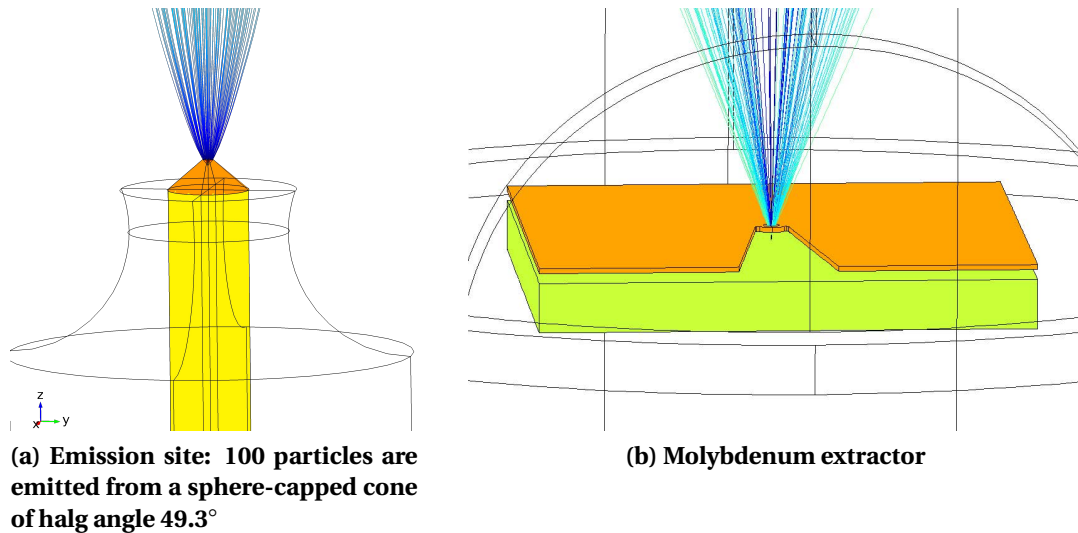


Figure 5.18: Simulated electrostatic environments in SEM with different voltage configurations

Three configurations, corresponding to the more promising identified above, were simulated, as shown in Figure 5.19. The simulations confirmed that if a non-zero field was present inside the shielded volume, particles would be decelerated and re-accelerated towards the emission site within a few microseconds (5.19a). In the simulations performed, no particle could in fact reach the shield and none could escape it. In terms of protecting the SEM tool against contamination, this configuration could be advantageous, although it is possible that the returning spray could directly contributed to degrading the image. In the other cases (5.19c and 5.19e), where negligible field was present inside the shield, this would not occur and the particles continued in a straight trajectory once cleared of the extractor, hitting the shield in $\approx 500ns$.

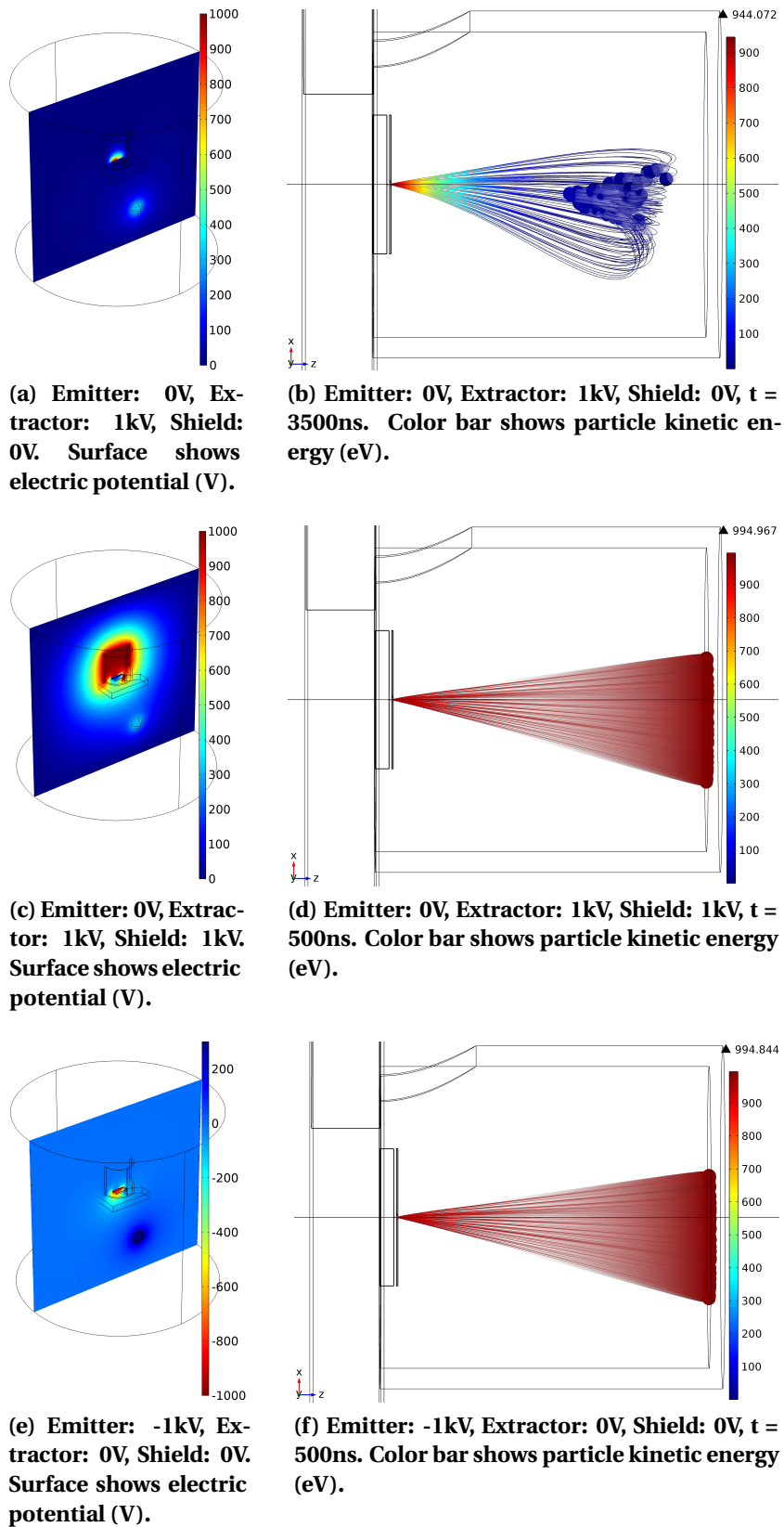


Figure 5.19: Simulated electrostatic environments in SEM with different voltage configurations

Summary

Table 5.1 summarizes the pros and cons of each configuration according to the above simulations. Configurations 1 and 2 are rejected due to the high danger of the shield being at high voltage, given its close proximity to the chamber walls. Configurations 4 and 5 are also not preferred, due to the difficulty for secondary electrons to clear the emitter surface, as shown by the 2d SE simulations. Configurations 3 and 6 remain interesting, although image quality was generally found to be better when observing a grounded emitter (configuration 3). This configuration, on the other hand, was expected to lead to particles returning to the emitter, although it was unclear whether these particles would have any effect on the image quality. Thus, due to the generally better image quality, this configuration was chosen and the observations presented here were conducted with the emitter and shield grounded while the extractor was kept at high voltage.

Table 5.1: Summary of voltage configurations for SEM observations.

	Applied potential			Emitted Polarity	Comment
	Emitter	Extractor	Shield		
1	Ground	+HV	+HV	Neg.	- Danger of damaging SEM tool due to HV proximity.- Possibility of electron emission from Field Emission.
2	Ground	-HV	-HV	Pos.	- Danger of damaging SEM tool due to HV proximity.
3	Ground	+HV	Ground	Neg.	- Possibility of electron emission from Field Emission. - Particles returning to emitter according to 3D electrospray particle tracing simulations. - Potentially better spray containment.
4	Ground	-HV	Ground	Pos.	- Expected lower image quality according to 2d SE particle tracing simulations. - Particles returning to emitter according to 3D electrospray particle tracing simulations. - Potentially better spray containment.
5	+HV	Ground	Ground	Pos.	- Expected lower image quality according to 2d SE particle tracing simulations.
6	-HV	Ground	Ground	Neg.	- Possibility of electron emission from Field Emission.

5.3 Results and analysis

Although a number of experiments were conducted, only two chips led to notable observations, which will be discussed in the next sections.

In the first case, a peculiar liquid bubble deformation was seen. In the second case, spray was achieved, although it was not possible to do any useful observations as soon as spray was initiated.

5.3.1 Liquid deformation

Liquid deformation was seen with a die (C2W4D36) bonded to a silicon extractor. Figure 5.20 shows SEM micrographs of the emitter before test.

After several (10-20) minutes in vacuum, potential was applied on the extractor. With 400V applied, a stable dark bubble appeared at the tip of the emitter, as shown in Figure 5.21. The bubble was stable enough that high resolution images could be taken, but gradually deformed with time. Figure 5.22 shows screen captures of a video recording the evolution of the bubble. Over 20 seconds, and while a constant voltage of 400V was applied to the emitter, the bubble entirely disappeared inside the capillary. It was initially possible to re-create the deformation by applying a higher voltage (490V), although the bubble again eventually disappeared. After this, it was not possible to recover the bubble, even with 1200V applied.

It was surprising that the bubble would stabilize as it did at the outer edge of the emitter tip. Referring to the holding pressure model presented in the appendix (section A.2), it is clear that in the absence of external factors, if sufficient electrical pressure was present to pull the liquid out of the capillary, it would also be sufficient to overcome the second pressure barrier, present at the capillary's outer edge. Figure 5.23 shows the pressure computed inside the liquid for the observed cases, with the emitter geometry and bubble shape observed. Negative pressures of 9.2 kPa and 12.2 kPa are respectively computed, with corresponding radii of curvatures of the

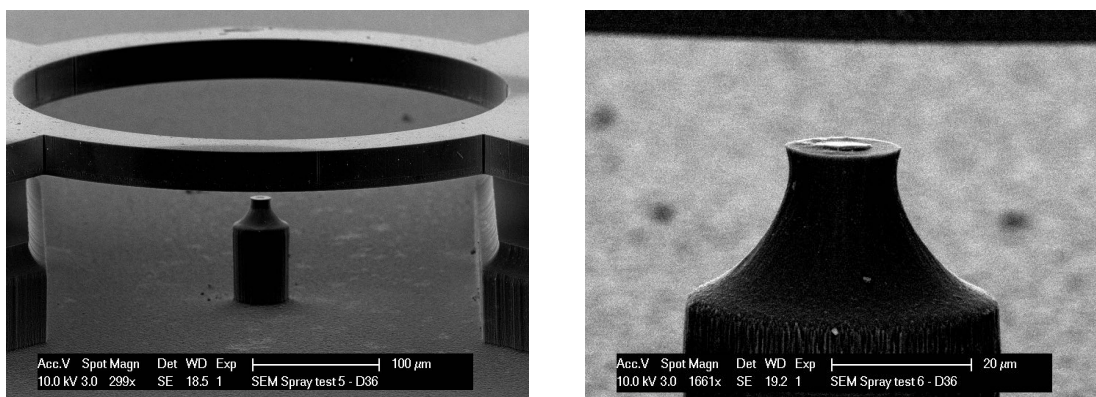


Figure 5.20: Test chip C2W4D36 before test, with liquid clearly visible at the emitter tip.

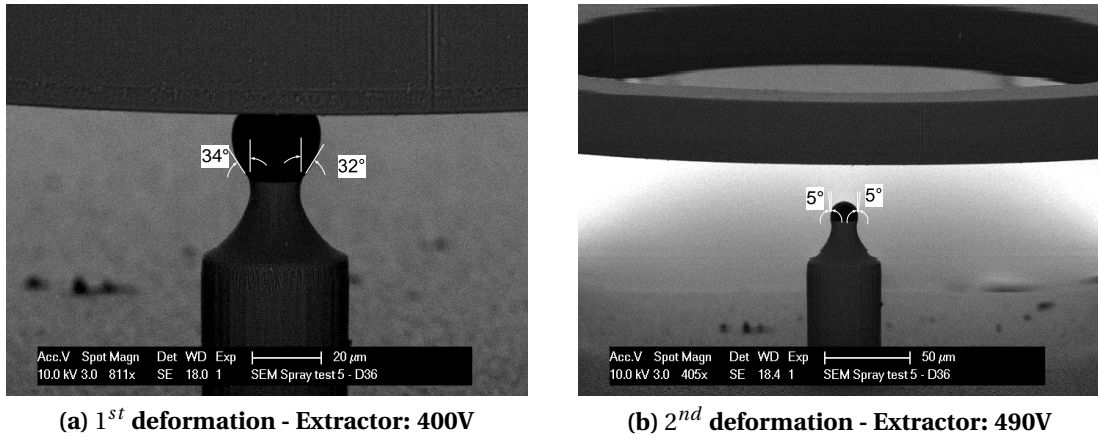


Figure 5.21: SEM micrographs of the emitter with a bubble of the ionic liquid $EMI - BF_4$ seen protruding from the tip. Annotated angles are relative to the vertical and are not compensated for sample tilt.

drops of $8.5\mu m$ and $7.2\mu m$. These internal pressures would respectively be compensated by normal electrical fields of 45.5 MV/m and 52.9 MV/m ($P_{elec} = \frac{\epsilon_0 E_n^2}{2}$).

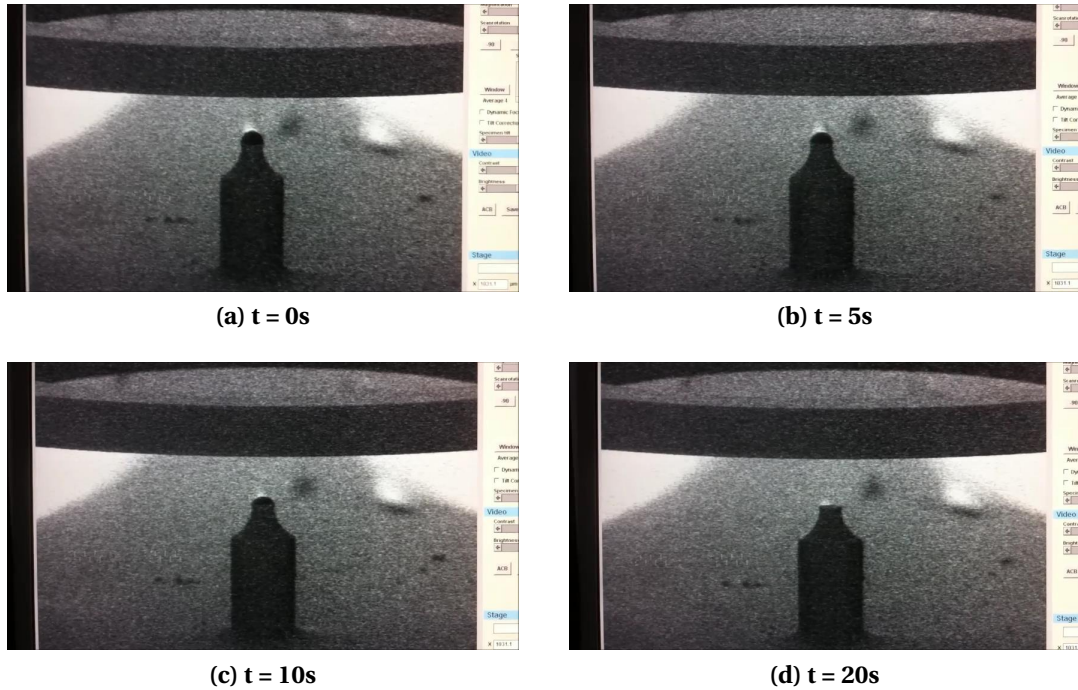


Figure 5.22: Screen captures of video recording showing deformation of ionic liquid "bubble" over time

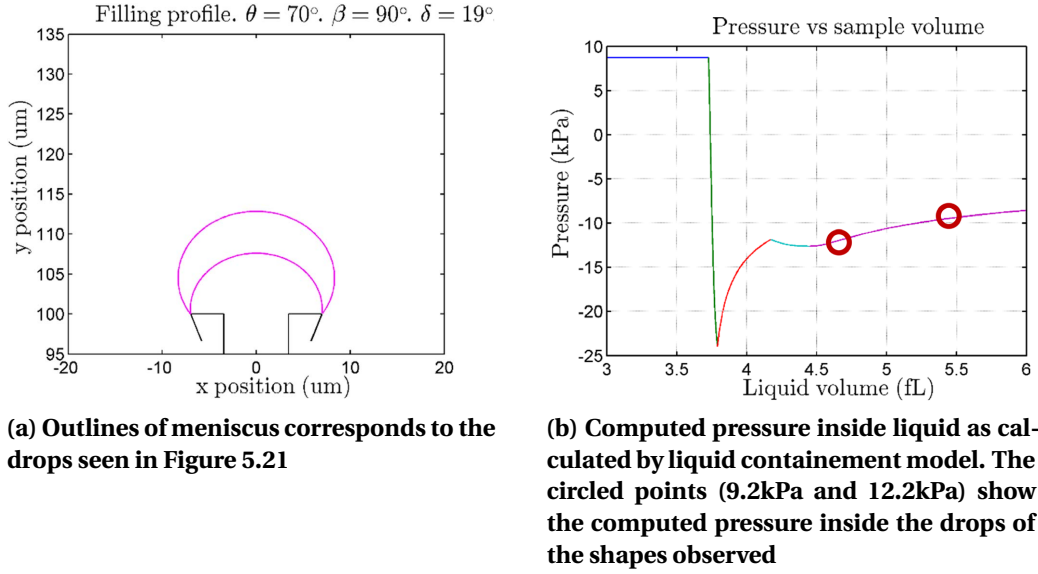


Figure 5.23: Pressure model corresponding to observed liquid deformations. $\beta = 90^\circ$ and $\delta \approx 19^\circ$, extractor ID = $400\mu m$, extractor gap = $50\mu m$. The liquid transport and containmentment model is presented in detail in the appendix, section A.2.

The COMSOL electrostatic environment used for the onset voltage simulations was used to simulate the voltage that would be required to generate such fields with the specific geometries observed. Plots of the geometries and electric field norms are shown in Figure 5.24. The simulations suggested that respectively 784V and 861V would be required to stabilize the liquid bubbles in the configurations observed. Thus the electric pressure present at 400-500V, while in the right order of magnitude to contribute significantly to the shape and stability of the droplet, would not be sufficient to hold the drop against its surface tension.

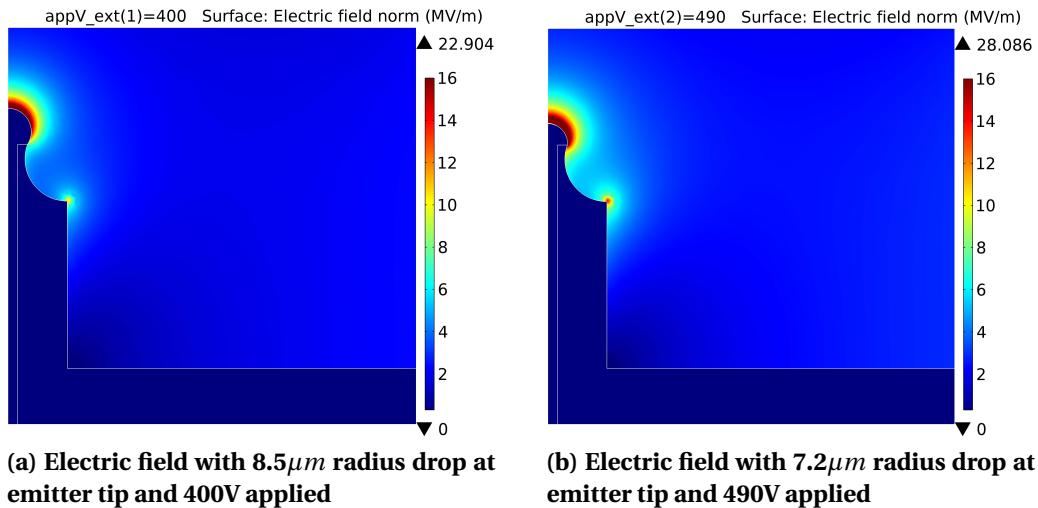


Figure 5.24: Electric field norm simulations corresponding to observed liquid deformations. $\beta = 90^\circ$ and $\delta \approx 19^\circ$, extractor ID = $400\mu m$, extractor gap = $50\mu m$.

Clearly, some factors invisible during the experiment and not considered in the simulation had an effect on the drop formation. This external contribution initially helped push the liquid out of the capillary and faded over time. It is possible that gas outgassing from the liquid could have had such a contribution, as shown in Figure 5.25. This simple diagram shows how, for the case of Figure 5.21a with 400V applied, the formation of a bubble which could have generated 6.9 kPa would explain the deformation. This hypothesis is also supported by the frequent observations of outgassing when subjecting this liquid (*EMI – BF₄*) to vacuum and the unstable nature of the observation.

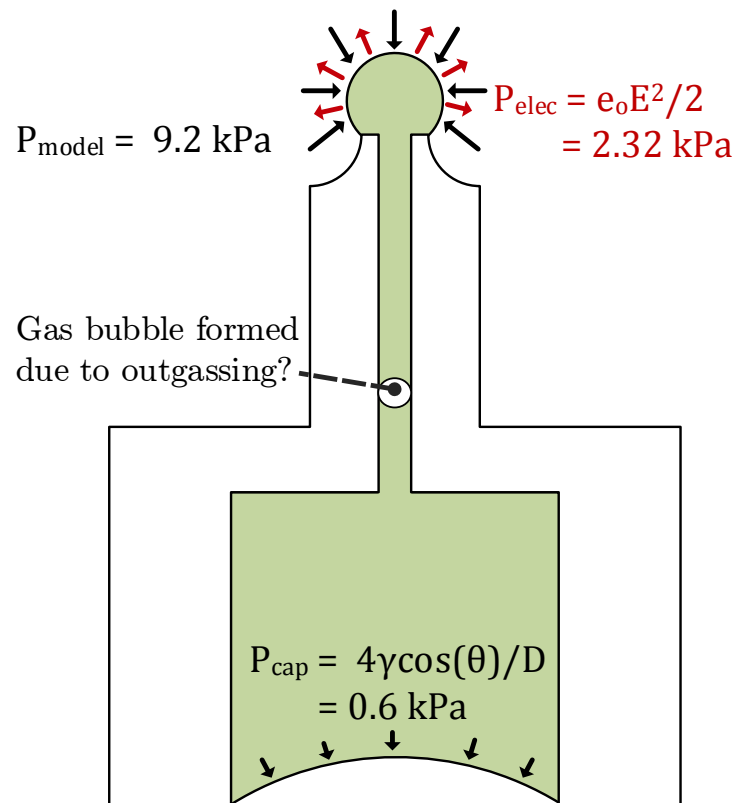


Figure 5.25: Diagram showing how an hypothetical bubble, generated from liquid outgassing in vacuum, could have formed to apply a pressure on the liquid column, pushing it out of the capillary. According to modeling and simulations, the pressure generated by this bubble would have been in the order of 6.9 kPa

5.3.2 Successful emission

It was finally possible to achieve emission using a die (C2W4D24, Figure 5.26) which had been cleaned and re-bonded after an initial unsuccessful spray attempt. Figure 5.26 shows the emitter before test, with the liquid clearly visible at the tip. A result of die-level bonding with Kapton tape, the emitter is misaligned laterally by $\approx 25\mu m$. Again in this experiment, the extractor was kept at positive high voltage while the emitter was grounded, so that emission of negatively charged particles was expected. The acceleration voltage of probing electrons generally set to the very high value of 25kV, for best image quality. Contrast and brightness, focusing and astigmatism as well as sample tilt had to be adjusted for each extraction voltage applied. A subset of the micrographs taken is shown in Figure 5.27.

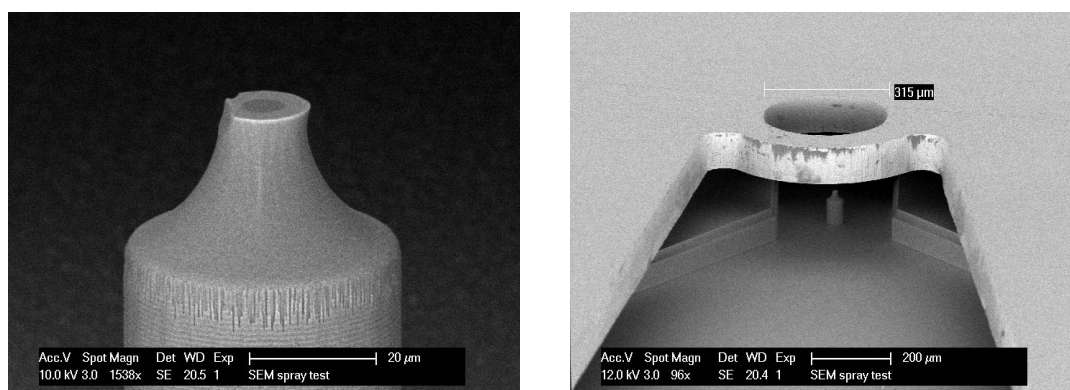


Figure 5.26: Sample C2W4D24 before test

Emission started on the first sweep at 1500V, and could be turned off and on by reducing and increasing the extraction voltage. Near onset, current collected by the shield was measured at -10 to -30 nA, an order of magnitude lower than the expected range. The spray could be sustained for a total time of ≈ 20 minutes. Most problematic was that as soon as emission started, no observation of the emitter tip was possible due to the screen become entirely white. Figure 5.27 shows three voltage sweeps, indicating the quality of images which could be obtained at this high voltage. As is seen in the images, the screen becomes saturated (or unsaturated) as the voltage is increased and spray initiates. This effect is more easily seen in Figure 5.28, which shows screen captures of a video recording of the experiment. Up to about -250nA of current could be measured at higher voltage (1700V). After a few minutes of spraying, current degraded to 0, as seen in Figure 5.29 and could not be re-established. It is likely that at this point, the small amount of propellant which had been placed in the reservoir was depleted. The reservoir on the backside of the chip could hold approximately 2360 pL of liquid. Assuming that 100% of the liquid was sprayed, and using the density of $EMI - BF_4$ (1.29 kg/m^3), a flow rate of $2.27E - 12 \text{ kg/s}$ can be calculated. Using an estimated average current of 100nA, this flow rate would be consistent with a 0.50/0.46/0.04 mix of $BF_4^- / [EMI - BF_4]BF_4^-$ droplets, where the droplets are 200x heavier than the monomers. This is a very coarse approximation, but generally corresponds well to time-of-flight observations, reinforcing the hypothesis that

propellant depletion occurred.

Unfortunately, it was not possible to re-initiate spray even after the die had been removed from the SEM and "refueled". In this second attempt, the chip was brought to -1700V (applied on the extractor) and no evidence of emission could be seen. Electrical breakdown occurred at -1700V and no further test could be carried out with this device.

Figure 5.30 shows optical and SEM micrographs of the thruster and assembly after test. The optical images show evidence of electrochemical degradation of the o-ring, with some remaining ionic liquid having taken a yellow-green color. Earlier tests, where the o-rings had been left soaking in ionic liquid for several days (without voltage applied), had shown no apparent degradation.

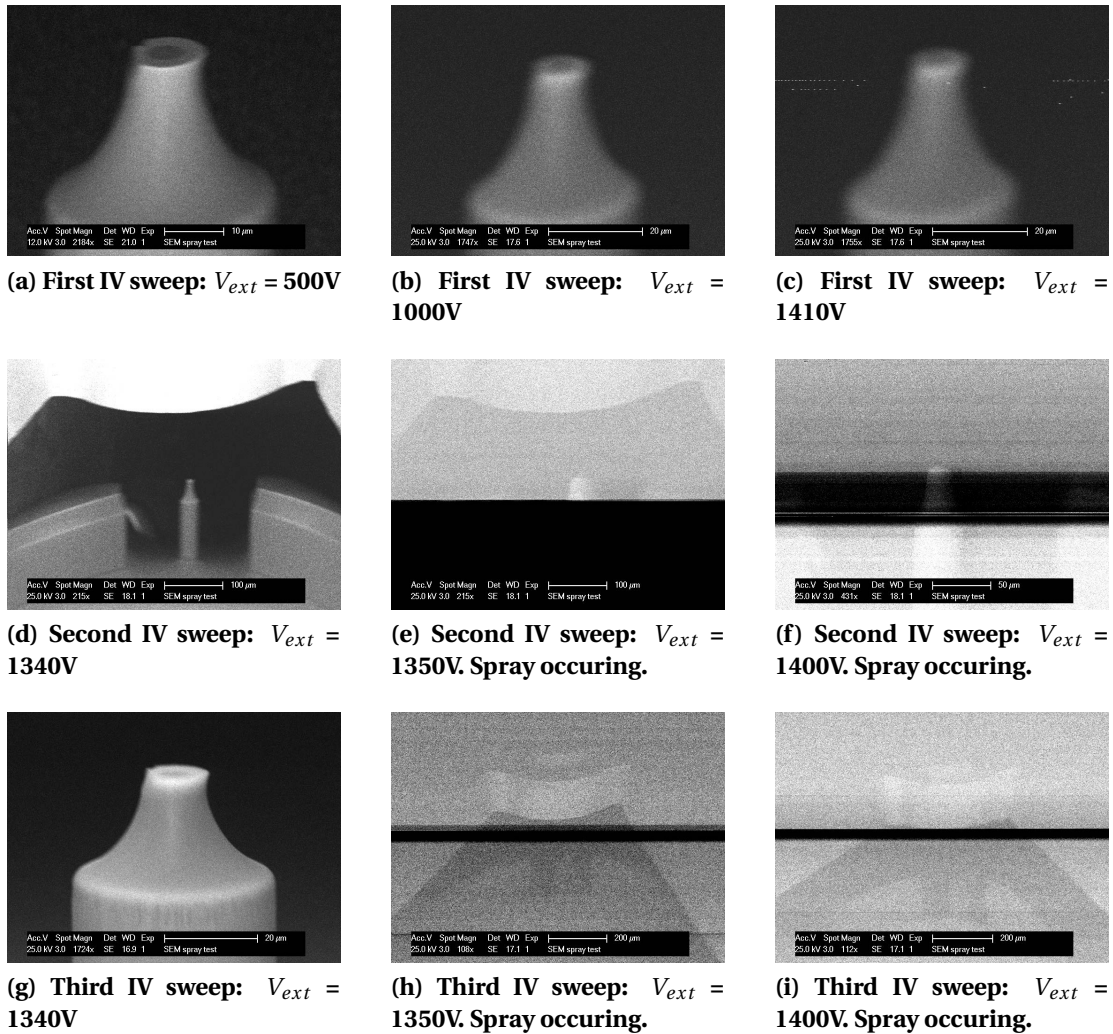


Figure 5.27: Three sequential IV sweeps of the first spray attempt and an IV sweep of the second spray attempt of re-worked chip C2W4D24. The second attempt was carried out three days after the first, following "re-fuelling".



(a) Emitter = 0V, Extractor = 1200V, Shield = 0V



(b) Emitter = 0V, Extractor = 1300V, Shield = 0V



(c) Emitter = 0V, Extractor = 1400V, Shield = 0V

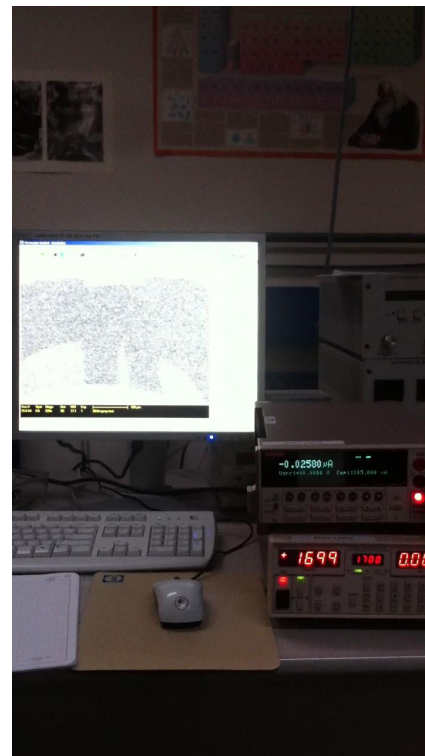


(d) Emitter = 0V, Extractor = 1500V, Shield = 0V

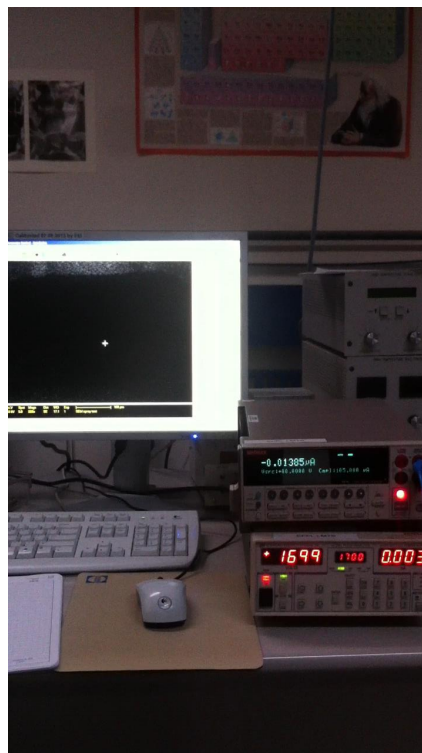
Figure 5.28: Screenshots of first video capture with increasing extractor voltage



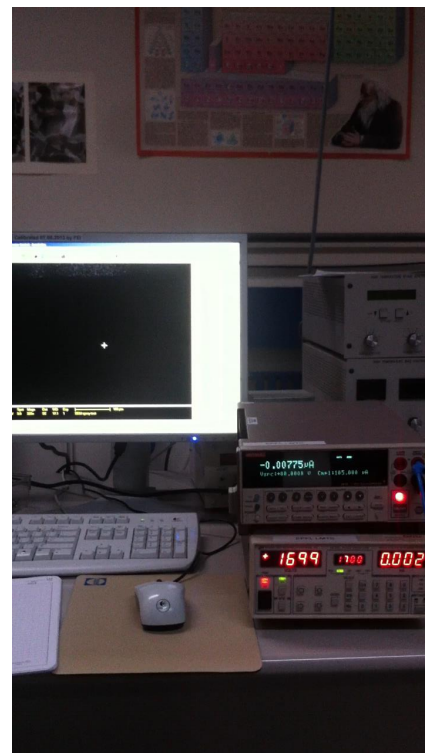
(a) Extractor = 1700V, $t = 0s$



(b) Extractor = 1700V, $t = 30s$

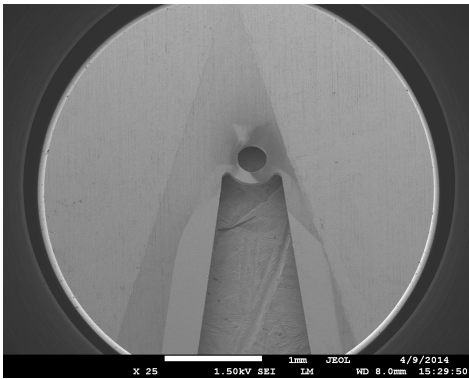


(c) Extractor = 1700V, $t = 35s$

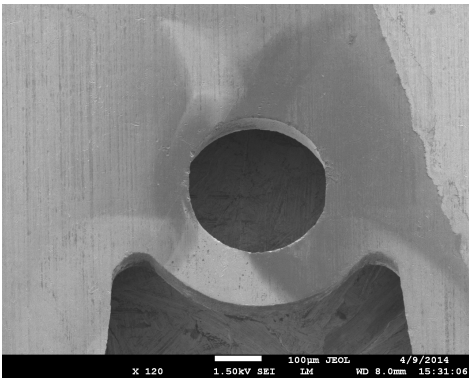


(d) Extractor = 1700V, $t = 45s$

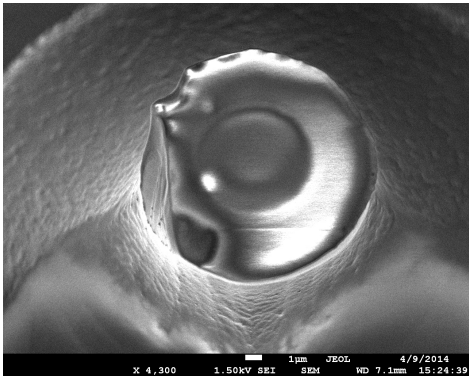
Figure 5.29: Screenshots of second video capture with constant extractor voltage of 1700V



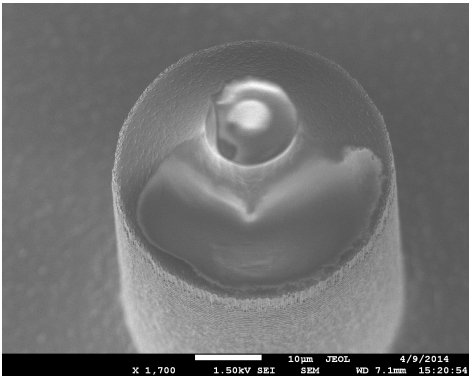
(a) Bottom of extractor



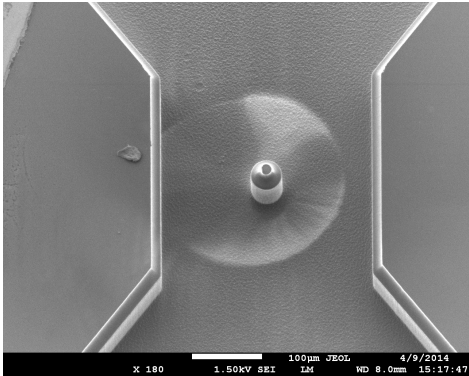
(b) Bottom of extractor



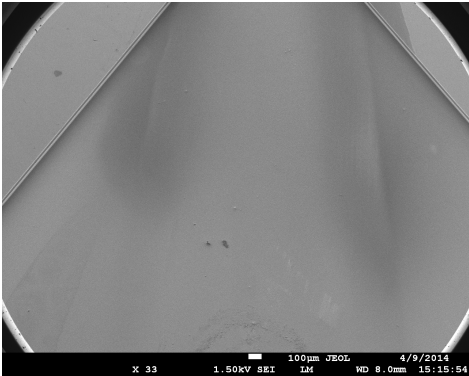
(c) Emitter tip



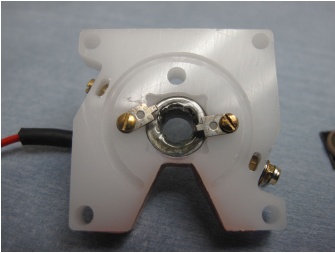
(d) Emitter tip



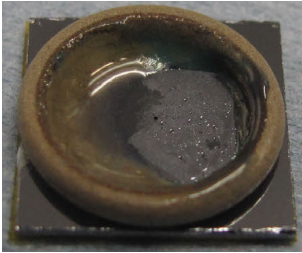
(e) Topside of emitter



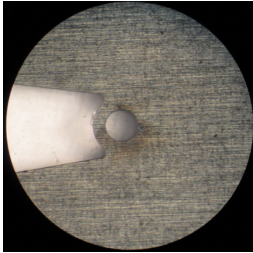
(f) Topside of emitter



(g) Frontside of test assembly



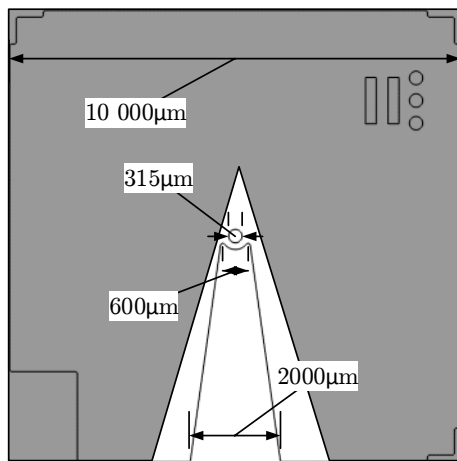
(h) Backside of chip



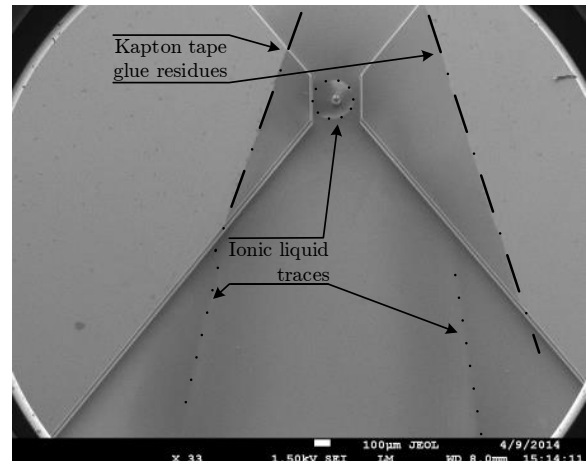
(i) Bottom of extractor

Figure 5.30: SEM and optical images of thruster chip and assembly after test

The SEM micrographs of Figure 5.30, taken after disassembly, are particularly interesting in that they show traces on the bottom of the extractor electrode and on the top surface of the emitter. Two triangular patterns are seen on the emitter surface (Figure 5.31). The first, well defined and absent from the bottom of the etched areas of the emitter chip correspond to glue residues from the Kapton tape used for bonding. The second set of patterns corresponds to the shape of the molybdenum extractor, even lining up with the actual alignment of the extractor as seen in Figure 5.26. These traces are consistent with a re-attraction of the sprayed liquid after emission, a situation predicted by the particle tracing simulations.



(a) Diagram of extractor with highlighted Kapton tape bonding region.



(b) SEM image of emitter showing glue and liquid traces on emitter tip.

Figure 5.31: Diagram and SEM image showing Kapton glue and spray residues visible on top surface of emitter after spray.

Yet the collected current measurements, taken on the shield itself, confirmed that many emitted charged particles did indeed reach it, in contradiction with the simulations performed. This discrepancy could be due to space charge effects, which were not considered in the COMSOL simulation and could force the particles towards the shield. The low current value, in the order of 10-30 nA close to onset is also consistent with only a small fraction of the emitted spray actually impacting the shield. At least according to the earlier simulations, it does not appear that charged particles could have escaped the shielded area and reached the detector, creating the saturation experienced. Nevertheless, it may be that the returning particle could have contributed to the bad image quality. The high voltage observations require very precise setting of the observation conditions with very high gain settings. The secondary electrons necessary for imaging do not, with the high voltages applied follow direct line of sight and follow bent trajectories to reach the detector. Small changes to the electrostatic environment resulting from the returning spray will certainly change the secondary electron trajectories, completely changing the detected signal and explaining the white and black screens.

It is unclear if conf. 6 in Table 5.1 would have led to better imaging during operation. This configuration could finally not be tested due to a lack of available test samples and time.

5.4 Summary

In this chapter, exploratory work towards in-situ observations of an electrospray inside a Scanning Electron Microscope was presented. Several constraints and lessons learned were listed which should be taken into account in order to complete these observations. In summary:

- Electric fields in the secondary electron path should be minimized, namely by reducing the operation voltage.
- High acceleration voltages for the probing electrons yield higher quality images when high extractor-emitter potentials are applied.
- H_2O absorption by the ionic liquid should be minimized, either by using very small amounts of liquid or re-fueling inside the SEM chamber
- Electrical contact application should be very reliable. Spring-loaded pins connected directly to the silicon were not ideal.
- Charging surfaces, especially in the secondary electron path should be minimized
- Care must be taken to have a very rigid assembly, as vibrations in the SEM will quickly degrade image quality
- For better image quality, working distances $\leq 20mm$ should be targeted.
- Care must be taken to avoid propellant from the reservoir. Metal cylinders, on which the o-ring and chip could rest are an ideal configuration.
- Not only the potential difference, but the specific way the high voltages are applied is critical, as it will affect the emitted particle trajectories after emission. The shield and extractor should be kept at the same potential to avoid particle deceleration.

After a number of experiments and iterations of the setup spanning over three years, it was eventually possible to generate a spray of particles in-situ. It seemed, however, that the presence of the spray itself was extremely detrimental to the imaging quality, such that no useful observation of an active Taylor cone could be made.

Some recommendations were made that should be considered if future measurements of this type were attempted. It is clear, however, that this observation scheme will in all cases be very difficult with the high electrostatic fields necessary for emission. Even without spray, the image quality was highly degraded, with micro sized features difficult to image. Hence, even if a cone could be observed in the SEM, it is uncertain whether the observation would be sufficiently precise to yield useful insight into the cone formation beyond what was already obtained.

6 Conclusion

The growing interest in small spacecraft to conduct technology demonstrations and scientific missions heralds a new era in space exploration. Yet such progress is held back by the absence of a miniature propulsion system capable of providing the high velocity changes required to complete orbital manoeuvres.

The work presented here is aimed at providing such a system, proposing a microfabricated electrospray thruster array operating in the Purely Ionic Regime. The thrusters described are some of the world's most advanced, pushing the limits of device integration with a two-level electrode stack assembled at wafer-level. The addition of a second electrode level, the world's first for this type of devices, was a particularly significant step for this technology. In addition to the improved performance, it enabled several new features critical to the usability of the system in real missions.

The achievements of this work can be split in four categories: silicon micro-thrusters development, in-situ SEM observations, propellant transport and containment, and polymer-based electrospray source for mass spectrometry. The last two elements are not presented in the bulk of the thesis, but rather serve as supporting documentation in the appendix. Nevertheless, it is useful to summarize their content here.

MicroThrust silicon thrusters

The central part of this work focused on the design, fabrication and test of a new generation of silicon electrospray thrusters, to be integrated in the MicroThrust (EU FP7 project) breadboard. They were the first electrospray thrusters with integrated accelerator and extractor electrodes, giving them a significant advantage in terms of capabilities (tunable power consumption, Thrust and I_{sp}) and performance (higher efficiency, beam focusing, higher thrust and I_{sp}).

A detailed design of the thrusters was presented, with careful modelling of the emitter's fluidic impedance, operating voltage and ion optics. Two versions of thrusters were presented, the first (v3a) with emitter densities up to 257 emitters/ cm^2 and the second (v3b), more aggressive,

Chapter 6. Conclusion

with 1527 emitters/cm².

These thrusters were fabricated following a new process, evolved from previous devices fabricated at LMTS. The new process, simpler and more reliable, allowed the fabrication of the smallest emitters to date, with inner diameters down to $6.9\mu\text{m}$ for $100\mu\text{m}$ deep capillaries and $5.7\mu\text{m}$ for $50\mu\text{m}$ deep capillaries. In both case the nonuniformity in fluidic impedance was estimated at less than 2%, orders of magnitude better than what was previously achieved. This process also introduced wafer-level bonding of the two-level electrode stack using laminated thin film. This method allowed high electrical insulation, proved more reliable than die-level bonding techniques and led to excellent alignments.

The MicroThrust compatible breadboard devices were tested by project partner QMUL and showed upwards of 90% ionic content with passive feeding, a record for this type of devices. Nevertheless, the small ionic content severely degraded the efficiency of the device, leading to specific impulses well below their required value. Characterization validated the basic concepts of the accelerator electrode, showing that the accelerators did not affect the emission process but successfully improved the performance of the thruster by focusing the beam and increasing the energy of the particles.

In-situ SEM observations

In-situ Scanning Electron Microscope (SEM) observations were conducted in an attempt to acquire better understanding of the formation and stability of the electrospray in the context of internally fed capillaries operating close to the Purely Ionic Regime. Detailed simulations of particle trajectories under high electric fields were presented, allowing a better understanding of the imaging mechanics and supporting the selection of the observation conditions. A number of difficulties related to this challenging setup were overcome to eventually create inside the SEM a stable spray for 20 minutes. Imaging of the Taylor cone, the structure formed at the tip of the emitter where atomization occurs, could not be achieved, most probably due to an interaction between the spray and the electrons used for imaging. However, a much better understanding of the spray and imaging mechanics was obtained and several lessons learned were listed.

Propellant transport and containment (Appendix A)

Several aspects of liquid transport were studied. First, an extensive characterization of the contact angle of two candidate propellants, $\text{EMI}-\text{BF}_4$ and $\text{EMI}-\text{Tf}_2\text{N}$, on several substrates was presented. The capacity of the internally fed emitters to pull liquid to their emission sites was modelled, as well as their ability to safely contain the liquid. With the dimensions typical to this work, the model showed that close to $30g_0$ of static acceleration could be supported before liquid spillage occurred, an important feature if the emitters were filled before spacecraft launch. Dynamic launch conditions were also studied, in particular in terms

of sinusoidal vibrations and shocks. The emitters were seen to be mechanically robust, with no damage observed in any case. Liquid was generally well contained, and a single drop was seen following a shock-test, although it was most likely not due to the shock itself.

Novel insulating chips for mass spectrometry (Appendix B)

Adapting the electrode process developed for the silicon micro-thruster devices, two novel designs of emitters were presented. Fabricated in glass and polymers, these devices were adapted to the requirements of Electro-Spray Ioniser (ESI) sources for Mass Spectrometry (MS). Although both were operated and could generate sprays using the ionic liquid $EMI - BF_4$, they suffered from severe liquid containment issues, preventing operation for more than a few minutes.

6.1 Future work

Microfabricated silicon thrusters

Naturally, the next step with regards to the microfabricated silicon devices will be the characterization of the v3b chips, which could not be completed within this work. First, the spray composition of the devices should be compared with the v3a chips. The v3b chips have smaller emitter inner diameters and are expected to operate closer to the PIR than the v3a chips. Secondly, validating the concept of "grouped accelerators", applied with the v3b design, would be groundbreaking for the technology. This grouping allows for much higher packing density of emitters, potentially moving the devices from marginally acceptable to well within the required specifications.

Next, the feeding system could be integrated with the chip. A porous reservoir, which would passively set a fixed negative backpressure holding the propellant, may be attractive to feed the liquid to the backside of the chip. This method could prove useful to prevent liquid overflow from the emitter tips. The controlled deposition of anti-wetting coating should also be investigated further.

In-situ SEM observations

It seems unlikely at this point that further SEM observations would yield sufficiently high quality images to yield useful insight regarding the Taylor cone shape and formation, beyond what can be obtained with an optical camera.

A researcher interested nonetheless should choose a configuration where the electrostatic environment away from the emission region is kept neutral to the extent possible. Thus a grounded extractor and shield seem inevitable. Setting the emitter to a high negative value may yield better results, since electrons would more easily escape the silicon emitter itself.

More simulations of the basic mechanisms of secondary electron generation and transport in high voltage conditions should be conducted. Preliminary simulations showed that it *should not* be possible to image the emitter at all once high voltage was applied, which is clearly not the case. More complex mechanisms (space charge, remote secondary electron generation) could be present which would allow an image to be captured. In themselves, such mechanisms could lead to relevant scientific breakthroughs and should be included in the simulation environment until the observed results can be reproduced.

Before continuing in-situ spray observations, it is recommended to first complete more fundamental experiments reproducing the electron transport. Test structures with features sandwiched between two parallel plates would be good vehicles to understand the trajectories of secondary electrons in high electric fields. These features could eventually include very sharp tips, thus observing solid features with extreme localized electric field.

Insulating ESI sources

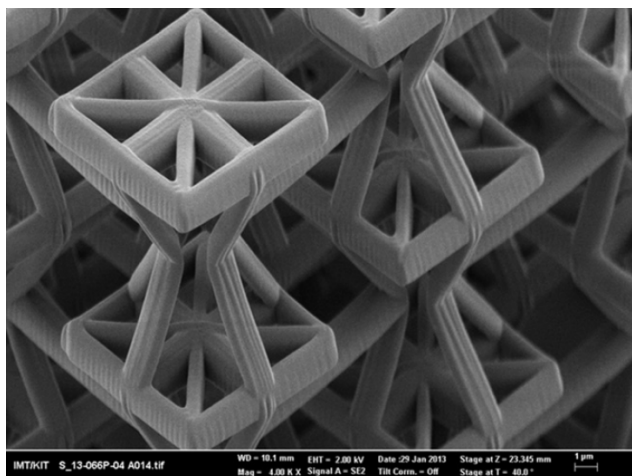
The devices shown in this work suffered from unacceptable wetting problems. Moving forward with the insulating ESI sources, the design should be improved to increase liquid containment. A first step would be an adjustment of the emitter design to include an exterior definition (as opposed to a holey-plate structure). Yet this would only mitigate the wetting problem and may still be insufficient.

A more promising alternative would be to use micro 3D printing to replace at least the emitter layer to create the insulating ESI sources. Using the micro-sandblasted glass wafer could still be used as a supporting structure for the printed emitters. Several avenues are possible, fabricating the emitters directly in polymers or glass. The NanoScribe¹ and FEMTOprint² systems are both recently released tools that could be used to complete the 3D prints. Figure 6.1 (a) and (b) show complex polymer structure that were fabricated with these tools. 3D printing would enable the design of complex emitters impossible to fabricate otherwise. An example of such design is shown in Figure 6.1 (c) and (d), which shows an hybrid internally fed - externally wetted tip. It may be also possible to include an extractor structure directly, fabricating the emitter/electrode stack in a monolithic bloc, with metal electrodes deposited in a final step.

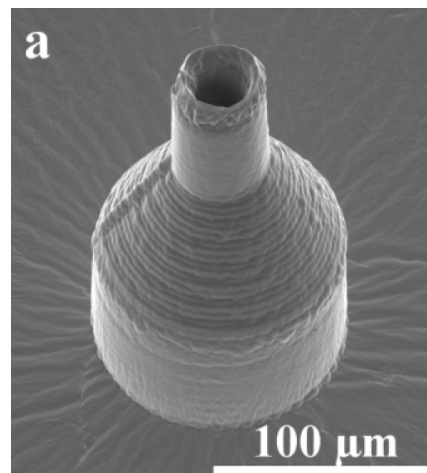
Although its potentially slow writing time should be monitored, 3D printing should be carefully investigated, as it almost certainly will be by other research groups over the coming years.

¹www.nanoscribe.de

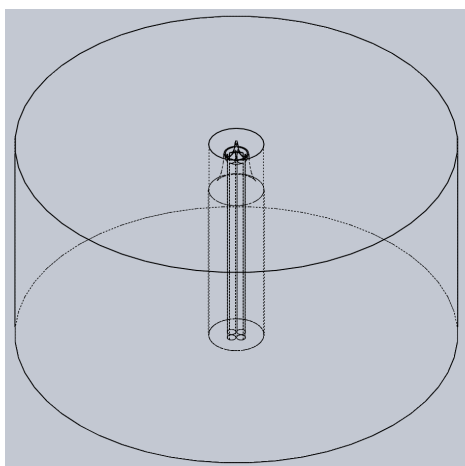
²www.femtoprint.ch



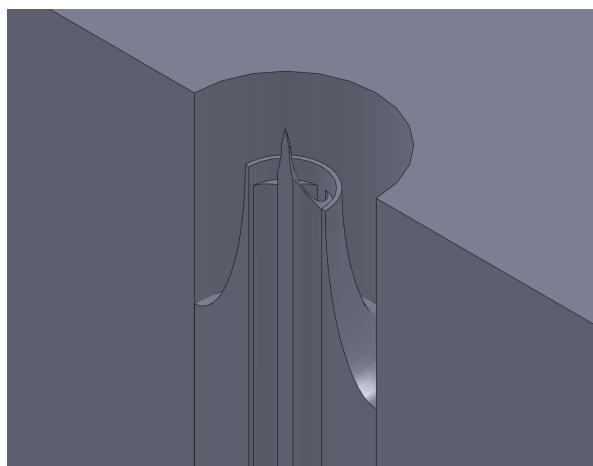
(a) SEM micrographs of 3D structure fabricated in polymer using NanoScribe system [125]



(b) SEM micrographs of PDMS structure replicated from glass mold patterned by femtosecond laser using the FEMTOPRINT system. [126]



(c) CAD drawing of complex emitter enabled by 3D printing



(d) CAD drawing of complex emitter enabled by 3D printing

Figure 6.1: 3D-printed structures. (a)-(b) Examples of structures enabled by 3D printing. (c)-(d) drawings of possible future insulator ESI source design.

Bibliography

- [1] Vadim Zakirov and Luming Li. Propulsion challenges for small spacecraft: 2005. *Tsinghua Science & Technology*, 11(5), 2006.
- [2] Wade. Mark. Encyclopedia Astronautica (<http://www.astronautix.com/index.html>), 2011.
- [3] EO_portal. Earth Observation Portal (<https://directory.eoportal.org/>).
- [4] Gunter Krebs. Gunter's Space Page (<http://space.skyrocket.de/>).
- [5] S Kenyon, CP Bridges, and Doug Liddle. STRaND-1: Use of a \$500 Smartphone as the Central Avionics of a Nanosatellite. In *62nd International Astronautical Congress*, pages 1–19, Cape Town, South Africa, 2011.
- [6] Daniel G. Courtney and Muriel Richard. 0032_EN_007_SSC. CubeSat Technology Pre-Developments, QB-50. Active Debris Removal - Micro-Propulsion System. Technical report, 2014.
- [7] Busek. Busek electrical propulsion (http://www.busek.com/technologies__main.htm), 2014.
- [8] Douglas Spence, Eric Ehrbar, Nate Rosenblad, Nathaniel Demmons, Tom Roy, Samuel Hoffman, Dan Williams, Vladimir Hruby, and Chris Tocci. Electrospray Propulsion Systems for Small Satellites. In *27th Annual AIAA/USU Conference on Small Satellites*, pages 1–7, 2013.
- [9] Juergen Mueller, Richard Hofer, and John K. Ziemer. Survey of propulsion technologies applicable to cubesats. 10-1646. Technical report, NASA, 2010.
- [10] JPL. Precision Formation Flying - Distributed Spacecraft Technology (<http://dst.jpl.nasa.gov/thrusters/index.htm>), 2014.
- [11] Andreas Tziolas, Konstantinos Konstantinidis, and Adam Crawl. Project Tin Tin - Interstellar Nano Mission to Alpha Centauri. In *63rd International Astronautical Congress*, number c, pages 1–9, Naples, Italy, 2015.

Bibliography

- [12] Muriel Richard, Federico Belloni, and Camille Pirat. D1.3: Mission Requirements and Propulsion System Specifications. Technical report, 2013.
- [13] Mike Meyer, Les Johnson, Dryan Palaszewski, Dan M. Goebel, and David Coote. In-Space Propulsion Systems Roadmap - Technology Area 02. Technical report, NASA, 2012.
- [14] G. Taylor. Disintegration of water drops in an electric field. *Proceedings of the Royal Society of London*, 280(1382):383–397, July 1964.
- [15] Manuel Gamero-Castaño and Juan Fernandez De La Mora. Direct measurement of ion evaporation kinetics from electrified liquid surfaces. *The Journal of Chemical Physics*, 113(2):815, 2000.
- [16] I. Romero-Sanz, R. Bocanegra, and Juan Fernandez De La Mora. Source of heavy molecular ions based on Taylor cones of ionic liquids operating in the pure ion evaporation regime. *Journal of Applied Physics*, 94(5):3599, 2003.
- [17] Blaise Laurent Patrick Gassend, Luis Fernando Velasquez-Garcia, Akintunde Ibitayo Akinwande, and Manuel Martínez-Sánchez. A microfabricated planar electrospray array ionic liquid ion source with integrated extractor. *Microelectromechanical Systems, Journal of*, 18(3):679–694, 2009.
- [18] Daniel G. Courtney, Hanqing Q Li, and Paulo C. Lozano. Emission measurements from planar arrays of porous ionic liquid ion sources. *Journal of Physics D: Applied Physics*, 45(48):485203, December 2012.
- [19] Weiwei Deng, James F. Klemic, Xiaohui Li, Mark a. Reed, and Alessandro Gomez. Increase of electrospray throughput using multiplexed microfabricated sources for the scalable generation of monodisperse droplets. *Journal of Aerosol Science*, 37(6):696–714, June 2006.
- [20] Giovanni Lenguito and Alessandro Gomez. Development of a multiplexed electrospray micro-thruster with post-acceleration and beam containment. *Journal of Applied Physics*, 114(15):154901, 2013.
- [21] John Zeleny. The electrical discharge from liquid points, and a hydrostatic method of measuring the electric intensity at their surfaces. In *Royal Soc. London Phys Rev*, volume 3, page 69. APS, February 1914.
- [22] John Zeleny. Instability of Electrified Liquid Surfaces. In *Camb. Philos. Soc. Phys Rev*, volume 10, page 1. APS, 1917.
- [23] John Zeleny. Electrical Discharges from Pointed Conductors. *Physical Review*, 16(2):102–125, 1920.
- [24] Juan Fernandez De La Mora. The Fluid Dynamics of Taylor Cones. *Annual Review of Fluid Mechanics*, 39(1):217–243, January 2006.

-
- [25] Adrian G. Bailey. Investigation of a single spraying site of a colloid thruster. *Journal of Physics D: Applied Physics*, 6(2):276, January 1973.
- [26] Flavia Tata Nardini, L Van Vliet, Pelle Rangsten, T Gronland, Berry Sanders, Herbert R. Shea, Muriel Noca, John P. W. Stark, Davina Di Cara, and Alexandra Bulit. MEMS based EP: Final report. TNO-DV 2010 C086 ITT. Technical report, 2010.
- [27] José Mariano Lopez Urdiales. *Progress in colloid propulsion*. PhD thesis, MIT, 2004.
- [28] Adrian G. Bailey, Jorg E. Bracher, and Hans J. Yon Rohden. A Capillary-Fed Annular Colloid Thruster. *Journal of Spacecraft and Rockets*, 9(7):518–521, July 1972.
- [29] C Petagna, H von Rohden, C Bartoli, and D Valentian. Field Emission Electric Propulsion(FEEP): Experimental investigations on continuous and pulsed modes of operation. In *20th International Electric Propulsion Conference*, Garmish-Partenkirchen, Germany, 1988.
- [30] Salvo Marcuccio, Nicola Giusti, and Alexander Tolstoguzov. Characterization of Linear Slit FEEP Using a Ionic Liquid Propellant. In *31st International Electric Propulsion Conference*, pages 1–10, 2009.
- [31] Salvo Marcuccio, P. Pergola, and Nicola Giusti. IL-Feep: A Simplified, Low Cost Electric Thruster For Micro- and Nano-Satellites. In *4s Symposium 2012*, pages 1–12, 2012.
- [32] Renato Krpoun. *Micromachined Electrospray Thrusters for Spacecraft Propulsion*. PhD thesis, 2009.
- [33] J. Gonzalez, G. Saccoccia, and H von Rohden. Field Emission Electric Propulsion: Experimental Investigations on Microthrust FEEP Thrusters. In *23rd International Electric Propulsion Conference*, Seattle, USA, 1993.
- [34] Paulo C. Lozano and Manuel Martínez-Sánchez. *Studies on the ion-droplet mixed regime in colloid thrusters*. PhD thesis, MIT, 2003.
- [35] Yu-Hui Chiu, B. L. Austin, Rainer A. Dressler, Dale J. Levandier, P. T. Murray, Paulo C. Lozano, and Manuel Martínez-Sánchez. Mass spectrometric analysis of colloid thruster ion emission from selected propellants. *Journal of Propulsion and Power*, 21(3):416–423, May 2005.
- [36] John K. Ziemer, Thomas M. Randolph, Garth W. Franklin, Vladimir Hruby, Douglas Spence, Nathaniel Demmons, Thomas Roy, Eric Ehrbar, Jurg Zwahlen, Roy Martin, and William Connolly. Colloid Micro-Newton Thrusters for the space technology 7 mission. In *2010 IEEE Aerospace Conference*, pages 1–19. Ieee, March 2010.
- [37] Paulo C. Lozano and Manuel Martínez-Sánchez. Ionic liquid ion sources: suppression of electrochemical reactions using voltage alternation. *Journal of colloid and interface science*, 280(1):149–54, December 2004.

Bibliography

- [38] Paulo C. Lozano and Manuel Martínez-Sánchez. Ionic liquid ion sources: characterization of externally wetted emitters. *Journal of Colloid and Interface Science*, 282(2):415–21, February 2005.
- [39] Paulo C. Lozano. Energy properties of an EMI-Im ionic liquid ion source. *Journal of Physics D: Applied Physics*, 39(1):126–134, January 2006.
- [40] S. Castro, C. Larriba, Juan Fernandez De La Mora, Paulo C. Lozano, S. Sumer, Y. Yoshida, and G. Saito. Effect of liquid properties on electrosprays from externally wetted ionic liquid ion sources. *Journal of Applied Physics*, 102(9):094310, 2007.
- [41] C. Larriba, S. Castro, Juan Fernandez De La Mora, and Paulo C. Lozano. Monoenergetic source of kilodalton ions from Taylor cones of ionic liquids. *Journal of Applied Physics*, 101(8):084303, 2007.
- [42] Natalya Brikner and Paulo C. Lozano. The role of upstream distal electrodes in mitigating electrochemical degradation of ionic liquid ion sources. *Applied Physics Letters*, 101(19):193504, 2012.
- [43] Luis Fernando Velasquez-Garcia, Akintunde Ibitayo Akinwande, and Manuel Martínez-Sánchez. A planar array of micro-fabricated electrospray emitters for thruster applications. *Journal of Microelectromechanical Systems*, 15(5):1272–1280, October 2006.
- [44] Blaise Laurent Patrick Gassend, Luis Fernando Velasquez-Garcia, and Akintunde Ibitayo Akinwande. Design and Fabrication of DRIE-Patterned Complex Needlelike Silicon Structures. *Journal of Microelectromechanical Systems*, 19(3):589–598, June 2010.
- [45] F A Hill, P.J. Ponce de Leon, and Luis Fernando Velasquez-Garcia. High-throughput Ionic Liquid Electrospray Sources Based on Dense Monolithic Arrays of Emitters with Integrated Extractor Grid and Carbon Nanotube Flow Control Structures. In *Transducers 2013*, number June, pages 2644–2647, 2013.
- [46] Robert S. Legge Jr. and Paulo C. Lozano. Performance of Heavy Ionic Liquids with Porous Metal Electrospray Emitters. In *44th AIAA/ASME/SAE/ASEE Joint Propulsion Conference and Exhibit*, number July, 2008.
- [47] Daniel G. Courtney and Paulo C. Lozano. Development of Ionic Liquid Electrospray Thrusters using Porous Emitter Substrates. In *International Conference on Space Technology and Science*, pages 1–6, 2009.
- [48] Robert S. Legge Jr. and Paulo C. Lozano. Electrospray Propulsion Based on Emitters Microfabricated in Porous Metals. *Journal of Propulsion and Power*, 27(2):485–495, March 2011.
- [49] Julie Xie, Michael D. Canonica, and Paulo C. Lozano. Fabrication of Electrospray Thrusters by Sintering Glass Microspheres. *49th AIAA/ASME/SAE/ASEE Joint Propulsion Conference and Exhibit*, pages 1–8, July 2013.

-
- [50] Chase S. Coffman, Louis Perna, Hanqing Li, and Paulo C. Lozano. On the Manufacturing and Emission Characteristics of a Novel Borosilicate Electro spray Source. In *49th AIAA/ASME/SAE/ASEE Joint Propulsion Conference and Exhibit*, pages 1–12, 2013.
- [51] Giovanni Lenguito, J Fernandez de la Mora, and Alessandro Gomez. Scaling up the power of an electro spray microthruster. *Journal of Micromechanics and Microengineering*, 24(5):055003, May 2014.
- [52] Vladimir Hruby, Manuel Gamero-Castaño, P. Falkos, and S. Shenoy. Micro Newton colloid thruster system development. In *27th International Electric Propulsion Conference*, pages 01–281, 2001.
- [53] Manuel Gamero-Castaño. The structure of electro spray beams in vacuum. *Journal of Fluid Mechanics*, 604:339–368, May 2008.
- [54] Manuel Gamero-Castaño. Characterization of the electro sprays of 1-ethyl-3-methylimidazolium bis (trifluoromethylsulfonyl) imide in vacuum. *Physics of fluids*, 20(3):032103, 2008.
- [55] Manuel Gamero-Castaño, Anna Torrents, Lorenzo Valdevit, and Jian-Guo Zheng. Pressure-Induced Amorphization in Silicon Caused by the Impact of Electro sprayed Nanodroplets. *Physical Review Letters*, 105(14):145701, September 2010.
- [56] Manuel Gamero-Castaño. Energy dissipation in electro sprays and the geometric scaling of the transition region of cone-jets. *Journal of Fluid Mechanics*, 662:493–513, August 2010.
- [57] JPL. Microfluidic Electro spray Propulsion for Small Spacecraft Missions (<http://microdevices.jpl.nasa.gov/news/news-microfluidic-electro-spray-propulsion.php>), 2014.
- [58] Weiwei Deng and Alessandro Gomez. Influence of space charge on the scale-up of multiplexed electro sprays. *Journal of Aerosol Science*, 38(10):1062–1078, October 2007.
- [59] David Garoz, C. Bueno, C. Larriba, S. Castro, I. Romero-Sanz, Juan Fernandez De La Mora, Y. Yoshida, and G. Saito. Taylor cones of ionic liquids from capillary tubes as sources of pure ions: The role of surface tension and electrical conductivity. *Journal of Applied Physics*, 102(6):064913, 2007.
- [60] W. Martino, Juan Fernandez De La Mora, Y. Yoshida, G. Saito, and J. Surface tension measurements of highly conducting ionic liquids. *Green Chemistry*, 8(4):390, 2006.
- [61] Giovanni Lenguito and Alessandro Gomez. Pressure-driven operation of microfabricated multiplexed electro sprays of ionic liquid solutions for space propulsion applications. *Journal of Microelectromechanical Systems*, 23(3):689–698, 2013.
- [62] Renato Krpoun and Herbert R. Shea. Integrated out-of-plane nanoelectro spray thruster arrays for spacecraft propulsion. *Journal of Micromechanics and . . .*, 19(4), April 2009.

Bibliography

- [63] Weiwei Deng and Alessandro Gomez. Full transient response of Taylor cones to a step change in electric field. *Microfluidics and Nanofluidics*, 12(1-4):383–393, September 2011.
- [64] Weiwei Deng and Alessandro Gomez. The role of electric charge in microdroplets impacting on conducting surfaces. *Physics of Fluids*, 22(5), 2010.
- [65] Brandon Lojewski, Weiwei Yang, Hongxu Duan, Chengying Xu, and Weiwei Deng. Design, Fabrication, and Characterization of Linear Multiplexed Electrospray Atomizers Micro-Machined from Metal and Polymers. *Aerosol Science and Technology*, 47(2):146–152, February 2013.
- [66] Weiwei Yang, Brandon Lojewski, Yan Wei, and Weiwei Deng. Interactions and deposition patterns of multiplexed electrosprays. *Journal of Aerosol Science*, 46:20–33, April 2012.
- [67] Hongxu Duan, Cheng Li, Weiwei Yang, Brandon Lojewski, Linan An, and Weiwei Deng. Near-Field Electrospray Microprinting of Polymer-Derived Ceramics. *Journal of Microelectromechanical Systems*, 22(1):2012–2014, 2013.
- [68] John P. W. Stark, R Stevens, Matthew S. Alexander, and Barry Kent. Fabrication and Operation of Microfabricated Emitters as Components for a Colloid Thruster. *Journal of Spacecraft and Rockets*, 41(6), July 2005.
- [69] L Wang, R Stevens, A Malik, P Rockett, Mark D. Paine, P Adkin, S Martyn, Katharine Lucy Smith, John P. W. Stark, and P Dobson. High-aspect-ratio silica nozzle fabrication for nano-emitter electrospray applications. *Microelectronic Engineering*, 84(5-8):1190–1193, May 2007.
- [70] Mark D. Paine. *A Micro-Fabricated Colloid Microthruster*. PhD thesis, University of Southampton, 2002.
- [71] John P. W. Stark, B. Stevens, Barry Kent, Mike Sandford, and Matthew S. Alexander. Micro-Fabrication and Operation Nano Emitters Suitable for a Colloid Thruster Array. In *4th Roundtable on Micro/Nanotechnologies in Space*, 2003.
- [72] Mark D. Paine, Stephen B. Gabriel, C.G.J. Schabmueller, and A.G.R. Evans. Realisation of very high voltage electrode-nozzle systems for MEMS. *Sensors and Actuators A: Physical*, 114(1):112–117, August 2004.
- [73] Matthew S. Alexander, Mark D. Paine, and John P. W. Stark. Pulsation modes and the effect of applied voltage on current and flow rate in nanoelectrospray. *Analytical Chemistry*, 78(8):2658–2664, April 2006.
- [74] Mark D. Paine, Matthew S. Alexander, Katharine Lucy Smith, and M Wang. Controlled electrospray pulsation for deposition of femtoliter fluid droplets onto surfaces. *Journal of Aerosol Science*, 38(3):315–324, March 2007.

-
- [75] Mark D. Paine. Transient electrospray behaviour following high voltage switching. *Microfluidics and nanofluidics*, 6(6):775–783, October 2009.
- [76] Katharine Lucy Smith, Matthew S. Alexander, Mark D. Paine, and John P. W. Stark. Scaling of a Colloid Thruster system for microNewton to milliNewton Thrust levels. In *30th International Electric Propulsion Conference*, pages 1–8, 2007.
- [77] Katharine Lucy Smith. *Characterisation of electrospray properties in high vacuum with a view to application in colloid thruster technology*. PhD thesis, 2005.
- [78] Katharine Lucy Smith, Matthew S. Alexander, and John P. W. Stark. The Effect of Molar Conductivity upon Current and Thrust in a Colloid Electrospray Thruster System. In *29th International Electric Propulsion Conference*, pages 1–6, 2005.
- [79] Katharine Lucy Smith, Matthew S. Alexander, and John P. W. Stark. Voltage effects on the volumetric flow rate in cone-jet mode electrospraying. *Journal of Applied Physics*, 99(6):064909, 2006.
- [80] Katharine Lucy Smith, Matthew S. Alexander, and John P. W. Stark. The sensitivity of volumetric flow rate to applied voltage in cone-jet mode electrospray and the influence of solution properties and emitter geometry. *Physics of Fluids*, 18(9):092104, 2006.
- [81] Gary A Schultz, T.N. Corso, S.J. Prosser, and Sheng Zhang. A fully integrated monolithic microchip electrospray device for mass spectrometry. *Analytical chemistry*, 72(17):4058–4063, 2000.
- [82] Patrick Griss, Jessica Melin, Johan Sjö Dahl, Johan Roeraade, and Göran Stemme. Development of micromachined hollow tips for protein analysis based on nanoelectrospray ionization mass spectrometry. *Journal of Micromechanics and Microengineering*, 12(5):682, September 2002.
- [83] Renato Krpoun and Herbert R. Shea. A method to determine the onset voltage of single and arrays of electrospray emitters. *Journal of Applied Physics*, 104(6):064511, 2008.
- [84] Renato Krpoun, M. Räber, and Herbert R. Shea. Microfabrication and test of an integrated colloid thruster. In *21st International Conference on Micro Electro Mechanical Systems*, pages 964–967, 2008.
- [85] Charles Ryan, Alex Daykin-Iliopoulos, John P W Stark, Ana Z Salaverri, Ernesto Vargas, Pelle Rangsten, S S C Nanospace, Uppsala Science Park, Jan Timmerman, Martin de Jong, Richard Visee, Laurens Van Vliet, Berry Sanders, Michiel Straathof, Flavia Tata Nardini, Viola Van Pul-verboom, Simon Dandavino, Subha Chakraborty, Daniel G. Courtney, Federico Belloni, Muriel Richard, and Herbert Shea. The MicroThrust MEMS electrospray thruster : results and conclusions. In *Space Propulsion 2014*, number May, pages 1–10, Cologne, Germany, 2014.

Bibliography

- [86] Richard Visée, Martin de Jong, and Jan Timmerman. Miniaturized HV Power Supply. In *33rd International Electric Propulsion Conference*, pages 1–8, Washington, D.C., 2013.
- [87] Paulo C. Lozano and Manuel Martínez-Sánchez. Efficiency Estimation of EMI-BF 4 Ionic Liquid Electrospray Thrusters. In *41st AIAA/ASME/SAE/ASEE Joint Propulsion Conference and Exhibit*, number July, pages 1–7, 2005.
- [88] Juan Fernandez De La Mora, J Navascues, and F Fernandez. Generation of submicron monodisperse aerosols in electrosprays. *Journal of Aerosol Science*, 21(1):673–676, 1990.
- [89] S Ergun. Fluid flow through packed columns. *Chemical Engineering Progress*, 48(2):89–94, 1952.
- [90] MC Thadani. Variation of local void fraction in randomly packed beds of equal spheres. *Industrial Engineering Chemistry*, 5(3), 1966.
- [91] J.S. Goodling, R.I. Vachon, W.S. Stelpflug, S.J. Ying, and M.S. Khader. Radial porosity distribution in cylindrical beds packed with spheres. *Powder Technology*, 35(1):23–29, May 1983.
- [92] GJ Auwerda and JL Kloosterman. Comparison of experiments and calculations of void fraction distributions in randomly stacked pebble beds. In *Advances in Reactor Physics to Power the Nuclear Renaissance*, 2010.
- [93] G. L. R. Mair. Emission from liquid metal ion sources. *Nuclear Instruments and Methods*, 172:567–576, 1980.
- [94] Blaise Laurent Patrick Gassend. *A Fully Microfabricated Two-Dimensional Electrospray Array with Applications to Space Propulsion by Blaise Laurent Patrick Gassend*. PhD thesis, Massachusetts Institute of Technology, 2007.
- [95] Timothy P. Fedkiw and Paulo C. Lozano. Development and characterization of an iodine field emission ion source for focused ion beam applications. *Journal of Vacuum Science & Technology B: Microelectronics and Nanometer Structures*, 27(6):2648, 2009.
- [96] Shawn W. Miller, Benjamin D. Prince, and Joshua L. Rovey. Capillary Extraction of the Ionic Liquid [Bmim][DCA] for Variable Flow Rate Operations. In *48th AIAA/ASME/SAE/ASEE Joint Propulsion Conference and Exhibit*, number August, pages 1–13, 2012.
- [97] Subha Chakraborty, Caglar Ataman, Simon Dandavino, and Herbert R. Shea. Microfabrication of an Electrospray Thruster for Small Spacecraft. In *Power MEMS*, 2012.
- [98] Hu Yanlin and Zip Code. Lifetime assessment of Hall thruster. In *33rd International Electric Propulsion Conference*, pages 1–8, 2013.

-
- [99] Ioannis G. Mikellides, Ira Katz, Richard R. Hofer, Dan M. Goebel, Kristi de Grys, and Alex Mathers. Magnetic shielding of the channel walls in a Hall plasma accelerator. *Physics of Plasmas*, 18(3):033501, 2011.
- [100] Dan M. Goebel and Ira Katz. Ion Thruster Accelerator Grids. In *Fundamentals of Electric Propulsion: Ion and Hall Thrusters*, number Dc, chapter Chapter 5,; pages 189–241. John Wiley edition, 2008.
- [101] Anthony Nicholas Zorzos and Paulo C. Lozano. The use of ionic liquid ion sources in focused ion beam applications. *Journal of Vacuum Science & Technology B: Microelectronics and Nanometer Structures*, 26(6):2097, 2008.
- [102] Weiwei Deng, CM Waits, and Alessandro Gomez. Digital electrospray for controlled deposition. *Review of Scientific Instruments*, 81(3):035114, March 2010.
- [103] Simon Dandavino, Caglar Ataman, Subha Chakraborty, Herbert R. Shea, Charles Ryan, and John P. W. Stark. Progress Towards a Miniaturized Electrospray Thruster for Propulsion of Small Spacecraft. In *48th AIAA/ASME/SAE/ASEE Joint Propulsion Conference and Exhibit*, number August, pages 1–13, Atlanta, Georgia, 2012.
- [104] Charles Ryan and John P. W. Stark. D3.3.1: Empirical model used to inform breadboard thrust head design. Technical report, 2012.
- [105] Caglar Ataman, Simon Dandavino, and Herbert R. Shea. Wafer-level Integrated Electrospray Emitters for a Pumpless Microthruster System Operation in High Efficiency Ion-Mode. In *IEEE MEMS*, Paris, France, 2012.
- [106] Anne-Gabrielle Pawlowski, Eric Belloy, Abdeljalil Sayah, and Martin Gijs. Powder blasting patterning technology for microfabrication of complex suspended structures in glass. *Microelectronic engineering*, 68:557–565, 2003.
- [107] Roger X. Lenard, Stanley H. Kraitz, John Nogan, and Carrie Schmidt. Progress in MEMS-Based Field Emission Thrusters at Sandia National Laboratories. In *43rd AIAA/ASME/SAE/ASEE Joint Propulsion Conference and Exhibit*, number July, 2007.
- [108] Wei-Sheng Lei, Ajay Kumar, and Rao Yalamanchili. Die singulation technologies for advanced packaging: A critical review. *Journal of Vacuum Science & Technology B: Microelectronics and Nanometer Structures*, 30(4):040801, 2012.
- [109] Charles Ryan, Alex Daykin-Iliopoulos, John P. W. Stark, Anna Z. Salaverri, Ernesto Vargas, Pelle Rangsten, Simon Dandavino, Caglar Ataman, Subha Chakraborty, Daniel G. Courtney, and Herbert R. Shea. Experimental progress towards the MicroThrust MEMS electrospray electric propulsion system. In *33rd International Electric Propulsion Conference*, pages 1–10, Washington, D.C., 2013.
- [110] P.R. Chiarot, S.I. Gubarenko, R.B. Mrad, and P.E. Sullivan. On the Pulsed and Transitional Behavior of an Electrified Fluid Interface. *Journal of Fluids Engineering*, 131(9):091202, 2009.

Bibliography

- [111] C. L. Enloe and J. R. Shell. Optimizing the energy resolution of planar retarding potential analyzers. *Review of Scientific Instruments*, 63(2):1788, 1992.
- [112] Simon Dandavino, Caglar Ataman, Charles Ryan, Subha Chakraborty, Daniel G. Courtney, John P. W. Stark, and Herbert R. Shea. Microfabricated electrospray emitter arrays with integrated extractor and accelerator electrodes for the propulsion of small spacecraft. *Journal of Micromechanics and Microengineering*, 24(7):075011, July 2014.
- [113] Yu-Hui Chiu, Geraldine Gaeta, Dale J. Levandier, Rainer A. Dressler, and J.a. Boatz. Vacuum electrospray ionization study of the ionic liquid, [Emim][Im]. *International Journal of Mass Spectrometry*, 265(2-3):146–158, September 2007.
- [114] Ioan Marginean, Lida Parvin, Linda Heffernan, and Akos Vertes. Flexing the Electrified Meniscus : The Birth of a Jet in Electrosprays. *Analytical Chemistry*, 76(14):4202–4207, 2004.
- [115] Si Tran, Doyoung Byun, Vu Nguyen, and Tae Kang. Liquid meniscus oscillation and drop ejection by ac voltage, pulsed dc voltage, and superimposing dc to ac voltages. *Physical Review E*, 80(2):026318, August 2009.
- [116] Matthew S. Alexander. Pulsating electrospray modes at the liquid-liquid interface. *Applied Physics Letters*, 92(14):144102, 2008.
- [117] B Praprotnik, W. Driesel, and Ch. Dietzsch. HV-TEM in-situ investigations of the tip shape of indium liquid metal ion emitter. *Surface Science*, 314:353–364, 1994.
- [118] W. Driesel, Ch. Dietzsch, H. Niedrig, and B. Praprotnik. HV TEM in situ investigations of the tip shape of a gallium liquid-metal ion/electron emitter. *Ultramicroscopy*, 57:45–58, 1995.
- [119] W. Driesel, Ch. Dietzsch, and R. Muhle. In situ observation of the tip shape of AuGe liquid alloy ion sources using a high voltage transmission electron microscope. *Journal of Vacuum Science & Technology B: Microelectronics and Nanometer Structures*, 14(5):3367, September 1996.
- [120] W. Driesel and Ch. Dietzsch. In situ HVTEM observation of the tip shape of tin liquid metal ion sources. *Applied surface science*, 93:179–190, 1996.
- [121] W. Driesel, Ch. Dietzsch, and M Möser. In situ HV TEM observation of the tip shape of lead liquid metal ion sources. *Journal of Physics D: Applied ...*, 2492, 1996.
- [122] W. Driesel, Ch. Dietzsch, and E Hesse. In situ observation of the tip shape of Co–Ge liquid alloy ion sources in a high voltage transmission electron microscope. *Journal of Vacuum Science & Technology B: Microelectronics and Nanometer Structures...*, 14(3):1621, May 1996.

-
- [123] KJ Terhune, LB King, K He, and J Cumings. In situ visualization of ionic liquid electro-spray emission using transmission electron microscopy. In *49th AIAA/ASME/SAE/ASEE Joint Propulsion Conference and Exhibit*, pages 1–15, 2013.
- [124] Jérôme Favre and Herbert R. Shea. Test bench for colloid thruster characterization. Technical Report January, EPFL, 2010.
- [125] Stefan Hengsbach and Andrés Díaz Lantada. Direct laser writing of auxetic structures: present capabilities and challenges. *Smart Materials and Structures*, 23(8):085033, August 2014.
- [126] Allison Schaap and Yves Bellouard. Molding topologically-complex 3D polymer microstructures from femtosecond laser machined glass. *Optical Materials Express*, 3(9):1428, August 2013.
- [127] A.F. Stalder, G. Kulik, D. Sage, L. Barbieri, and P. Hoffmann. A snake-based approach to accurate determination of both contact points and contact angles. *Colloids and Surfaces A: Physicochemical and Engineering Aspects*, 286(1-3):92–103, September 2006.
- [128] Mathieu Roulet. Capillary tip shape optimization for electrospray microthrusters. Technical report, 2011.
- [129] PF Man and CH Mastrangelo. Microfabricated capillarity-driven stop valve sample injector. *Systems, 1998. MEMS*, pages 45–50, 1998.
- [130] Basil Huber. Study of Capillary Liquid Retention in Vibration. Technical Report December, 2012.
- [131] Jeannot Frieden. *Characterisation of Low Impact Energy Induced Damage in Composite Plates with Embedded Optical Sensors*. PhD thesis, EPFL, 2011.
- [132] Tom Irvine. An introduction to the shock response spectrum. Technical report, 2012.
- [133] M Yamashita and JB Fenn. Electrospray ion source. Another variation on the free-jet theme. *The Journal of Physical Chemistry*, 434(125):4451–4459, 1984.
- [134] Sander Koster and Elisabeth Verpoorte. A decade of microfluidic analysis coupled with electrospray mass spectrometry: an overview. *Lab on a chip*, 7(11):1394–412, November 2007.
- [135] Tiina Sikanen, Sami Franssila, Tiina J. Kauppila, Risto Kostiainen, Tapio Kotiaho, and Raimo A. Ketola. Microchip technology in mass spectrometry. *Mass spectrometry reviews*, pages 351–391, 2010.
- [136] Xiaojun Feng, Bi-Feng Liu, Jianjun Li, and Xin Liu. Advances in coupling microfluidic chips to mass spectrometry. *Mass spectrometry reviews*, 2000, 2014.

Bibliography

- [137] Bernard Legrand, Alison E Ashcroft, Lionel Buchaillot, and Steve Arscott. SOI-based nanoelectrospray emitter tips for mass spectrometry: a coupled MEMS and microfluidic design. *Journal of Micromechanics and Microengineering*, 17(3):509–514, March 2007.
- [138] Woong Kim, Mingquan Guo, Peidong Yang, and Daojing Wang. Microfabricated monolithic multinozzle emitters for nanoelectrospray mass spectrometry. *Analytical chemistry*, 79(10):3703–3707, 2007.
- [139] L Sainiemi, T Nissila, V Jokinen, T Sikanen, T Kotiaho, R Kostiainen, R Ketola, and Sami Franssila. Fabrication and fluidic characterization of silicon micropillar array electrospray ionization chip. *Sensors and Actuators B: Chemical*, 132(2):380–387, June 2008.
- [140] Peter Hoffmann, Ulrich Häusig, Philipp Schulze, and Detlev Belder. Microfluidic glass chips with an integrated nanospray emitter for coupling to a mass spectrometer. *Angewandte Chemie (International ed. in English)*, 46(26):4913–6, January 2007.
- [141] Malin Svedberg, Monica Veszelei, Jan Axelsson, Mattias Vangbo, and Fredrik Nikolajeff. Poly(dimethylsiloxane) microchip: microchannel with integrated open electrospray tip. *Lab on a chip*, 4(4):322–7, August 2004.
- [142] M Schilling, W Nigge, and A Rudzinski. A new on-chip ESI nozzle for coupling of MS with microfluidic devices. *Lab on a chip*, 4(3):220–4, June 2004.
- [143] J S Kim and D R Knapp. Miniaturized multichannel electrospray ionization emitters on poly(dimethylsiloxane) microfluidic devices. *Electrophoresis*, 22(18):3993–9, October 2001.
- [144] K Tang, Y Lin, D W Matson, T Kim, and R D Smith. Generation of multiple electrosprays using microfabricated emitter arrays for improved mass spectrometric sensitivity. *Analytical chemistry*, 73(8):1658–63, April 2001.
- [145] Marion Sausse Lhernould and Pierre Lambert. Compact polymer multi-nozzles electrospray device with integrated microfluidic feeding system. *Journal of Electrostatics*, 69(4):313–319, August 2011.
- [146] T C Rohner, J S Rossier, and Hubert H Girault. Polymer microspray with an integrated thick-film microelectrode. *Analytical chemistry*, 73(22):5353–7, November 2001.
- [147] Loic Dayon, Melanie Abonnenc, Prudent, Michel, Niels Lion, and Hubert H Girault. Multitrack electrospray chips. *Journal of Mass Spectrometry*, 41:1484–1490, 2006.
- [148] Séverine Le Gac, Steve Arscott, Cécile Cren-Olivé, and Christian Rolando. Two dimensional microfabricated sources for nanoelectrospray. *Journal of Mass Spectrometry*, 38(12):1259–64, December 2003.
- [149] Larry Licklider, XQ Wang, and Amish Desai. A micromachined chip-based electrospray source for mass spectrometry. *Analytical Chemistry*, 72(2):367–375, 2000.

- [150] Jun Kameoka, Reid Orth, Bojan Ilic, David Czaplewski, Tim Wachs, and H G Craighead. An electrospray ionization source for integration with microfluidics. *Analytical chemistry*, 74(22):5897–901, November 2002.
- [151] Jean-Marie Dethy, Bradley L Ackermann, Claude Delatour, Jack D Henion, and Gary a Schultz. Demonstration of direct bioanalysis of drugs in plasma using nanoelectrospray infusion from a silicon chip coupled with tandem mass spectrometry. *Analytical chemistry*, 75(4):805–11, February 2003.
- [152] Sheng Zhang, Colleen K Van Pelt, and Jack D Henion. Automated chip-based nanoelectrospray-mass spectrometry for rapid identification of proteins separated by two-dimensional gel electrophoresis. *Electrophoresis*, 24(21):3620–32, November 2003.

Appendices **Part**

A Liquid transport and containment

Liquid containment plays a critical role in the operation and failure of electrospray emitters. A potential advantage of internally fed capillaries, as opposed to externally fed or porous types of emitters, is a more robust and well defined feeding mechanism. In this appendix, the propensity of the ionic liquids to fill and be contained in the micro capillaries is studied.

First, in section A.1, a characterization of the wetting properties (contact angle) of the commonly used ionic liquid propellants $EMI - Tf_2N$ and $EMI - BF_4$ on several microfabrication surfaces is detailed. A wetting surface, with low contact angle, will more easily transport the liquid away from the desired areas (emitter) and potentially lead to electrical leakage currents and short circuits, as shown in Figure A.1. Conversely, material used for reservoirs and liquid feedthroughs should in most cases be highly wetting.

In section A.2, a model, experimentally validated, is then proposed to describe the resulting filling and holding pressures generated by the capillaries. The holding pressures are particularly relevant in the case where the capillary emitters would be filled during spacecraft launch. In the worst case, we can imagine the emitters pointing down during launch and attached to a filled propellant reservoir of $\approx 10\text{cm}$ height. The holding pressures are representative of the static acceleration that could be supported by filled capillaries without spilling.

In section A.3, shock and vibration experiments are used to further characterize liquid containment under dynamic conditions.

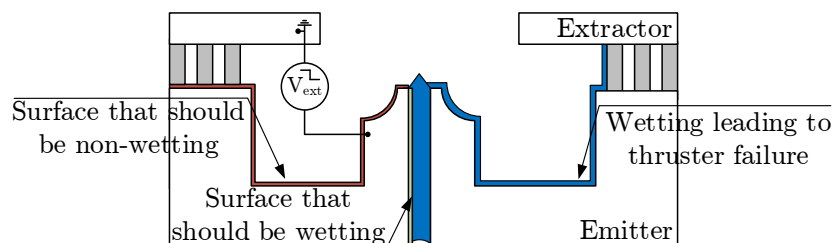


Figure A.1: Diagram of device failure caused by liquid wetting on emitter exterior.

A.1 Contact angle measurements

A.1.1 Setup and procedure

The sessile drop method was used to measure the contact angles of two candidate ionic liquids ($EMI - Tf_2N$ and $EMI - BF_4$, purchased from IoLiTec) on several surfaces which could be used either as material in the upstream liquid delivery system or to coat the chip itself. This method consists of dropping small amounts of liquid on a substrate and measuring by profile observation the angle θ_c at the edge of the drop. Figure A.2 shows a diagram of such a drop, labelling as well the interfacial surface tensions of the solid-liquid, solid-air and liquid-air interfaces, respectively γ_{sl} , γ_{sv} and γ_{lv} .

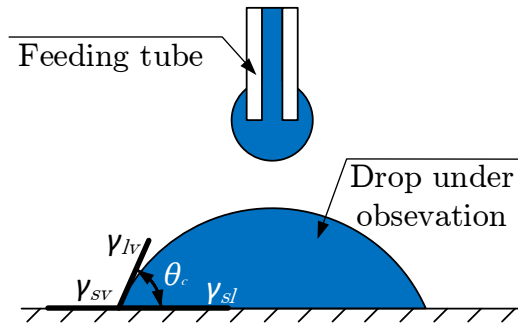


Figure A.2: Diagram of sessile drop technique. The contact angle θ_c , specific to a liquid-surface combination, is captured by observing the profile of a drop resting on the test substrate.

The surface tensions are related through the contact angle θ_c by Eq. A.1.

$$\cos \theta_c = \frac{\gamma_{sv} - \gamma_{sl}}{\gamma_{lv}} \quad (A.1)$$

To avoid reported [60] ionic liquid contamination by ambient humidity, part of the experiment was performed in vacuum (below 10^{-5} mbar), thus demanding a particular setup (Figure A.3). The liquid was kept in a secondary vacuum chamber with a submersed $150\mu m$ inner diameter glass capillary. Ionic liquid was transferred to the primary chamber and the substrates by pressurizing the secondary chamber with nitrogen. The substrates were placed on an aluminium tray attached to a linear motion mechanical feed-through. This allowed several drops to be placed alongside on a given substrate and several substrates tested without breaking vacuum, considerably reducing experiment time.

At the beginning of each test sequence, the transfer capillary was flushed for at least 30 minutes in a reservoir to eliminate all liquid in the capillary which would have been exposed to air when the main chamber was vented. Drops were then placed (falling under their own weight) on the substrates with a USB camera imaging from within the chamber. Snapshots from the videos were then analyzed with the ImageJ open source software using the DropSnake [127]

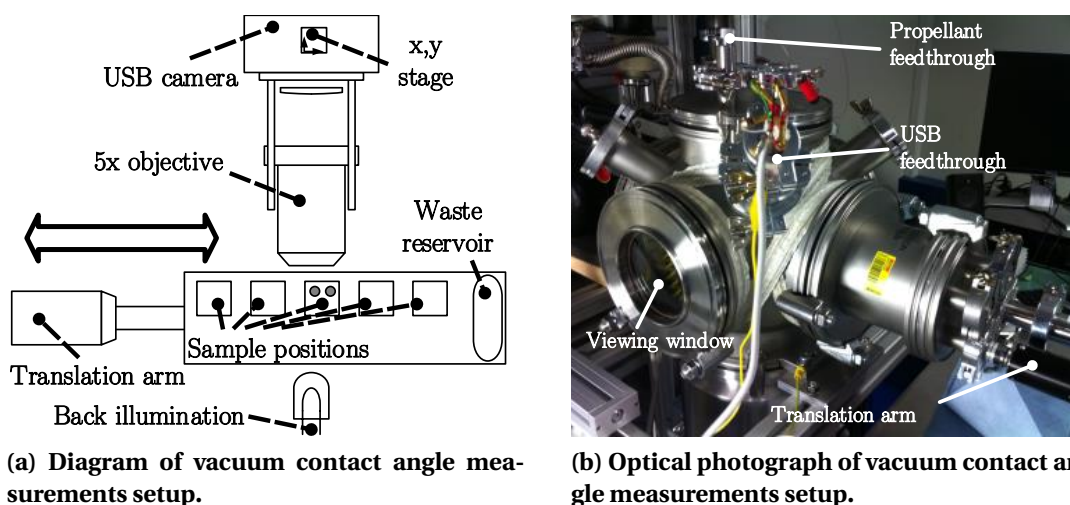


Figure A.3: Vacuum contact angle measurement setup. A 1-d translation arm, accessible from outside the chamber is used to position the sample in view of the USB digital microscope. Drops are applied by pressurizing a second propellant chamber, transferring liquid through a glass capillary.

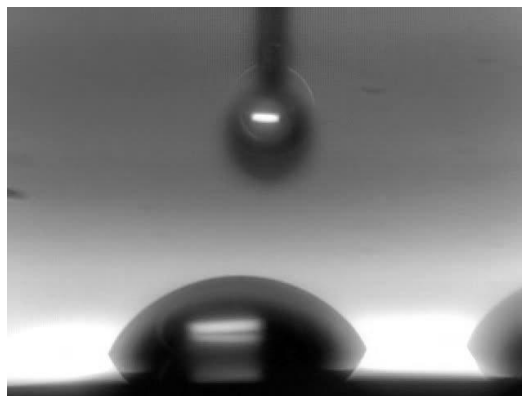
plugin. Substrate temperature was controlled using a thermoelectric module (TE1-19908L) in closed feedback with a Pt1000 temperature probe. It remained at approximately 30°C for “ambient” tests and was increased to 80°C for high temperature tests. Configuration and assembly of the Thermo-Electric Cooler (TEC) was done by semester student Mathieu Roulet [128].

Two candidate ionic liquid propellants, $EMI - BF_4$ and $EMI - Tf_2N$ were studied on 11 primary surfaces: polished silicon, silicon dioxide, silicon nitride, gold, platinum, aluminum, glass, Teflon and three layers deposited by Molecular Vapour Deposition (MVD A, B, C). MVD A, meant to be “hydrophobic”, was a silane-based coating and showed lowest surface energy. MVD C was a metal-oxide based coating and showed the highest surface energy values among MVD A,B and C coatings. All measurements were then retaken on the vented chamber, after at least one hour of exposition to ambient air. Three additional surfaces, Parylene-C, “oxidized” silicon and the laminated film MX5050 were later tested using a conventional goniometer, in ambient air at room temperature. The “oxidized” silicon surface was in fact the face of a completed thruster chip having a thin layer of native oxide. Example images of drops used for contact angle measurement are shown in Figure A.4.

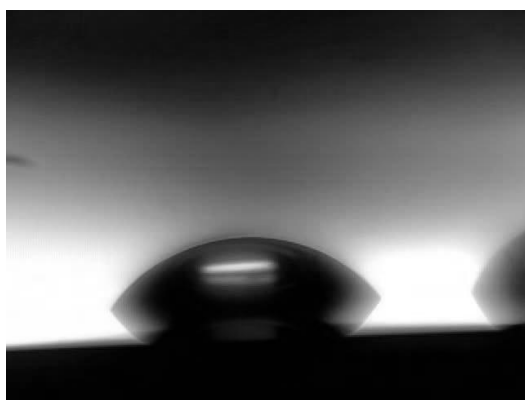
Appendix A. Liquid transport and containment



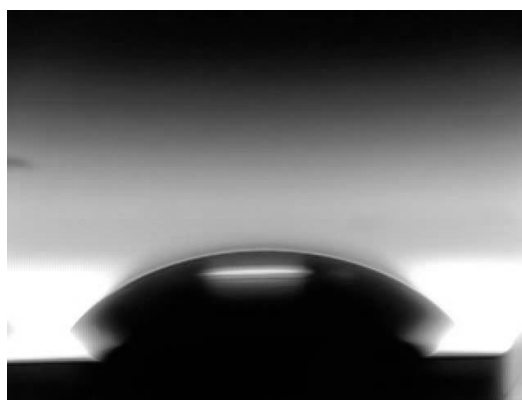
(a) $EMI - BF_4$ on MVD B, in air at $80^\circ C$



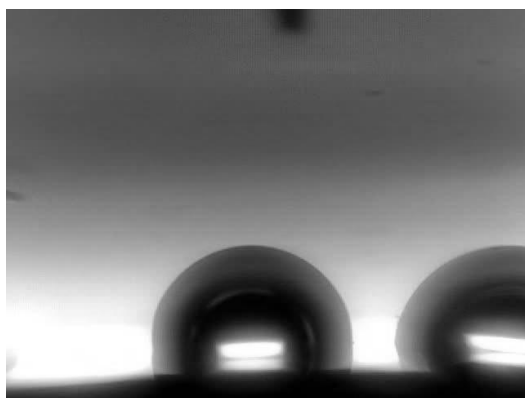
(b) $EMI - BF_4$ on SiO_2 , in vacuum at $30^\circ C$



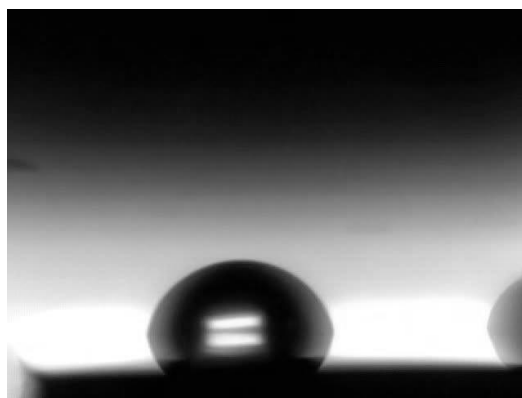
(c) $EMI - BF_4$ on Au, in vacuum at $30^\circ C$



(d) $EMI - Tf_2N$ on Au, in vacuum at $80^\circ C$



(e) $EMI - BF_4$ on MVD A, in air at $30^\circ C$



(f) $EMI - Tf_2N$ on Si, in air at $30^\circ C$

Figure A.4: Example images of drops for contact angle measurements. The overlaid drop profile fitted using the DropSnake plugin [127] can be seen in (a). In (b), the feeding capillary, with a small drop suspended, can be seen.

A.1.2 Results and analysis

Results of average contact angle in vacuum and at room temperature are shown in Figure A.5. $EMI - BF_4$, with its higher reported surface tension ($44.3 \times 10^{-3} \text{ N cm}^{-1}$ @ 22-25°C [60]), had larger contact angles with all surfaces tested than $EMI - Tf_2N$ ($35.2 \times 10^{-3} \text{ N cm}^{-1}$ @ 22-25°C [60]). Two surfaces, polished silicon and MVD A, exhibited contact angles larger than 90° , making them good candidates as non-wetting surfaces. Silicon, however, does not remain "hydrophobic": the contact angle reduces over time as a layer of native oxide appears. None of the surfaces tested with $EMI - Tf_2N$ exhibited larger than 90° contact angles. In most cases, the surfaces did not exhibit any significant dependence on substrate temperature (Figure A.6), a positive element from the system perspective. Except for platinum with Tf_2N at room temperature, the ionic liquids showed practically no change in contact angle when subjected to air (Figure A.7).

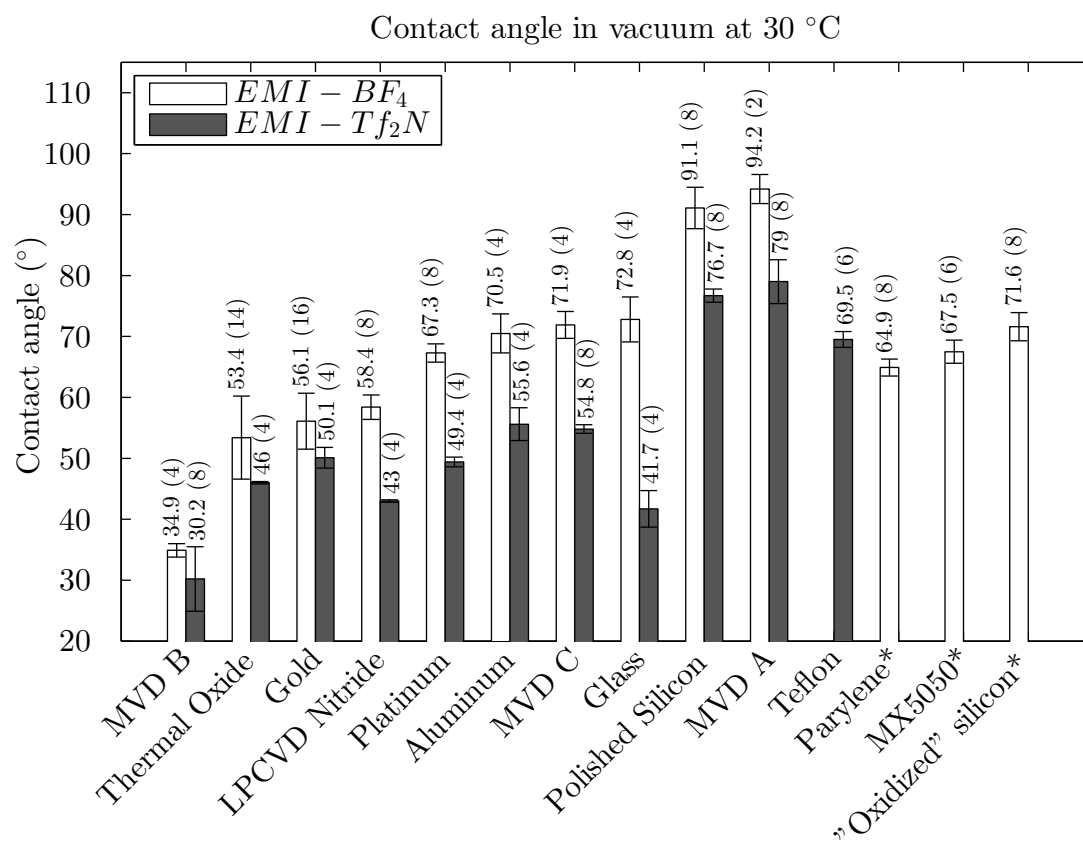


Figure A.5: Contact angle measurements for $EMI - Tf_2N$ and $EMI - BF_4$ at room temperature in vacuum. Error bars: $\pm 1\sigma$; Paranthesis: sample size. *Results of these surfaces were taken in ambient at room temperature.

Appendix A. Liquid transport and containment

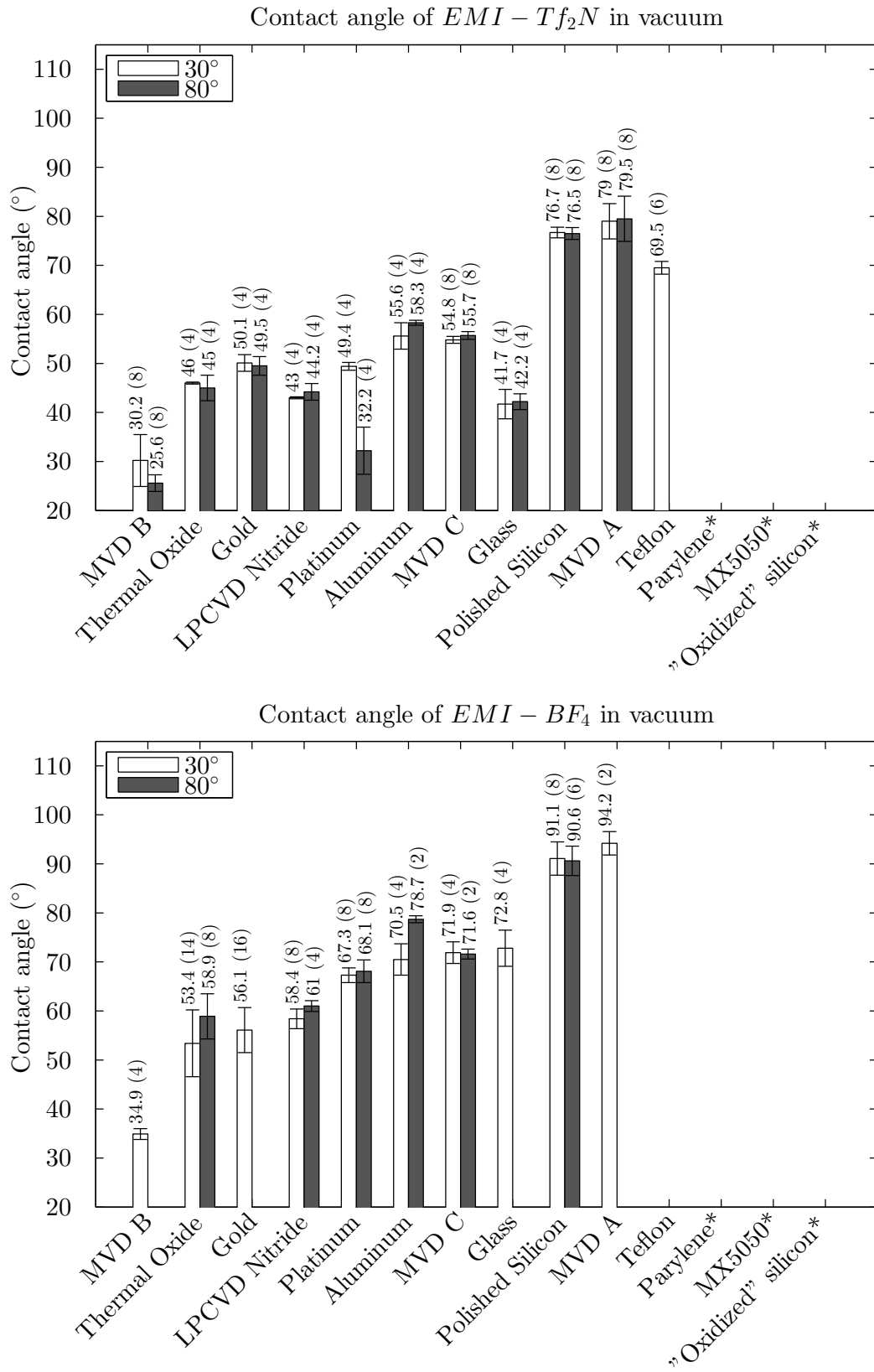


Figure A.6: Temperature influence on contact angle. Error bars: $\pm 1\sigma$; Paranthesis: sample size.

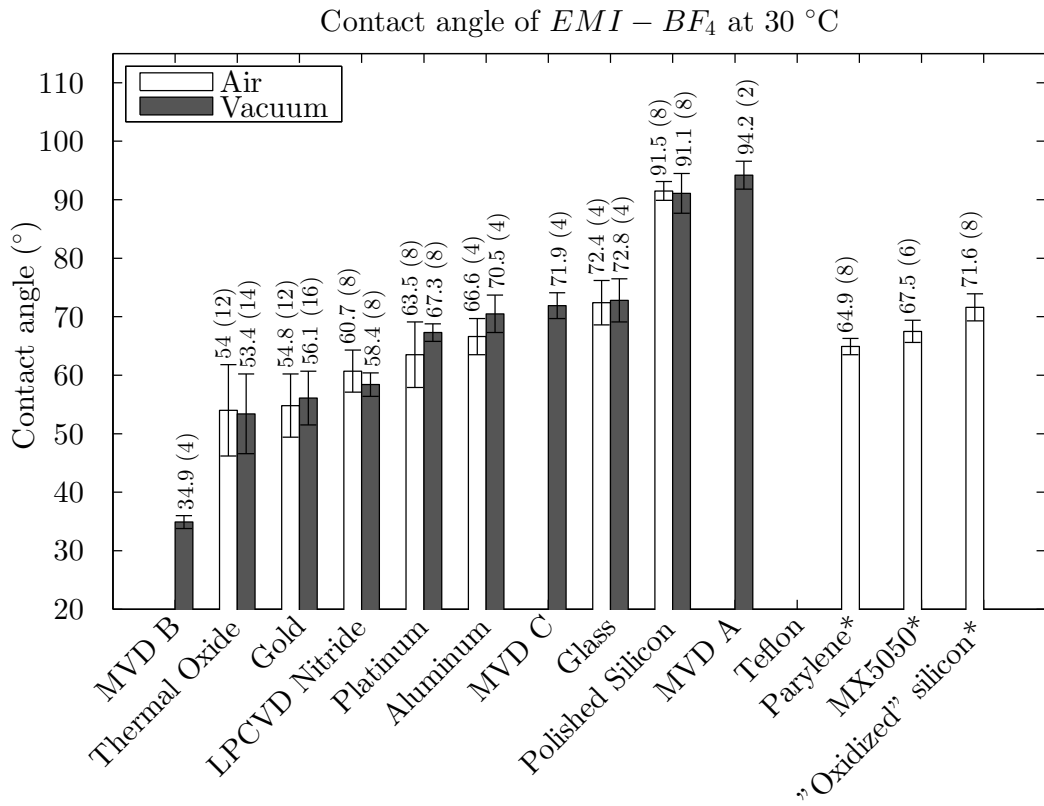
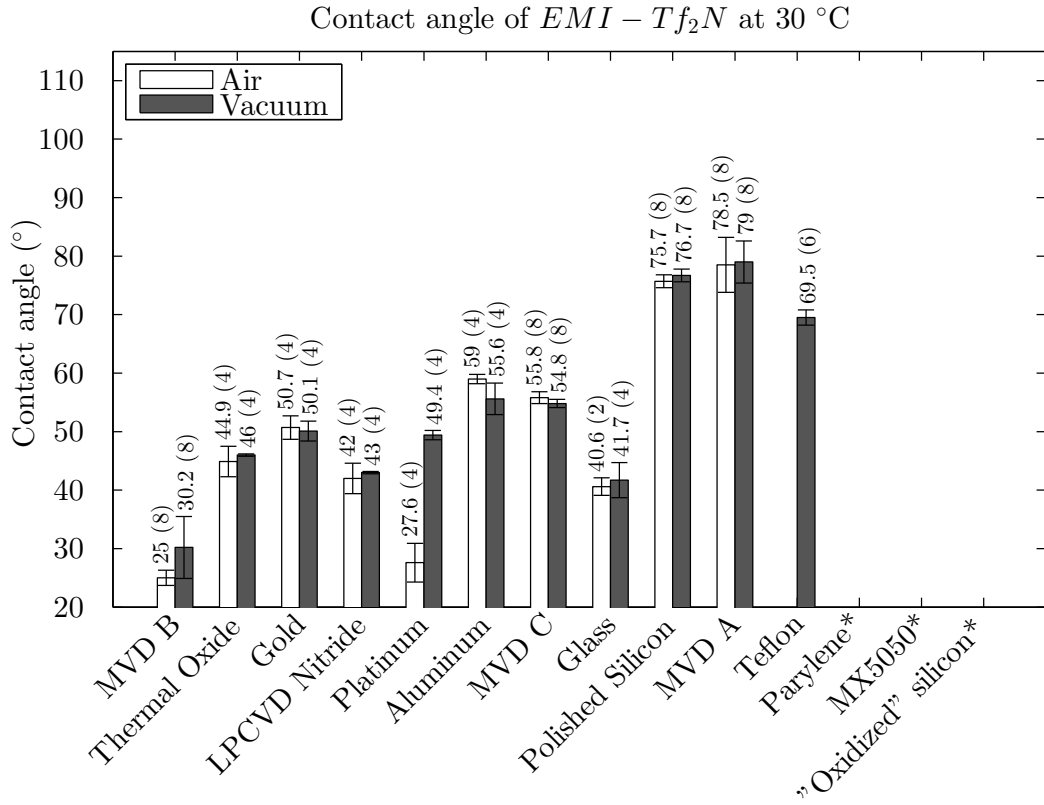


Figure A.7: Environment influence on contact angle. Error bars: $\pm 1\sigma$; Paranthesis: sample size.

A.2 Capillary filling and holding pressure model

A.2.1 Introduction

The contact angle data found in the previous section provides an indication of the wetting behavior of the tested liquids. With this information, an analytical model was developed to provide a quantitative estimate of the filling pressure, acting on the liquid as it fills the capillary, and the holding pressure, which will retain the liquid inside the capillary. In the context of a spacecraft launch, the holding pressure can be related to a maximum static acceleration that could be supported before liquid spillage occurred.

The model was adapted from Man et al. [129] (Figure A.8), who used it to describe the flow in passive microfluidic valves. The model presented here differs first in terms of geometry: here an axisymmetric cylindrical capillary is considered as opposed to a two-dimensional channel. This model also includes liquid wetting to the exterior edge of an emitter tip (Regions IV-V) in Figure A.9, which the original did not.

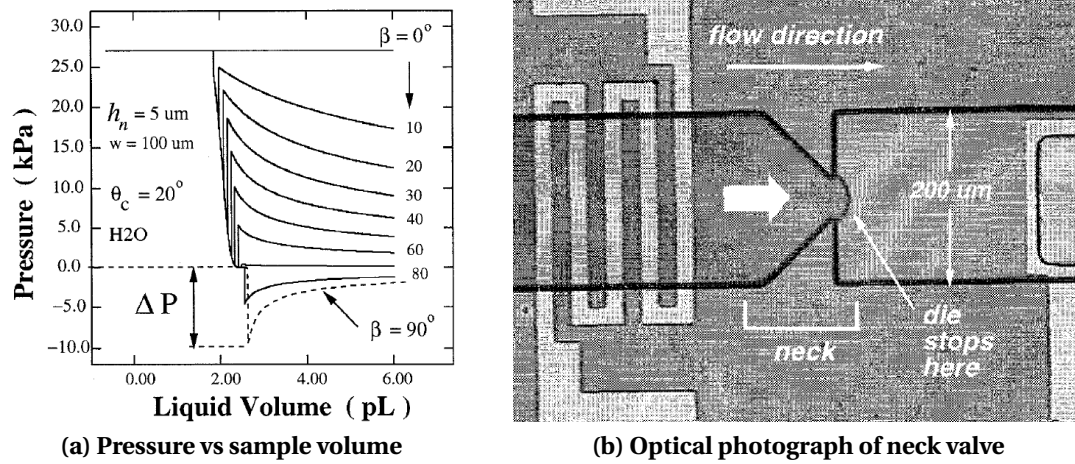


Figure A.8: Graph of pressure barriers and fabricated unidirectionnal valve from Man et al. [129]

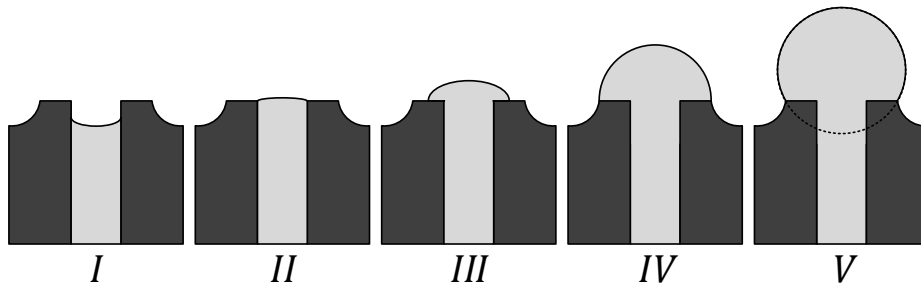


Figure A.9: Cross section of five regimes considered for liquid transport model.

The model results from the first law of thermodynamics and describes the pressure across a meniscus by comparing changes in surface to changes in volume as a liquid is transported through a capillary. The analysis presented here is constrained to "wetting" liquids, i.e. to contact angles ranging from 0° to 90° . The model does not aim to provide time-scales for the liquid displacement. As such it considers quasi-static cases, describing the equilibrium between the liquid and its environment in different configurations.

The objective of the model, in addition to describing the liquid shape in the different regimes, is to calculate the pressure barriers which can occur when transiting from regime to another.

A.2.2 Model description

The first law of thermodynamics states that for a closed, quasi-static system, the change in internal energy of the system is equal to the heat supplied to the system minus the work performed:

$$dU_T = dQ - PdV \quad (\text{A.2})$$

For a small liquid column inside a capillary, this work corresponds to the change in volume multiplied by its internal pressure. Considering an adiabatic situation, and assuming an infinite supply of liquid from a reservoir which does not generate any backpressure, the internal pressure P of the liquid can be written as:

$$P = -\frac{dU_T}{dV} \quad (\text{A.3})$$

where V is its volume and U_T its total energy as defined in Figure A.10. This corresponds to a situation where the system is not closed, but where the aspects of the system not included in this model do not affect the shape and pressure generated by the meniscus. In other words, the reservoir supplying liquid to the chip would provide negligible pressure. Gravity, or any other external source of energy, is neglected. Thus Eq. A.3 represents the pressure inside the liquid resulting from the wetting of the liquid surface.

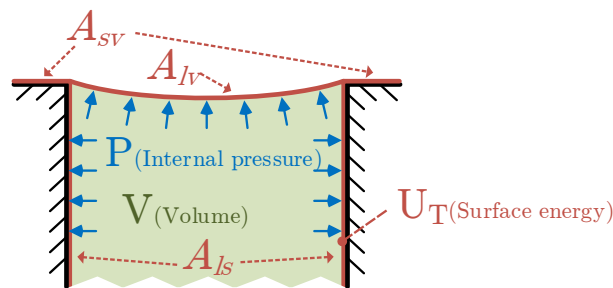


Figure A.10: Cross-section diagram of a capillary tip, showing the internal pressure P , volume V and surface energy U_T . A_{sl} , A_{sv} and A_{lv} are the solid-liquid, solid-vapor and liquid-vapor areas

Appendix A. Liquid transport and containment

For capillary filling, the only type of energy that varies is the interfacial energy, the product of the surface area and the surface tension:

$$U_T = A_{sl}\gamma_{sl} + A_{sv}\gamma_{sv} + A_{lv}\gamma_{lv} = U_0 - \gamma_{lv}(A_{sl}\cos\theta_c - A_{lv}) \quad (\text{A.4})$$

where A_{sl} , A_{sv} , A_{lv} , γ_{sl} , γ_{sv} and γ_{lv} are the surface areas and interfacial surface tensions of the solid-liquid, solid-vapor and liquid-vapor interfaces as shown in Figure A.10. Since the sum of the wetted (A_{sl}) and non-wetted (A_{lv}) areas is constant, $U_0 = (A_{sl} + A_{sv})\gamma_{sv}$ is a constant which disappears when U_T is derived. As before, θ_c is the natural contact angle. For an "hydrophilic" interface ($0^\circ \leq \theta \leq 90^\circ$), the total energy is then reduced as the wetted area is increased. For any liquid, the energy is also reduced as the liquid-vapor area is reduced. From equations A.3 and A.4, it is clear that the internal pressure of the liquid (P) can be calculated by computing the surface areas of the three interfaces as the liquid volume expands.

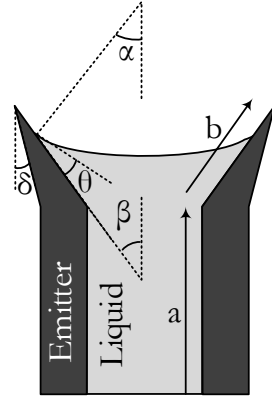
These computations were done for the case of a cylindrical capillary, splitting the progress of the liquid column in five regimes, as shown in Figure A.9. In the first regime, the liquid is contained inside the capillary and, as liquid is added, fills it with a spherical front forming the natural contact angle (θ_c) with the solid. In the second regime, the liquid reaches the opening, deforming beyond its natural contact angle until it forms the angle θ_c with the tip. In regime III, the liquid expands beyond the opening until it reaches the edge of the tip. It then deforms in an increasingly complete sphere until its edge forms the angle θ_c with the vertical capillary sidewall (Regimes IV and V). The model stops when the angle θ_c is reached, not continuing with the wetting of the vertical sidewall. For flexibility of the model, the capillary tip is allowed to be non-horizontal (as defined by angle β) and the emitter edge to be non-vertical (with angle δ), as shown in Figure A.11. Thrusters fabricated in this work always have a $\beta \approx 0^\circ$ while δ was seen to vary from 0° to $\approx 20^\circ$.

General formulas

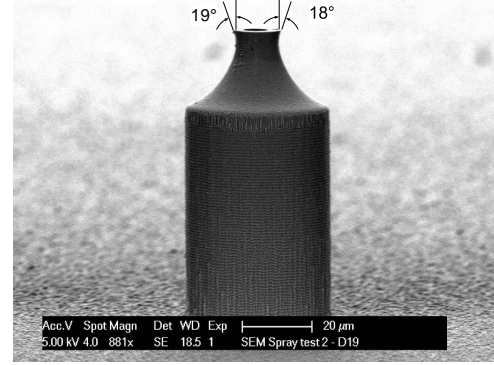
The model requires the computation of the surfaces and volumes of liquid segments inside and at the tip of a cylindrical capillary. A recurring structure is a spherical cap, which will generally terminate the liquid column. Formulas describing the surface and volume of a spherical cap as a function of its height (h) and the diameter (D) of its base are well known, but it is useful to replace the height by the angle (α) which is subtended by the half-cap (Figure A.12). In this section, these are derived, while the liquid column's surface and volume for each regime are described in the next section.

The radius of the meniscus (R) is related to the diameter (D) and subtended angle (α) as:

$$R = \frac{D}{2 \sin \alpha} \quad (\text{A.5})$$



(a) Parameter labeling.



(b) Annotated SEM micrograph of actual emitter.

Figure A.11: SEM micrograph and labeling of parameters relevant to the model. a ($0 \leq a \leq L$) is the progression of liquid inside the capillary and b ($0 \leq b \leq OD$) is the progression on the capillary tip. The angles β ($0 \leq \beta \leq 90^\circ$) and δ ($-90^\circ \leq \delta \leq \beta$) define the geometry. θ is the solid-liquid contact angle and α is the solid half-angle of the spherical front.

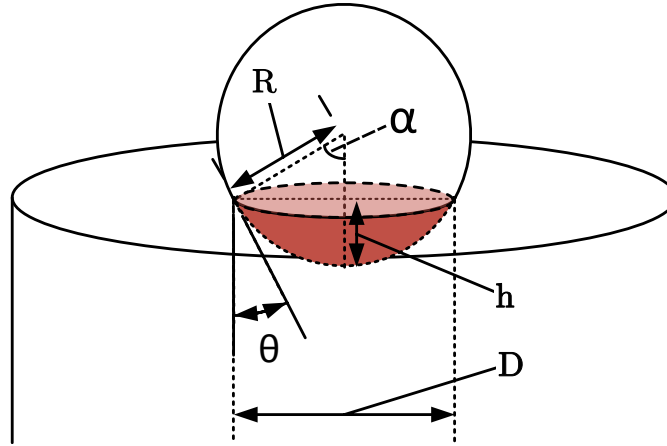


Figure A.12: Sphere with cap outlined above capillary

Additionally, the height (h) of the spherical recess is given by:

$$h = R - R \cos \alpha = \frac{D}{2} \frac{(1 - \cos \alpha)}{\sin \alpha} \quad (\text{A.6})$$

Appendix A. Liquid transport and containment

The surface and volume of the spherical cap are then:

$$A_{cap} = \pi \left(\left(\frac{D}{2} \right)^2 + h^2 \right) = \frac{\pi D^2}{2} \frac{(1 - \cos \alpha)}{\sin^2 \alpha} \quad (\text{A.7})$$

$$V_{cap} = \frac{\pi h}{6} \left(3 \left(\frac{D}{2} \right)^2 + h^2 \right) = \frac{\pi}{24} \left(\frac{D}{\sin \alpha} \right)^3 (2 - \cos \alpha (3 - \cos^2 \alpha)) \quad (\text{A.8})$$

Regime I

In the first regime, the liquid column advances in the capillary with a spherical front contacting the walls with the equilibrium angle θ_c . Hence a very "hydrophilic" liquid with a small contact angle will have a high internal pressure, resulting in a strong force driving it to move into the capillary. A liquid with $\theta_c = 90^\circ$ will not be driven to move in or out of the capillary ($P = 0$) while an "hydrophobic" liquid will have negative pressure and be pushed out of the capillary. This is reflected by Eq. A.11, which corresponds to the well know capillary pressure.

Regime I ($\alpha = 90^\circ - \theta_c$, $a = 0$ to L , $b = 0$)

As the column penetrates a distance a in the capillary, the interfacial energy U_I is straightforwardly obtained from Eq. A.4 using the basic equation for a cylinder for the solid-liquid interface ($A_{sl} = \pi a D$) and Eq. A.7 for the liquid-vapor interface (A_{lv}):

$$U_I = U_0 - \pi D \gamma_{lv} \left(\cos \theta_c a - \frac{D}{2} \left(\frac{1 - \cos \alpha}{\sin^2 \alpha} \right) \right) \quad (\text{A.9})$$

Similarly, the volume is calculated using Eq. A.8:

$$V_I = \frac{\pi D^2}{4} \left(a - \frac{D}{6 \sin^3 \alpha} (2 - \cos \alpha (3 - \cos^2 \alpha)) \right) \quad (\text{A.10})$$

The pressure inside the liquid as it wets the capillary is then derived, obtaining the well-known capillary pressure equation:

$$P_I = - \frac{dU_I}{dV_I} = - \frac{\frac{dU_I}{da}}{\frac{dV_I}{da}} = \frac{\pi D \gamma_{lv} \cos \theta_c}{\frac{\pi D^2}{4}} = \frac{4 \gamma_{lv} \cos \theta_c}{D} \quad (\text{A.11})$$

Regime II

When the liquid reaches a sudden broadening of the capillary, it will, if the volume is forced to increase, deform its advancing front until it again reaches its natural contact angle. For sufficiently large values of beta ($\beta > 90^\circ - \theta_c$), the meniscus will flip its curvature, leading to a negative pressure and effectively forcing the liquid inside the capillary. The half-angle α of the spherical cap will thus be forced from $90^\circ - \theta_c$ to $90^\circ - \theta_c - \beta$:

Regime II ($\alpha = 90^\circ - \theta_c$ to $90^\circ - \theta_c - \beta$, $a = L$, $b = 0$)

In this regime, the liquid-solid interface remains constant but the liquid-gas area changes:

$$U_{II} = U_0 - \pi D \gamma_{lv} \left(\cos \theta_c L - \frac{D}{2} \left(\frac{1 - \cos \alpha}{\sin^2 \alpha} \right) \right) \quad (\text{A.12})$$

$$\frac{dU_{II}}{d\alpha} = \frac{\pi D^2 \gamma_{lv}}{2} \left(\frac{\sin^2 \alpha \sin \alpha - (1 - \cos \alpha) 2 \sin \alpha \cos \alpha}{\sin^4 \alpha} \right) \quad (\text{A.13})$$

$$\frac{dU_{II}}{d\alpha} = \frac{\pi D^2 \gamma_{lv}}{2} \frac{(1 - \cos \alpha)^2}{\sin^3 \alpha} \quad (\text{A.14})$$

The volume and its derivative can also be calculated:

$$V_{II} = \frac{\pi D^2}{4} \left(L - \frac{D}{6 \sin^3 \alpha} (2 - \cos \alpha (3 - \cos^2 \alpha)) \right) \quad (\text{A.15})$$

$$\frac{dV_{II}}{d\alpha} = \frac{-\pi D^3}{24} \left(\frac{-3 \cos \alpha (2 - 3 \cos \alpha + \cos^3 \alpha)}{\sin^4 \alpha} + \frac{(3 \sin \alpha - 3 \cos^2 \alpha \sin \alpha)}{\sin^3 \alpha} \right) \quad (\text{A.16})$$

$$\frac{dV_{II}}{d\alpha} = \frac{-\pi D^3}{8} \frac{(1 - \cos \alpha)^2}{\sin^4 \alpha} \quad (\text{A.17})$$

Finally, the pressure is calculated:

$$P_{II} = -\frac{dU_{II}}{dV_{II}} = -\frac{\frac{dU_{II}}{d\alpha}}{\frac{dV_{II}}{d\alpha}} = \frac{\frac{\pi D^2 \gamma_{lv}}{2} \frac{(1 - \cos \alpha)^2}{\sin^3 \alpha}}{\frac{-\pi D^3}{8} \frac{(1 - \cos \alpha)^2}{\sin^4 \alpha}} = \frac{4 \gamma_{lv} \sin \alpha}{D} \quad (\text{A.18})$$

The pressure in this regime is most negative when $\alpha = 90^\circ - \theta_c - \beta$. In the case of a flat tip ($\beta = 90^\circ$), this becomes:

$$P_{Hold_1} = -\frac{4 \gamma_{lv} \sin \theta_c}{D} \quad (\text{A.19})$$

Appendix A. Liquid transport and containment

Regime III

In the third regime, the meniscus which now has the half-angle $\alpha = 90^\circ - \theta_c - \beta$ expands beyond the broadening and "spills" out of the capillary. The broadening angle β becomes relevant. The distance b_{max} to which the liquid can propagate corresponds to the width of the plateau at the tip of the capillary. The interfacial energy is obtained taking into account a broadening of the base of the spherical cap with the advance of the liquid. This new inner diameter is equal to $D + 2b \sin \beta$. In addition, the solid-liquid area is now a combination of the capillary interior and a cone with half-angle β , base diameter $D_2 = D + 2b \sin \beta$ truncated at a distance $b \cos \beta$ from its base.

Regime III ($\alpha = 90^\circ - \theta_c - \beta$, $a = L$, $b = 0$ to b_{max})

Combining the surfaces, the energy is obtained:

$$U_{III} = U_0 - \pi \gamma_{lv} \left((DL + b(D + b \sin \beta)) \cos \theta_c - \frac{1 - \cos \alpha}{2 \sin^2 \alpha} (D + 2b \sin \beta)^2 \right) \quad (A.20)$$

$$\frac{dU_{III}}{db} = -\pi \gamma_{lv} \left((D + 2b \sin \beta) \cos \theta_c - 2 \frac{1 - \cos \alpha}{\sin^2 \alpha} \sin \beta (D + 2b \sin \beta) \right) \quad (A.21)$$

$$\frac{dU_{III}}{db} = -\pi \gamma_{lv} (D + 2b \sin \beta) \left(\cos \theta_c - 2 \frac{1 - \cos \alpha}{\sin^2 \alpha} \sin \beta \right) \quad (A.22)$$

The volume is also obtained from the combination of the cylinder, truncated cone and cap:

$$V_{III} = \frac{\pi D^2 L}{4} + \frac{\pi b \cos \beta}{12} (4b^2 \sin^2 \beta + 6bD \sin \beta + 3D^2) - \dots$$

$$\frac{\pi (2 - \cos \alpha (3 - \cos^2 \alpha))}{24 \sin^3 \alpha} (D + 2b \sin \beta)^3 \quad (A.23)$$

$$\frac{dV_{III}}{db} = \frac{\pi}{4} \left(\cos \beta (D + 2b \sin \beta)^2 - \frac{(2 - \cos \alpha (3 - \cos^2 \alpha))}{\sin^3 \alpha} (D + 2b \sin \beta)^2 \sin \beta \right) \quad (A.24)$$

$$\frac{dV_{III}}{db} = \frac{\pi}{4} (D + 2b \sin \beta)^2 \left(\cos \beta - \frac{\sin \beta (2 - \cos \alpha (3 - \cos^2 \alpha))}{\sin^3 \alpha} \right) \quad (A.25)$$

Finally, the pressure is obtained as before:

$$P_{III} = -\frac{dU_{III}}{dV_{III}} = -\frac{\frac{dU_{III}}{db}}{\frac{dV_{III}}{db}} \quad (A.26)$$

$$P_{III} = \frac{4\gamma_{lv} \sin \alpha}{(D + 2b \sin \beta) \sin^3 \alpha \cos \beta - (2 - \cos \alpha (3 - \cos^2 \alpha)) \sin \beta} \quad (A.27)$$

Regime IV

Once the liquid reaches the edge of the capillary, it will reach another pressure barrier. If the liquid is again pushed by applying a backpressure, the liquid meniscus will deform spherically until it is able to wet the vertical edge of the capillary. This deformation can be divided in two regimes. In regime IV, the meniscus reaches a half-sphere, with central point on the plane of the emitter. In regime V, the center point will move upwards from the plane and the sphere will become increasingly complete.

Regime IV ($\alpha = 90^\circ - \theta_c - \beta$ to -90° , $a = L$, $b = b_{max}$)

$$U_{IV} = U_0 - \pi\gamma_{lv} \left((DL + b(D + b \sin \beta)) \cos \theta_c - \frac{1 - \cos \alpha}{2 \sin^2 \alpha} (D + 2b \sin \beta)^2 \right) \quad (\text{A.28})$$

$$\frac{dU_{IV}}{d\alpha} = \frac{\pi\gamma_{lv} (D + 2b \sin \beta)^2}{2} \left(\frac{\sin^2 \alpha \sin \alpha - (1 - \cos \alpha) 2 \sin \alpha \cos \alpha}{\sin^4 \alpha} \right) \quad (\text{A.29})$$

$$\frac{dU_{IV}}{d\alpha} = \frac{\pi\gamma_{lv} (D + 2b \sin \beta)^2}{2} \frac{(\cos \alpha - 1)^2}{\sin^3 \alpha} \quad (\text{A.30})$$

$$(\text{A.31})$$

$$V_{IV} = \frac{\pi D^2 L}{4} + \frac{\pi b \cos \beta}{12} (4b^2 \sin^2 \beta + 6bD \sin \beta + 3D^2) - \dots$$

$$\frac{\pi (2 - \cos \alpha (3 - \cos^2 \alpha))}{24 \sin^3 \alpha} (D + 2b \sin \beta)^3 \quad (\text{A.32})$$

$$\frac{dV_{IV}}{d\alpha} = -\frac{\pi (D + 2b \sin \beta)^3}{8} \left(\frac{1 - \cos \alpha (2 + \cos \alpha (\sin^2 \alpha - 2 + \cos^2 \alpha))}{\sin^4 \alpha} \right) \quad (\text{A.33})$$

$$\frac{dV_{IV}}{d\alpha} = -\frac{\pi (D + 2b \sin \beta)^3}{8} \frac{(\cos \alpha - 1)^2}{\sin^4 \alpha} \quad (\text{A.34})$$

Thus in region IV, the pressure is given as:

$$P_{IV} = -\frac{dU_{IV}}{dV_{IV}} = -\frac{\frac{dU_{IV}}{d\alpha}}{\frac{dV_{IV}}{d\alpha}} = \frac{\frac{\pi\gamma_{lv} (D + 2b \sin \beta)^2 (\cos \alpha - 1)^2}{2 \sin^3 \alpha}}{\frac{\pi (D + 2b \sin \beta)^3 (\cos \alpha - 1)^2}{8 \sin^4 \alpha}} = \frac{4\gamma_{lv} \sin \alpha}{D + 2b \sin \beta} \quad (\text{A.35})$$

Appendix A. Liquid transport and containment

Regime V

In regime V, the drop continues to deform spherically, beyond the shape of a half sphere. It is convenient to compute the surface and volume of the drop by subtracting the surface and volume of a spherical cap from a complete sphere.

Regime V ($\alpha = 90^\circ$ to $90^\circ - \theta_c + \delta$, $a = L$, $b = b_{max}$)

The surface area and volume of the drop:

$$A_{drop} = \pi D^2 - \frac{\pi D^2 (1 - \cos \alpha)}{2 \sin^2 \alpha} = \frac{\pi (D + 2b \sin \beta)^2}{2} \left(\frac{1 + \cos \alpha (1 - 2 \cos \alpha)}{\sin^4 \alpha} \right) \quad (A.36)$$

$$V_{drop} = \frac{4\pi D^3}{24} - \frac{\pi D^3 (2 - \cos \alpha (3 - \cos^2 \alpha))}{24 \sin^3 \alpha} \quad (A.37)$$

$$V_{drop} = \frac{\pi (D + 2b \sin \beta)^3}{24} \left(\frac{4 \sin^3 \alpha - 2 + 3 \cos \alpha - \cos^3 \alpha}{\sin^6 \alpha} \right) \quad (A.38)$$

The surface energy and volume in Regime V:

$$U_V = U_0 - \pi \gamma_{lv} ((DL + b(D + b \sin \beta)) \cos \theta_c) + \dots \\ \pi \gamma_{lv} \left(\frac{(D + 2b \sin \beta)^2}{2} \left(\frac{1 + \cos \alpha (1 - 2 \cos \alpha)}{\sin^4 \alpha} \right) \right) \quad (A.39)$$

$$\frac{dU_V}{d\alpha} = - \frac{\pi \gamma_{lv} (D + 2b \sin \beta)^2}{2 \sin^5 \alpha} (1 + \cos^2 \alpha (3 - 4 \cos \alpha)) \quad (A.40)$$

$$V_V = \frac{\pi D^2 L}{4} + \frac{\pi b \cos \beta}{12} (4b^2 \sin^2 \beta + 6bD \sin \beta + 3D^2) + \dots \\ \frac{\pi (D + 2b \sin \beta)^3}{24} \left(\frac{4 \sin^3 \alpha - 2 + 3 \cos \alpha - \cos^3 \alpha}{\sin^6 \alpha} \right) \quad (A.41)$$

$$\frac{dV_V}{d\alpha} = - \frac{\pi (D + 2b \sin \beta)^3}{8 \sin^7 \alpha} (1 + \cos \alpha (4 \sin \alpha - 4 + \dots \\ \cos \alpha (4 - \cos \alpha (4 \sin \alpha + \cos \alpha)))) \quad (A.42)$$

The pressure is calculated as before:

$$P_V = - \frac{4\gamma_{lv} \sin^2 \alpha}{(D + 2b \sin \beta)} \frac{(1 + \cos^2 \alpha (3 - 4 \cos \alpha))}{(1 + \cos \alpha (4 \sin \alpha - 4 + \cos \alpha (4 - \cos \alpha (4 \sin \alpha + \cos \alpha))))} \quad (A.43)$$

A.2.3 Model summary

To visualize the entire system, the energy and pressure can be plotted as a function of the volume for all five regimes. These plots are shown in Figure A.13 for the energy and Figure A.14 for the pressure. Figure A.15 shows 2D cross section diagrams of the modeled cases. In all cases, the contact angle θ_c is set to 45° . The curves show six cases, representing β values of 30° , 60° and 90° and δ values of 0° and 20° . The lines corresponding to the different values of δ are indistinguishable since the only effect of δ is to change the maximum size of the simulated sphere.

Looking at the curve minimums, we see that, depending on the value of θ_c and β , up to two pressure barriers, corresponding to the curve minimums, are experienced by the meniscus. The first barrier occurs when the liquid column is standing at the broadening ($a = L$, $b = 0$) and the liquid meniscus is deformed just so that it almost reached its natural contact angle with the tip (Regime II, $\alpha = 90^\circ - \theta_c - \beta$). It occurs only if α is negative. The second barrier, always present, occurs when the liquid reaches the outer edge of the capillary tip and is deformed into a half-sphere (Regime IV, $\alpha = -90^\circ$). These two holding pressures are given by Eq. A.44 and Eq. A.45.

$$P_{Hold_1} = \frac{4\gamma_{lv} \sin \alpha}{D} = \frac{4\gamma_{lv} \cos(\theta_c + \beta)}{D} \quad (\text{A.44})$$

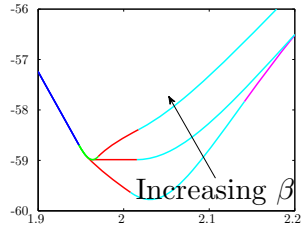
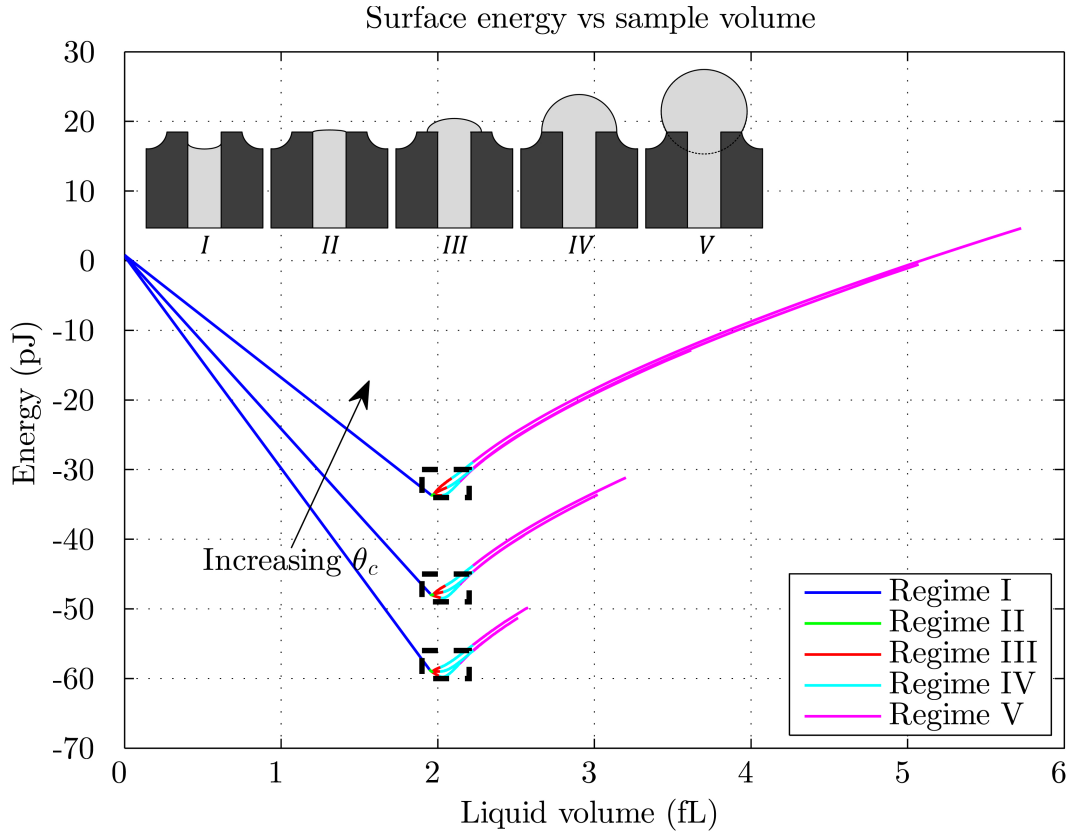
$$P_{Hold_2} = \frac{4\gamma_{lv} \sin \alpha}{D + 2b \sin \beta} = -\frac{4\gamma_{lv}}{D + 2b \sin \beta} \quad (\text{A.45})$$

In the case of a flat tip ($\beta = 90^\circ$, $\delta = 0^\circ$), these simplify to Eq. A.46 and Eq. A.47:

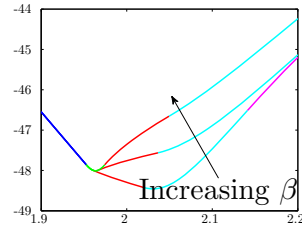
$$P_{Hold_1} = -\frac{4\gamma_{lv} \sin \theta_c}{D} \quad (\text{A.46})$$

$$P_{Hold_2} = \frac{4\gamma_{lv} \sin \alpha}{D + 2b \sin \beta} = -\frac{4\gamma_{lv}}{D + 2b} \quad (\text{A.47})$$

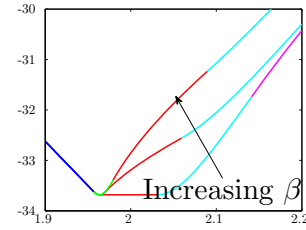
Equation Eq. A.46 and Eq. A.11 indicate that while a more wetting liquid (low θ_c) will have a higher *capillary pressure* and more easily fill the capillary, it will be less resistant to spillage. Up to about $\theta_c = 20^\circ$, the second barrier will be strongest. A liquid with higher θ_c will on the other hand have a higher *holding pressure*. Figure A.16a represents the above graphically. As respresented in Figure A.16b, both the "filling" and the "holding" are increased by having a smaller inner diameter (D) capillary. Figure A.16b also plots the maximum static acceleration that could be supported by a 10cm column of $EMI - BF_4$ under these pressures.



(b) Zoom $\theta_c = 30^\circ$, Corresponding to bottom dashed region in (a)



(c) Zoom $\theta_c = 45^\circ$, Corresponding to middle dashed region in (a)



(d) Zoom $\theta_c = 60^\circ$, Corresponding to upper dashed region in (a)

Figure A.13: Surface energy (pJ) vs volume(fL) for a $5\mu\text{m}$ ID, $10\mu\text{m}$ OD capillary. $\theta_c = 30^\circ, 45^\circ, 60^\circ$; $\beta = 30^\circ, 60^\circ, 90^\circ$. The figures (b),(c),(d) correspond to close up views of the three dashed region in (a)

A.2. Capillary filling and holding pressure model

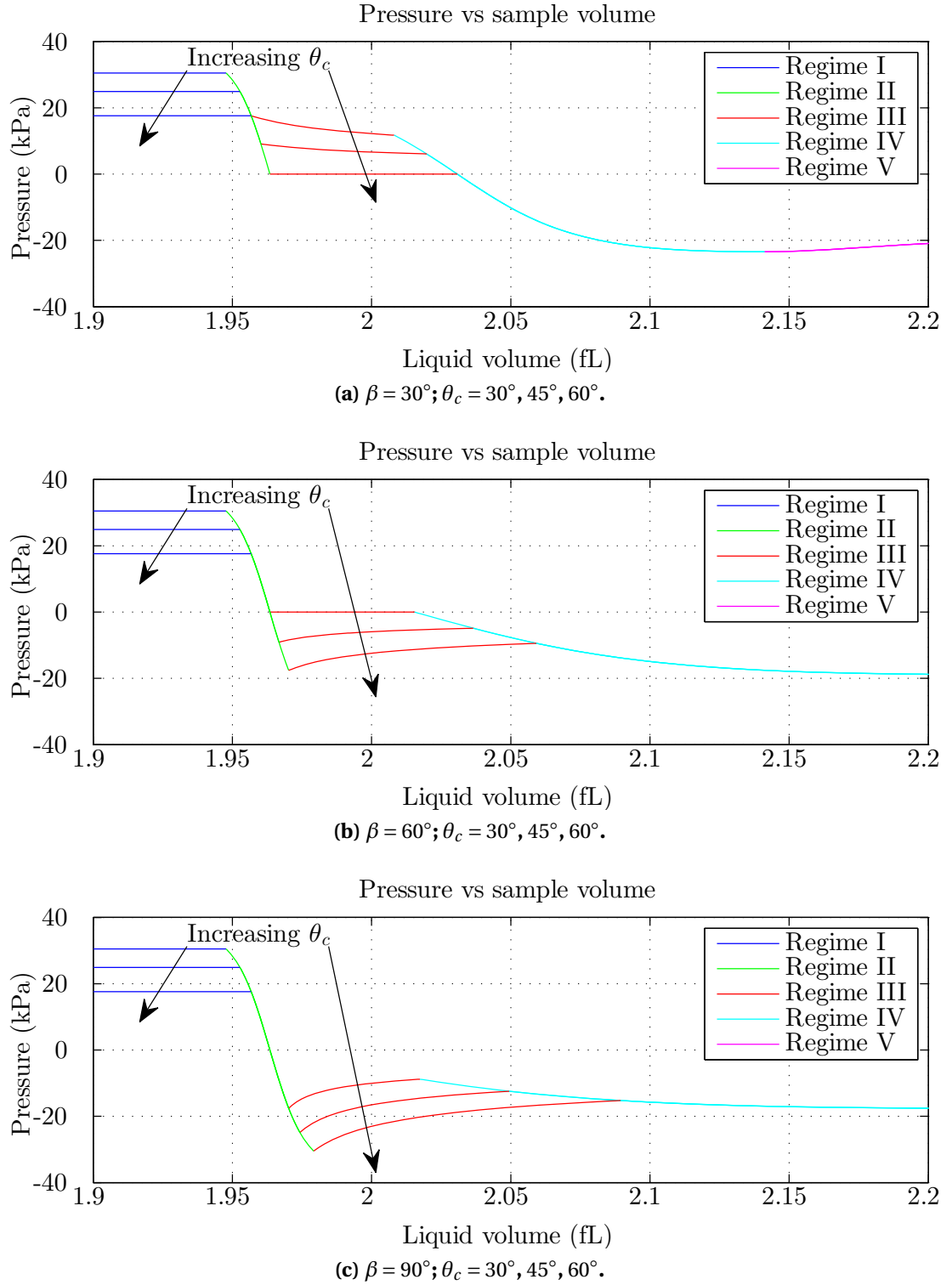


Figure A.14: Pressure (kPa) vs volume(fL) for a $5\mu\text{m}$ ID, $10\mu\text{m}$ OD capillary. $\theta_c = 30^\circ, 45^\circ, 60^\circ$; $\beta = 30^\circ, 60^\circ, 90^\circ$

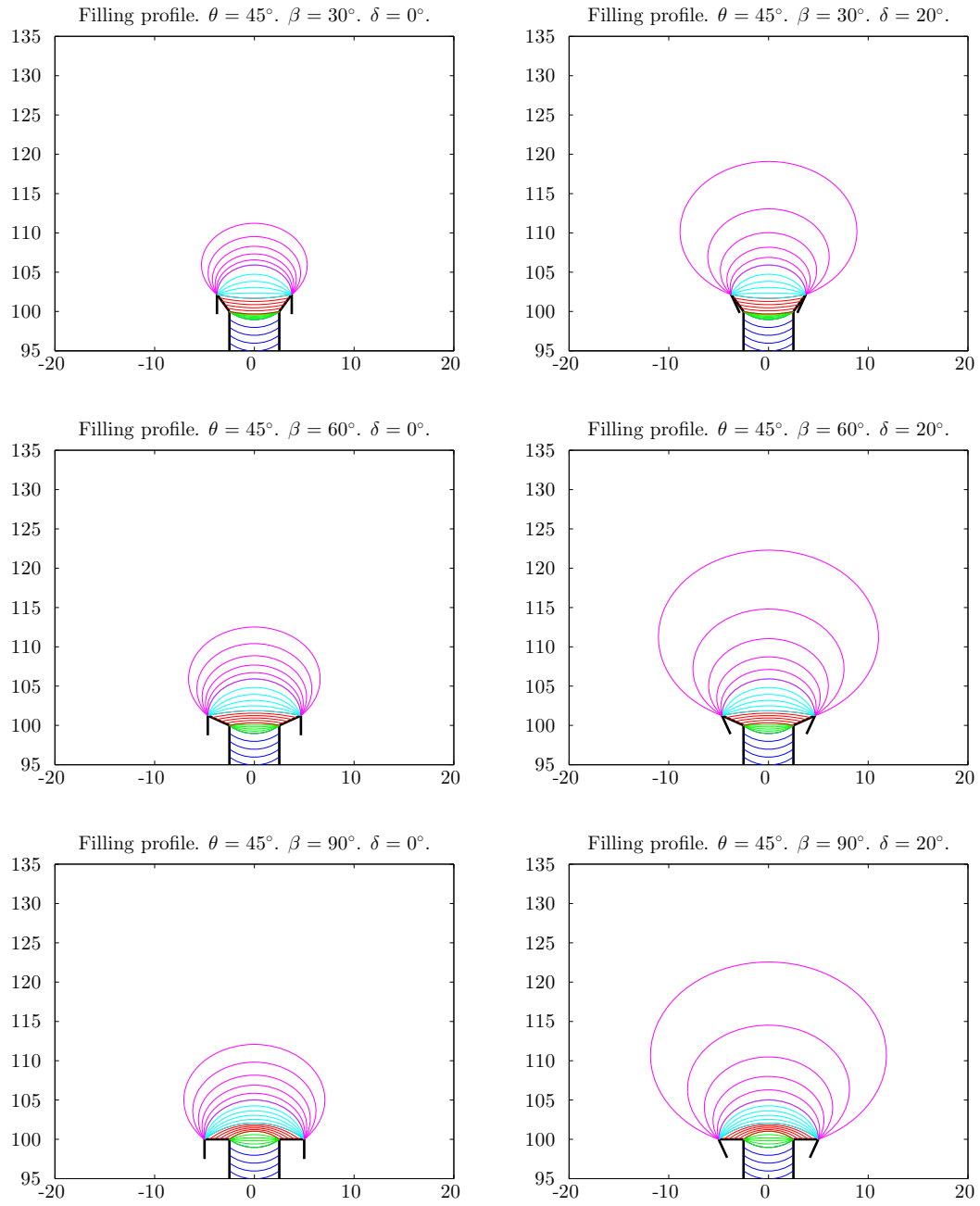
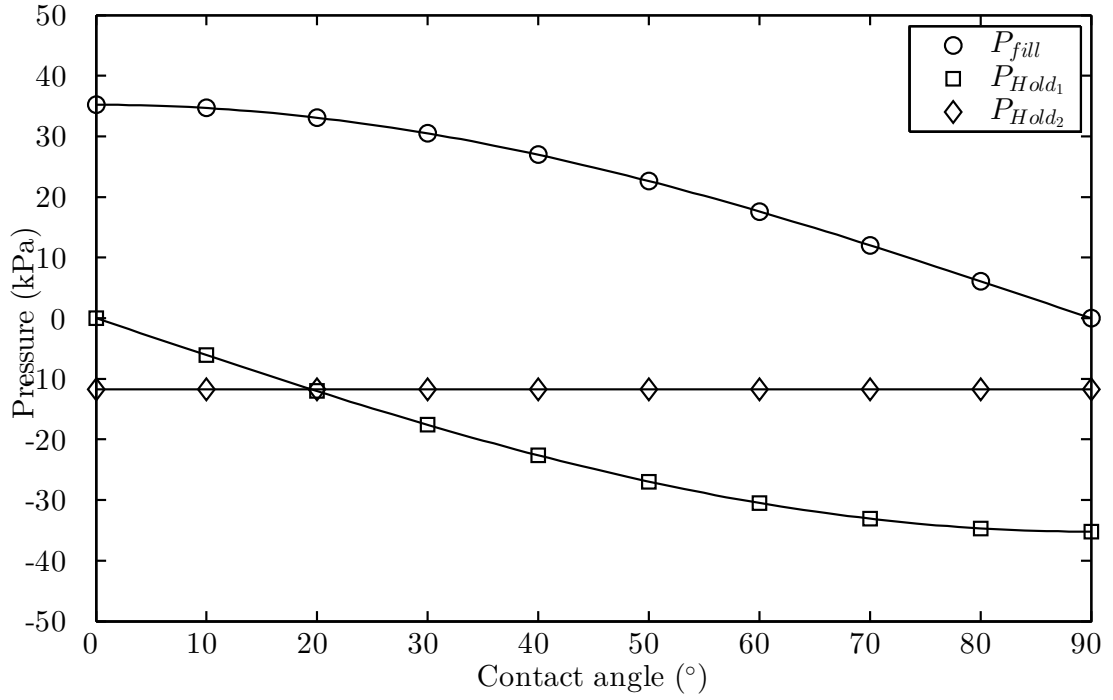
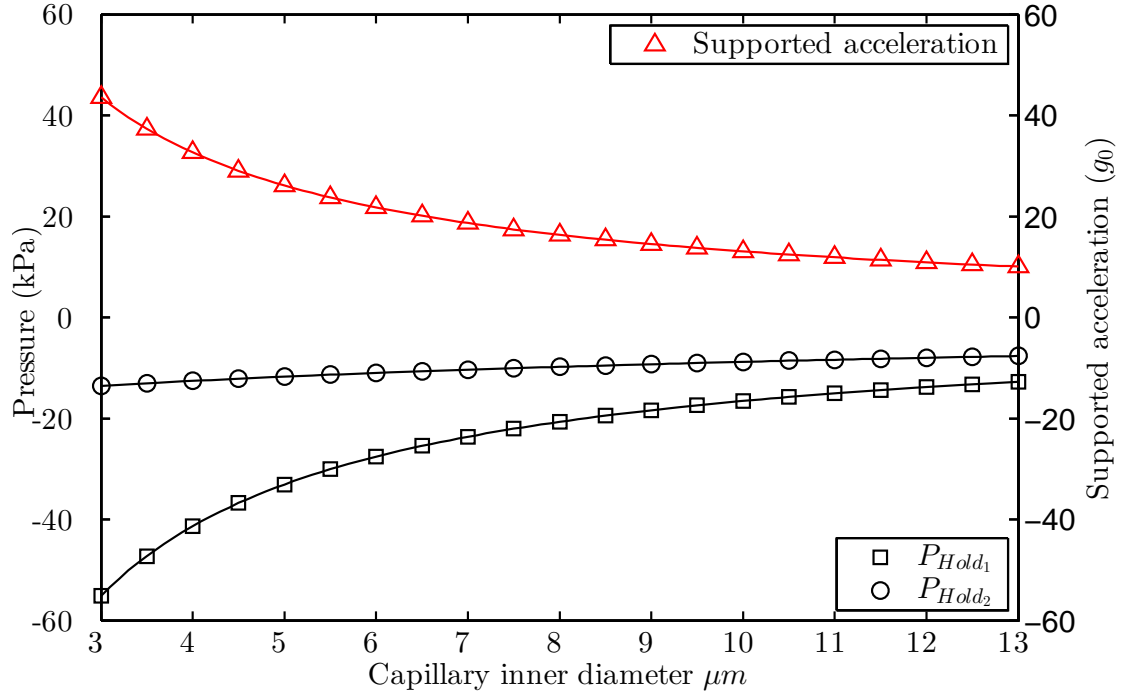


Figure A.15: Filling profiles of liquid meniscus for several emitter geometries.

A.2. Capillary filling and holding pressure model



(a) Filling and holding pressure for a 5 μm ID capillary with the ionic liquid EMI-BF₄

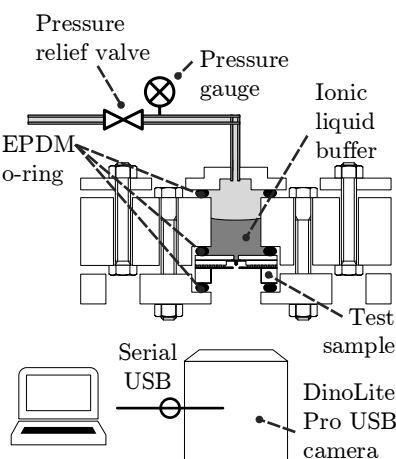


(b) Holding pressure and maximum supported acceleration for a 5 μm ID capillary with the ionic liquid EMI-BF₄ and contact angle $\theta_c = 70^\circ$

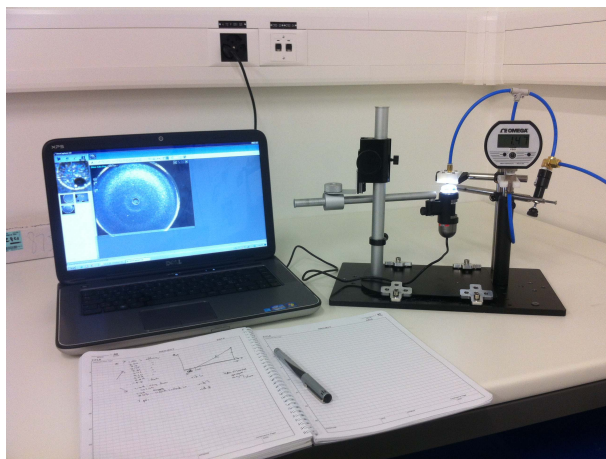
Figure A.16: Holding pressures vs contact angle and capillary inner diameter

A.2.4 Experimental validation of holding pressure

A simple setup (Figure A.17) was used to validate the results obtained from the analytical model. Seven die were subjected to the holding pressure tests with the ionic liquid $EMI - BF_4$. Each die was first inspected in the SEM to measure the dimensions of the capillary inner diameters. The die were then clamped between two polyoxymethylene (POM) plates and loaded in vacuum with a small amount (≈ 5 mm reservoir filling) of liquid, in a manner similar to that of the contact angle measurements. After clamping an additional adapter POM plate, they were connected to the nitrogen supply line through a pressure relief valve. Three EPDM rubber o-rings were used to ensure good sealing. The pressure was varied manually and read on a pressure gauge (Omega DPG1000B-15G). A DinoLite PRO USB camera was used to observe the front of the die (looking up), monitoring the pressure at which liquid can be seen to overflow from the emitter tips. Using the value of $71.6 \pm 2.3^\circ$ for the contact angle, we compute, using equation Eq. A.46, a range of expected holding pressure: 36.9 ± 0.8 kPa (1σ).



(a) Diagram of hold pressure setup.



(b) Optical photograph of hold pressure setup.

Figure A.17: Holding pressure test setup. Nitrogen is used to pressurize a sealed reservoir. Looking upwards, a USB camera monitors liquid overflow.

Table A.1 shows the expected and measured holding pressure for each tested die. Since cleaning of the die could leave residues which would change the effective inner diameter, each die was tested once. The global averages and standard deviations are also given (36.9 ± 0.8 kPa and 29.9 ± 4.0 kPa for the expected and measured pressures). The results are in good agreement, although the measured holding pressures are slightly lower than expected. Aside from one sample, chips with single emitters appeared to have holding pressures closer to their expected values. In the case of arrays, only the "first" bursting emitter is reported. In fact, several emitters in those die required larger pressures for the liquid to overflow. However, these later holding pressures were considered invalid, since part of the array was already flowing.

For a 10cm reservoir, over $20g_0$ could still be withheld, even in the worst case measured ($p_{\text{Hold}} = 25.4$ kPa). This value is well above the maximal $5g_0$ seen by an Ariane 5 launcher,

A.3. Liquid retention under vibration and shock

Table A.1: Expected and measured holding pressure values.

Die ID	Array size	Average inner diameter (μm)	Expected holding pressure (kPa)	Measured holding pressure (kPa)
L1W6D05	1	4.5	37.1 ± 0.5	35.9
L1W6D06	1	4.5	37.1 ± 0.5	25.4
L1W6D09	1	4.7	35.6 ± 0.5	33.4
L1W6D15	19	4.5	37.1 ± 0.5	25.4
L1W6D18	19	4.6	36.6 ± 0.5	28.1
L1W6D31	19	4.4	37.9 ± 0.5	31.4
L1W6D20	61	4.5	37.1 ± 0.5	29.6
Average			36.9 ± 0.8	29.9 ± 0.4

indicating that no propellant spillage should occur during a launch, at least resulting from static acceleration.

In the next section, liquid containment is further studied in this launch environment, this time considering dynamic shock and vibration conditions.

A.3 Liquid retention under vibration and shock

The microthrusters can at launch be subjected to intense shock and vibrations which could potentially lead to permanent device damage. In addition, filled capillaries would again face the additional requirements of containing the propellant under these conditions.

Thus preliminary shock and vibration tests were performed on the MicroThrust chips. The results were compared against typical levels (Ariane 5 acceptance, for vibrations, LISA Pathfinder mission, for shock) as shown in Figure A.18. The LISA Pathfinder requirements, provided through internal communications by ESA, are good upper bounds for the shock tests due to their harshness and the relevance of the mission to electrospray propulsion.

The vibration tests were carried out as part of a semester project by student Basil Huber, and much of the results reproduced here are more extensively presented in his report “Study of Capillary Liquid Retention in Vibration” [130].

The die used for these shock and vibration tests were single emitters and arrays of up to 19 emitters. They did not have a bonded extractor electrode to allow easier observation of the sample before and after test. The liquid used for all the tests was $EMI - BF_4$.

For both experiments, optical microscope and SEM observations were used to evaluate whether liquid had spilled out of the emitters. While not perfect, a tradeoff led to this solution as the most viable to determine spillage. Indeed, quantitative methods such as weight measurement would not have the required sensitivity to detect minuscule drops. In-situ ob-

servation, with a high speed camera, was also attempted, but it was not possible to combined the large magnification required for emitter observation with their displacement during test. Electrical measurements would also have been difficult due to the already conductive nature of silicon.

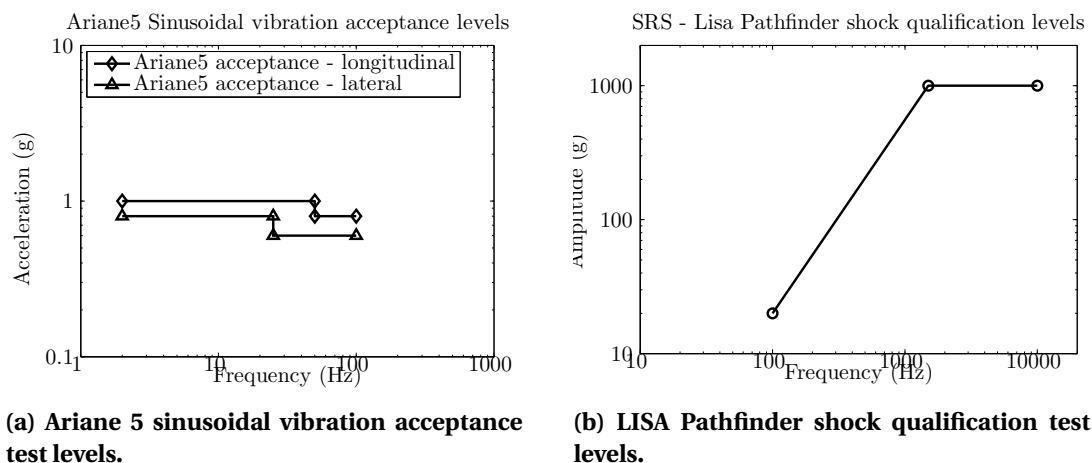


Figure A.18: Acceptance and qualification of vibration and shock tests.

A.3.1 Vibration tests

Setup and procedure

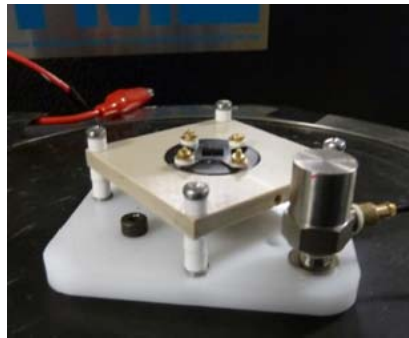
Figure A.19a is an optical image of the magnetic excitation table (Vibration Exciter System V (body 4805, head 4811) of Bruel and Kjoer) available from EPFL's SAMLAB. The table was controlled by an external amplifier and could provide a broad range of vibration. The main limitations were at low frequency, as the table could not achieve greater than 12.7mm displacement and 1.27 m/s velocity

The test samples were clamped using the a test assembly machined from a ThorLabs aluminum lens-cap Figure A.19c. The assembly itself was attached to a Teflon holder screwed to the shaker table via a POM adapter Figure A.19b. An accelerometer was bolted directly to the POM adapter, a few centimeters from the test sample. FEM simulations of a coarse assembly model performed in COMSOL showed that its fundamental resonance frequency was above 6 kHz Figure A.20, ensuring that the assembly would not dampen low frequency vibrations.

Three die were tested under soft or "harsh" conditions (See Table A.2). Aside from <10Hz frequencies, the levels tested were much higher than the acceptance levels of Ariane5. Each datapoint in Figure A.21 represents a vibration experiment, before and after which the sample was inspected optically. In the test sequence, all amplitudes were tested at a certain frequency (with increasing level) before proceeding to the next, higher frequency. At the end of the sequence, the samples were re-inspected with the SEM.



(a) EPFL SAMLAB's magnetic shaker table.



(b) Sample attached to table via POM adapter



(c) Test sample mounted on test assembly

Figure A.19: Sinusoidal vibration test setup.

Table A.2: Sinusoidal vibration tests results.

Sample	Number of emitters	Test levels	Results
V1	01	Soft	No observed spillage
V2	19	Harsh	No observed spillage
V3	01	Harsh	No observed spillage

Results and analysis

Figure A.23 shows before and after SEM micrographs of the die subjected to the sinusoidal vibrations. No evidence of spillage or damaged emitters was seen for any of the tested die. On several die (e.g. Figure A.23b), however, it was possible to see particles or flakes at the surface of the liquid meniscus. EDX analysis (Figure A.22) showed traces of carbon, fluorine, sodium and aluminum. The fluorine was probably detected due to the presence of $EMI - BF_4$ on the particle or could have been a residue from the Vapour HF BOX etch. Carbon could have been SEM contamination, as well as the faint traces of other elements. One possibility is that the particles would in fact be flakes of BOX silicon dioxide or DRIE polymer dislodged during vibration.

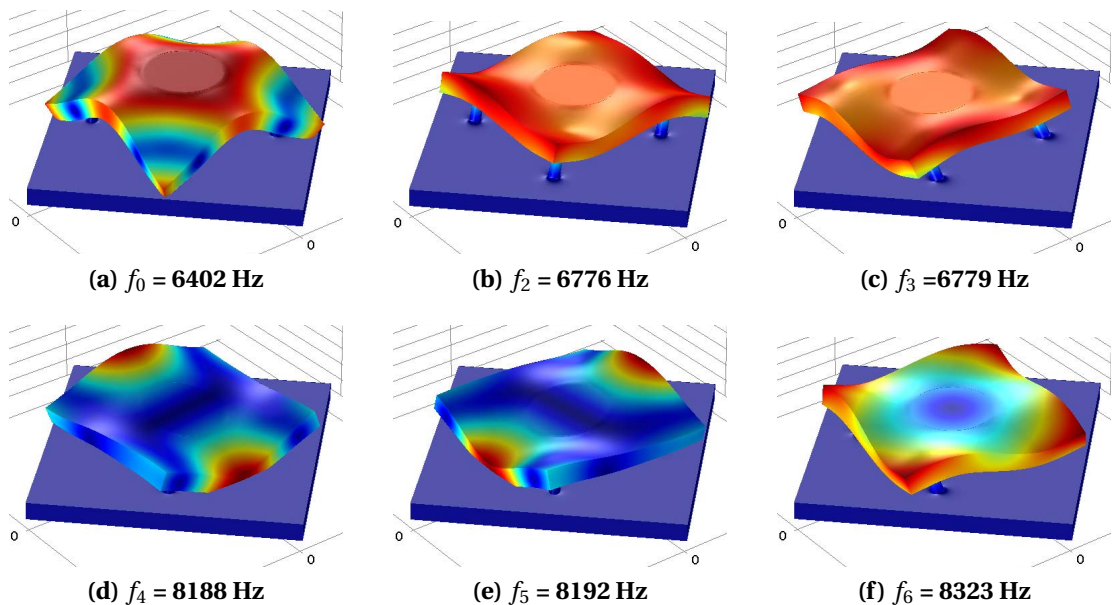


Figure A.20: Six first resonant modes of vibration test attachment bracket

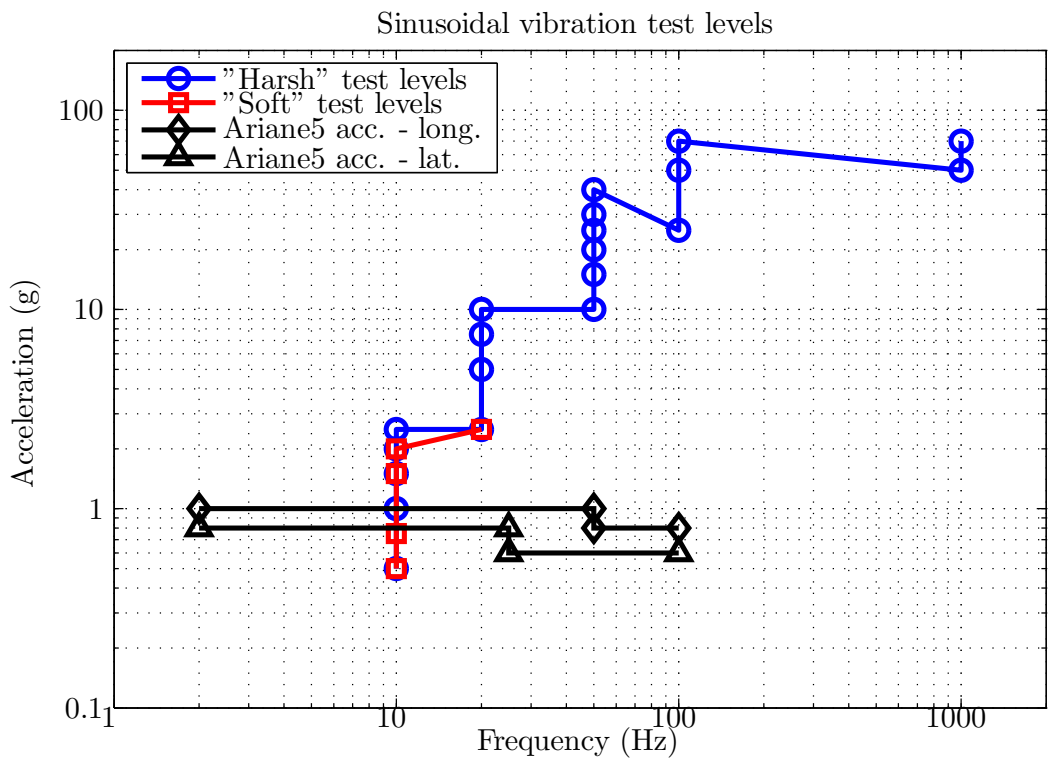
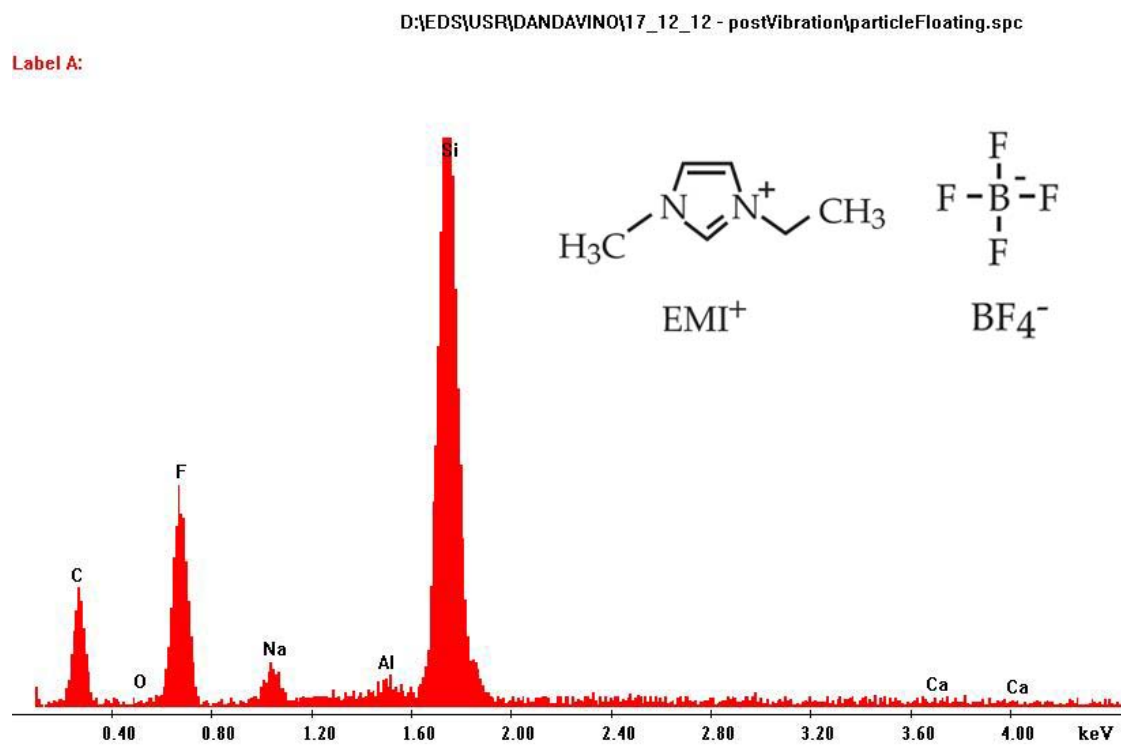
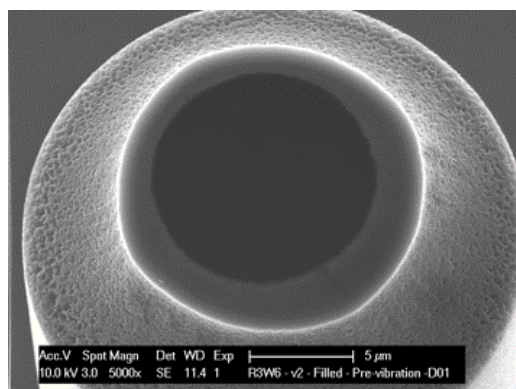


Figure A.21: Levels considered for vibration test. Devices are incrementally tested from lower to higher acceleration and lower to higher frequency with inspections between each step. Devices are subjected to either "soft" or "harsh" test levels.

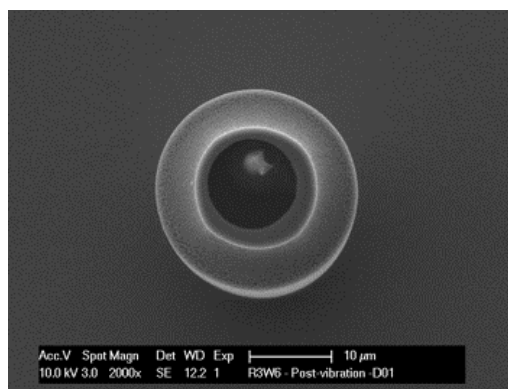
A.3. Liquid retention under vibration and shock



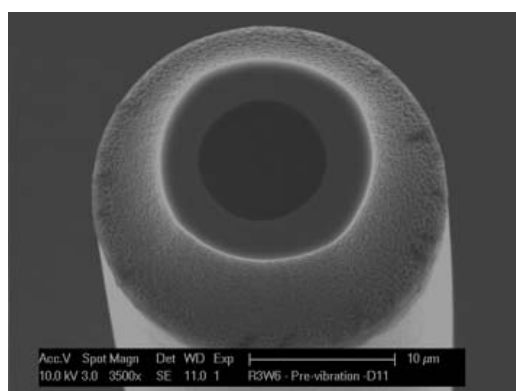
Appendix A. Liquid transport and containment



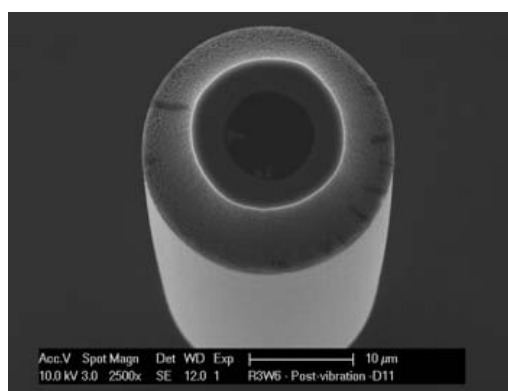
(a) Sample V1 before test



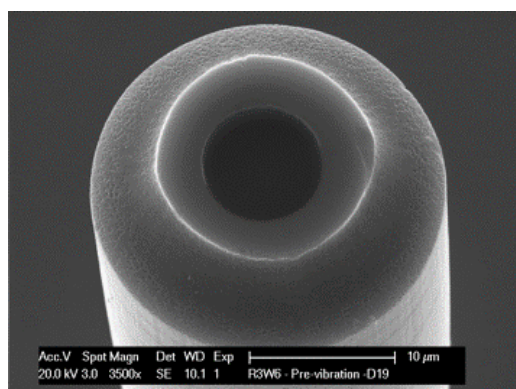
(b) Sample V1 after test



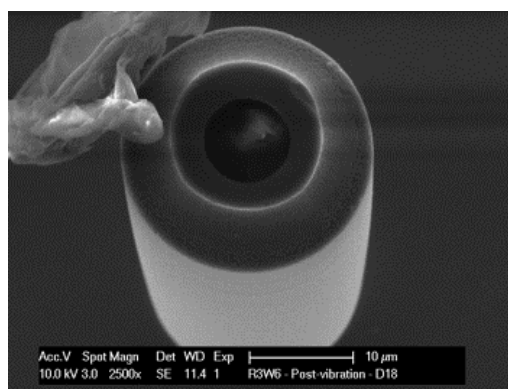
(c) Sample V2 before test



(d) Sample V2 after test



(e) Sample V3 before test



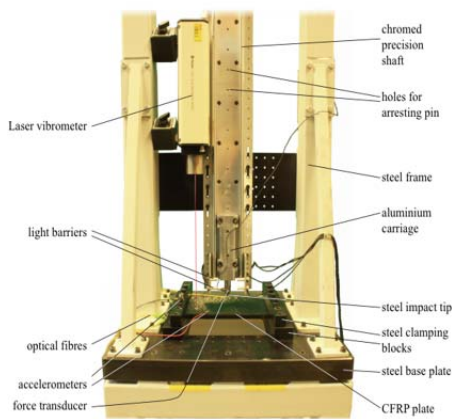
(f) Sample V3 after test

Figure A.23: SEM micrographs of emitters before and after sinusoidal vibration tests. No evidence of emitter damage or liquid spillage was seen in any test performed. The large particle in (f) is due to contamination during handling.

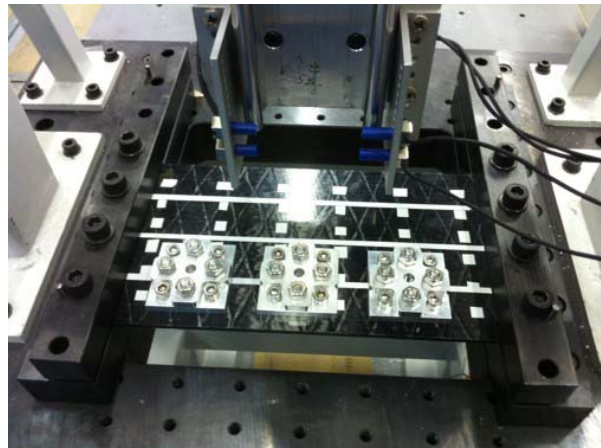
A.3.2 Shock tests

Setup and procedure

Shock tests were performed at EPFL's LMAF laboratory (Laboratory of Applied Mechanics and Reliability Analysis) in a drop tower constructed by J. Frieden [131]. The tower (Figure A.24a) employed a weight which could be dropped from a maximum height of 1855mm. A Carbon Fibre Reinforced Polymer (CFRP) plate was used to receive the shock. A force sensor was integrated in the contact head which triggered data acquisition.



(a) Diagram of tower, reproduced from [131]



(b) Optical image of drop tower with three mounted samples on CFRP plate. In the actual tests, the plate was turned upside down and the weight fell directly over the test sample to maximize shock.

Figure A.24: Diagram and image of shock test setup

The test samples were mounted on the CFRP plate using aluminum brackets (Figure A.24b). The samples were sandwiched between the two brackets, which were in turn bolted to the CFRP plate. The weight was dropped on the backside of the plate so that maximum shock would be propagated to the sample. L-brackets were also fabricated to orient devices laterally to the propagating shockwaves (Figure A.25).

Acquisition was done with an accelerometer attached to the aluminum bracket using bee's wax and connected to a PC via an external amplifier and data acquisition card. The data recording was performed using LabView, and was triggered when the weight hit the plate. The results were then exported to a text file and analyzed using Matlab. The Shock Response Spectrum was generated using the Smallwood algorithm through a routine written by T. Irvine [132]. As is commonly done, a Q-factor of 10, corresponding to 5% damping, was used.

Six samples were tested according to the conditions in Table A.3. Figure A.26 shows images of the tested emitters before filling with the ionic liquid $EMI - BF_4$.

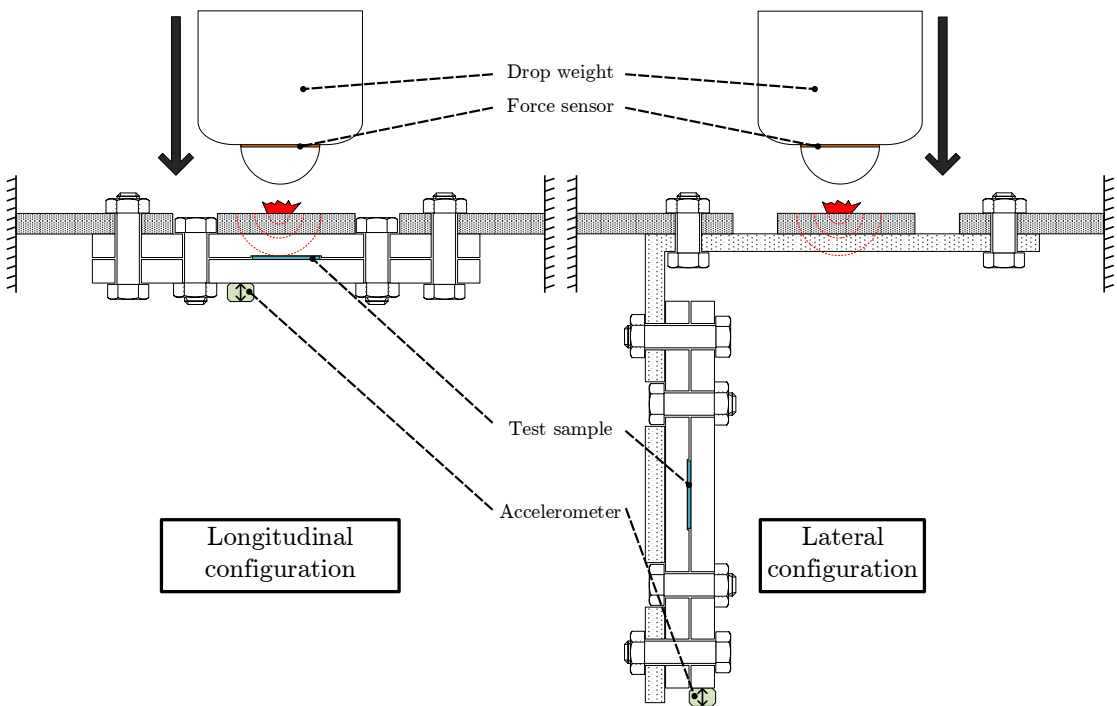


Figure A.25: Longitudinal and lateral shock test assemblies.

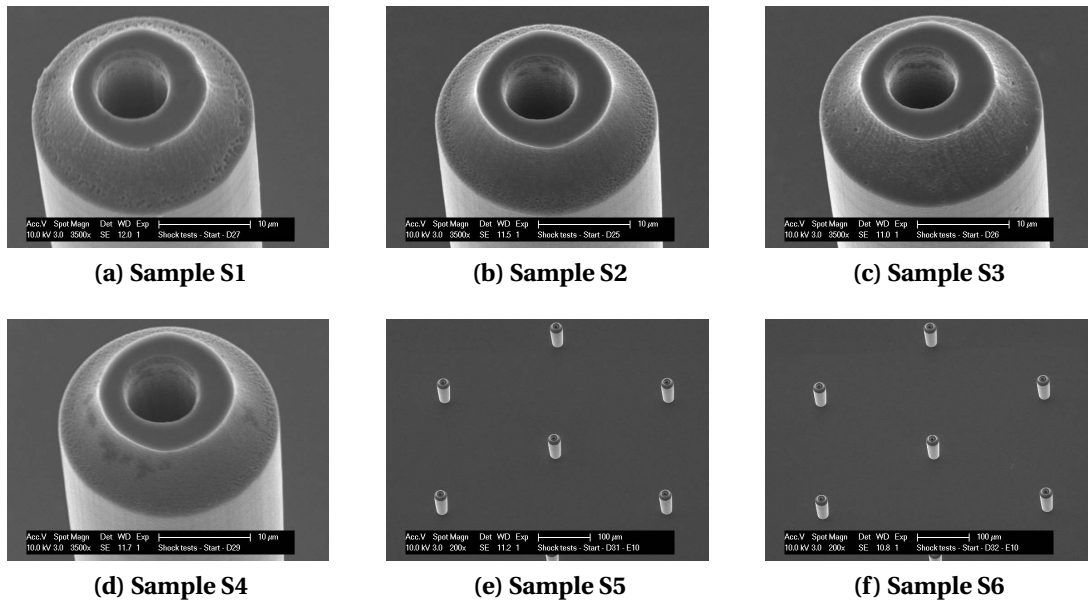


Figure A.26: SEM micrographs of emitters before filling with $EMI - BF_4$.

A.3. Liquid retention under vibration and shock

Table A.3: Shock tests conditions.

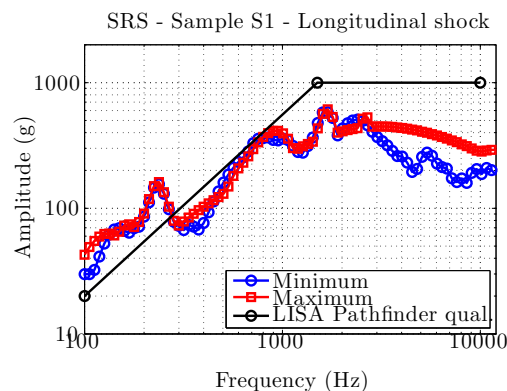
Sample	Number of emitters	Drop height (mm)	Configuration	Results
S1	01	500	Longitudinal	No observed spillage
S2	01	750	Longitudinal	One drop observed
S3	01	750	Longitudinal	No observed spillage
S4	19	750	Longitudinal	No observed spillage
S5	01	750	Lateral	No observed spillage
S6	19	750	Lateral	No observed spillage

Results and analysis

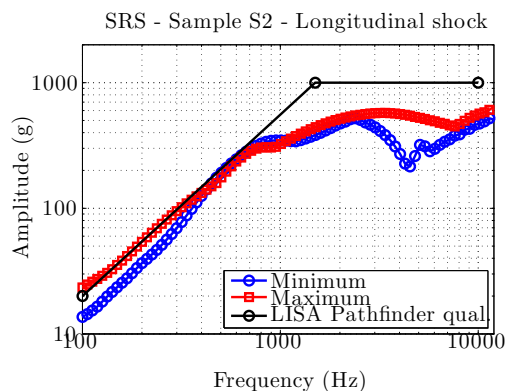
Figure A.27 shows the Shock Response Spectrums (SRS) of the tested samples. With a 750mm drop, at 10 kHz approximately 4000 m/s^2 ($\approx 400\text{g}$) can be generated in the longitudinal axis and 800 m/s^2 (80g) in the lateral direction. This is below the Lisa qualification level of 1000g but, at least for the longitudinal tests, in the right order of magnitude.

Figure A.28 shows images of three devices before and after shock. The images shown here are only a small sample of the observations made and only show the single emitter devices. While in most cases, no drop was observed, for sample S2 a small drop of ionic liquid was seen approximately $25\mu\text{m}$ away from the emitter. Figure A.29 shows a close-up SEM micrograph of this drop. The rest of the sample, including the emitter tip, was however unaffected by the shock.

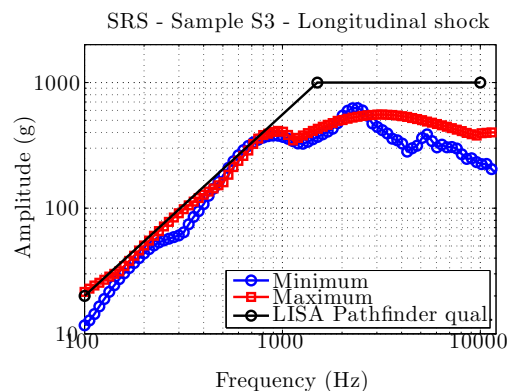
Whether this drop indeed resulted from liquid escaping the containment of the capillary, or whether it resulted from contamination during handling is unclear. Considering that the liquid meniscus at the tip of the emitter was unchanged and that the other samples being subjected to the same test levels did not exhibit any liquid spillage, the second explanation is thought more likely. In any case, more extensive testing would be required before qualifying the devices for spaceflight.



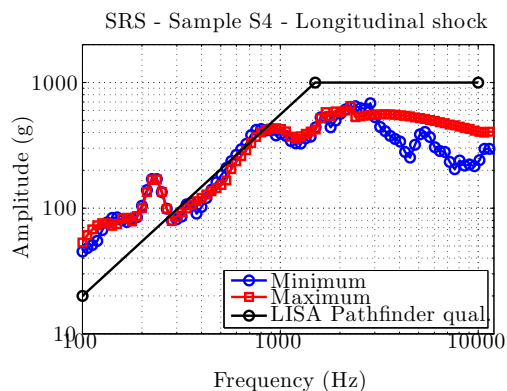
(a) Shock Response Spectrum of shock applied on sample S1



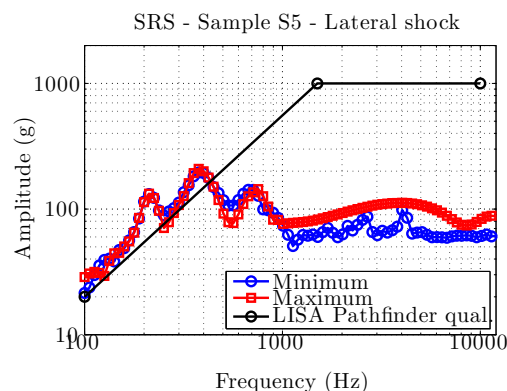
(b) Shock Response Spectrum of shock applied on sample S2



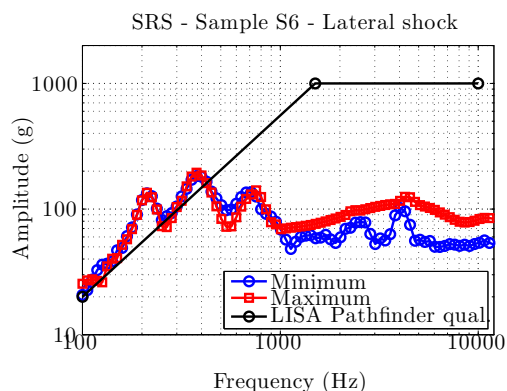
(c) Shock Response Spectrum of shock applied on sample S3



(d) Shock Response Spectrum of shock applied on sample S4



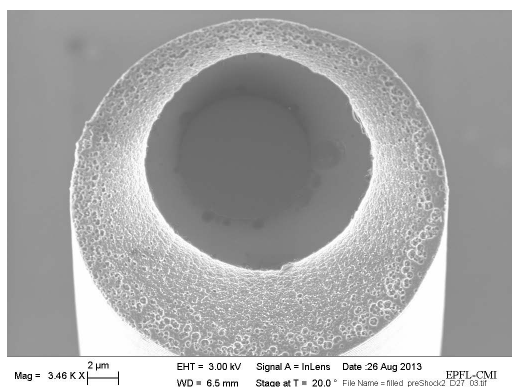
(e) Shock Response Spectrum of shock applied on sample S5



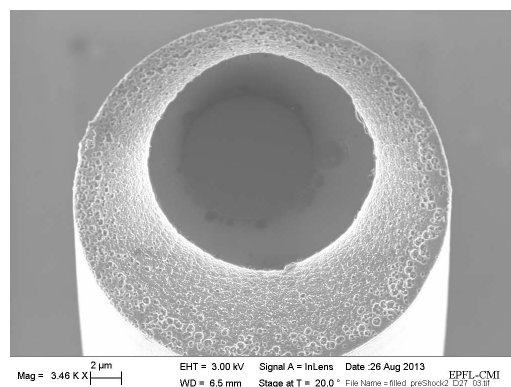
(f) Shock Response Spectrum of shock applied on sample S6

Figure A.27: Shock Response Spectrums of shock applied on all samples

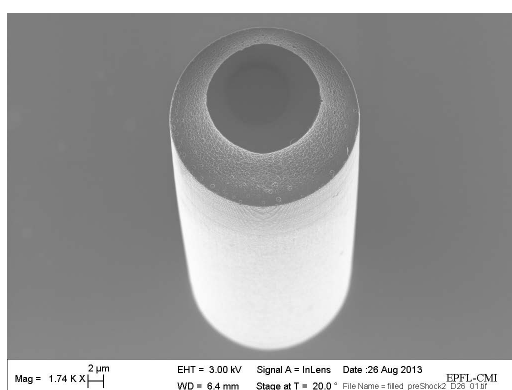
A.3. Liquid retention under vibration and shock



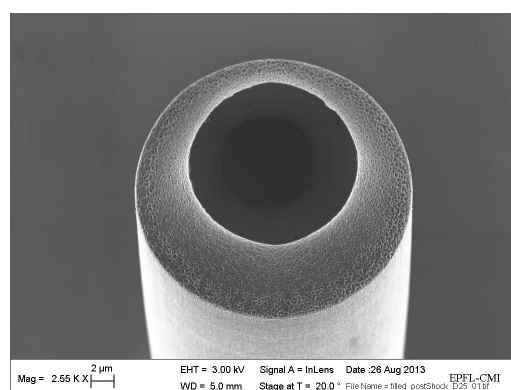
(a) Sample S1 before shock



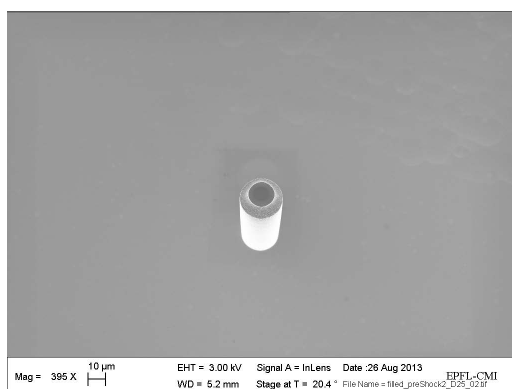
(b) Sample S1 after shock



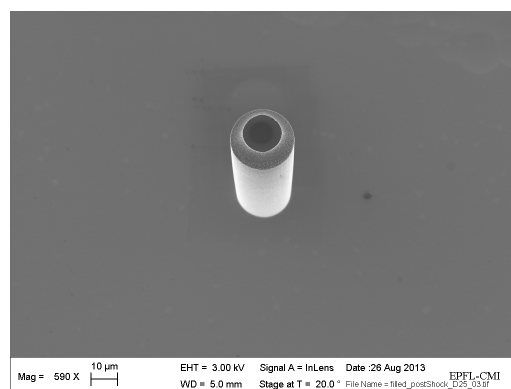
(c) Sample S3 before shock



(d) Sample S3 after shock



(e) Sample S2 before shock



(f) Sample S2 after shock

Figure A.28: Shock test results. No evidence of emitter damage was seen in any test performed. For one sample (f), a small drop of ionic liquid was seen 25 μm from the emitter.

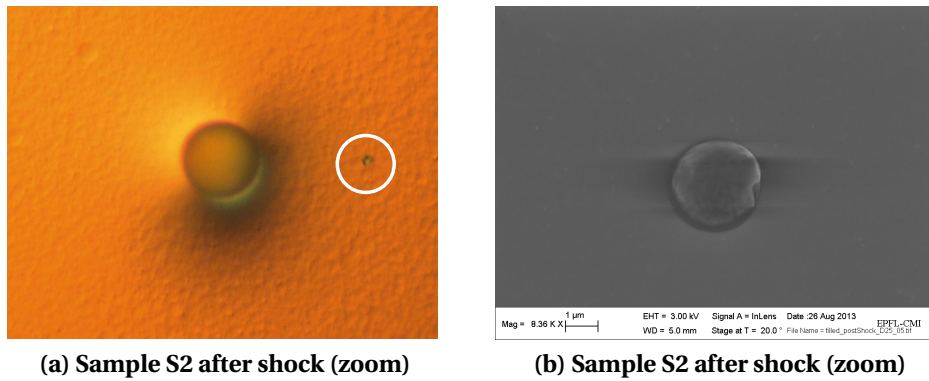


Figure A.29: Shock test results.

A.4 Summary of liquid transport and containment

In this appendix, several aspects of liquid transport were studied. Taking advantage of the well defined geometries of internally fed capillary emitters, it was possible to model with a high degree of confidence the emitter's ability to pull and hold liquid. For a small, $4.5\mu\text{m}$ emitter, the model showed that close to 37 kPa of pressure could be held, enough to support about $29 g_0$ of static acceleration. The model also confirmed that in the absence of external factors, the emitters would exert a strong filling pressure, pulling liquid from the reservoir to their emission site. This feature is critical to ensuring compatibility with different kinds of reservoirs (e.g. porous) and ensure full propellant consumption.

Before proposing such a model, it was necessary to characterize the contact angles of two propellant candidates ($EMI - BF_4$ and $EMI - T f_2 N$) on several surfaces which could be used in the system. It was found that $EMI - BF_4$ was in all cases less wetting, with contact angles generally in the range of 55° to 75° . An hydrophobic coating, deposited by Molecular Vapour Deposition, was seen to yield just over 90° contact angle, making it a reasonable candidate to prevent liquid spillage, assuming that it could be deposited selectively on the right surfaces.

Liquid containment was also studied under shock and vibration conditions similar to those encountered in a spacecraft launch. For all vibration tests performed, no loss of containment was observed. In the case of shock tests, a single drop was found close to an emitter, although it is unclear whether this drop resulted from sample contamination during handling or liquid being ejected from the emitter tip. Throughout all shock and vibration tests, no broken emitter were observed, confirming that they have good structural integrity.

B Insulating electrospray ionisers for mass spectrometry

The silicon based emitters described until now are some of the most advanced in terms of feature size, uniformity, electrode integration and robustness. They nevertheless have the disadvantages of being costly and difficult to produce. While potentially acceptable for spacecraft propulsion applications, this represents a major drawback in other fields, such as mass spectrometry, where emitters are often changed to avoid cross-contamination.

Yet, as is often the case, the developments aimed at the spatial applications can lead to exciting breakthroughs for Earth-based ones.

In this appendix, spacecraft propulsion is temporarily left aside and attention is shifted to how the methods and processes developed for the thruster device could be applied to fabricate electrospray ionisers for mass spectrometry (ESI-MS). This field of research is in constant evolution, and went through many advances since John Fenn and Koichi Tanaka received in 2002 the Nobel Prize in Chemistry for their work in it.

Of central interest is the 2-level electrode process, which can serve as the basis for a new kind of emitter chip, fabricated almost entirely of insulators. Using insulator materials, high voltage is constrained to the functional parts of the device, namely the conductive liquid and the electrodes. Doing so adds robustness to the design in terms of electrical leakage currents and breakdowns, two common sources of device failure. It also helps to limit stray electrical fields, between the electrodes and the substrate, which may result in lower operation voltage.

Two variants of such emitters, labelled "insulator/bonded" and "insulator/buried" and shown in Figure B.1 have been designed, fabricated and operated, as will be shown in this chapter.

Although the emitters suffered from short lifetimes, as is often the case with first prototypes, sprays could be initiated in both cases and useful lessons learned which will guide the design of future generations.

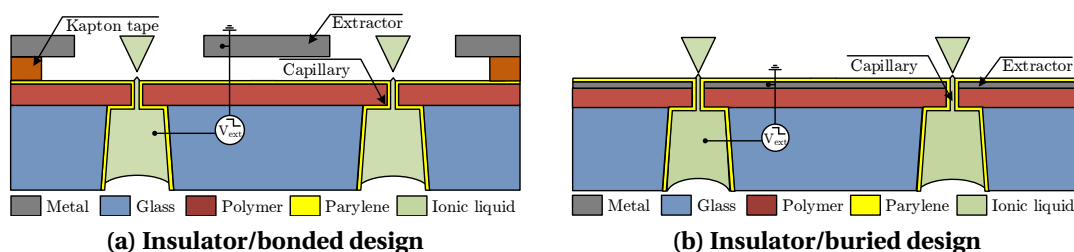


Figure B.1: Cross section diagrams of insulator emitters

B.1 An overview of electrospray ionisers for mass spectrometry

Electrospray ionisation (ESI) is a technique first reported in 1984 by Yamashita and Fenn [133] to produce ionised molecules which can be analysed in a mass spectrometer (MS). Figure B.2 illustrates the process, where gas-phase ions are produced from their liquid state by ESI.

The process begins with the formation of an electrospray plume composed of charged analyte molecules solvated inside droplets of a carrier liquid. Thus ESI sources do not operate in the ionic regime, but rather in droplet mode. Once free, the droplets shrink, as solvent is evaporated, increasing the charge concentration, and Coulomb forces lead to droplet fission. Eventually, only charged analyte molecules remain and are analysed with the mass spectrometer.

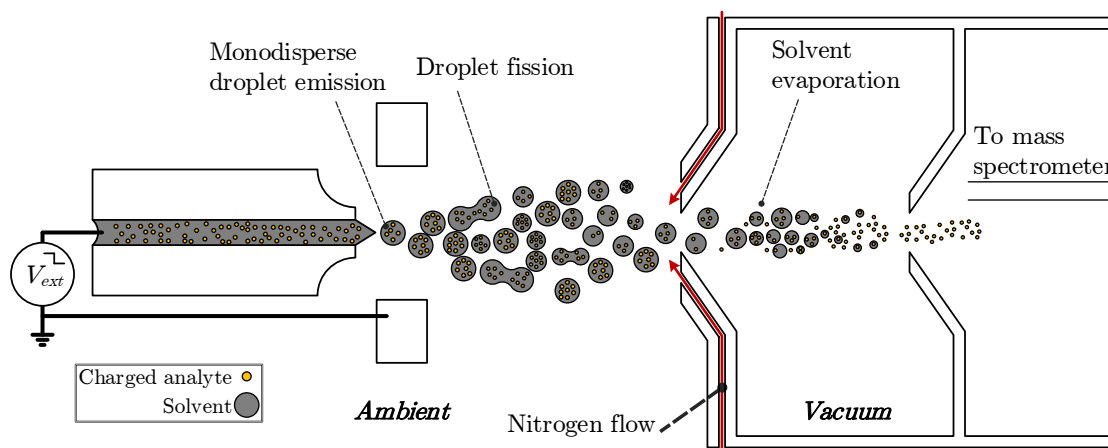


Figure B.2: Diagram of Electrospray Ionisation (ESI) process for Mass Spectrometry (MS)

One aspect of this technique which has been the subject of enormous attention in the last 20 years is the creation of emitters capable of reliably producing the required sprays. While initially microfabricated from silicon, the trend is increasingly to produce emitters with less fab-intensive techniques. At the same time, the materials constituting the emitters have generally shifted from silicon to insulators such as glass and polymers.

In addition to the often lower cost, machining in insulators has the advantage of allowing

very high electrical potentials to be applied at various locations on the chip, a useful feature for several applications of microfluidics, such as electrophoresis. Material transparency can also be beneficial, among other things to monitor liquid displacement, bubble formation and leaks.

Reviews detailing the different types of emitters fabricated over the last 15 years were done by Koster (2007, [134]), Sikanen (2010, [135]) and Feng (2014, [136]). These reviews list a number of ESI-MS devices, fabricated in a variety of materials, such as silicon/ SiO_2 [69, 82, 137–139], glass [140], PDMS [141], PMMA [142], polycarbonate [143–145], polyimide, PET [146, 147], SU8 [148] and Parylene-C [149, 150]. Several of these devices are shown in Figure B.3.

The dimensions of the emitters have also been consistently reduced over the last decade. Emitters with small inner diameters are attractive for several reasons. While reaching a purely ionic regime may not be desired for this type of applications, it is nevertheless useful to minimize the emitted droplet size. For one, ion suppression effects, which result from the competition of several analyte molecules within a sprayed droplet, will be reduced with small droplets [134]. With smaller droplets and lower flow rates, the sample volume required for an experiment will also be reduced, given sufficient tool sensitivity. On the other hand, variable arrays of emitters can, if need be, be used to tailor the analysis throughput (flow rate) while retaining the small droplets [65].

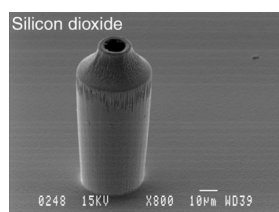
A critical element in mass spectrometry is that the amount of dead volumes should be minimized in the fluidic system. These dead volumes can lead to wasted analyte, longer waiting time in experiments, potential cross-contaminations and disturbed flows. Thus the trend has been to push the limits of ioniser integration, increasingly including complex fluidic components on chip [135, 136]. The work presented here is a bio-compatible electrospray ioniser which could be wafer-level integrated to lab-on-a-chip components.

Most of the devices produced until now however are in-plane, and are limited in terms of array size and density. Emitters protruding from the edge of a chip (Figure B.3 c, d, e, f, g, h, i, j, k, l) are also less manufacturable and typically more difficult to handle than out-of-plane (Figure B.3 a, b, m, n, o) emitters.

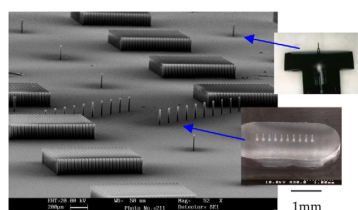
The out-of-plane feature may be one reason why the dominant ESI-MS devices now available on the market, the Advion¹ TriVersa NanoMate® is an array® of 400 out-of plane silicon microemitters [151, 152]. These chips, some images of which are shown in Figure B.4 and Figure B.5, were developed over the last 10-15 years but remain, at ≈1000 USD a piece, an expensive component.

¹www.advion.com

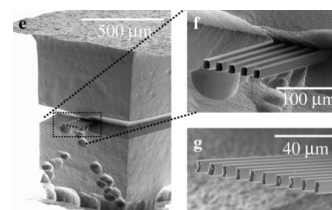
Appendix B. Insulating electrospray ionisers for mass spectrometry



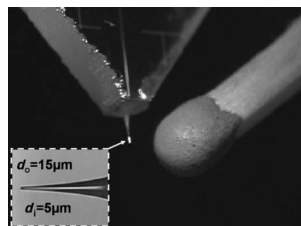
(a) Griss 2002, SiO_2 [82]



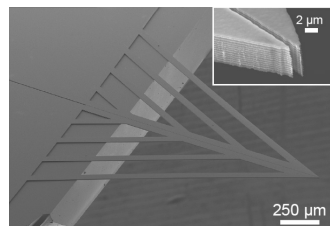
(b) Wang 2007, SiO_2 [69]



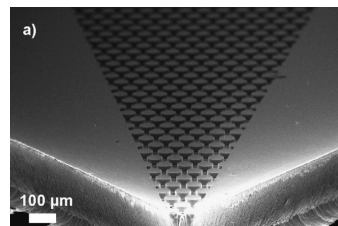
(c) Kim 2007, SiO_2 [138]



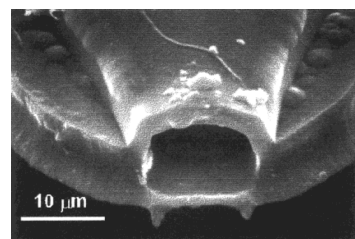
(d) Hoffmann 2007, glass [140]



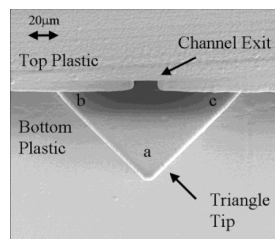
(e) Legrand 2007, silicon [137]



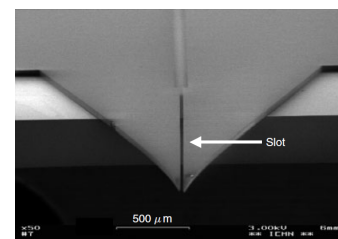
(f) Sainiemi 2008, silicon [139]



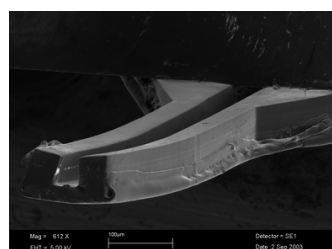
(g) Licklider 2000, parylene-c [149]



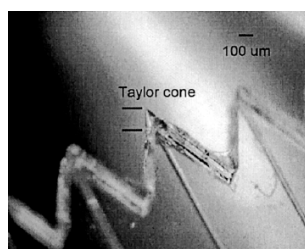
(h) Kameoka 2002, parylene-c [150]



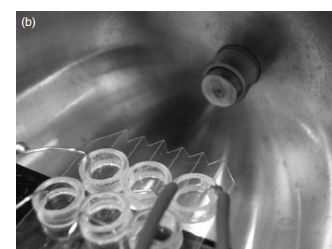
(i) Le Gac 2003, SU8 [148]



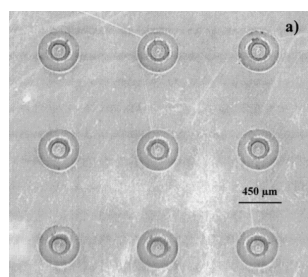
(j) Svedberg 2004, PDMS [141]



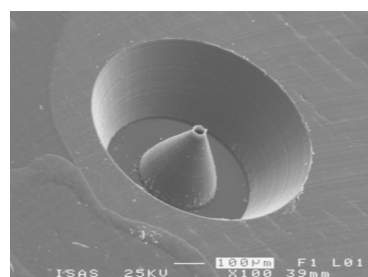
(k) Kim 2001, polycarbonate [143]



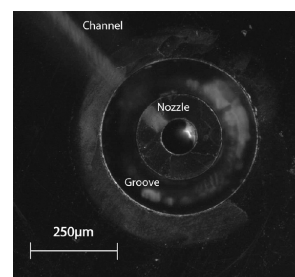
(l) Dayon 2006, PET [147]



(m) Tang 2001, polycarbonate [144]



(n) Schilling 2004, PMMA [142]



(o) Lhernould 2011, polycarbonate [145]

Figure B.3: Various types of electrospray emitters for mass spectrometry

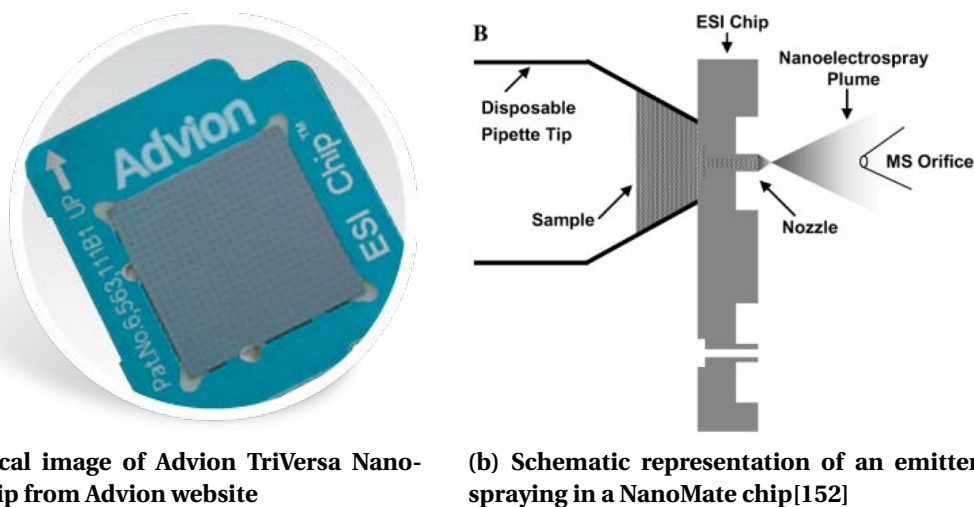
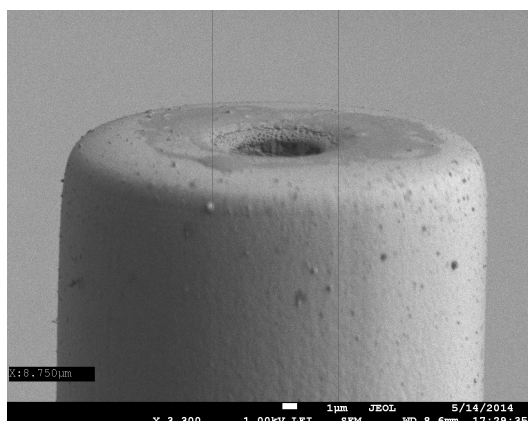


Figure B.4: Optical image and schematic operation diagram of Advion TriVersa NanoMate®

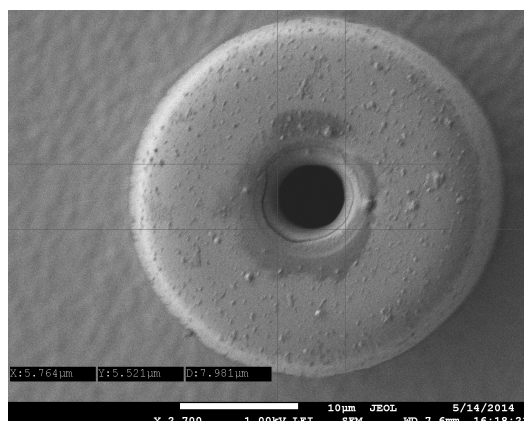
A great advantage of the Advion emitters is their portability, being compatible with many mass spectrometry tools. Advion also developed a robust setup to perform analysis on many samples automatically. Using a robotic arm, analyte solution is captured and transferred to one of 400 emitters included in the $2.5 \times 2.5 \text{ cm}^2$ chip using a conductive disposable plastic pipette. To generate a spray, 1.5-3kV are applied between the analyte liquid and the extractor buried in the ESI chip, before a flow is forced through the emitter. While early Advion devices sprayed with a flow rate of 100-200nL/min, the latest chips support smaller flow rates of 20nL/min. After spraying or when local emitter failure occurs, the pipette moves to the next emitter in the array. The high voltage is applied through the pipette itself while the extractor, buried under an insulating layer, is grounded. This design is similar to the insulator/buried design proposed here. Due to its similar configuration, the insulator/buried chips were tested in an ambient setup resembling the Advion one, while the insulator/bonded devices were tested in a more standard vacuum setup.

Thus the work presented here aims to propose some alternative emitter devices that could be used for ESI-MS. The devices presented combine the advantages of being out-of-plane, insulating and easily fabricated. They are also compatible with a novel method to tune the inner diameter of the emitters, using the controlled deposition of Parylene-C coating. This fine tuning would enable precise control of the emitted droplet size, leading to exciting research avenues in the field of ESI-MS.

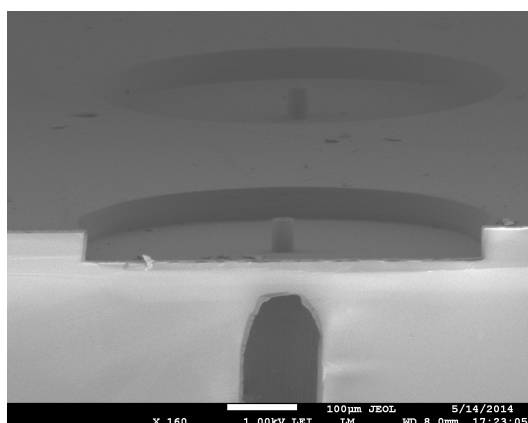
In the following sections, the design, fabrication and test of these novel devices will be discussed.



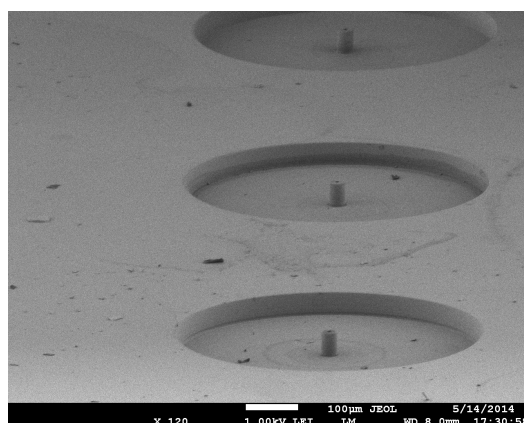
(a) Cross-section of Advion emitter tip



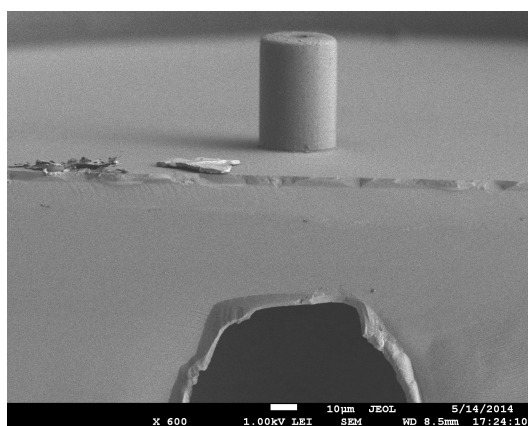
(b) Top view of Advion emitter tip



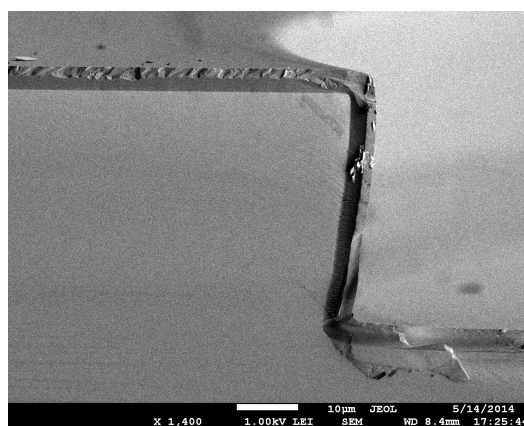
(c) Cross-section of Advion emitter tip



(d) Array of Advion emitters



(e) Cross-section of emitter tip and feedthrough reservoir



(f) Cross-section of cleaved sample showing multi-layer surface finish. This section corresponds to the edge of the circular feature in image (c)

Figure B.5: SEM micrographs of Advion TriVersa Nanomate® emitters

B.2 Design and fabrication

Two designs are proposed in this work. The first (Figure B.6 a-b) is more similar to the silicon thrusters and requires the die or wafer-level bonding of an extractor to the emitter chip. The second (Figure B.6 c-d) has the extractor electrode buried within the structure, below the tip of the emitter. This buried extractor concept is regularly used in the mass spectrometry field, where the sources are often described as having an "integrated extractor". Thus it is very interesting to comparing both types of emitters, evaluating the pros and cons of each.

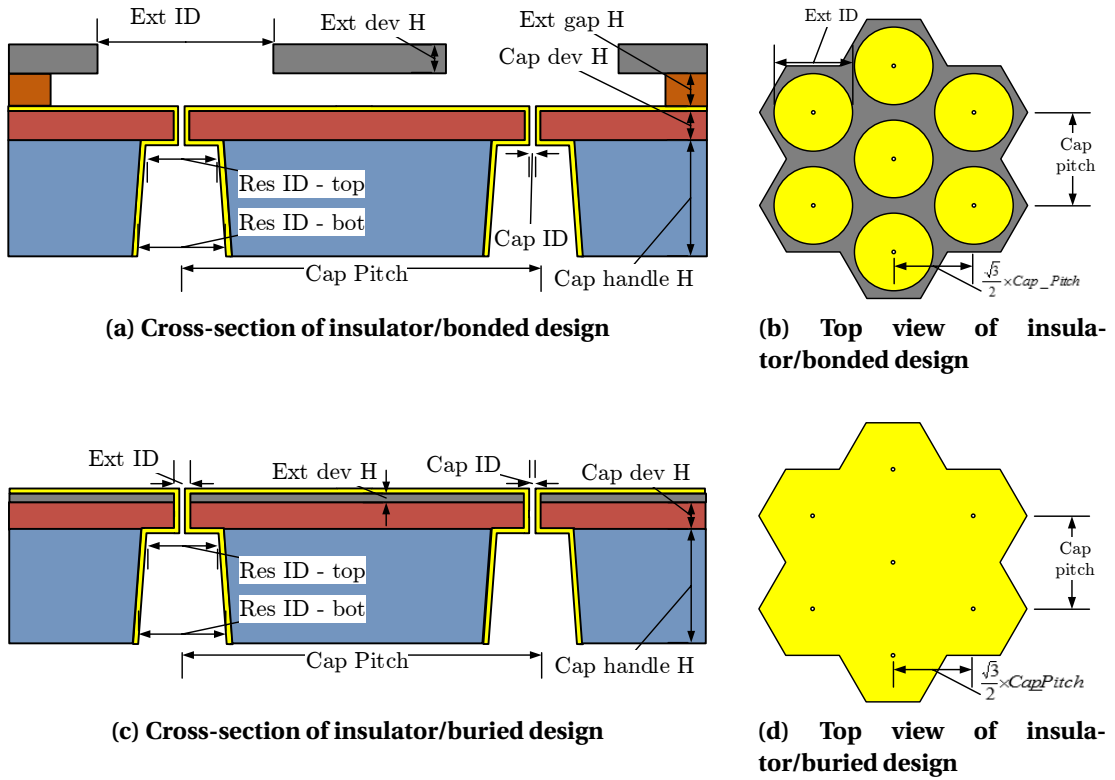


Figure B.6: Cross-section and top-view diagrams of insulator/bonded and insulator/buried designs with key dimensions labelled.

For both designs, the emitter itself was patterned by developing a laminated $50\mu\text{m}$ thick film (MX5050). Down to $30\mu\text{m}$ openings could reliably be patterned in the film, determining the achievable inner diameter of the emitters. This inner diameter could however be further reduced by the conformal deposition of thick Parylene-C. The emitters were designed to be small, to reduce droplet size, although PIR was not targeted. Parylene-C was used to reduce the inner diameters down to $10\mu\text{m}$ from the original $30\mu\text{m}$. Figure B.7 shows how the expected fluidic impedance of the insulating emitters compares to the microfabricated silicon emitters. The impedance of the fabricated emitters was thus about 2 orders of magnitude lower than the silicon emitters, although it could eventually be reduced further by thicker Parylene-C deposition. It was expected that the lower impedance would yield a lower ionic content,

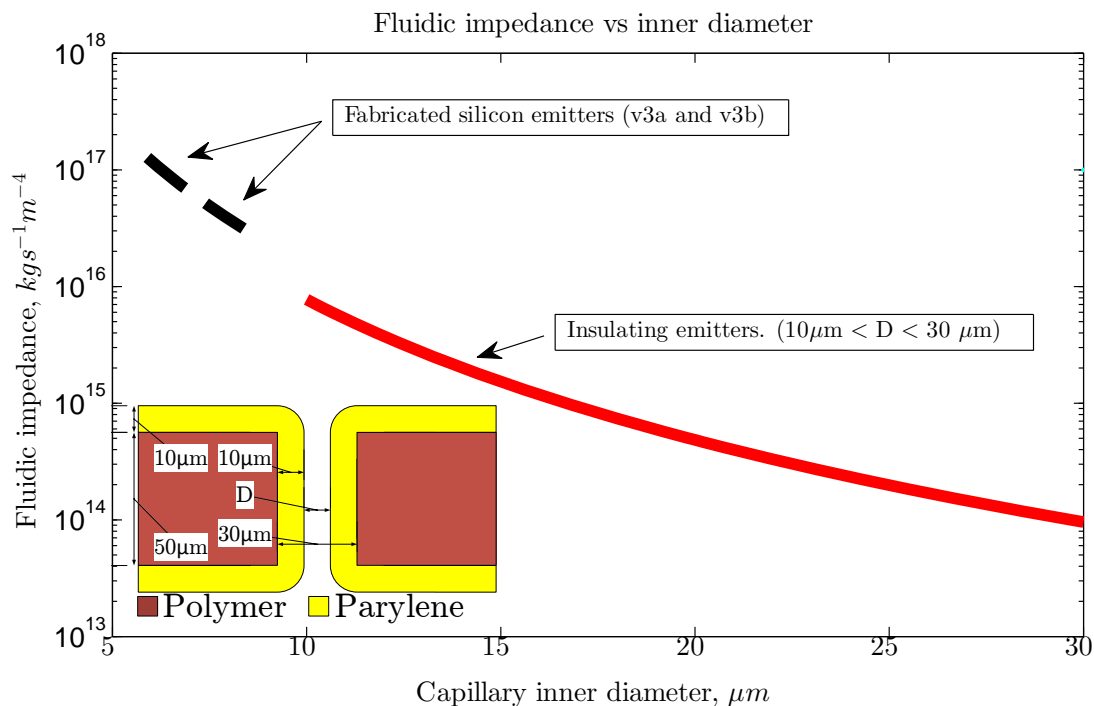


Figure B.7: Fluidic impedance of insulating emitters. Parylene-C is used to reduce the inner diameter from $30 \mu\text{m}$ down to $10 \mu\text{m}$, as shown in the inset.

operating in a mode more common to mass spectrometry. A second generation prototype could attempt to prepare ESI sources operating with a higher ionic content, comparing the effect on sensitivity.

Both designs had in common several dimensions relative to the emitter pitch and reservoir so that they could be fabricated from the same starting glass substrates. As prototype chips, density was not of primary concern and the emitter pitch was set to 1 mm . The diameter of the reservoir, micro-sandblasted from a glass wafer, was set to $400 \mu\text{m}$, although it was expected that a $15\text{-}20^\circ$ slope in the reservoir side-wall would gradually reduce this diameter to $\approx 240 \mu\text{m}$. Once again, glass wafers of $250 \mu\text{m}$ thickness were used. The reservoir diameter was meant to be small to reduce stray electrical fields yet remain easily manufacturable by micro-sandblasting. Electrostatic simulations (shown in the next section), indicate however that this diameter actually has very little impact on the electrical field at the emitter tip.

In addition to single-emitter chips, arrays of 7 and 19 emitters were fabricated, with a density of $115 \text{ emitters/cm}^2$. Extractors were fabricated with inner diameters of 200, 250, 300 and $350 \mu\text{m}$, allowing from 26° to 41° beam half-angle clearance.

Table B.1 and Table B.2 list the designed dimensions (labeled in Figure B.6), in some cases including metrology of fabricated devices.

B.2. Design and fabrication

Table B.1: Nominal and measured dimensions common to both insulator designs. (All dimensions in micrometers. \pm value corresponds to standard deviation σ , number in parenthesis corresponds to sample size.)

Feature	Identification	Nominal	Measured
Reservoir inner diameter - top	Res ID - bot	400	364 ± 9.6 (5)
Reservoir inner diameter - bottom	Res ID - top	240	209 ± 5.9 (5)
Emitter pitch	Cap pitch	1000	-
Emitter handle thickness	Cap handle H	250	-
Emitter device thickness	Cap dev H	50	-
Number of emitters	n_{em}	1/7/19	-
Calculated dimensions			
Emitter density (emitters/cm ²)	ρ_{em}	115	-

Table B.2: Nominal and measured dimensions specific to bonded and buried insulator designs. (All dimensions in micrometers except beam half-angle in degrees. \pm value corresponds to standard deviation σ , number in parenthesis corresponds to sample size.)

			insulator/bonded				insulator/ buried	
			No coating		Parylene-C coated			
Id.			Nom.	Meas.	Nom.	Meas.	Nom.	Meas.
Emitter inner diameter	Cap ID		30	28.0 ± 1.2 (5)	10	-	10	9.7 (1)
Extractor								
Extractor electrode diameter	Ext ID		200/250/ 300/350	-	N/A	-	N/A	-
Extractor electrode thickness	Ext dev H		100	-	0.4	-	0.4	-
Extractor-emitter gap	Ext gap H		100	-	N/A	-	N/A	-
Calculated dimensions								
Beam half-angle (clearout)-ext	θ_h ext		26/32/37/41	-	N/A	-	N/A	-

B.2.1 Onset voltage simulations

Following the same procedure described earlier, COMSOL simulations were run with these designs to compare the insulating emitters with their silicon counterparts. Figure B.8 shows simulation results of each design where the surface indicates the electric potential and the streamlines the electric field reaching the Taylor cone. The simulations show that a critical electric field can be achieved, even with the insulator/buried design where the extractor is situated $10\mu\text{m}$ below the emitter.

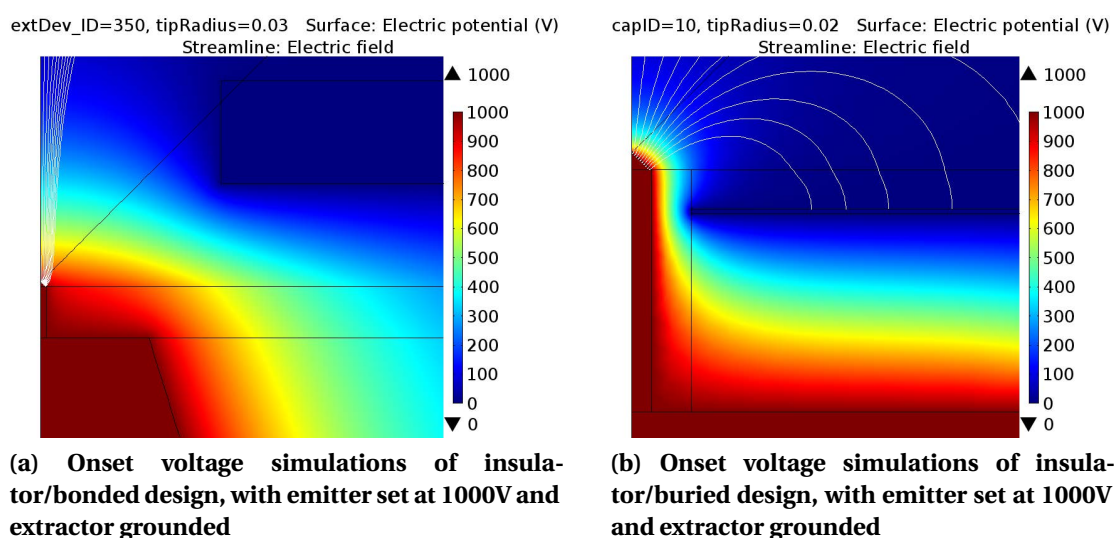
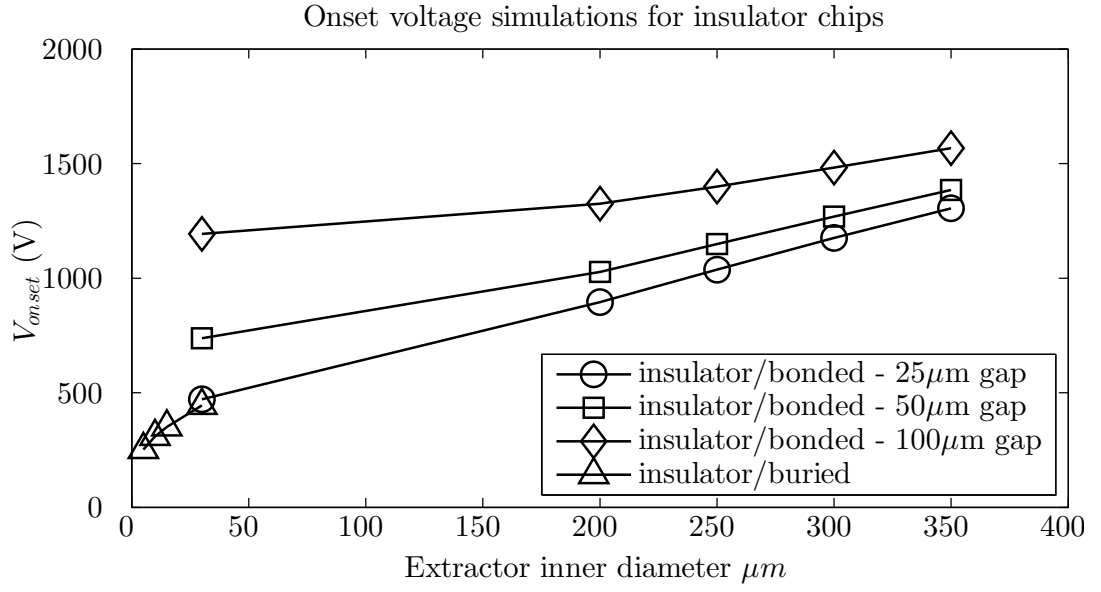


Figure B.8: Onset voltage simulations for insulator emitter chips.

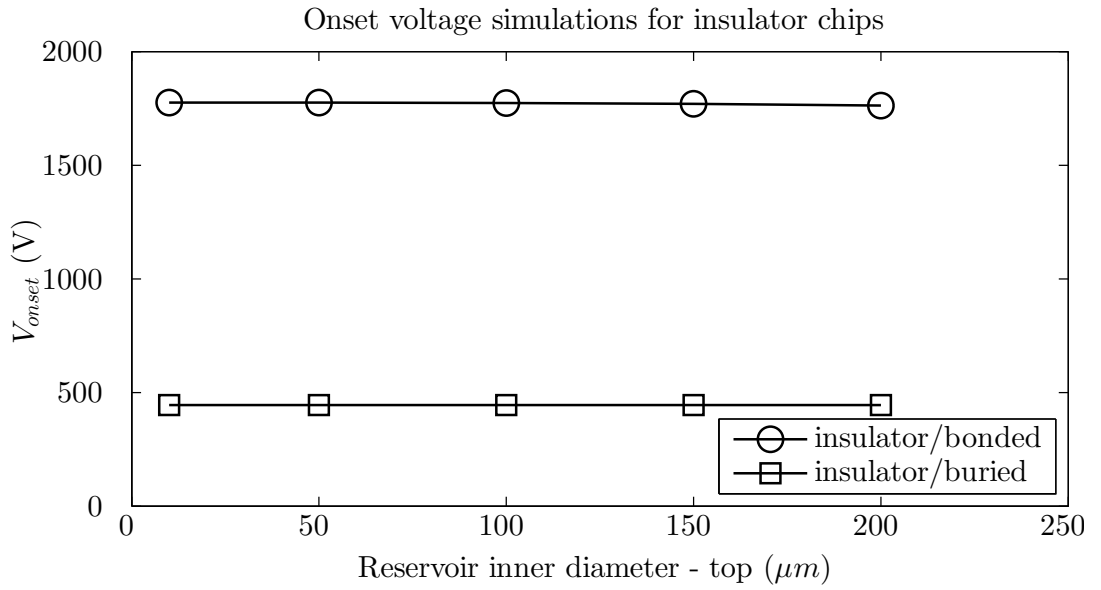
In Figure B.9a, the onset voltages of both designs are compared for several extractor inner diameters. For the insulator/buried design, the extractor inner diameter follows the emitter inner diameter. Three insulator/bonded traces are plotted, corresponding to different extractor gaps (i.e. thickness of bonding layer).

The simulations, however, are idealized cases making several debatable assumptions. First, they do not consider the rounded shape of the emitter edge, a feature unavoidable for the buried extractor design (See inset of Figure B.7). This rounding will at least lead to a widening of the Taylor cone base. A second major assumption is that the liquid is contained at the inner diameter of the emitter, in other words that no spillage occurs.

If liquid spilled out of the capillary, it would certainly affect the field conditions and may prevent operation altogether. The current design, with no exterior definition of the emitter to physically contain the spill, would be particularly affected.



(a) Simulated onset voltage for bonded and buried insulating chips as a function of extractor inner diameter. For the insulator/bonded design, three different gaps (25 μm , 50 μm and 100 μm) are simulated



(b) Simulated onset voltage for bonded and buried insulating chips as a function of reservoir inner diameter (top).

Figure B.9: Onset voltage simulations for insulator emitter chips.

Appendix B. Insulating electrospray ionisers for mass spectrometry

The diagram in Figure B.10 sketches how liquid spilling out of the capillary would be damaging to the ESI operation for both designs. For the bonded extractor type, operation may continue even after spillage occurred, although a short circuit would occur once liquid reached the extractor electrode. For the buried extractor design, it may be entirely impossible to form a Taylor cone and reach the required field enhancement for electrospray with the conductive liquid covering the electrode. In both cases, this issue may be mitigated with the proper application of an anti-wetting coating or by ensuring a negative pressure in the Taylor cone.

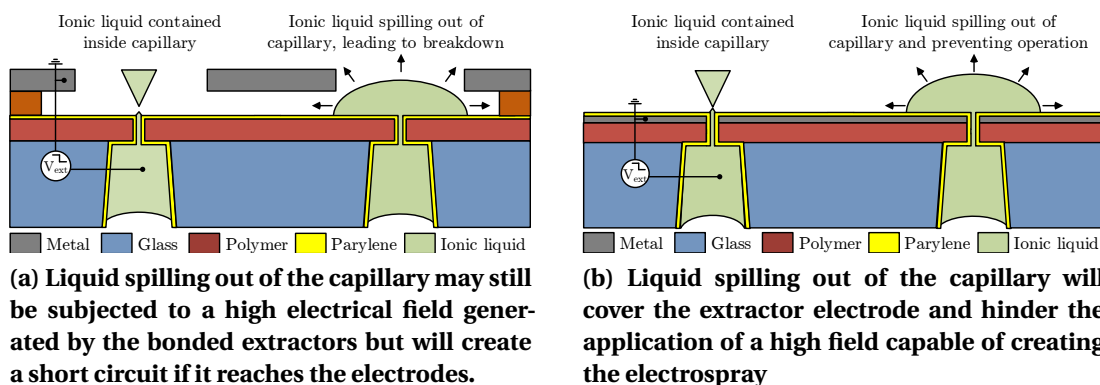


Figure B.10: Diagram of ionic liquid spilling out of the capillary, leading to electrical breakdown in the bonded extractor (a) design or preventing Taylor cone formation in the buried extractor (a) design.

One element that can certainly be concluded from the simulations, though, is that the radial fields in the vicinity of the cone in the buried extractor design will be much larger (Figure B.11), an element which may make liquid containment more difficult. Figure B.11 shows how the radial electric field compare for both designs.

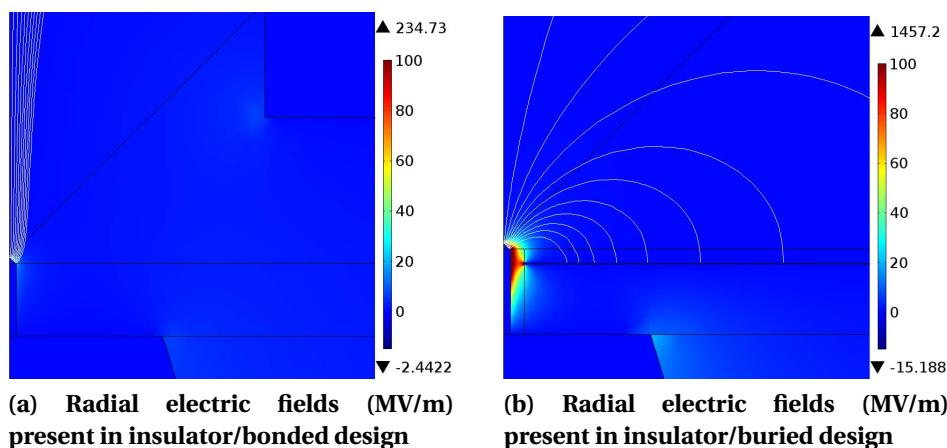


Figure B.11: Radial electric field simulations in insulator designs, with emitter set at 1000V and extractor grounded. Surface coloring represented radial electric field in MV/m. White streamlines represent electric field lines.

B.2.2 Fabrication

The fabrication steps yielding the two types of insulating devices are shown in Figure B.12. A great advantage of these processes are their low cost and simplicity. With the starting material available, the complete processes can comfortably be completed in a single day, with a cost in the range of 10 CHF per chip, roughly a tenth of its silicon equivalent.

For both insulator designs, the process starts with the patterning of thin ($250\mu\text{m}$) glass by micro-sandblasting (Figures I-a and II-a). This glass serves as the mechanical support for the emitters, which are directly patterned in the laminated $50\mu\text{m}$ thick MX5050 film (Figure B.12 I-b and II-b). Conformal Parylene-C deposition is subsequently used to reduce the emitter inner diameters, as shown in (Figure B.12 I-c).

The deposition of Parylene-C is a novel way to reduce the inner diameter of the emitter. Parylene is also bio-compatible, making it an ideal material to encapsulate the chip. Depositions ranging from 200nm to $10\mu\text{m}$ are routinely run by CMI staff in Lausanne, allowing for great control in the fluidic impedance. Multiple depositions can also be used to achieve layers thicker than $10\mu\text{m}$. A drawback of this process is the rounded edges at the emitter tip, which are detrimental for liquid containment. Thus it remains advantageous to fabricate emitters as fine as possible in the laminated film, potentially requiring thinner Parylene-C depositions.

In the insulator/buried process, a thin layer of metal (400nm aluminum), serving as the extractor electrode, is sputtered on the laminated film before Parylene-C deposition (Figure B.12 II-c). While the deposition of the Parylene completes the insulator/buried process, the insulator/bonded process additionally requires bonding to an extractor (Figure B.12 I-D). The extractor can be a one or two-level microfabricated electrode bonded at die or wafer level.

In this work die-level bonding of a laser machined molybdenum extractors was used, again reducing fabrication costs and time. Parylene-C and metal depositions were also done at die level, to allow for more flexibility. In fact, chips of both designs were fabricated from the same starting wafer, which had been diced after emitter patterning ($48 \times 1 \text{ cm}^2$ chips/wafer). Of the insulator/bonded design, 10 chips received $10\mu\text{m}$ thick depositions, reducing the emitter inner diameters to $9.5\text{-}10\mu\text{m}$, while others received no deposition at all. 12 chips (insulator/buried) additionally received the buried extractor deposition before a $10\mu\text{m}$ thick Parylene-C depositions. For these chips, it was necessary to protect the edges of the chips by Kapton tape during deposition, so that contact with the buried extractor could be made. This method was not optimal since Parylene-C started de-laminating when the Kapton tape was removed. This de-lamination is seen in Figure B.14e, where the areas away from the emitter have a lighter color. In a real product this procedure could be avoided by a clever use of through wafer vias or by wire-bonding before Parylene-C deposition.

Figure B.13 and Figure B.14 show optical and SEM images of fabricated insulator/bonded and insulator/buried emitters.

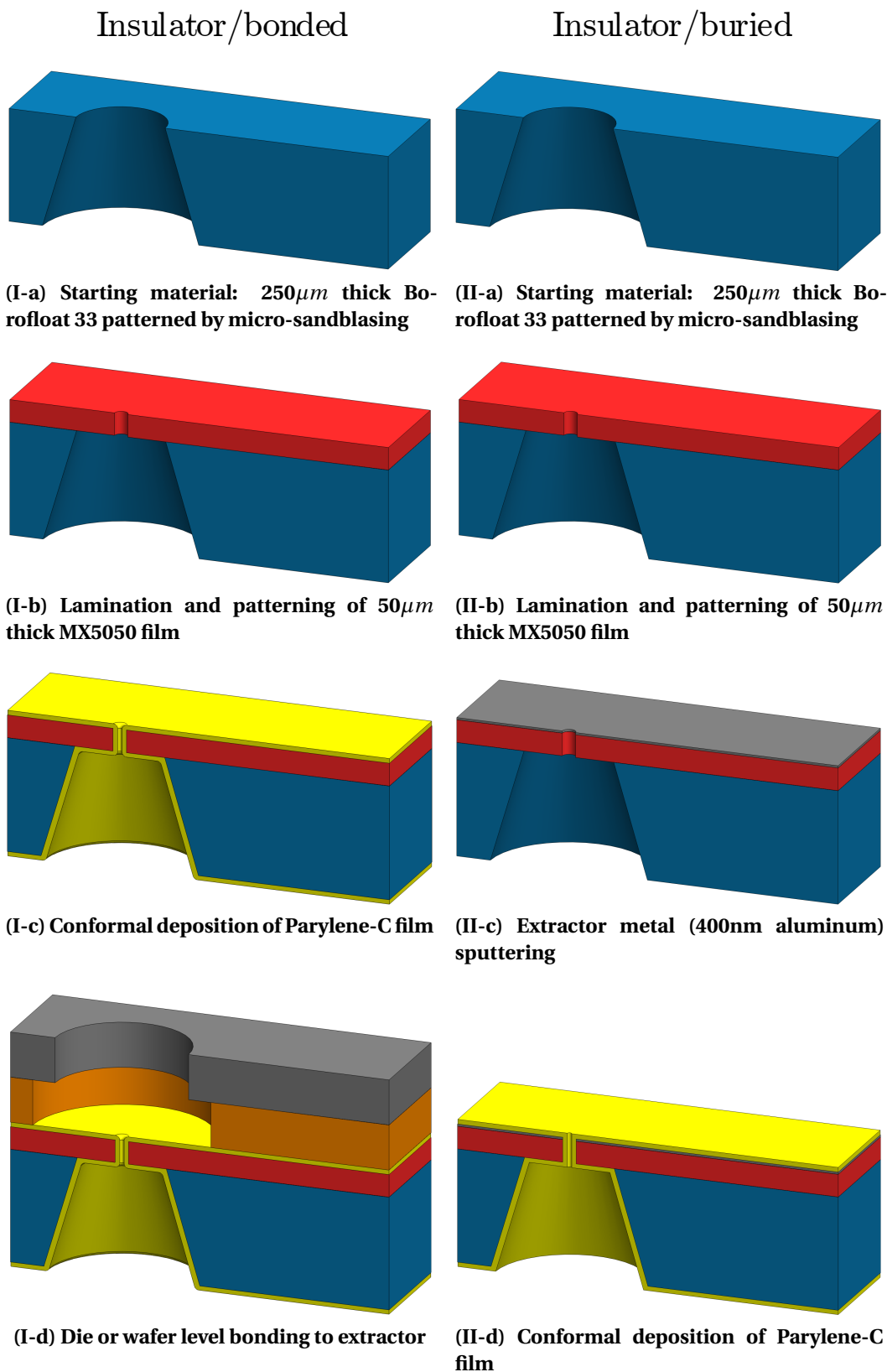
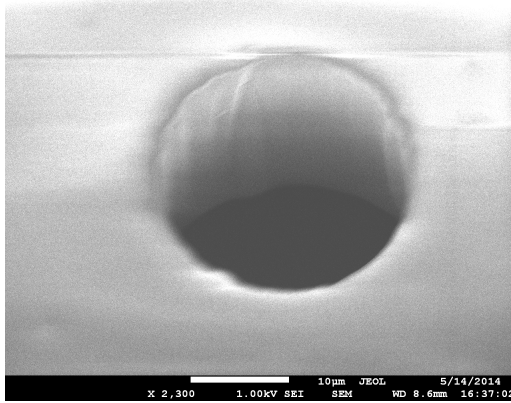
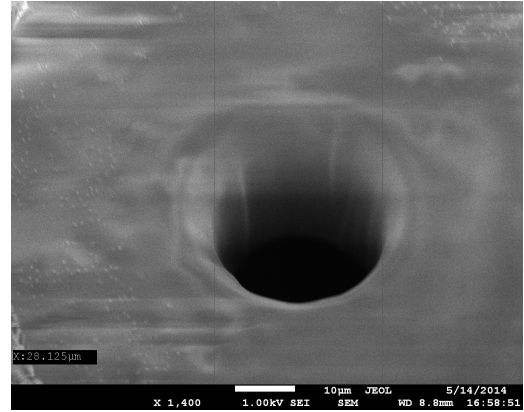


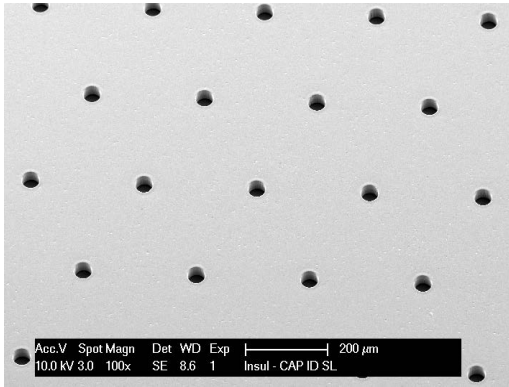
Figure B.12: Fabrication steps of bonded (left) and buried (right) insulating emitters.



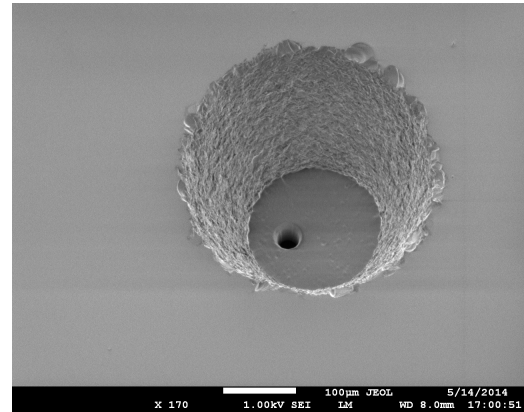
(a) SEM micrograph of insulator/bonded emitter front-side



(b) SEM micrograph of insulator/bonded emitter back-side



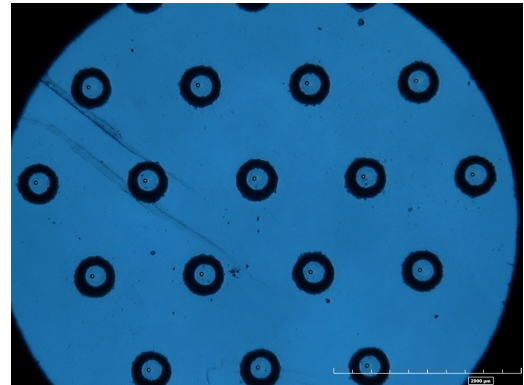
(c) SEM micrograph of insulator/bonded emitter array (test structure)



(d) SEM micrograph of insulator/bonded emitter reservoir back-side

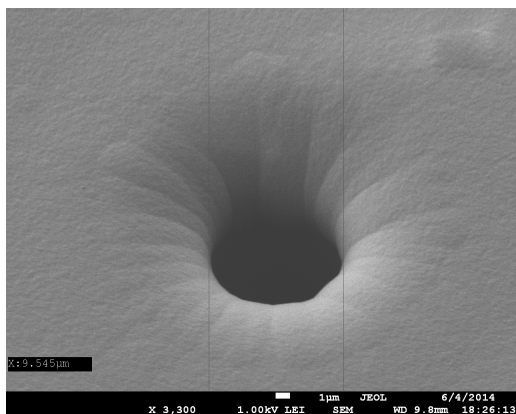


(e) Optical image of insulator/bonded emitter reservoir back-side

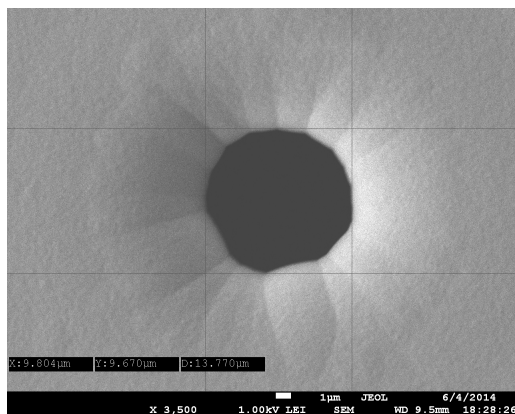


(f) Optical image of insulator/bonded emitter array back-side

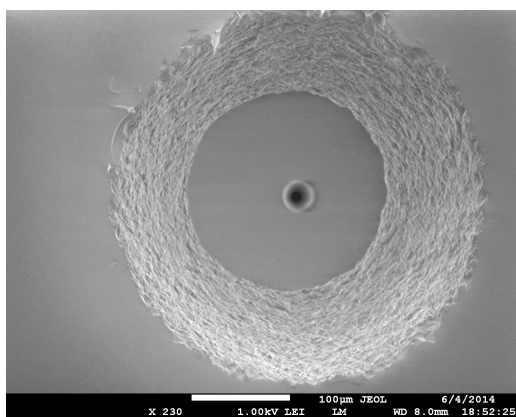
Figure B.13: Optical and SEM images of insulator/bonded type insulating emitters



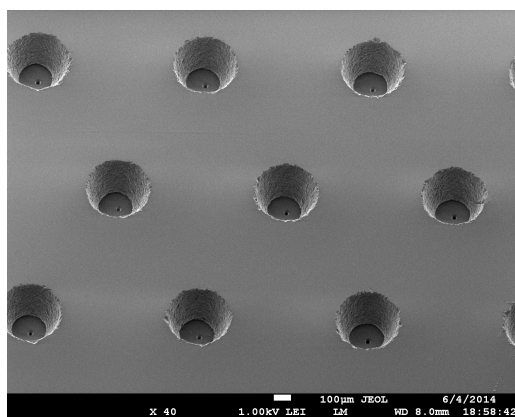
(a) SEM micrograph of insulator/buried emitter front-side



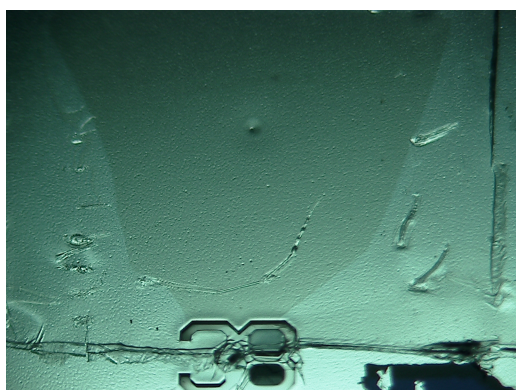
(b) SEM micrograph of insulator/buried emitter front-side



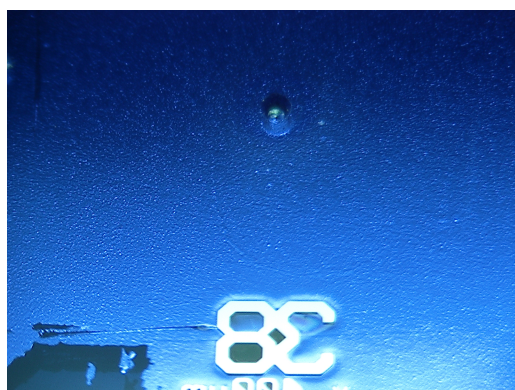
(c) SEM micrograph of insulator/buried emitter back-side



(d) SEM micrograph of insulator/buried emitter array back-side



(e) Optical image of single-emitter insulator/buried chip front-side. Lighter region corresponds to areas where the deposited Parylene-C delaminated during protective Kapton tape removal.



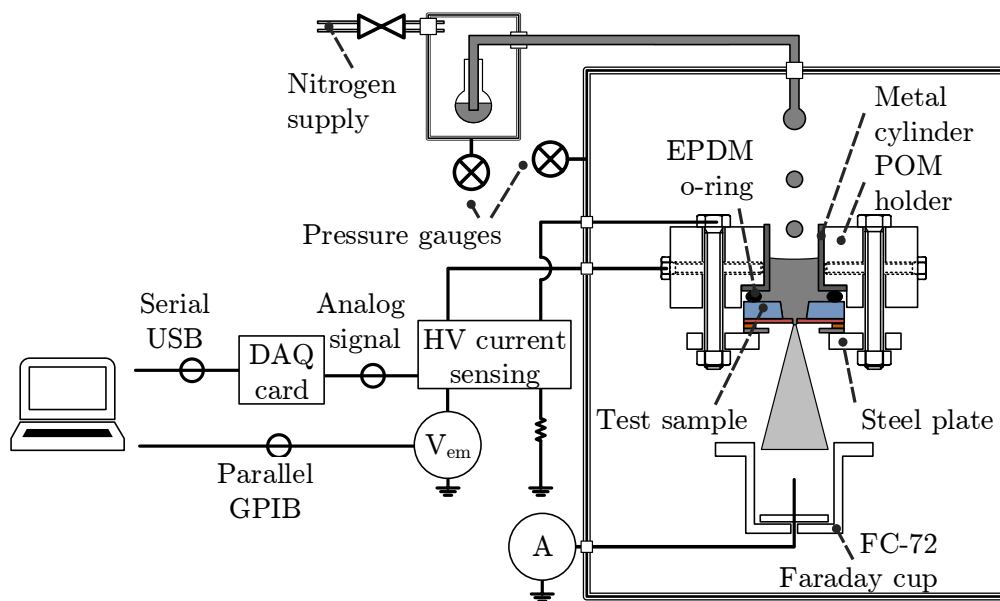
(f) Optical image of single-emitter insulator/buried chip back-side

Figure B.14: Optical and SEM images of insulator/buried design insulating emitters

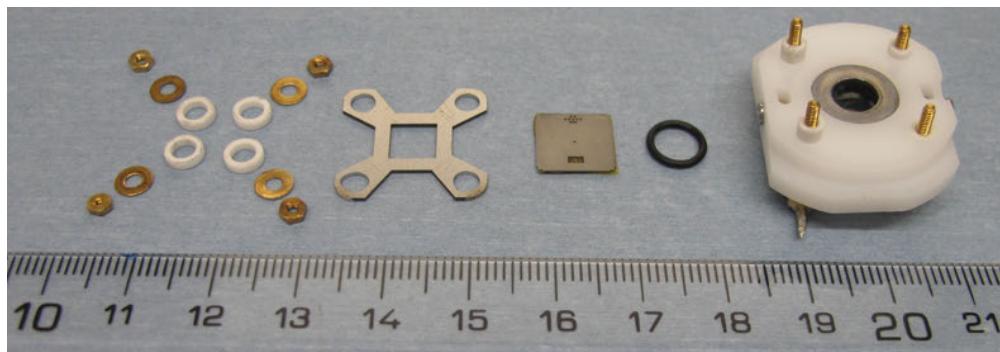
B.3 Test - insulator/bonded chips

B.3.1 Setup and procedure

Figure B.15a shows a diagram of the test setup used for the initial characterization of the insulator/bonded emitters. The setup was similar to the one presented in chapter 4 and was an improved version of the one originally used by Krpoun [62]. It was composed of a large vacuum chamber, where the emitter chip and current detector were installed. A second vacuum chamber held a large reservoir of ionic liquid and could be pressurized with nitrogen to transfer liquid to the emitter backside via a glass capillary. In these experiments, the ionic liquid $EMI - BF_4$ was used.



(a) Standard test setup



(b) Optical image of exploded mounting assembly

Figure B.15: Diagram of standard test setup used to test the insulator/bonded chips and die assembly components.

Appendix B. Insulating electrospray ionisers for mass spectrometry

The chip itself was mounted on a POM holder similar to the one used for the SEM in-situ observations and pointed downwards. One principal difference with this assembly was that an EPDM rubber o-ring was used to seal the backside of the chip, a material more resistant to degradation. In all the experiments performed with this o-ring, no evidence of degradation was observed. A steel laser machined plate was used to press the chip against the o-ring and establish contact with the extractor.

Connections to the extractor and emitter were done via metal screws accessed on the back and side of the holder. A Stanford Research System PS350/5000V source was used to provide the high voltage applied on the emitter, and the extractor was grounded through a 50Ω resistance. Both connections were fed through a HV current sensing circuitry designed by fellow PhD student S. Chakraborty. This circuit used two AD210 isolation amplifiers to read the currents on the high voltage lines and provide two proportional analog voltage outputs, fed to a National Instruments USB-6211 data acquisition card. This card also accepted an analog signal from the picoammeter. The digital outputs of the DAQ card were forwarded via USB to a computer, on which MATLAB was used to record signals and control the instruments through an Agilent 82357A GPIB interface.

Typically, $\approx 5\text{mm}$ of liquid was transferred to the reservoir, leading to a gravity pressure head of approximately 0.63 mbar on the back of the chip. Spray was collected using a FC-72 Faraday cup with no electron suppression grid installed and current was measured using a KT6487 picoammeter. During experiments, pressure was kept below 1×10^{-5} mbar.

B.3.2 Results

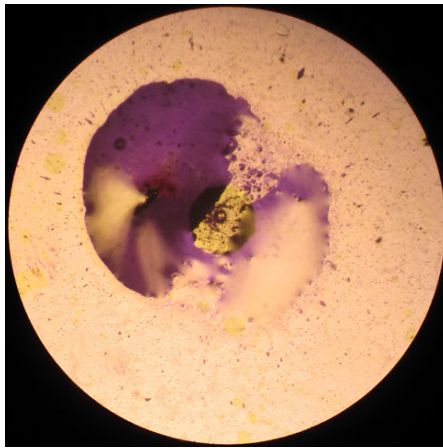
Several insulator/bonded die were tested in the setup described above, both with and without the Parylene-C coating to reduce the inner diameter, as listed in Table B.3. The die generally proved to be much easier to work with in terms of leakage current and electrical breakdown than the silicon ones. In the absence of liquid overflow, 2-3kV extraction voltage could routinely be applied without any leakage issue.

In most cases, however, it was not possible to achieve stable emission before ionic liquid spillage led to device failure. De-bonding of the chips and inspection after failure always revealed traces of liquid on the emitter top-side and extractor bottom-side. The region around the emitter opening was often completely destroyed, a sign of catastrophic electrical breakdown melting the laminated film. Figure B.16 shows optical images of die 04 after test. The emitter was de-bonded from the extractor using a sharp blade.

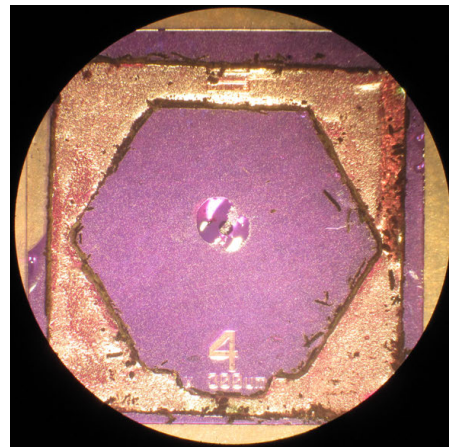
B.3. Test - insulator/bonded chips

Table B.3: Summary of tested insulator/bonded chips.

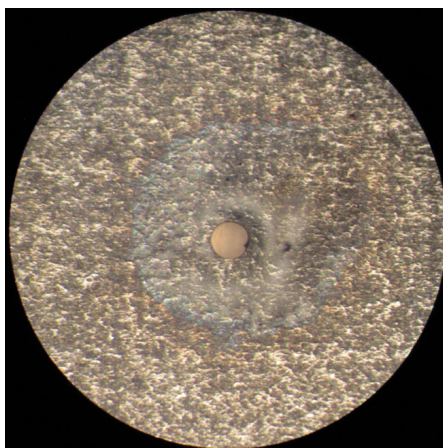
Die ID	Parylene-C thickness	Extractor ID	Result
03	None	250 μm	No stable emission, short circuit around 2000V
04	None	200 μm	No stable emission, some bursts at 2450V, short circuit around 2000V
27	None	300 μm	No stable emission, some bursts at 2600V, short circuit around 2000V
09	10 μm	300 μm	Stable emission at 2850V
15	10 μm	250 μm	Too much liquid transferred, Failed due to liquid leakage on backside
16	10 μm	350 μm	Die cracked in assembly, Failed due to liquid leakage on frontside



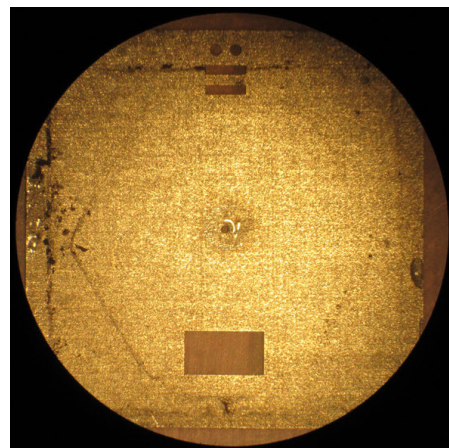
(a) Emitter front-side



(b) Emitter front-side



(c) Extractor back-side



(d) Extractor back-side

Figure B.16: Die 04 after test showing traces of liquid around emitter area on front-side of emitter and back-side of extractor

Appendix B. Insulating electrospray ionisers for mass spectrometry

For die 09, a die coated with $10\mu\text{m}$ Parylene-C, it was possible to achieve a brief stable emission, although at much higher voltage than expected. After several voltage sweeps, in some cases reaching up to 2800V where no spray occurred, emission finally started at 2850 V on the 13th sweep. Figure B.17 shows current plots for this sweep between 2500V and 2850V. Initially, only sporadic bursts were seen, but at 2850V a stable current of $\approx 730\text{nA}$ began and lasted for several seconds. The base current was extremely stable although $\approx 10\text{ Hz}$ bursts were superimposed. The extractor current stayed below 5nA for the entire voltage sweep. Following this, repeated sweeps led to nothing but sporadic bursts until the 19th sweep, where periodic bursts patterns could be seen starting at 1750V. Figure B.18 and Figure B.19 show the burst patterns in the 1700-2500V range.

After several more sweeps, including in negative emitter polarity, heavy leakage currents appeared and subsequent testing was no longer possible. Disassembly of the chip revealed that the chip was completely wetted on its front and that the emitter was heavily damaged (Figure B.20).

It seems that during the 13th sweep, liquid was still contained within the capillary and that a stable cone could be formed. Once voltage was released at the end of the sweep, liquid could have remained on the emitter frontside and in any case it was no longer possible to re-create a stable cone. The oscillations observed in the later spray may have been caused by spray emitted directly from droplets on the film surface or by an imbalance between the available flow rate and emitted current. A detailed model of the mechanisms involved was not investigated here, as the limited amount of data and the final state of the chip, damaged and flooded, made its validation difficult.

B.3. Test - insulator/bonded chips

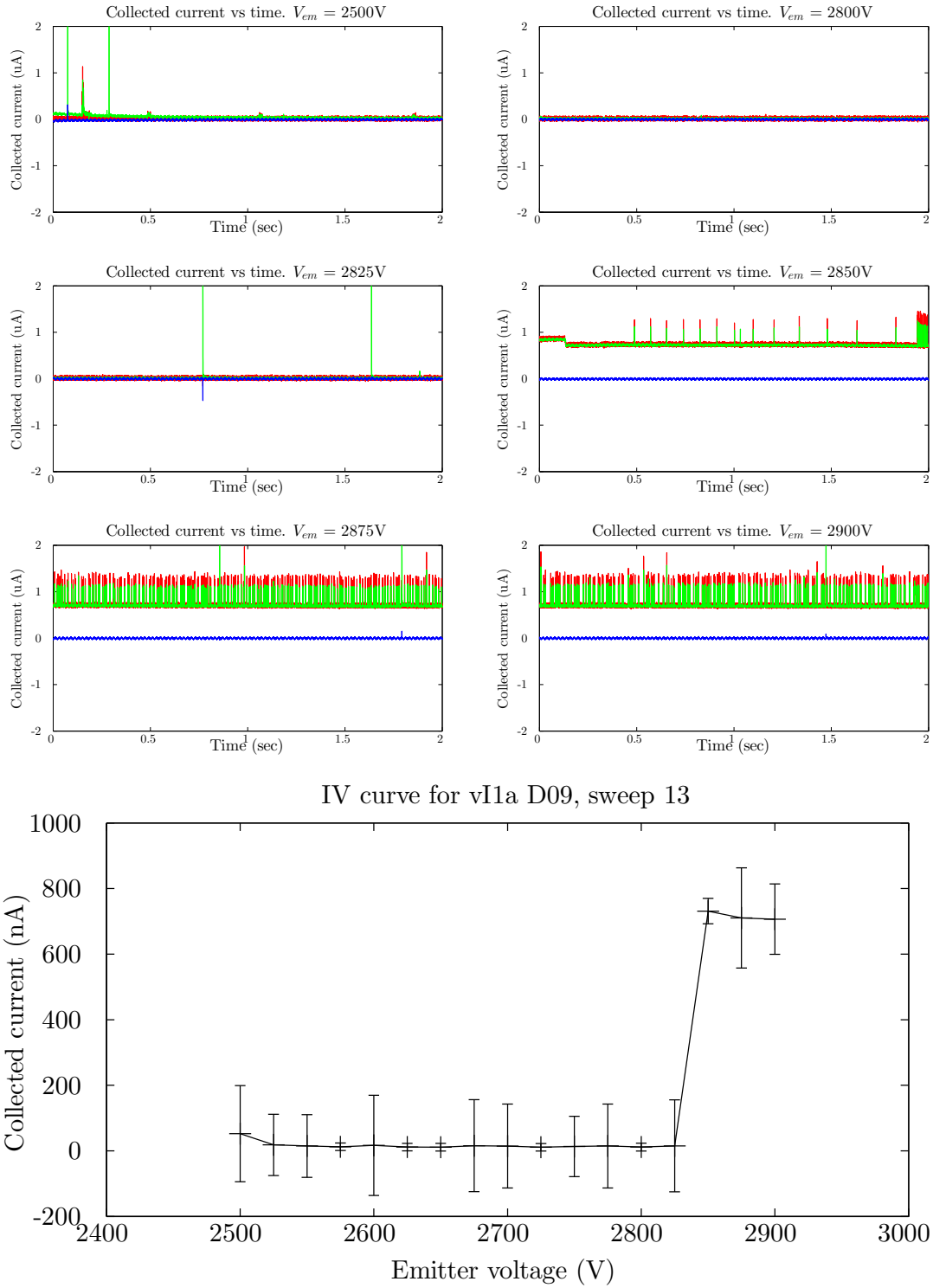


Figure B.17: Current plots with varying voltage for the 13th voltage sweep of die 09 (insulator/bonded type). Stable emission begins at 2850V. After just under 2s of spray, high frequency bursts are superimposed on the baseline current and remain for the duration of the experiment. Red curve: Emitter current; Green curve: Collected current; Blue curve: Extractor current

Appendix B. Insulating electrospray ionisers for mass spectrometry

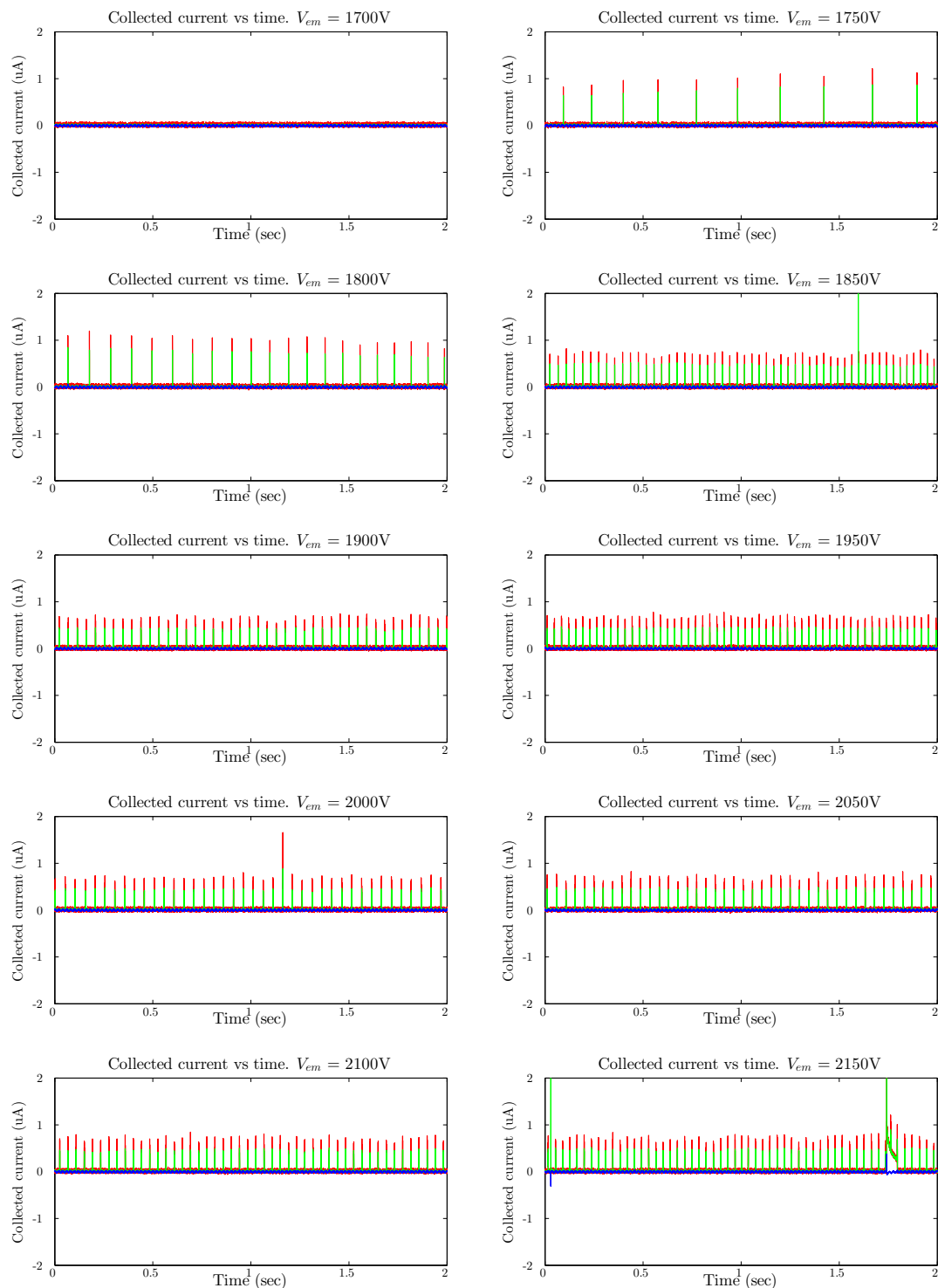


Figure B.18: Current plots with varying voltage for the 19th voltage sweep of die 09 (insulator/bonded type). Except at 2150V, no "stable" current is collected, although regular bursts are consistently recorded. Red curve: Emitter current; Green curve: Collected current; Blue curve: Extractor current. (1700V-2150V range)

B.3. Test - insulator/bonded chips

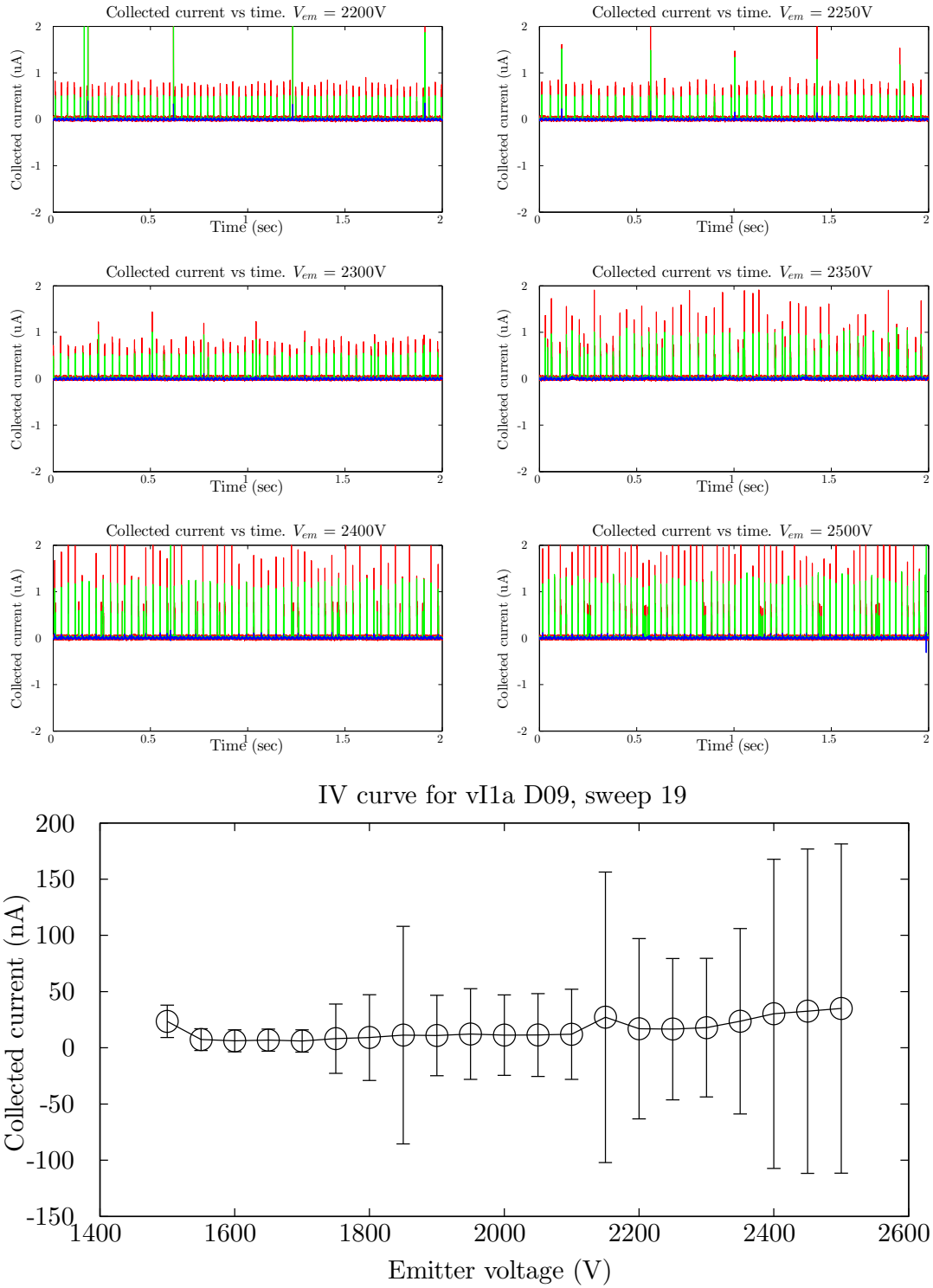
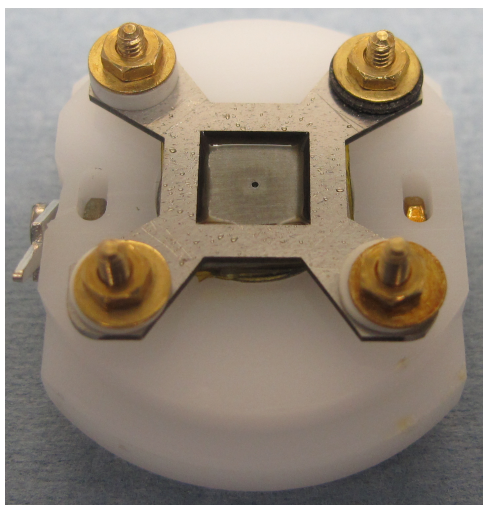
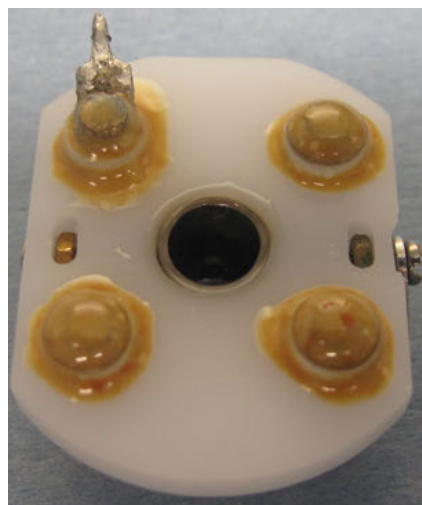


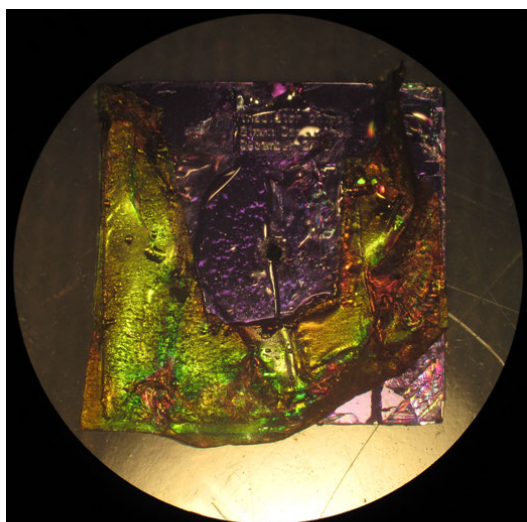
Figure B.19: Current plots with varying voltage for the 19th voltage sweep of die 09 (insulator/bonded type). Except at 2150V, no "stable" current is collected, although regular bursts are consistently recorded. Red curve: Emitter current; Green curve: Collected current; Blue curve: Extractor current. (2200V-2500V range)



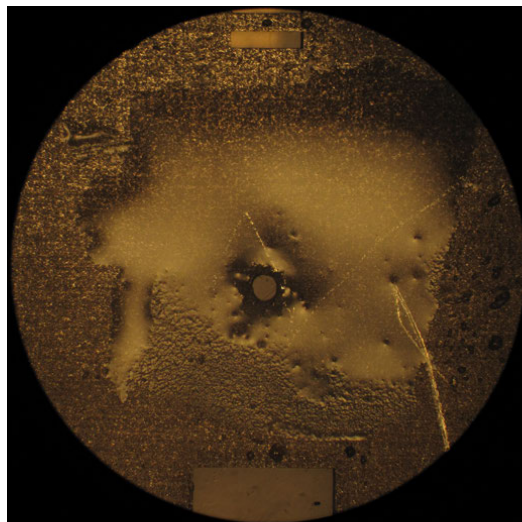
(a) Front-side of assembly



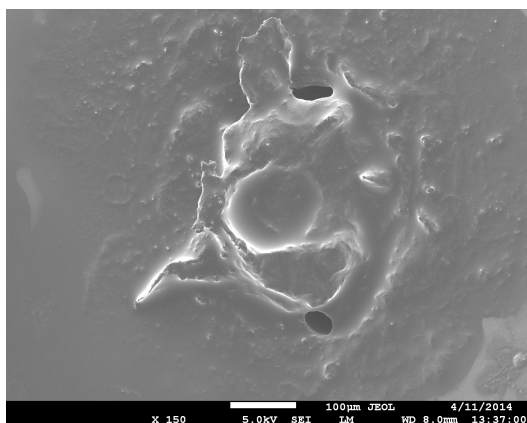
(b) Back-side of assembly



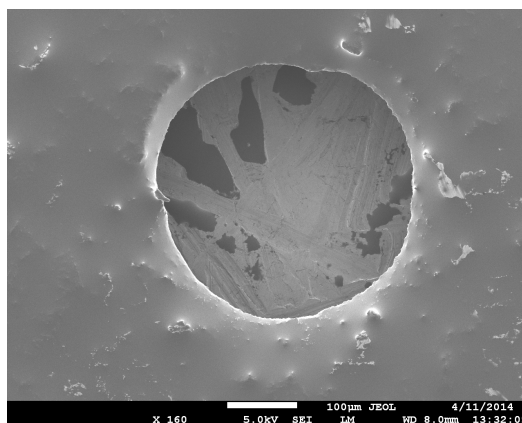
(c) Front-side of emitter



(d) Back-side of emitter



(e) Front-side of emitter



(f) Back-side of extractor

Figure B.20: Insulator/bonded die 09 after spray

B.4 Test - insulator/buried chips

B.4.1 Setup and procedure

The buried extractor chips were tested in a setup different to the one of the insulator/bonded chips. This setup was meant to be similar to the one used by Advion to operate their ESI-MS chips. One objective was to provide a first validation of the chip operation, before testing the devices with a real mass spectrometer in the actual Advion setup. This last step could not be completed within this thesis.

Several features of this setup justified significant differences in the chip assembly and test procedure. A principal difference was that the devices were operated in ambient air. To a large extent, this was permitted by the Parylene-C encapsulation of the extractor which allowed large potential differences to be applied without electrical breakdown. Operating in ambient conditions was very advantageous since it allowed much more flexibility in terms of assembly, spray observation and vibration damping. A second major difference was that, similarly to the Advion chips, the emitters were operated with active flow control. The flow was driven by a NE-500 syringe pump connected serially to a desktop computer. Using a Hamilton Gastight No. 1750, 500 μ L syringe, this pump could force liquid in a large range of flow rates (5-100 000 nL/min). The latest Advion chips are operated with 20 nL/min flows, whereas their earlier generation required 100-200 nL/min flow rate. The syringe was connected using glass and Teflon tubing to a Nanoport glued to the backside of a plexiglass holder. The standard Advion conductive plastic pipette was glued on the other side of this holder. Assembly parts were laser machined in transparent plexiglass so that liquid could be observed as it travelled through the assembly, a useful feature to avoid long waiting times with the liquid being very slowly pushed through the system. The ionic liquid $EMI - BF_4$ was also used in these experiments.

Three helical springs, equidistant from the contact point, were used to press the pipette against the backside of the chip, which was clamped on a different plexiglass holder. In an attempt to prevent excessive force to be applied on the backside of the chip, helical springs were also installed in-between the two holders. Nevertheless, several chips were cracked during assembly when too much force was applied. Conversely, insufficient or unequal force application led in some cases to liquid leakage on the backside of the chip. Going forward, a more controlled force application method would be necessary.

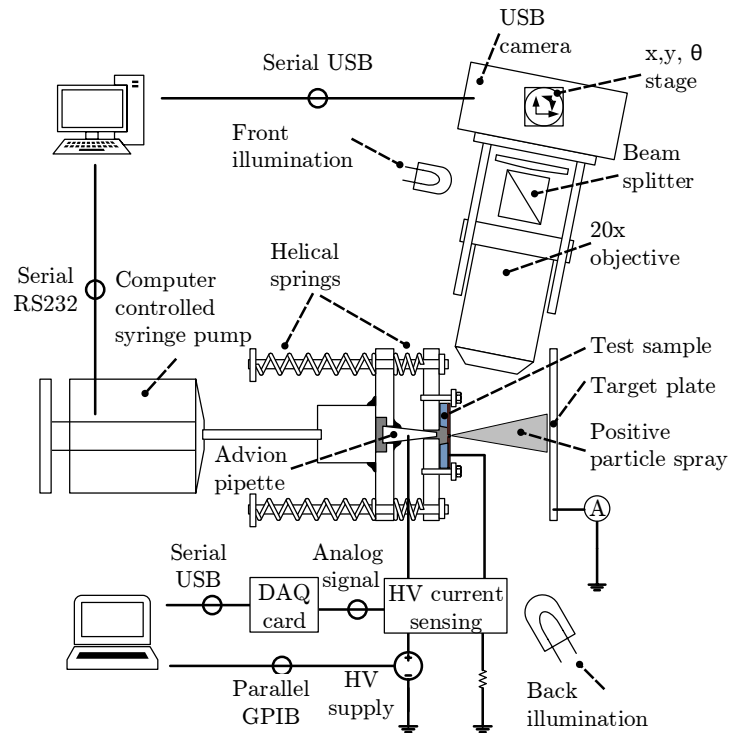
A USB CCD camera compatible with a 20x microscope objective (Leica N Plan L 20x/0.40) was used make recordings of the emitter region during operation. Two light source, one providing front illumination through a beam splitter and the other placed behind the emitter were adjusted to get optimal lighting conditions. This camera was also connected to the desktop computer which controlled the pump.

Connections to the emitter was done using a high voltage clamp attached to the pipette itself, while extractor ground was applied by a PCB pushing the chip against the pipette. Emitted current was collected by a steel target plate situated ≈ 3 cm from the emitter, with no

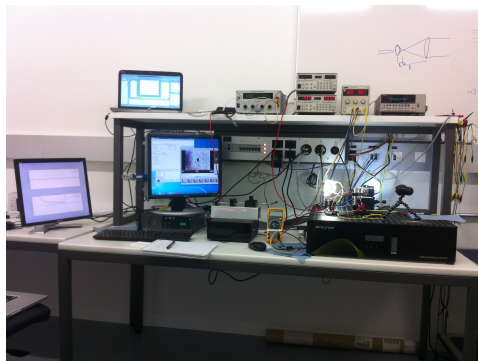
Appendix B. Insulating electrospray ionisers for mass spectrometry

secondary electron suppression grid installed. The same HV current sensing circuitry and MATLAB control routine as the one described earlier were used to drive the voltages and collect current data at 1000 Hz. Using two computers to control different parts of the experiment was convenient, since capturing high-data rate video (5.7 Mbps) and running the MATLAB program simultaneously on the same computer could have led to software slow-downs or crashes.

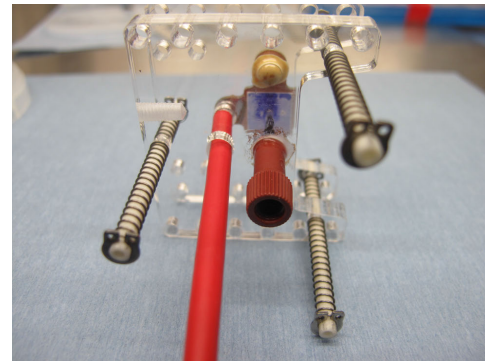
Figure B.21 shows a diagram and optical images of the test setup.



(a) Diagram of flow controlled buried extractor test setup



(b) Optical image of test setup



(c) Optical image of plexiglass insulator/buried test assembly

Figure B.21: Optical images and setup diagram of flow controlled spray test used to test the "insulator/buried" chips.

B.4.2 Results

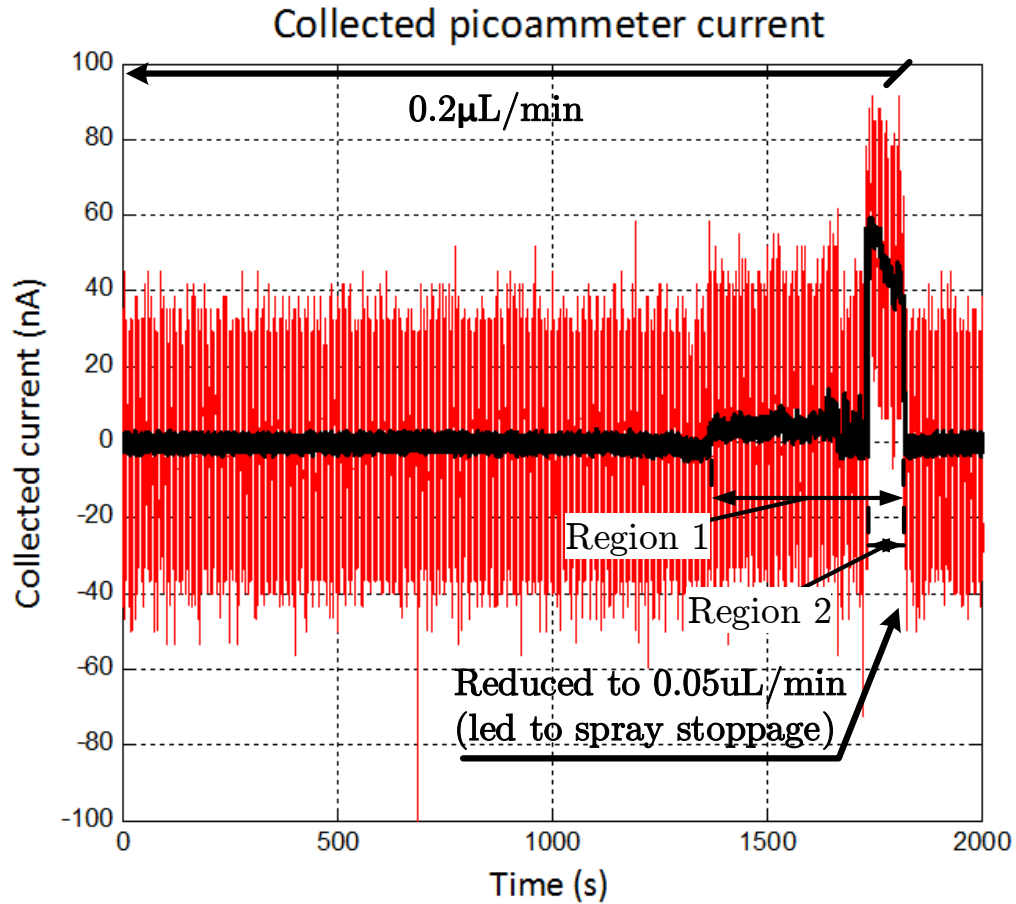
Table B.4: Summary of tested insulator/buried chips.

Die ID	Result
42	Chip eventually overflowed before voltage was applied with flow rate of $10\mu\text{L}/\text{min}$
36	Chip eventually overflowed while 2000V was applied with flow rate of $10\mu\text{L}/\text{min}$
43	After > 6 hours pumping at low flow rate, spray initiated for several minutes with $0.2\mu\text{L}/\text{min}$ flow rate. Catastrophic breakdown eventually occurred.

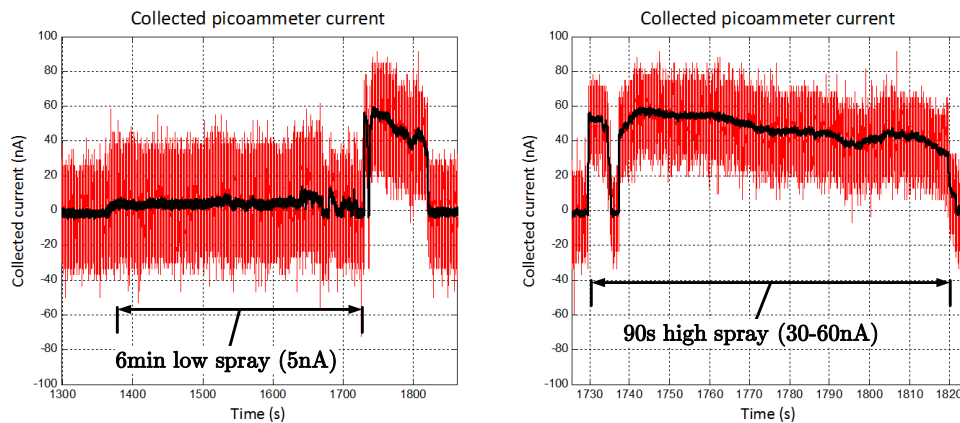
Three chips were tested to validate the setup and demonstrate proof of concept of the spray, as listed in Table B.4. These experiments proved to be particularly long due to the flow control configuration. The first chips were first run with a high flow rate ($10\mu\text{L}/\text{min}$), in order to evaluate the waiting times involved and the quality of the images that could be recorded.

For die 43, the flow rate was adjusted to the much lower value of $0.2\mu\text{L}/\text{min}$ with 3000V applied on the emitter. In all cases, high voltage was applied before flow was driven. Spray started after just over 6 hours wait and continued for about 7m30s with this flow rate. It stopped when the flow rate was manually reduced to $0.05\mu\text{L}/\text{min}$. Following this, it was not possible to re-initiate spray and electrical breakdown eventually occurred. During the first 6 minutes of spray, collected current stayed at the relatively low value of 5nA, before increasing suddenly to $\approx 50\text{nA}$. This high spray continued for 90s, except for a brief moment when it stopped completely. Figure B.22 shows the current traces captured in a 2000s period during which spray occurred. The current is relatively noisy, and a 100ms running average is superimposed on the 1000Hz raw data.

Video recording could capture activity in the emitter region although it was difficult to properly see a Taylor cone structure. Screen captures of the video recording are shown in Figure B.23, focusing on the period when spray initiates. Synchronisation of the video and collected current measurements was done using the timestamps of the video and collected current result files generated by MATLAB. The video showed subtle features for the first 6 minutes and an apparent widening of the emitter around the time when high spray initiated. This widening could be due to a degradation of the Parylene-C in contact with the ionic liquid or may be an optical effect due to a widening of the emission site.



(a) Collected current measurements of 2000s period during which spray occurred with insulator/buried die 43.



(b) Close-up view of collected current corresponding to Region 1 in image (a).

(c) Close-up view of collected current corresponding to Region 2 in image (a)

Figure B.22: Collected current emitted from d43 emitter. Spray initiated after > 6 hours at $0.2\mu\text{L}/\text{min}$ flow with 3000V applied and continued for 7m30s, when the flow rate was manually decreased. The first part of the spray was at the low current value of 5nA while the last 90s was at the higher value of 30-60nA, decreasing over time. Red line is raw current data (collected at 1000Hz) while black line is 100ms running average.

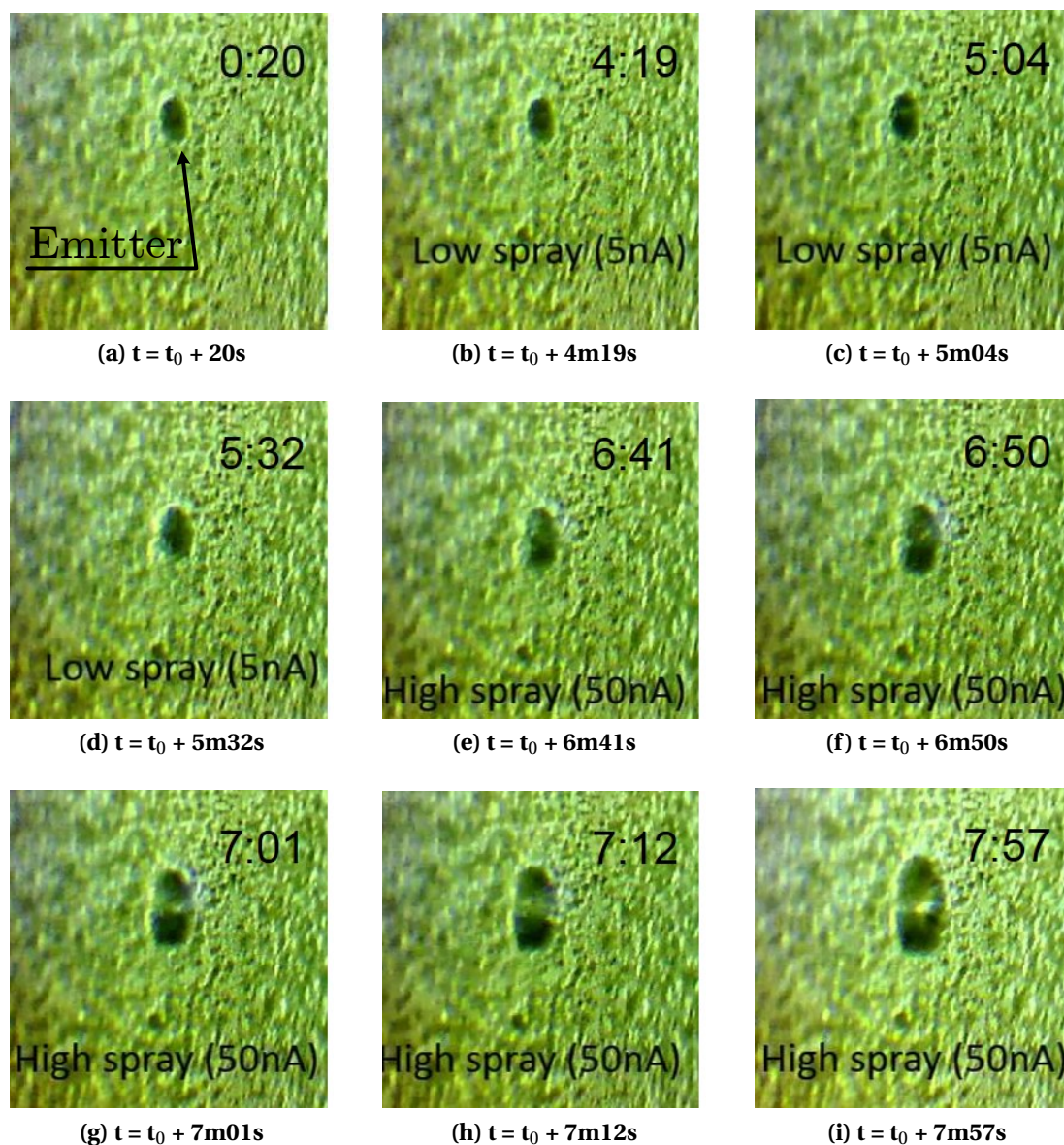


Figure B.23: Still frames extracted from D43 video recording. Although difficult to see, activity is visible when spray initiates (b), in particular during the high spray periods (e-i). t_0 is an arbitrary time when the video recording started, a few minutes before emission. (5 minutes videos were constantly being recorded and deleted to avoid very large files.)

After several more minutes at $0.2\mu\text{L}/\text{min}$, with no current measured, several successive breakdown events occurred in the emitter region, hinting that the Parylene-C insulation separating the extractor and the liquid was no longer sufficient. Screen captures of the first three breakdown events are shown in Figure B.24. The second breakdown event is particularly interesting as it clearly shows that the breakdown initiated at the emitter edge (Figures B.24f and B.24g). Once a first breakdown occurred, clearly the device was unusable. Figure B.25 shows optical images of the assembly and SEM images of the chip after test. The frontside of the emitter is seen to be entirely wetted, even before disassembly, most likely a result of pumping liquid even after the emitter had been destroyed by the breakdown events. The SEM images confirm that the laminated film was attacked, both on the front and back of the emitter.

Yet these results were encouraging in that they proved that spray could be initiated with the buried design chips and sustained for several minutes. This timeframe may in fact already be sufficient in the context of mass spectrometry, where emitters are regularly changed to avoid cross contamination, but could be extended by using a more robust setup with lower flow rate. As with the insulator/bonded chips, reducing wetting using the controlled deposition of non-wetting layers or by patterning the emitter surface would also be beneficial.

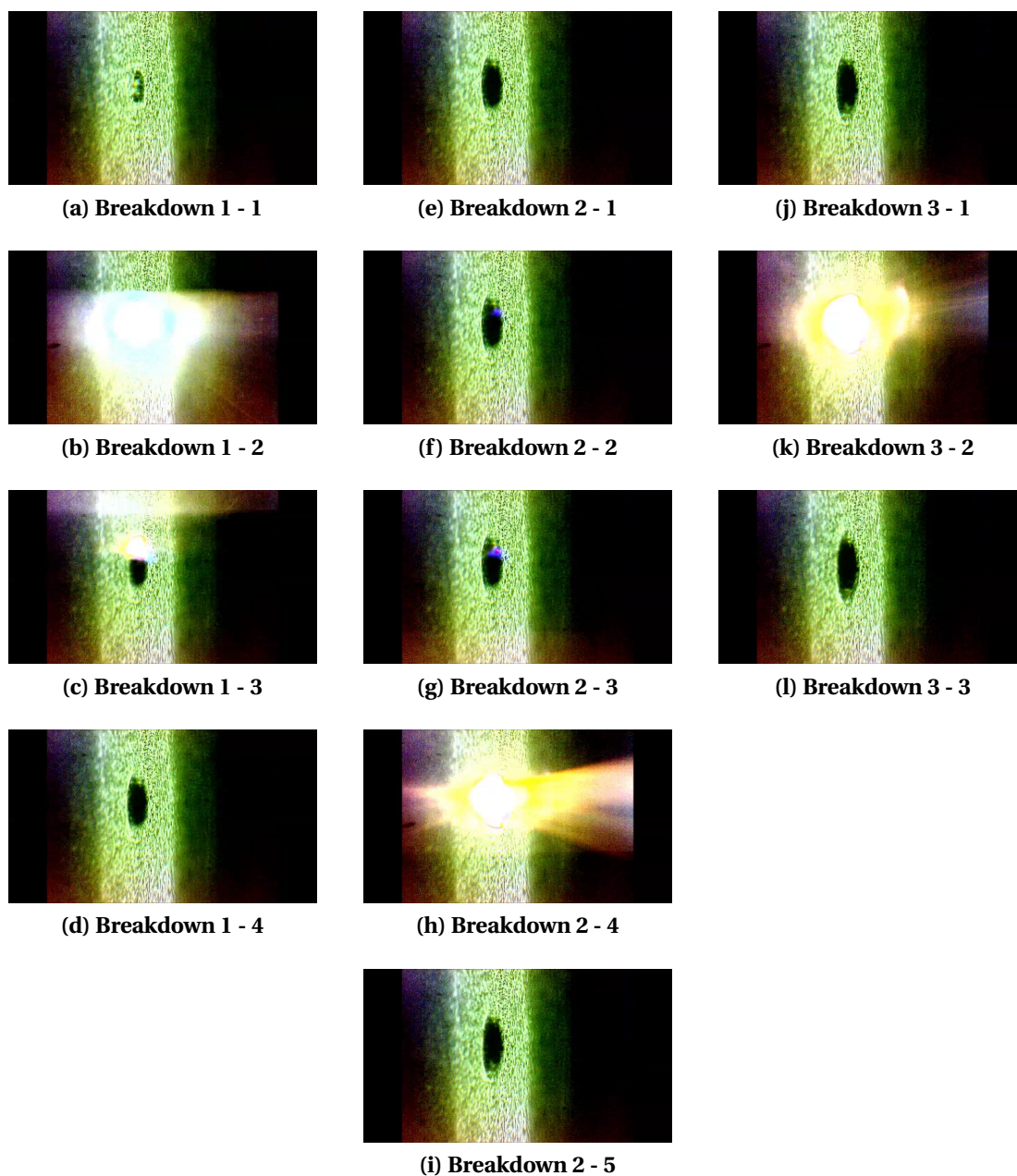
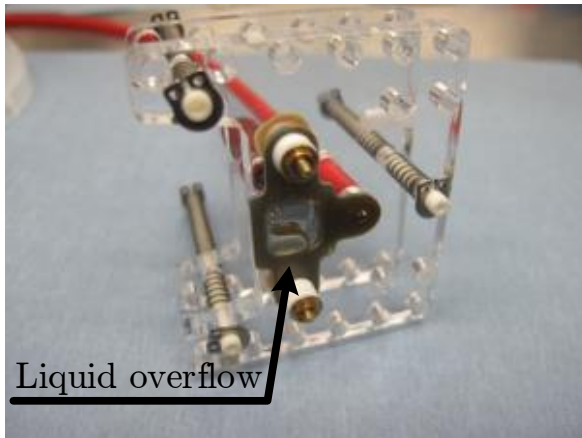
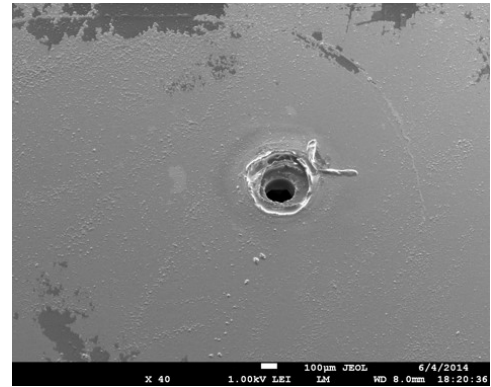


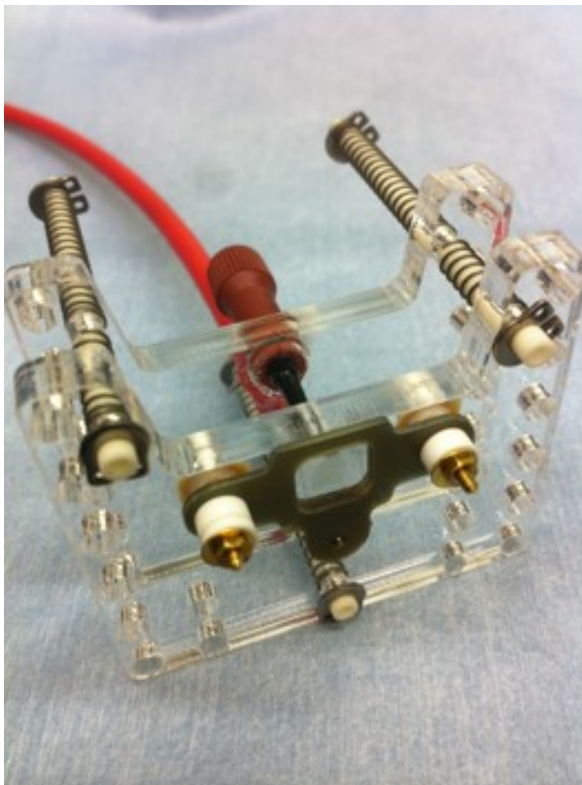
Figure B.24: Still frames extracted from D43 video recording showing three breakdown events. Each frame is separated by 34ms



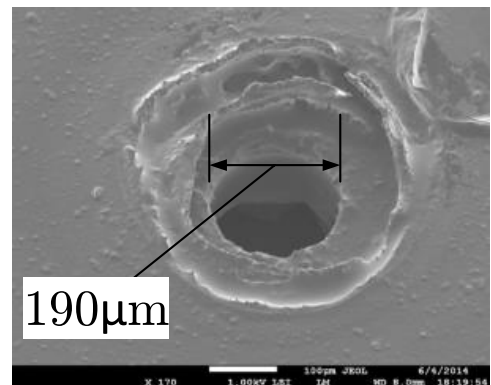
(a) Optical image of assembly after D43 failure



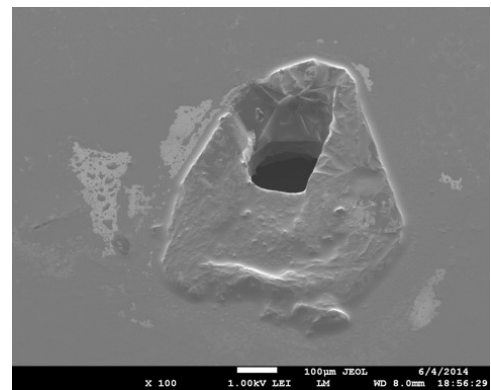
(c) Frontside of D43 after failure



(b) Optical image of assembly after D43 failure



(d) Frontside of D43 after failure



(e) Backside of D43 after failure

Figure B.25: Optical images and SEM micrographs of D43 (insulator/buried) assembly and die after fail. A large pool of liquid is seen on the front of the die (a), which is highly damaged. The emitter feature is almost entirely gone, with the remaining feature approximately corresponding to the glass reservoir opening.

B.5 Insulator chips summary

In this chapter, two novel designs of insulating emitters which could act as Electrospray Ionisers for Mass Spectrometry (ESI-MS) were presented. Insulating emitters have the advantage of being much easier and less costly to produce in addition to using materials compatible with most lab-on-a chip devices. They are also useful to constrain high voltages to functional regions of the devices.

Both designs employed the know how and techniques developed when fabricating the silicon electrospray thrusters. The first design was more conventional, with an extractor bonded to the chip in a final fabrication step. The second, "buried extractor" design, encapsulated the extractor below $10\mu\text{m}$ of Parylene-C. Parylene-C was also used to reduce the inner diameter of the bonded chips, a novel approach to increase emitter fluidic impedance.

Proof of concept operation of both designs was demonstrated. The first design generated sprays up to 730nA, while the second, which also operated with active flow control, emitted up to 60nA of current. The nature of the emitted species, with Time-Of-Flight or Mass Spectrometry, was not measured.

The first design suffered from rapid degradation due to liquid spillage creating leakage current and electrical breakdown, while the second appeared more robust against this problem, at least in the timeframe considered. Breakdown remained a problem for the second design, though, and was observed in the emitter region, possibly due to a degradation of the Parylene-C insulation layer after prolonged exposure to the ionic liquid $EMI - BF_4$. This degradation may have been amplified electrically by the high potential (3000V) applied across this layer.

The second design generally showed more promise, although the collected current levels were an order of magnitude lower. However, the assembly and test setup should be improved to get more reliable spray results. Ideally, the chip should be integrated in the Advion setup, and measurements made using a commonly used solvated analyte instead of $EMI - BF_4$.

In both cases, the chips should be modified to improve liquid containment. Controlled deposition of an hydrophobic layer may help in this regard, although it may also be necessary to modify the design to avoid a planar emission surface. Patterning of an outer edge to the emitters would be a first step provide some improvement.

Step N°	Description	Equipment	Location	Program / Parameters	Target	Remarks	Metrology
0 PROCESS PREPARATION							
0.01	Wafer ordering	N/A	N/A			Ordering wafer with 1.5 µm oxide and RCA cleaning already done	
0.02	Visual inspection	N/A	N/A			Check for scratches and defects	
0.03	Ellipsometry thickness measurement	Sopra GES SE	CMI - Zone 3	5 pt			Start_OxThick
0.04	Wafer thickness measurement	Nikon DIGIMICRO	CMI - Zone 5				WAFER_thick
0.05	Wafer scribe	Diamond tip	CMI - Zone 2 (back)			Scribe: Run, Wafer ID	
1 PHOTOLITHOGRAPHY - [CAP_TOP_1] (Front side - First mask)							
1.01	Dehydration/Priming	TeplaGGAbatch	CMI - Zone 2	7 min 500W/400ml/min O ₂			
1.02	AZ ECI 3027 Coating & bake	RiteTrac	CMI - Zone 1	C. AZ ECI_1um0	1.1 µm	CRITICAL TO HAVE NO EBR	
1.03	PR Expose	SussMicrotec MAG8BA6	CMI - Zone 6	Hard contact / LSZ(10W)		6.6 sec (66 ml/cm²)	
1.04	PR Development & bake	RiteTrac	CMI - Zone 1	DEV_AZ_ECI_1um0			
1.05	Backside cleaning	Spin-Rinse-Dry	CMI - Zone 1	Recipe 1			
1.06	Visual inspection	Nikon Optiphot 200 (or equivalent)	CMI - Zone 1	Resolution and alignment, 5pt			Cap_Top_1_CD_DEV
2 OXIDE ETCH (ANISOTROPIC RIE)							
2.01	Dry Oxide Etch	SPTS	CMI - Zone 2	SiO ₂ _PR2:1	1.5 µm	4min	
2.02	Ellipsometry thickness measurement	Sopra GES SE	CMI - Zone 3	2 pt			
2.03	Visual inspection	Nikon Optiphot 200 (or equivalent)	CMI - Zone 1	Resolution, 5pt			Cap_Top_1_CD_HM
2.04	Dry resist strip	TeplaGGAbatch	CMI - Zone 2	10 min 500W/400ml/min O ₂			
2.05	Kapton tape application	N/A					
3 SILICON ETCH (ANISOTROPIC DRIE)							
3.01	Dry Silicon Etch	Alcatel AMS 200	CMI - Zone 2	SOI_ACCURATE--	50 µm	End point detection not working, 13min	
3.02	Etch depth measurement	Bruker Dektak XT surface profiler	CMI - Zone 4	2 pt on test structures			Cap_Top_1_Depth
3.03	Ellipsometry thickness measurement	Sopra GES SE	CMI - Zone 3	5 pt			Cap_Top_1_OxThick
3.04	Ellipsometry thickness measurement	Sopra GES SE	CMI - Zone 3	2 pt			Cap_Top_1_BoxThick
3.05	Visual inspection	Nikon Optiphot 200 (or equivalent)	CMI - Zone 2				
4 WAFER CLEANING							
4.01	Kapton tape removal 1	Wetbench	CMI - Zone 6	Remove tape while submersed in acetone			
4.02	Kapton tape removal 2 - Rinse	Wetbench	CMI - Zone 6	Rinse in isopropanol			
4.03	Kapton tape removal 3	Wetbench	CMI - Zone 6	Rub away excess glue with q tip			
4.04	Piranha1: H ₂ SO ₄	Ultrafab Wetbench	CMI - Zone 2			Add 200ml H2O2	
4.05	Piranha2: H ₂ SO ₄	Ultrafab Wetbench	CMI - Zone 2				
4.06	Rinse (QDR)	Ultrafab Wetbench	CMI - Zone 2				
4.07	Rinse (Trickle Tank)	Ultrafab Wetbench	CMI - Zone 2		12 MΩ*cm		
4.08	Spin Rinser Dryer	Semtool	CMI - Zone 2				
4.09	O2 clean	TeplaGGAbatch	CMI - Zone 2	10 min 500W/400ml/min O ₂			
4.1	Visual inspection	Nikon Optiphot 200 (or equivalent)	CMI - Zone 1				
5 PHOTOLITHOGRAPHY - [CAP_BOT_1] (Back side - Front to back alignment)							
5.01	Dehydration/Priming	TeplaGGAbatch	CMI - Zone 1	7 min 500W/400ml/min O ₂			
5.02	AZ ECI 3027 Coating & bake	RiteTrac	CMI - Zone 1	C. AZ ECI_1um0	1.1 µm	CRITICAL TO HAVE NO EBR	
5.03	PR Expose	SussMicrotec MAG8BA6	CMI - Zone 6	Hard contact/LSZ(10W)/Front-to-back		66ml/cm2	
5.04	PR Development & bake	RiteTrac	CMI - Zone 1	DEV_AZ_ECI_1um0			
5.05	Backside cleaning	Spin-Rinse-Dry	CMI - Zone 1	Recipe 1			
5.06	Visual inspection	Nikon Optiphot 200 (or equivalent)	CMI - Zone 1				
6 OXIDE ETCH (ANISOTROPIC RIE)							
6.01	Dry Oxide Etch	SPTS	CMI - Zone 2	SiO ₂ _PR2:1	1.0 µm	4min	
6.02	Ellipsometry thickness measurement	Sopra GES SE	CMI - Zone 3	2 pt			

6.03	Dry Silicon Etch	Alcatel AMS 200		CMI - Zone 2	SOI_ACCURATE--	1 µm	To pattern alignment marks into silicon	
6.04	Dry resist strip	TeplaGGAbatch (or equivalent)		CMI - Zone 2	10 min 500W/400ml/min O ₂			
7 SILICON ETCH (ANISOTROPIC DRIE)								
7.01	Dry Silicon Etch	Alcatel 601		CMI - Zone 2	SI_ambian2	380 µm	End point detection not working. About 45min	
7.02	Etch depth measurement	Bruker DekTak XT surface profiler		CMI - Zone 4	2 pt on test structures			Cap_Bot_1_Depth
7.04	Ellipsometry thickness measurement	Sopra GES SE		CMI - Zone 3	2 pt on test structures			Cap_Bot_1_BoxThick
7.04	Visual Inspection	Nikon Optiphot 200 (or equivalent)		CMI - Zone 2				Cap_Bot_1_CaparyVision
7.05	Visual Inspection	Nikon Optiphot 200 (or equivalent)		CMI - Zone 2				Cap_Bot_1_CapID
8 WAFER CLEANING								
8.05	Piranha1: H ₂ SO ₄	Ultrafab Wetbench		CMI - Zone 2			Add 200ml H2O2	
8.06	Piranha2: H ₂ SO ₄	Ultrafab Wetbench		CMI - Zone 2				
8.07	Rinse (QDR)	Ultrafab Wetbench		CMI - Zone 2				
8.08	Rinse (Trickle Tank)	Ultrafab Wetbench		CMI - Zone 2		12 MΩ*cm		
8.09	Spin Rinser Dryer	Semtool		CMI - Zone 2				
8.1	O2 Clean	TeplaGGAbatch		CMI - Zone 2	10 min 500W/400ml/min O ₂			
8.11	Visual Inspection	Nikon Optiphot 200 (or equivalent)		CMI - Zone 1				
9 PHOTOLITHOGRAPHY - [CAP_TOP_2] (Front side - Laminated Resist - Front to front)								
9.01	Priming	TeplaGGAbatch (or equivalent)		CMI - Zone 2	10 min 500W/400ml/min O ₂			
9.02	Dehydration	Hot plate or oven		CMI - Zone 1	5 min @ 100°C or 30 min @ 150°C			
9.03	MAX5015 lamination	PhotoPro33		CMI - Zone 13	100°C/Speed 2/Mount		CRITICAL TO SKIP POST-LAMINATION BAKE	
9.05	PR Expose	MJB4		CMI - Zone 13	20-65mJ/cm2 (3 sec)		CRITICAL TO SKIP POST-EXPOSURE BAKE	
9.07	PR Development: Na ₂ CO ₃ 1%	Wetbench		CMI - Zone 13	60 sec		Use submerged pliette to jet developer around, especially in large areas	
9.08	Rinse	Wetbench		CMI - Zone 13			Only rinse as long as it takes to transport beaker to spin dryer	
9.09	Fast dry	Manual resist spinner		CMI - Zone 13	STD-3000-RPM			
9.10	Visual Inspection	Nikon Optiphot 200 (or equivalent)		CMI - Zone 2	Resolution and alignment			Cap_Top_2_Align
10 OXIDE ETCH (ANISOTROPIC)								
10.01	Dry Oxide Etch	SPTS		CMI - Zone 2	SiO ₂ _PR2:1	1.5 µm	4min	
10.02	Visual Inspection	Nikon Optiphot 200 (or equivalent)		CMI - Zone 2				
11 PLASMA ETCH (ISOTROPIC & ANISOTROPIC)								
11.01	Isotropic Plasma Etch	Alcatel AMS 200		CMI - Zone 2	SI_isotrope_bias	8 µm	about 2min total	
11.02	Visual Inspection	Nikon Optiphot 200 (or equivalent)		CMI - Zone 2	2 pt on test structures		May need to re-etch to complete	Cap_Top_2_CD_IsotEtch
11.03	Anisotropic Plasma Etch	Alcatel AMS 200		CMI - Zone 2				
11.04	Visual Inspection	Nikon Optiphot 200 (or equivalent)		CMI - Zone 2	5 pt			
11.05	Etch depth measurement	Bruker DekTak XT surface profiler		CMI - Zone 4	2 pt on test structures			Cap_Top_2_Depth
11.06	PR Stripping: SVC-14	Wetbench		CMI - Zone 13				
11.07	Rinsing	Wetbench		CMI - Zone 13				
11.08	N2 Gun drying	Spin dryer		CMI - Zone 13				
12 OXIDE HARD MASK REMOVAL								
12.01	Descum	TeplaGGAbatch		CMI - Zone 1	10 min 500W/400ml/min O ₂			
12.02	BHF Etch	Plade oxide wetbench		CMI - Zone 2	30 min	1.5 µm		
12.03	Rinse (FFR)			CMI - Zone 2				
12.05	Rinse (Trickle Tank)			CMI - Zone 2				
12.06	Spin Rinser Dryer	Semtool		CMI - Zone 2				
12.07	Rinse (Trickle Tank)			CMI - Zone 2				
12.07	Spin Rinser Dryer			CMI - Zone 2				
12.08	Descum	Semtool		CMI - Zone 1	7 min 500W/400ml/min O ₂			
12.09	Visual Inspection	TeplaGGAbatch		CMI - Zone 2				
12.09	Visual Inspection	µScope & SEM		CMI - Zone 2				
13 HF VAPOUR PHASE RELEASE								
13.01	Vapor HF	Idonus VHF		CMI - Zone 5		2.0 µm		
13.02	Visual Inspection	µScope & SEM		CMI - Zone 6				

Step N°	Description	Equipment	Training received ?	Location	Program / Parameters	Target	Remarks	Metrology
PROCESS PREPARATION								
0.01	Wafer ordering	N/A	Yes					
A01 GLASS WAFER PREPARATION								
A01.01	Handout wafers for backgrind	N/A	N/A	N/A				
A01.02	Backgrind	DAG810	N/A	CMI+ - Zone 11			300µm handle remaining	
A01.03	Apply protective tape on backside	Powatec Wafer Mounter P-200	N/A	CMI+ - Zone 10				
A01.04	CMP	Mecapol EA60	Yes	CMI - Zone 5	Any pad: 5/85/80; Slurry 1501-50	5µm	15minutes to hide grinding patterns. 150um ring	
A01.05	Remove protective tape	Powatec UV Curing U-200	N/A	CMI+ - Zone 10				
A01.06	Wafer thickness measurement	Nikon DIGIMICRO	N/A	CMI - Zone 5			Glass_Thick	
A01.07	Ship wafers to Icoflex	N/A	N/A					
A01.08	Inspection	Nikon Optiphot 200 (or equivalent)	N/A	CMI - Zone 1				
B02 PHOTOGRAPHY - [EXT_DEVICE] [Front side - First mask]								
B02.01	Dehydration/Priming	Plasma O2	Yes	CMI - Zone 2	10 min 500W 400ml/min O2			
B02.02	AZ ECI 3027 Coating & bake	RiteTrac	Yes	CMI - Zone 1	C_AZ_ECI_1um5	1.5 µm		
B02.03	PR Expose	SussMicrotec MA6&BA6	Yes	CMI - Zone 1	Hard contact / L52(10W)		7.5 sec (75 ml/cm²)	
B02.04	PR Development & bake	RiteTrac	Yes	CMI - Zone 1	DEV_AZ_ECI_1um5			
B02.05	Backside cleaning	Spin-Rinse-Dry	Yes	CMI - Zone 1	Recipe 1			
B02.06	Inspection	Nikon Optiphot 200 (or equivalent)	N/A	CMI - Zone 1				
B03 SILICON ETCH (ANISOTROPIC DRIE)								
B03.01	Dry Silicon Etch	Alcatel AMS 200	Yes	CMI - Zone 2	SOI_ACCURATE--	55 µm	End point detection not working. 11minh	
B03.02	Etch depth measurement	Brüker DekTak XT surface profiler	Yes	CMI - Zone 4	2 pt on test structures			Ext_Dev_Depth
B03.03	Dry resist strip	TephaGibatch (or equivalent)	Yes	CMI - Zone 2	10 min 500W/400ml/min O2			
B03.04	Inspection	Nikon Optiphot 200 (or equivalent)	N/A	CMI - Zone 2				
C01 WAFER CLEANING								
C01.01	Piranha1: H2SO4	Ultrafab Wetbench	Yes	CMI - Zone 2			Add 200ml H2O2	
C01.02	Piranha2: H2SO4	Ultrafab Wetbench	Yes	CMI - Zone 2				
C01.03	Rinse (QDR)	Ultrafab Wetbench	Yes	CMI - Zone 2				
C01.04	Rinse (Trickle Tank)	Ultrafab Wetbench	Yes	CMI - Zone 2		12 MΩ*cm		
C01.05	Spin Rinser Dryer	Semitoool	Yes	CMI - Zone 2				
C01.06	Oxygen plasma clean	Plasma O2	Yes	CMI - Zone 2	10 min 500W 400ml/min O2			
D01 WAFER BONDING								
D01.07	Wafer alignment	SussMicrotec MA6&BA6	Yes	CMI - Zone 1	Alignment without spacers			
D01.08	Anodic bonding	SBG bonder	Yes	CMI - Zone 6	SDA_Si_Py_Vac_Is		Anodic bonding of SOI to Pyrex	
D01.09	Inspection	Nikon Optiphot 200 (or equivalent)	N/A	CMI - Zone 1	Alignment; 2pt	5µm		Bond_Align
E01 WAFER CLEANING (SODIUM)								
E01.10	HCl cleaning procedure...	Ultrafab Wetbench	No	CMI - Zone 5				
E01.11	Rinse (QDR)	Ultrafab Wetbench	No	CMI - Zone 5				
E01.12	Rinse (Trickle Tank)	Ultrafab Wetbench	No	CMI - Zone 5				
E01.13	Spin Rinser Dryer	Semitoool	No	CMI - Zone 5				
F02 PARYLENE DEPOSITION (Front side - Blanket)								
F02.01	Apply protective tape on backside	Powatec Wafer Mounter P-200	N/A	CMI+ - Zone 10			SKIP THIS STEP	
F02.02	Handout wafers for parylene deposition		N/A				SKIP THIS STEP	
F02.03	Parylene deposition	Comelec C-30-S	N/A	CMI+ - Zone 10		2µm	SKIP THIS STEP	
F02.04	Remove protective tape	Powatec UV Curing U-200	N/A	CMI+ - Zone 10			SKIP THIS STEP	
F02.05	Inspection	Nikon Optiphot 200 (or equivalent)	N/A	CMI - Zone 2			SKIP THIS STEP	
G03 WAFER THINNING								

C03.01	Handout wafers for backgrind			N/A					
C03.02	Backgrind	DA6810		N/A				320um	60um handle remaining. Ask to leave tape on backside if possible
C03.03	Apply protective tape on backside	Powatec Wafer Mounter P-200		N/A					
C03.04	CMP	Mecapol E460		Yes					
C03.05	Rinse and dry	Mecapol E460		Yes					
C03.06	Remove protective tape	Powatec UV Curing U-200		N/A					Rinse well with water gun right away, then with fountain
C03.07	Wafer thickness measurement	Nikon DIGIMICRO		N/A					
C03.08	Inspection	Nikon Optiphot 200 (or equivalent)		N/A					Elect_Thick
BHF Clean									
C03.09	BHF Etch	Plade oxide wetbench		Yes		30 sec			probably ok to leave up to 60 sec
C03.10	Rinse (FFR)	Plade oxide wetbench		Yes					
C03.11	Rinse (Trickle Tank)	Plade oxide wetbench		Yes					
C03.12	Spin Rinser Dryer	Semitoool		N/A					
C03.13	Inspection	Nikon Optiphot 200 (or equivalent)		Yes					
PARYLENE ETCH									
C03.14	Parylene removal	Tepla/Gabbatch (or equivalent)		Yes		10 min 500W/400m/min O ₂			SKIP THIS STEP
C03.15	Inspection	Nikon Optiphot 200 (or equivalent)		N/A					SKIP THIS STEP
C04 SiO ₂ SPUTTERING									
C04.02	SiO ₂ sputtering	Spider 600		Yes				2um	
C04.03	Ellipsometry thickness measurement	Sopra GES SE		Yes		5 pt			Insulator_ OxThick
C05 SHADOW MASK ALIGNMENT 1									
C05.01	Shadow mask alignment	SussMicrotec MA68BA6		Yes					
C05.02	Inspection	µScope & SEM		Yes					
C06 METAL DEPOSITION 1									
C06.01	Chromium/Gold evaporation	LAB 600H		Yes				0.02/0.2	
C06.02	Shadow mask disassembly	N/A		N/A					
C06.03	Inspection	Nikon Optiphot 200 (or equivalent)		Yes					
C07 SHADOW MASK ALIGNMENT 2									
C07.01	Shadow mask alignment	SussMicrotec MA68BA6		Yes					
C07.02	Inspection	Nikon Optiphot 200 (or equivalent)		Yes					
C08 METAL DEPOSITION 2									
C08.01	Chromium/Gold evaporation	LAB 600H		Yes				0.02/0.2	
C08.02	Shadow mask disassembly	N/A		N/A					
C08.03	Inspection	Nikon Optiphot 200 (or equivalent)		Yes					Elect_Align

SIMON DANDAVINO

PERSONAL INFORMATION

email: sdandavino@gmail.com

phone: +41 78 905 9785

WORK EXPERIENCE

04/2008-06/2010
Bromont, Canada

Engineering Professional, DALSA SEMICONDUCTOR

Managed a project development team for a next generation MEMS product · interacted with upper management and clients, updating on project status and problem resolution · led problem resolution teams (8D format) for critical production line issues · designed and characterized electro-mechanical test structures for process monitoring and long term reliability control · monitored process performance through in-line data analysis and SPC charts.

Ref.: Stéphane MARTEL · +1 (450) 534 2321 · stephane.martel@teledynedalsa.com

01/2006-09/2007
Copenhagen,
Denmark

Translator, WORKBRIDGE (Part-time)

Performed both English to French and French to English translations of software interfaces and technical/legal documents · prepared and conducted on-site, operation specific, training sessions.

Ref.: Nicolas GRAFF ANDERSEN · +45 33 44 75 00 · info@workbridge.com

EDUCATION

09/2010-10/2014
Neuchâtel,
Switzerland

PhD, ECOLE POLYTECHNIQUE FÉDÉRALE DE LAUSANNE

Thesis: *Microfabricated Electrospray Thrusters for a Modular Spacecraft Propulsion System*

Description: This work focused on the development of a revolutionary micropropulsion technology that would enable space exploration missions with small spacecraft.

The work performed included the detailed design, modeling and simulations of the devices, as well as their cleanroom fabrication and characterization in relevant environments.

Advisor: Prof. Herbert SHEA

09/2005-09/2007
Copenhagen,
Denmark

M.Sc in Electronics, TECHNICAL UNIVERSITY OF DENMARK

Thesis: *Development of Resonator Based Atomic Oxygen Sensor System for Spacecraft Applications* · Received grade: Outstanding (12/12)

Description: This thesis describes a novel microfabricated sensor capable of the precise detection of atomic oxygen in the Earth's upper atmosphere.

The thesis included the entire design process, from the selection of an application to performance testing, including modeling, design and fabrication.

Advisors: Prof. Zachary DAVIS, Dr. Jan HALES, & Prof. Winnie SVENDSEN

09/2001-05/2005
Montreal, Canada

B.Eng. in Electrical Engineering, MCGILL UNIVERSITY

Testing Manager for McGill University's solar vehicle team · J.W. McConnell Entrance scholarship · McGill Rowing Club · McGill Ultimate Team, Exchange semester with the University of New South Wales in Sydney, Australia

PUBLICATIONS

*Journal of
Micromechanics
and
Microengineering,*
24(7), 075011

Microfabricated electrospray emitter arrays with integrated extractor and accelerator electrodes for the propulsion of small spacecraft

Authors: Simon DANDAVINO, Caglar ATAMAN, Charles RYAN, Subha CHAKRABORTY, Daniel COURTNEY, John P.W. STARK, Herbert SHEA

*Journal of the
American Society
for Mass
Spectrometry,*
25(8), 136473.

A ToF-MS with a Highly Efficient Electrostatic Ion Guide for Characterization of Ionic Liquid Electrospray Sources

Authors: Subha CHAKRABORTY, Caglar ATAMAN, Daniel COURTNEY, Simon DANDAVINO, Herbert SHEA

OTHER INFORMATION

Languages

FRENCH · Mother tongue

ENGLISH · Fluent

SPANISH · Basic (A1-A2)

GERMAN · Basic (A1 - simple words and phrases only)

DANISH · Basic (A1 - simple words and phrases only)

*Communication
Skills*

Strong ability to synthesize and explain complex information acquired through several international conference presentations and taught university classes.

Good didactic skills gained through trainer experience at Workbridge, supervising students and sports team coaching

*Organizational /
managerial skills*

Excellent project management skills as reflected by the successful GGES REXUS 12 project, a student experiment launched in 2012 on a sounding rocket from Kiruna, Sweden

Strong team-leading abilities acquired as coach and captain of beginner and competitive Ultimate Frisbee teams

Job-related skills

Strong ability to work and thrive within a team.

Good resilience acquired through work in the industry and as a doctoral student

Great curiosity and interest in other cultures resulting in travel to over 30 countries on 6 continents

Computer Skills

Windows, Mac, Matlab, SolidWorks, Coventor, ANSYS, Latex, FileMaker Pro, Visio, Microsoft Project.

Awards

2012 & 2013 · Swiss Open Champion, Flying Angels Bern (Ultimate Frisbee)

2011 · European Open Champion, Flying Angels Bern (Ultimate Frisbee)

2001 · McGill University Certificate of Merit

Interests

Competitive Ultimate Frisbee · Travelling · Cinema · Learning

September 15, 2014